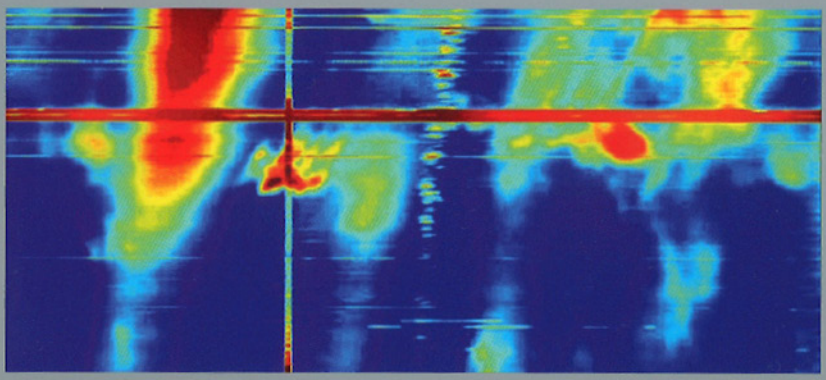
V. Melnik, H. O. Rucker

Decameter Radio Emission of the Sun



AUSTRIAN
ACADEMY
OF SCIENCES
PRESS

V. Melnik, H. O. Rucker

Decameter Radio Emission of the Sun

Planetery Radio Emmissions

V. Melnik, H. O. Rucker

Decameter Radio Emission of the Sun

AUSTRIAN
ACADEMY
OF SCIENCES
PRESS

Published with the support of the DDr. Franz-Josef Mayer-Gunthof Wissenschafts- und Forschungsstiftung and the Open Access Funds of the OEAW.



The Commission for Astronomy of the Austrian Academy of Sciences supported the work on this volume.

All rights reserved.
Copyright © Austrian Academy of Sciences, Vienna 2024
ISBN 978-3-7001-9568-9
Proof Reading: Lektorat Berlin, Berlin
Printed: Ferdindand Berger & Söhne, Horn
https://epub.oeaw.ac.at/9568-9
https://verlag.oeaw.ac.at
Made in Europe.

Accepted by the publication committee of the Division of Mathematics and
Natural Sciences of the Austrian Academy of Sciences by:

Andrea Bachmaier, Christa Cuchiero, Karlheinz Erb, Gerhard Herndl, Sofia Kantorovich,
Josef Smolen, Christoph Spötl, Miriam Unterlass

This publication was subject to international and anonymous peer review.
Peer review is an essential part of the Austrian Academy of Sciences Press evaluation process.
Before any book can be accepted for publication, it is assessed by international specialists and
ultimately must be approved by the Austrian Academy of Sciences Publication Committee.

The paper used in this publication is DIN EN ISO 9706 certified
and meets the requirements for permanent archiving of written cultural property.

Contents

1 Introduction **13**

2 Decameter Radio Telescopes UTR-2, URAN-2 and GURT **17**
2.1 Radio telescope UTR-2 and interferometer URAN . . 17
2.2 GURT 22
2.3 Comparative analysis of solar observations by the single antenna and large array 24
2.3.1 Space observations by the WIND/Waves instrument at 9 MHz – 13.8 MHz 29

3 Solar Activity **35**
3.1 History: the Sun as a goddess 35
3.2 First observations of the Sun 35
3.3 First scientific observations and measurements 37
3.4 Solar phenomena at active regions 38
3.5 Explosive events 40

4 Radio Emission of the Quiet Sun **43**
4.1 Radio emission of the quiet Sun at decameter wavelengths 43
4.1.1 Observations of the quiet Sun by URAN-2 . . . 46
4.1.2 Observations of the quiet Sun by UTR-2 48
4.2 Sizes and brightness temperature of the quiet Sun at decameter wavelengths 51
4.2.1 Radio emission of the quiet Sun at 20 and 25 MHz – sizes and brightness temperatures . . . 51

5 Type III Bursts **61**
5.1 Introductory remarks 61
5.2 Fast Type III bursts 66
5.3 Type III bursts with fine time structure 73
5.4 Type IIIb 75
5.4.1 Observations 77
5.5 Powerful Type III bursts 80
5.6 Type III bursts with changing sign of drift rate 85
5.7 "Dog-leg" Type III bursts at the decameter wavelengths 90
5.7.1 Observations 92

5.7.2 Interpretation of the observations 95
5.8 Decameter Type IIIb-III pairs 97
5.8.1 Observations 99
5.8.2 Discussion 103
5.9 Trios 108
5.9.1 Trio of Type IIIb and Type III bursts 108
5.10 Spatial sizes and heights of Type III radio emission at the decameter wavelengths 115
5.10.1 Sizes of Type III sources and heights of their radio emission at frequencies 20 and 25 MHz . 115
5.11 Inverted U- and J-bursts 124
5.12 Observations of the solar U-bursts harmonic pair with new radio telescope GURT 131

6 Type II Bursts **139**
6.1 Solar Type II bursts at frequencies 10 MHz - 30 MHz 139
6.1.1 Study of the decameter Type II bursts with rich fine and superfine structures 148
6.2 Type II burst with herringbone structures 155
6.2.1 Analysis and discussion 158
6.3 Tadpoles - a new type of solar radio bursts 163

7 Type IV Bursts **171**
7.1 Decameter Type IV burst associated with a behind-limb CME observed on November 7, 2013 171
7.1.1 Observations 172
7.1.2 Interpretation of the observations 175
7.2 Decameter Type IV bursts observed in the years 2003-2006 180
7.3 Properties of decameter Type IV bursts 188
7.4 "Fingerprint" fine structure of decameter Type IV burst 194
7.4.1 Sub-bursts in emission and absorption 207
7.5 Oscillations of Type IV bursts 211
7.5.1 Quasi-periodic variations of radio emission . . . 215
7.6 Absorption bursts 221
7.6.1 Observations and their analysis 223
7.6.2 Level of absorption 227
7.6.3 Size of absorbing region 230

8 Drift Pairs Bursts **233**
8.1 Properties of decameter drift pairs 233
8.1.1 Drift pairs in the decameter range 233
8.2 Polarization of drift pairs 243

9 S-Bursts **249**
9.1 Properties of decameter S-bursts 249
9.2 Groups of decameter S-bursts 254
9.2.1 Observations 255
9.2.2 Analysis of observations 257

10 Spikes **261**
10.1 Decameter spikes 261
10.1.1 Observations 261
10.1.2 Dependence of decameter-spike parameters on the location of active regions 264
10.2 Storm of decameter spikes 267
10.2.1 The storm of decameter spikes during the event of June 14, 2012 267

11 Unusual Solar Bursts **277**
11.1 Caterpillar bursts 277
11.1.1 Discussion 283
11.2 New class of solar bursts with cut-off frequency 286

12 Propagation and Radio Emission of Electron Beams in the Solar Corona **295**

13 Radio Seismology of the Outer Solar Corona **299**
13.1 Observations and their interpretation 302

Bibliography **303**

Index **330**

Acknowledgements

This book comprises a condensed and systematized collection of scientific results about the decameter radio emission of the Sun, obtained by the world-largest radio telescope in the decameter wavelength regime, UTR-2, at Kharkiv (Ukraine) and by the radio telescope URAN-2 at Poltava (Ukraine). The authors emphasize the efforts of the scientists, engineers, and technicians involved in providing ground- and space-based instruments for solar observations: A. Konovalenko, V. Zakharenko, O. Ulyanov, N. Kalinichenko, A. Stanislavsky, V. Dorovskyy, N. Shevchuk, M. Sidorchuk, S. Stepkin, V. Shepelev, P. Tokarsky, I. Bubnov, S. Yerin, A. Brazhenko, A. Frantsuzenko, E.P. Abranin, A. Lecacheux, P. Zarka, P. Kleewein, G. Mann, J.-L. Bougeret, M.L. Kaiser, M. Maksimovic, C. Briand, Y. Leblanc, N. Gopalswamy, S. Poedts, J. Magdalenic, T. Zaqarashvily, B. Shergelashvili, and M. Panchenko. The authors are grateful to M. Scherf for the editorial design.

1 Introduction

Soon after the discovery of radio waves the search for celestial radio signals started. Sir Oliver Lodge (Lodge, 1906) and Charles Nordmann (Nordmann, 1903) were among the first to experimentally try to detect radiation from the Sun. By studying statics and interferences which made trouble in commercial radio telephony, Karl Jansky (member of the staff of the Bell Telephone Laboratories) in January 1932 detected a signal he initially suspected originated from the Sun. However, Jansky (Jansky, 1982) correctly attributed this "cosmic radio noise" to the center of our galaxy.

This "cosmic radio noise" measured as weak and thus considered of no practical importance, it was not before the days of World War II that by means of the British antiaircraft radars Stanley Hey and his team (1942) could attribute the source of interference to the Sun, published years later (Hey, 1946). Also G.C. Southworth (Bell Telephone Laboratories) in 1942 independently detected radio emission of the Sun. And in 1943 Grote Reber (Reber, 1984) was the third to independently discover the Sun as source of radio waves. Investigations by J.S. Hey provided evidence that outbursts of radio energy were connected to the presence of a large and active sunspot on the visible disk of the Sun.

Ongoing research determined that solar radio emission evidently is based on a non-thermal emission process. Theoretical explanation led to the general assumption that electron streams initiate plasma oscillations, subsequently converted into radio waves. These electromagnetic waves have frequencies close to the local plasma frequency and can be emitted where the solar electron density enables radio waves to escape.

Solar radio bursts connected to solar flares exhibit intense outbursts, and their spectral appearance indicates a rapid motion of the radio source within the solar corona. Decreasing electron density with increasing distance from the Sun is combined with diminish-

ing plasma frequency, so the movement of the radio source can be tracked via the radio wave signatures in the respective dynamic spectra. It is the structure of these radio wave signatures in the frequency versus time visualization which enables a classification of the radio bursts. A subsequent detailed analysis of corresponding observations leads to the knowledge of the inherent solar plasma parameters, of the radio source motion, and of radio waves characteristics and their propagation. The present book concentrates on the decameter radio emission of the Sun as observed by the giant ground-based Ukrainian UTR-2 and URAN-2 radio telescopes, mainly in the frequency range from 8 MHz to 32 MHz, with a few additional observations from the French Nançay radio telescope and radio waves measurements by the STEREO spacecraft.

The participating UTR-2, URAN-2 radio telescopes, along with the recently constructed GURT, are described in detail in Chapter 2. Despite the advantage of not being limited by terrestrial ionospheric frequencies, space-borne observatories have a significant disadvantage compared to large ground-based radio observatories in terms of the effective antenna area needed to resolve weak solar outbursts and their spectral details.

Chapter 3 is devoted to a short glimpse of history of solar activity observations and defines some fundamental solar parameters. Solar activity comprises active regions on the solar disk and includes explosive events, both closely connected to solar radio bursts. Radio emission of the quiet Sun is the topic of Chapter 4, in detail described by observations of the URAN-2 and UTR-2 radio telescopes, with indications of sizes of radio sources and their brightness temperatures.

The most common – and most studied – components of sporadic solar radio emission are the Type III bursts, described in Chapter 5. Their spectral appearance comprise a frequency range from 1 GHz to 20 kHz, drifting from high to low frequencies, with involved fluxes from a few solar flux units (1 s.f.u. $= 10^4$ Jansky $= 10^{-22}$ W/(m^{2}Hz)) up to 10^6 s.f.u.. Variations of the Type III bursts comprise Type IIIb and "dog-leg" Type III bursts, other variations appear in the dynamic spectra as pairs and trios. Electron streams in closed magnetic structures (arcs or loops) may initiate so-called U-bursts and J-bursts.

Chapter 6 deals with Type II bursts that are associated with shock waves travelling through the solar corona. The newly developed dig-

ital spectropolarimeter as backend facility of the UTR-2 radio telescope enabled the detection of fine structures within the Type II bursts and of a new type of solar radio bursts – the tadpoles. Type IV bursts, analyzed in Chapter 7, are classified in stationary bursts (connected to coronal arcs), and in moving Type IV bursts (connected to Coronal Mass Ejections, CMEs). Interesting features are the so-called "fingerprint" fine structures, absorption bursts, and bursts with quasi-periodic variations due to oscillations of solar trans-equatorial magnetic loops.

Drift pairs bursts (Chapter 8) are another separate class of solar radio phenomena, however associated with Type III bursts. Their characteristic consists of two short features separated by about 1 – 2 s with either forward or reverse drift, depending on their drift from high (low) towards low (high) frequency with regard to time. Chapter 9 focuses on S-bursts, in the past named as „fast drift storm bursts". Investigations revealed an association with the position of active regions on the solar disk. All observed S-bursts appear over the background of other solar radio emissions as e.g., Type III and IIIb bursts. Apparently the S-bursts move through a solar plasma of high level Langmuir turbulence. Solar decameter spikes (Chapter 10) have been categorized as bursts with short duration (< 0.1 s) and narrow frequency bandwidth (1 % – 3 % of observed frequency). The short duration may be related to the rate of particle collisions in the corresponding solar coronal plasma.

To date, all radio bursts could be categorized as specific types, such as Type II, Type III, or Type IV, however there are still unusual solar bursts (Chapter 11) like caterpillar bursts, with a frequency cutoff and apparently generated in a behind-the-limb region of the Sun. They have features such as high-frequency cutoff, half-flux duration, and polarization.

Chapter 12 provides a brief glimpse into the propagation and radio emission of electron beams in the solar corona, where high-energy electrons can generate Langmuir waves at large distances from the injection place. Finally, Chapter 13 deals with radio seismology of the solar corona, already partially addressed in Chapter 7, where the observed periodic oscillations of radio emission is a consequence of oscillating magnetic structures, further triggering Langmuir oscillations. This allows for an estimation of specific plasma parameters of

the outer solar corona.

All present and future observations by ground-based radio telescopes and by spacecraft (e.g. Solar Orbiter) will provide a valuable complement to the rich variety of solar decameter radio emission described in this book.

2 Decameter Radio Telescopes UTR-2, URAN-2 and GURT

By the beginning of the 1970s, a new radio telescope called UTR-2 (Ukrainian T-shape Radio telescope, model 2), one of the largest decameter wavelength instruments in the world, had been constructed and started its operation near Kharkiv (Braude et al., 1978). In the 1970s-80s the UTR-2 system was upgraded with a supplement called URAN (Ukrainian Radio interferometer of the Academy of Sciences), a VLBI system consisting of four smaller radio telescopes in the same frequency range 8 MHz - 32 MHz (Megn et al., 1997). In 2008 construction commenced on a new generation of radio telescope with an area of about 1 km^2 and frequency band 8 MHz - 80 MHz that was referred to as GURT (Giant Ukrainian Radio Telescope) (Konovalenko et al., 2016).

2.1 Radio telescope UTR-2 and interferometer URAN

The UTR-2 radio telescope (Figures 2.1 and 2.2, Table 2.1) has the following distinctive features: large linear dimensions (2 km $\times$ 1km), large effective area (140 000m^2), high filling factor, high directivity (the width of the main beam is about 0.5°), low level of side lobes, wide frequency range (8 MHz - 32 MHz), simultaneous multi-beam capability, electronic control of the beam steering within a wide range of the two sky coordinates, high dynamic range, high interference immunity, flexible configuration, continuous surveillance of the parameters of the radio telescope systems, robustness to climatic factors, reliability, and ecological safety. These features of UTR-2 and its design



Figure 2.1: *The radio telescope UTR-2 consisting of West-East (a) and North-South (b) arms.*

make it a unique instrument, both powerful and flexible enough for solving problems that hinder observations in the decameter waveband.

Fig. 2.2 shows the configuration of the UTR-2 and GURT. UTR-2 is located at coordinates 36°56′29″ E and 49°38′10″ N (Braude et al., 1978). The T-shaped radio telescope is split into 12 subarrays (sections) that form three arms (North, South and West). North and South arms are identical and consist of 720 wideband fat dipoles each (120 rows × 6 dipoles). The West arm consists of 600 dipoles (100 rows × 6 dipoles). Dipoles are spaced in the North-South and East-West directions by 7.5 and 9 m, respectively (in each arm). The radio

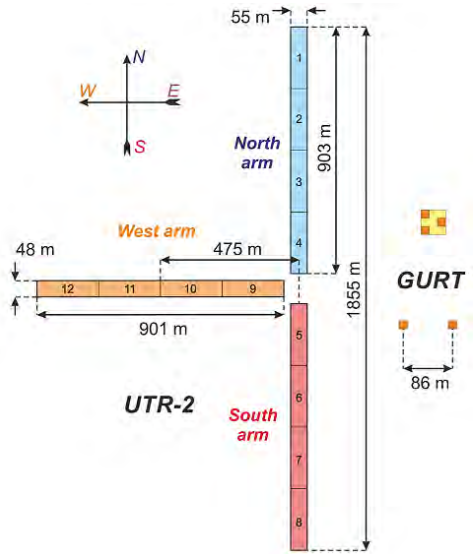


Figure 2.2: *Geometrical configurations of the UTR-2 and GURT radio telescopes.*

Table 2.1: *Main parameters of Ukrainian decameter telescopes. IRA NASU = Institute of Radio Astronomy, National Academy of Sciences of Ukraine; PGO NASU = Poltava Geometrical Observatory, National Academy of Sciences of Ukraine; PMI NASU = Physical Mechanical Institute, National Academy of Sciences of Ukraine.*

Radio telescope	Location	Frequency range, MHz	Maximum effective area, m^2	Number of elements, polarization	Distance from UTR-2 (from the LOFAR Superterp), km	Synthesis or VLBI resolution (λ/D) at 25 MHz
UTR-2	Kharkiv, IRA NASU	8 - 32	140 000	2040, 1 linear	0 (∼2100)	25'×25'
URAN-1	Zmiiv, IRA NASU	8 - 32	5 000	96, 2 linear	42 (∼2050)	59"
URAN-2	Poltava, PGO NASU	8 - 32	28 000	512, 2 linear	153 (∼1950)	16"
URAN-3	Lviv, PMI NASU	8 - 32	14 000	256, 2 linear	946 (∼1150)	2.6"
URAN-4	Odesa, IRA NASU	8 - 32	7 300	128, 2 linear	613 (∼1850)	4"
GURT	Kharkiv, IRA NASU	8 - 80	350	25, 2 linear	0 (∼2100)	20.5°

telescope has a broadband multistage time delay phasing system and a distributed antenna amplification system. At the output of the full radio telescope 5 antenna beams shifted by 0.5° in declination can be formed simultaneously in a similar way. Signals from the 12 sections can also be processed in parallel, allowing implementation of digital aperture synthesis that provides a resolution of about 0.5° in a field of view $2^\circ \times 3^\circ$. Currently the output signals of the five beams (or signals from the outputs of any section, section combinations etc.) are transferred to five dual-input digital signal processors.

It is commonly known that the T-shaped configuration of the radio telescope is equivalent to a "cross" configuration with the dimension of its longest arm in terms of uv-plane coverage, beam shape and width. In particular, whereas the "knife" antenna pattern of "North-South" and "West" arms of UTR-2 at 25 MHz has $20' \times 12^\circ$ and $12^\circ \times 40'$ half power beam widths (HPBW) respectively, their cross-correlation product (pencil beam) is ≈25' for the zenith direction at the same frequency.

It should be mentioned that a correlation radio telescope such as UTR-2 is not sensitive to the galactic background radiation nor to continuous radio objects with an angular size over three degrees because the distances between North, South and West arms are non-zero. The continuous emissions can be recorded separately because the real time dynamic spectra of the total signal from the North-South arm and the signal from West arm, as well as the amplitude and phase of the cross-correlation spectra are processed and recorded by parallel digital signal processors.

The sensitivity of UTR-2 can be derived from the radiometer equation. Its effective area (A_{eff}) when it is pointed to zenith is approximately equal to its geometric area - about 140 000 m^2 at the central operational frequency (20 MHz). The system temperature in the decameter waveband is determined mainly by the galactic background which is ≈40 000 K at 20 MHz. Neglecting the confusion effect, the fluctuation sensitivity ΔS_{min} of the UTR-2 array with an integration time $\Delta t = 1$ h and a bandwidth $\Delta f = 3$ MHz is:

$$S_{sens} = \frac{2kT}{A_{eff}\sqrt{\Delta f \Delta t}} = \frac{2 \times 1.38 \times 10^{-23} \times 4 \times 10^4}{1.4 \times 10^5 \sqrt{3 \times 10^6 \times 3.6 \times 10^3}} \approx 10\,\text{mJy}. \tag{2.1}$$

In general, the sensitivity of UTR-2 varies from a few mJy to several Jy. It depends on the type of observation (subject or not to confusion effects), observing frequency, object coordinates, integration time, frequency resolution, and beam pointing direction (in local coordinates). As illustrated below, the upgraded system enables low-frequency observations with unprecedented qualitative (access to new targets) and quantitative (enhanced sensitivity) characteristics.

The radio telescope UTR-2 is used for observations according to different scientific programs. As a rule,solar observations are carried out on summer months ($\pm$ 3 - 4 hours around central meridian).

A system of decameter interferometers URAN (Ukrainian Radio interferometer of Academy National) was created on the basis of UTR-2 radio telescope (Megn et al., 1997). The system consists of four radio telescopes of smaller sizes (see Fig. 2.3) that can either operate jointly with UTR-2 as a VLBI network (Table 2.1) or record signals independently at each array.

The radio telescope URAN-2 is the second one on effective square (after UTR-2) in the system URAN (Fig. 2.4) (Konovalenko et al., 2016). Its effective square equals to 28 000 m^2. Its beaming is $3.5° \times 7°$ at 20 MHz. The radio telescope URAN-2 can measure polarization. Since 2011 on each day solar observations have been carried out.

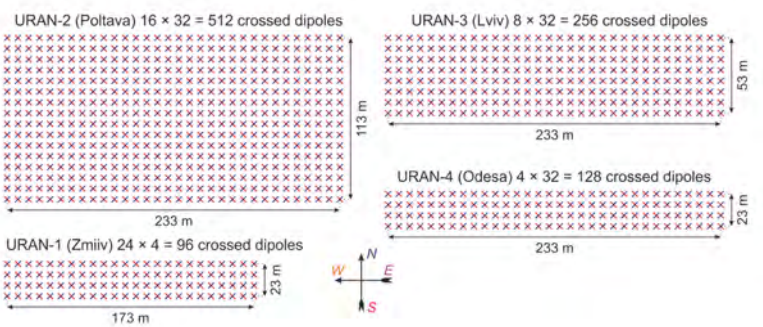


Figure 2.3: *Geometrical configurations of the four URAN radio telescopes.*



Figure 2.4: *The radio telescope URAN-2.*

2.2 GURT

The GURT system is an extension of UTR-2 in terms of spatial dimensions and frequency range located nearby it (Fig. 2.5). The goals of creating this new instrument include the enhancement of UTR-2 functional properties and contribution to the progress of low frequency radio astronomy in synergy with other distant instruments. The basic part of this telescope is a square regular subarray made of 25 active dipoles (5×5) (Konovalenko et al., 2016). The available area of the UTR-2 observatory exceeds one square kilometer. The construction of new subarrays is successive, spanning over a period of time, as resources become available. Five subarrays have already been installed, equipped, and are operational now (2019). The distance between the crossed dipole antenna elements is 3.75 m, the suspension height is 1.6 m. The subarray design provides a wide frequency coverage from 8 to 80 MHz, high sensitivity (the galactic background level exceeds their self-noise by more than 7 dB), and high RFI immunity (achieved due to high dynamic range of the dipole amplifier: input IP3 (intercept point of 3rd order) is 30 dBm, relatively to 1 mW). The effective area at the central frequency is about 350 m^2 (as confirmed by computer simulations and direct measurements) The HPBW of a single subarray beam at 40 MHz is about 20.40°. The estimate is consistent with the direct measurements of

$22 \pm 2°$. The above subarray geometry provides a high filling factor which is important for a number of research tasks. Phasing inside a subarray is accomplished by analogue devices whereas the phasing between subarrays is planned to be digital. A powerful dedicated digital recorder for the GURT system has been developed at the IRA NASU (see Table 2.2) (Ryabov et al., 2010; Zakharenko et al., 2016). It is designed for spectral analysis of a band up to 80 MHz (at a sampling frequency of 160 MHz), with high spectral and temporal resolutions, high dynamic range and several operation modes including real time FFT, waveform recording, auto- and cross-correlation spectral measurements, addition and subtraction regime between the two input channels, normalization, and programmable signal delay. These advanced capabilities of the receiver create a great number of opportunities for observation management.

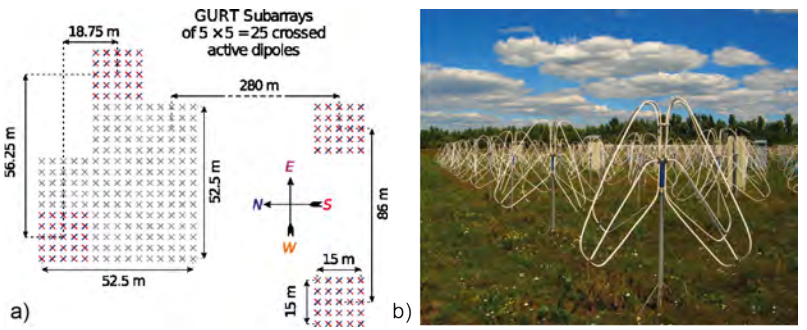


Figure 2.5: *(a) Geometrical configuration of existing GURT subarrays of orthogonal dipoles. Fully commissioned and operational subarrays are enhanced displayed, whereas grey antennas indicate installed subarrays not yet connected to back-ends.(b) Cluster of GURT subarrays.*

All radio telescopes discussed here are used for solar observations. The radio telescope UTR-2 has been observing the Sun since 1970 over the course of three summer months for a period of 6 hours, generally beginning around noon. Since 2011, the URAN-2 radio telescope has carried out observations year round over the course of 6 - 8 hours depending on the season. The GURT radio telescope

Table 2.2: *New generation of broad-band digital spectral processors for UTR-2 and GURT. DSP = Digital Spectral Polarimeter; ADR = Analog Digital Receiver.*

Parameters	DSP–UTR-2	ADR–GURT
Frequency band (MHz)	8 - 32	8 - 80
Number of frequency channels	8 192	16 384
Frequency resolution (kHz)	4	5.450
Time resolution (msec)	0.5	0.183
ADC resolution (bits)	16	16
Dynamic range (dB)	90	90
Input channels	2	2
On-line real-time possibilities		
Fast Fourier Transform	+	+
Waveform (unlimited duration)	+	+
Auto- and complex cross-correlation spectra	+	+
Sum-Subtraction mode	−	+
Signals normalization	−	+
Signals delaying	−	+

occasionally observes solar radio emissions.

2.3 Comparative analysis of solar observations by the single antenna and large array

The radio emissions of the Sun are registered by radio telescopes of different sizes,from single antennas that are mounted on spacecraft such as WIND, STEREO, SOLAR ORBITER and others, to antenna arrays consisting of hundreds or even thousands of antennas such as LOFAR, UTR-2, and URAN 2. Overlapping frequency ranges of spacecraft and ground-based observations provide opportunities to compare instruments as well as observational data. From the sensitivity of radio telescopes a well-known result follows from Equation 2.2 that for increasing sensitivity also the effective area A_{eff} has to increase. The different sensitivity of radio telescopes manifests itself in particular in the potential observability, such as that weak solar

bursts that cannot be observed by single antennas can be observed by large arrays. Moreover in some cases even fine structures of a burst can be registered. In this section we compare results of observations by means of radio telescopes with different effective areas, i. e. with a single antenna and with the radio telescope UTR-2 consisting of thousands of single antennas.

$$S_{sens} = \frac{2kT}{A_{eff}\sqrt{\Delta f \Delta t}} \tag{2.2}$$

Typically, observations of solar radio emissions in the framework of the telescope UTR-2 are carried out by 4 sections of the "North" or "South" antenna arms. In this case the antenna directional pattern covers all the size of the solar upper corona from which decameter radio bursts are generated. These four banks are grouped into an antenna array of 720 dipoles ($A_{eff} = 900 \times 52m^2$), enabling the reception of a signal in the continuous frequency band from 8 to 32 MHz. As a recording back-end, we use a two-channel discrete spectrum analyzer (DSP), and simultaneous solar signals from the two antennas can be recorded. The first antenna had four banks of the antenna arm "South", and the second contained only one dipole of the antenna arm "North". The observations were obtained between August 15 - 27, 2007 during three hours before noon and afternoon. We observed some weak solar events. The tracking of the solar motion in the sky by the antenna directional pattern of UTR-2 is performed electronically by switching the phase-shift network of the telescope antenna. The observation range was between 18.5 and 30.5 MHz. The calibration was carried out by the noise generator with the well-known spectral density for both antenna channels simultaneously. The solar radio emission is generally assumed to be emitted near the local plasma frequency. According to the density model of the corona as from Mann et al. (1999), the plasma levels of 30, 20, 10 MHz correspond to radial distances of 1.78, 2.08, 2.94 solar radii from the center of the Sun, respectively. Since the back-end in the solar observations was the same for both antennas, it is convenient to choose a measure of their sensitivity in the following form:

$$p = \frac{T_A}{S_0} = \frac{A_{eff}10^{-22}}{2k}\text{K/sfu} \tag{2.3}$$

where T_A is the equivalent antenna temperature, S_0 the flux density in sfu (1 s.f.u. = 10^{-22}Wm^{-2}Hz^{-1}), k the Boltzmann constant. Four banks of the antenna arm "South" give a sensitivity of $\approx$K/sfu, and a single dipole (receiving over a perfect conducting ground plane) has only $\approx$228 K/sfu at 18.5 MHz, decreasing to $\approx$84 K/sfu at 30.5 MHz. One of these records is represented in Fig. 2.6. The top panel shows the dynamic spectrum, received by the array of 720 dipoles, and the bottom panel demonstrates a dynamical spectrum of emission received by only one dipole. About 10:34:35 UT in August 21, 2007, we have detected a single Type III solar burst with a weak flux. From these figures it is clearly seen that the detection of such solar bursts is hardly possible for one dipole. The WIND spectrum records do not show any burst at that time (see `ftp://stereowaves.gsfc.nasa.gov/windrad2/rad2pdf/`). The burst flux density was probably less than the minimum detectable value of the instrument. The other restriction, leaving traces on the observations by one dipole, is that its performance does not permit analyzing the fine structure of decameter bursts in detail. As a significant example, consider Fig. 2.7. It presents the spectrograms demonstrating a set of solar bursts with different features in intensity, that were observed in August 17, 2007, at about 9:50 UT. The spectrogram, obtained by one dipole, mainly shows the strongest burst, and it just does not resemble the set of bursts that is represented in the top panel. In contrast to the burst in Fig. 2.6, for which the intensity and the duration increased uniformly with the decay of burst, the peculiarity of the given set of bursts is that their intensity and duration were irregular in frequency. However, this can be tracked more or less successfully in the top panel of Fig. 2.7, which provides a sufficient resolution of this event in intensity owing to the considerable dominance of the array in effective area. The WIND spectrum also cannot resolve any fine structure of this event, although the strongest burst is noticeable. Generally speaking, we are of the opinion that the antenna array of 720 dipoles has a considerable advantage for the study of weak solar bursts as well as for the analysis of fine structures for strong bursts.

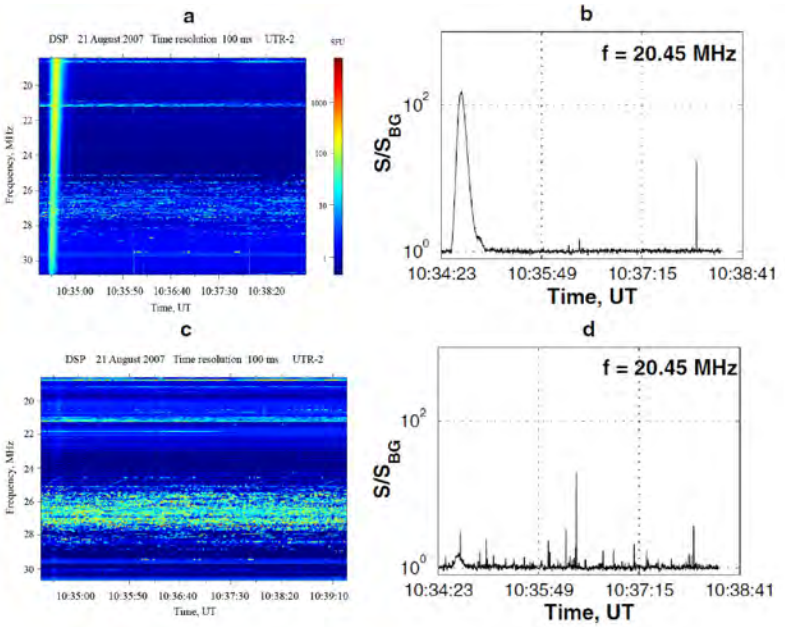


Figure 2.6: *Single solar Type III burst with about 100 sfu in intensity (August 21, 2007): top panel (a and b) corresponds to measurements by the antenna array of 720 dipoles; bottom panel (c and d) is the result by one dipole (both records simultaneously). The right panels (b and d) show the same profile of the burst, measured by the antennas in relative units to the background-flux-density level.*

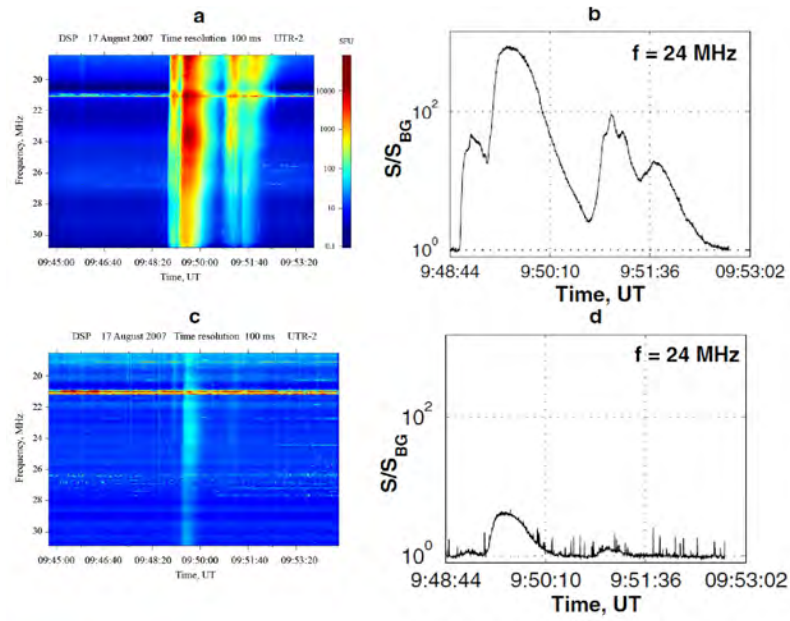


Figure 2.7: *Set of bursts (August 17, 2007) with various features in intensity: top left panel is a spectrogram, obtained by the antenna array of 720 dipoles; bottom left panel demonstrates the result by one dipole (both observations simultaneously). On the right the top and bottom panels are profiles of this event given in relative units to the background-flux-density level.*

2.3.1 Space observations by the WIND/Waves instrument at 9 MHz – 13.8 MHz

The spacecraft WIND is located in the Lagrangian point L1 between the Earth and the Sun, where the gravitational force from the Earth on this spacecraft is balanced by the gravitation force on the spacecraft from the Sun. This point is located about 1.5 million km from the Earth. However, the distance from the spacecraft to the Sun is more than 99 times that distance. As given by Kraus (1966), the flux density of radio emission observed at the distance r is reciprocal to the square of the distance. Therefore, the antenna of the WIND spacecraft receives a signal that is only about 2% stronger than the same antenna located at Earth, if we do not account for scattering, absorption and reflection of radio emission in the terrestrial ionosphere and near-Earth space. However, increasing the antenna's effective area for any spacecraft is problematic, whereas for any ground-based antenna this is easily possible by building an antenna array. The spectral power, received by an antenna, is directly proportional to its effective area. This means that the array of 720 dipoles increases the spectral density of received signals by the factor of 720. In addition, there is an appreciable advantage in interference protection. This problem of the one-dipole antenna of the spacecraft WIND, STEREO or others is obvious if compared with ground-based instruments such as the radio telescope UTR-2 in the form of the array of 720 dipoles applied for solar observations. Both instruments share a common part of the frequency range, overlapping at about 9 MHz – 13.8 MHz. Here we can compare their capability in the solar burst study. In this case, the delay between simultaneous records of WIND and UTR-2 because of different spatial locations is only about 5 s, but to detect spectral features from the records themselves is impossible, as 256 equally-spaced frequency channels are sequentially switched in the receiver RAD2 of the spacecraft WIND during every 16.192 s.

We have chosen a number of solar radio events with different intensity features, that were simultaneously observed by the WIND spacecraft and the UTR-2 radio telescope, and compared them between each other from the obtained records. The frequency band 12 MHz of DSP, used now in the normal mode of UTR-2, is usually started at about 18.5 MHz because of troubles with a strong inter-

ference at lower frequencies. In order to save the overlapping in the frequency band, we have decided to analyze the data of solar events, measured by the 60-channel spectrograph where its frequency range 9 MHz – 30 MHz is covered by 60 frequency channels. Its features are described in the paper of Mel'nik et al. (2004) together with the Digital Spectropolarimeter (DSP). In Fig. 2.8 there is a corresponding illustration. It shows a registration of solar bursts that were observed on July 6, 2006, simultaneously by both instruments. The spectra distinctly indicate that only the most intensive fragments of this event are detectable for the WIND Waves instrument from its RAD2 records. As for the measurements, received by the UTR-2 radio telescope, they even demonstrate a more detailed structure of this event: So up to ten different bursts are visible. The sensitivity and the temporal resolution of the RAD2 receiver for the fine analysis of such events is insufficient. The fine structure is not distinguishable. In fact, from the scan of the WIND Waves instrument at 9 MHz – 13.8 MHz one can see the Type III burst at 8:20 UT and a fragment of the cloud structure of the Type II burst at 8:45 UT. In the same time from the scan, obtained by UTR-2, one can succeed in finding various details of the given event, about which we could only guess from the WIND data.

The antennas of the WIND Waves instrument are short dipoles in much of their respective frequency range. Let us determine a performance of such an antenna for receiving the decameter solar radio emission. In this case the system noise temperature T_{sys} is produced basically by the galactic background radiation. The galactic emission has been studied for a long time by many observers (see Krymkin (1971); Cane (1979); Manning and Dulk (2001); Dulk et al. (2001) and references therein). Cane (1979) suggested to describe the flux density of the galactic background radiation in beam (measured in units of $Wm^{-2}Hz^{-1}sterad^{-1}$) at the frequency range 1 MHz – 100 MHz in a clear functional form with a maximum at the frequency of about 3 MHz. The expression may be approximated to within 2.4% at the frequency range 10 MHz – 100 MHz by a simpler equation

$$I_v = I_{gal}\nu^{-0.52} + I_{ext}\nu^{-0.8}, \tag{2.4}$$

where ν is the frequency in MHz. The first term describes the galactic contribution, and the second corresponds to the extragalactic

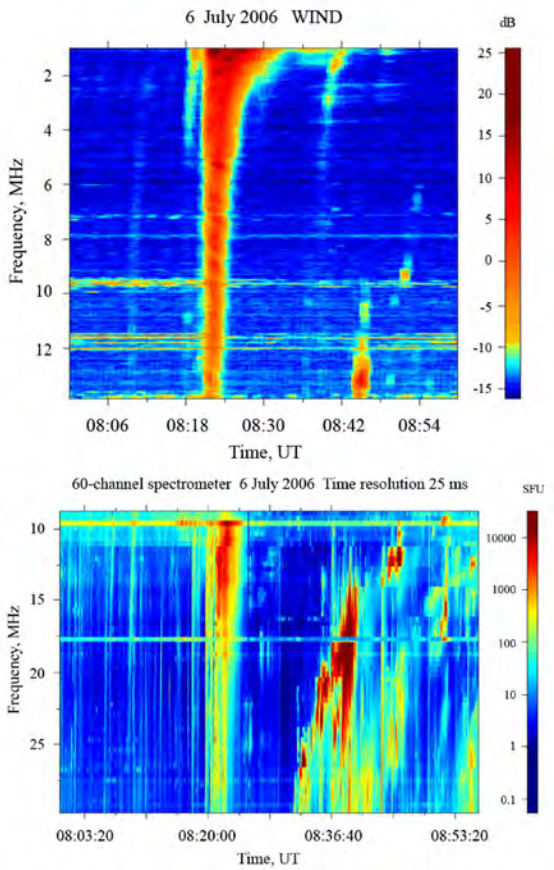


Figure 2.8: *Set of solar bursts, observed in July 6, 2006, at 8:00 – 9:00 UT: bottom panel shows records by the antenna array of 720 dipoles (UTR-2); top panel represents measurements of the spacecraft WIND (both observations are simultaneous). 60-channel records of the UTR-2 array are expressed in terms of solar flux units (sfu), and the WIND data are represented with respect to a background level.*

radiation. In this equation the parameters are equal to

$$I_{gal} = 2.48 \times 10^{-20} \mathrm{Wm}^{-2}\mathrm{Hz}^{-1}\mathrm{sterad}^{-1} \quad (2.5)$$

$$I_{ext} = 1.06 \times 10^{-20} \mathrm{Wm}^{-2}\mathrm{Hz}^{-1}\mathrm{sterad}^{-1} \quad (2.6)$$

Of course, the flux density of the galactic background radiation also depends on the solar location in the sky. Over large solid angles away from the galactic plane the flux density I_{gal} is fairly constant and Equation (2.5) is applicable. However, near the galactic plane an enhancement is superposed on the isotropic component and displays a much richer structure in dependence of angle (see an interesting analysis of this problem in the paper of Manning and Dulk (2001)). The sky map may be divided into the two flux density regions using galactic coordinates, as it was shown in Joardar and Bhattacharya (2007), but in our study we will not account for the structure of galactic background radiation. We restrict ourselves by Eqs. (2.4) and (2.5) in this consideration. Using the Rayleigh-Jeans law, at 9 MHz – 13.8 MHz it is not difficult to calculate the brightness temperature of the galactic background radiation. In particular, for the frequency 25 MHz it is about 28300 K that is in agreement with the measurements reported in the works of Krymkin (1971) and Konovalenko et al. (2007). The beam solid angle of the WIND-spacecraft antenna is $\Omega_a = 8\pi/3\,\mathrm{sterad}$ (assuming, it receives in a homogeneous medium of infinite extent). Consistent with Kraus (1966), its effective area equals $A_{eff} = 3\lambda^2/8\pi$, where λ is the wavelength of radio emission. As a measure of the telescope performance, we apply the System Equivalent Solar Flux Density (SESFD) similar to the general definition of SEFD (Stanimirovic et al., 2002). Consider a 1.0 s.f.u. point source, the antenna temperature due to this source is expressed in terms of the K/sfu value defined in Equation (2.3). The SESFD is the point source flux density (in s.f.u.) which produces the antenna temperature $T_A = T_{sys}$, namely

$$SESFD = T_{sys}/p. \quad (2.7)$$

For the antenna array of 720 dipoles with the sensitivity equal to 170000 K/sfu and the system noise temperature 130000 K at

13.8 MHz, the SESFD is less than 1 s.f.u., whereas for the WIND-spacecraft antenna with the sensitivity 204 K/sfu at the same frequency, the SESFD amounts to 637 s.f.u. The brightness temperature of galactic background radiation is averaged in the solid angle of the antenna patterns, and the brightness temperature of solar radio bursts will be directly proportional to the effective area of the receiving antennas. In this comparative analysis we do not account for any losses in the antennas themselves and their feeder systems, as well as the signal-to-noise ratio per beam due to the back-end. The effective area of this array and its antenna temperature (determined by the sky region) also depends on the angular direction, but we do not consider these details. Nevertheless, this analysis is able to compare the performance of these instruments. Regarding the system noise temperature for the antenna array of 720 dipoles, there is (in comparison with galactic background radiation) an appreciable contribution of quiet solar emissions. Under these conditions, due to the quiet solar emissions, the system noise temperature increases by about 30 % – 40 % in frequency dependence.

It should also be mentioned that there are difficulties of decameter radio observations for any ground-based dipole in the daytime because of high levels of terrestrial interference that are represented in the bottom panels of Figs. 2.6 and 2.7. Due to the selectivity of the UTR-2 array of 720 dipoles, it has proved to be a most valuable instrument for the observation of solar radio bursts. Another point should be mentioned: In the frequency range 9 MHz – 14 MHz the solar events often occur with the duration of tens of seconds and less (Abranin et al., 1979; Mel'nik et al., 2004; Melnik et al., 2005; Mel'Nik et al., 2005a; Chernov et al., 2007b; Konovalenko et al., 2007), and therefore the temporal resolution of the receiver RAD2 of the spacecraft WIND with 16 s is too rough for a detailed temporal analysis.

In summary, the evident advantage of space observations is to carry out continuous measurements in time and beyond the transparency bounds of the terrestrial ionosphere (lower than 7 MHz – 9 MHz) which is problematic for ground-based instruments. As a result, the sufficiently strong events can be detected by spacecraft, but any fine structure is washed out. In this context the ground-based radio telescopes such as UTR-2, LOFAR, LWA have a clear advantage.

3 Solar Activity

3.1 History: the Sun as a goddess

In ancient times mankind worshipped the Sun as a god bringing light, warmth, and growth into nature. The early Egyptians would come to believe that this god, referred to as "Ra" was the creator of the world. The appearance of this god was in human form with a falcon head and crowned with a Sun disc. Day by day he would sail over the sky in a barque emerging in the east in the morning and sailing into the underworld in the evening, only to be reborn early the next day.

Another culture with the Sun god was the prehispanic Mexicans, who had a profound devotion and respect for the Sun. Mesoamerican civilization connected their veneration of the Sun with the cult of water and rain, where, following a dry season, Earth became again fertile. The Aztecs, who flourished between the 14th and 16th century A.D., considered the universe to be a living entity, with the Sun as its center. The Sun Stone, which symbolizes the power of the Sun, is also the Aztec Calendar.

3.2 First observations of the Sun

Solar features like sunspots were familiar to ancient astronomers, of course, and were simply observed with the naked eye. But it was not until the invention of the optical telescope in the early 17th century, when Galileo Galilei made the first telescopic observations as can be seen in drawings (Fig. 3.1). The German astronomer Christoph Scheiner also made drawings of sunspots, which he published in Scheiner (1630). Over 200 years later, his compatriot and amateur astronomer Samuel Heinrich Schwabe discovered the sunspot cycle in 1843 by tracking the passage of sunspots across the Sun and

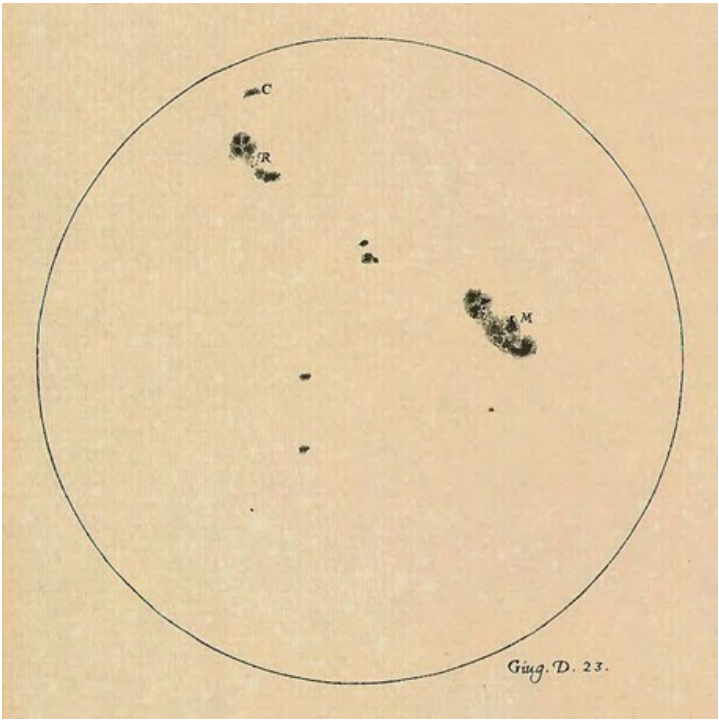


Figure 3.1: *Illustration of sunspots by Galileo observed in 1613 (Galileo Project, Rice University).*

unravelled the number of sunspots varying with a regular period. The Swiss astronomer Rudolf Wolf determined this period to be 11 years and in 1849 he introduced the sunspot relative number as the sum of all actually observed sunspots plus 10 times the number of sunspot groups. This relative number is still in use up to the present day. Further studies by the British scientist Christopher Richard Carrington enabled the detection of the differential rotation of the Sun and the equatorwards drift of the sunspots. Together with the Englishman and amateur astronomer Richard Hodgson, in September 1859 both witnessed an outbreak in a large sunspot, the first observation of a solar flare.

3.3 First scientific observations and measurements

Monitoring of the Sun by means of photographs began in 1860 which led to the very powerful method of spectroscopy enabling the analysis of solar elements and their physical state. Already in the early 19th century (1802) the Englishmen W.H. Wollaston first observed dark lines in the solar spectrum, independently rediscovered in 1814 by Joseph von Fraunhofer, who subsequently systematically studied this phenomenon and measured their wavelengths. The lines observed by both Wollaston and Fraunhofer can be attributed to the absorption properties of the elements in the upper solar atmospheric layers. (However, some of the lines are also result of the constituents of the terrestrial atmosphere.) These so-called Fraunhofer lines are produced by resonance absorption of the gases in the solar photosphere. Thus, these lines make it possible to draw conclusions on the chemical composition and temperature of the solar atmosphere. However, the high coronal temperature could not be determined until measurements of coronal spectral lines have been performed in 1940 by the German astrophysicist W. Grotrian.

A suddden increase of solar brightness is connected with a solar flare, an optically observable flash in the visible electromagnetic spectrum, especially in the H alpha emission line of hydrogen. This phenomenon can now be measured also in other wavelengths, from radio waves to gamma-rays.

Following the relation

$$v_c = \lambda f, \tag{3.1}$$

the optical astronomy towards longer wavelengths range leads into the range of infrared astronomy and via the range of microwave astronomy into the range of radio waves, whereas towards shorter wavelenghts we find the UV and the X-ray astronomy. Nowadays in all wavelength regimes solar observations of flares and their affiliated phenomena like plasma ejections are performed.

The central body of our solar system has a mean radius of 695 700 km and comprises a mass of $\approx 1.99 \times 10^{24}$ kg which corresponds to a Sun/Earth ratio of 333 000. The Sun exhibits a sidereal rotation

period of 25.449 terrestrial days at 16 degrees latitude; the actual rotation rate varies with latitude L as

$$D_{rot} = (14.37 - 2.33\sin^2 L - 1.56\sin^4 L) \text{ deg/day}. \quad (3.2)$$

The inner layers of the Sun include the core, the radiative zone, and the convection zone. The outer layers comprise the photosphere, the chromosphere, the transition region, and the corona. In the solar core, fusion takes place (hydrogen fusion into helium), which is the source of energy for luminocity and solar activity. The magnetic field is generated in the convection zone as a combined effect of convection and solar rotation (Benz, 2002). The outer layers, i.e. the solar atmosphere, differ by thickness, height, temperature and composition. The temperature at the bottom of the photosphere is approx. 6600 K, at the top of the photosphere 4400 K, just 500 km apart in height. Granulation covers most of the photosphere, i.e. the solar surface. The chromosphere thickness is determined as about 2500 km and at the top of the chromosphere the temperature is approx. 30 000 K. The transition region is a very narrow layer with a mere 100 km thickness. Observations yielded an abrupt rise up to about 500 000 K into the outermost layer of the Sun, the corona. The corona itself exhibits temperatures up to a few million K. Low density regions and almost vertical magnetic field structures define so-called coronal holes where main part of the solar wind is released into interplanetary space. It is these outer layers where solar activity takes place and where the solar magnetic field is main driver of this activity.

3.4 Solar phenomena at active regions

Evidence of the solar magnetic field is manifested in the occurrence of sunspots. It is the case, however, that the emergence of magnetic flux occurs everywhere on the surface of the Sun. With field strengths of up to 2000 G magnetic knots are localized magnetic areas with just a few hundreds km in diameter. Together with sunspots they are stable and long-lived phenomena on the solar surface.

Active regions on the Sun exhibit especially strong magnetic fields, solar storms like solar flares and coronal mass ejections (CMEs) are ejected out of active regions. Visual manifestation of active regions

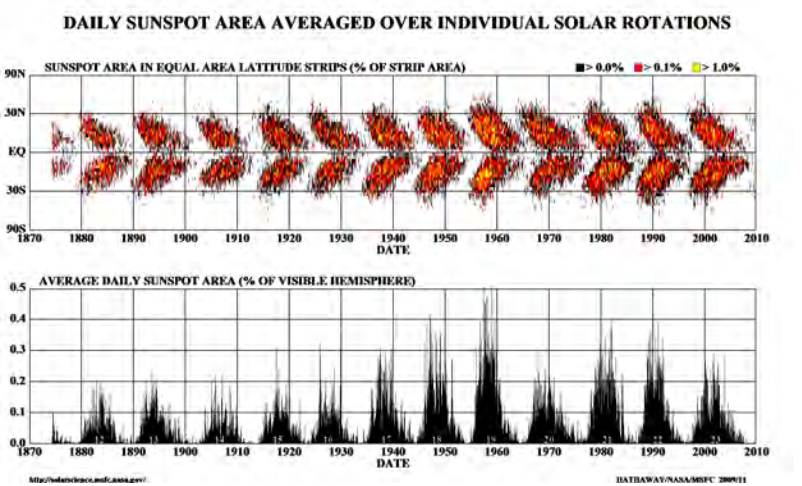


Figure 3.2: *The butterfly diagram, i.e. the motion of sunspots over the surface of the Sun in dependence of time (top). The averaged daily sunspot area in the solar cycles during the past 150 years (bottom) (`http://solarscience.msfc.nasa.gov/`).*

are the sunspots and so-called coronal loops, magnetic arcs filled with plasma. This plasma is in steady motion along active region magnetic loops, where spiculae and surges represent upward flows.

Structure and appearance of sunspots are the darker central region (umbra) with a cooler temperature (4000 K) than the surrounding area (i.e. the photosphere with about 5800 K), and a less dark outer region, called the penumbra. Sunspots in the photosphere have a lifetime of ca. $50 - 60$ days, thus approx. 2 solar sidereal rotations. The number of sunspots varies in time, exhibiting a maximum and a mininum, a cycle of on average 11 years (discovered by the German amateur astronomer S.H. Schwabe in 1843), but may vary between 9 and 14 years. The (above mentioned) relative sunspot (or Wolf) number has recently been updated in order to enable a reliable comparison of nowadays sunspot observations with data from the past, obtained by different instrumentation including the naked eye (Clette, 2021).

The observed solar sunspot cycle of approx. 11 years comprises a pair of sunspots, e.g., in the Northern solar hemisphere (around 30° to 45° latitude) with magnetic polarity South-North, and slowly approaching with proceding North polarity towards the solar equator from the North, whereas in the Southern solar hemisphere a pair of sunspots with polarity North-South, is slowly approaching with proceding South polarity towards the solar equator from the South. The following solar cycle sees a vice versa sequence of polarity of sunspot pairs approaching the solar equator from both hemispheric sides. A so-called "butterfly diagram" (Fig. 3.2) can be constructed, a graphical display of sunspot motion, first developped in 1904 by the English astronomer E.W. Maunder. This change in magnetic polarity is in fact the consequence of the Sun's magnetic reversal with a full period of around 22 years.

3.5 Explosive events

Solar activity is prominently represented by solar flares, which are enormous explosions appearing as a sudden brightening in white light. Flares also emit X-rays, UV radiation and radio waves, thus they are a strong source of electromagnetic radiation, in addition to huge clouds of electrons, ions and atoms ejected through the corona into interplanetary space. So-called coronal mass ejections (CMEs) are connected to strong solar flares, although weak solar flares are not necessarily accompanied by CMEs.

In flares particles are accelerated up to peak energies of approx. 10 GeV where the highly ionized plasma gets heated within minutes. This turbulent plasma is a manifestation of strong deviations from thermodynamic equilibrium. Main cause is the complex structure of magnetic fields of sunspot groups, where the turbulence may lead to reconnection which in turn is responsible to heating and plasma motion. Shocks and further turbulent areas are created which propagate along magnetic flux tubes (Rust, 1979).

The sudden release of magnetic energy by reconnection is at the origin of the extreme acceleration of charged particles. This reconnection occurs at closely adjacent magnetic loops, arcades of magnetic field lines, leaving parts of helical magnetic field lines unconnected.

A violent expansion of this unconnected magnetic field and inherent plasma occurs which leads to the formation of a coronal mass ejection (CME).

Solar flares comprise a wide range of energy released over many orders of magnitude. Solar flares are classified by their peak flux of X-rays (W/m^2 within the wavelength of 1 to 8 Ångströms) using the letters A, B, C, M, or X, with A classifying a peak flux $< 10^{-7} W/m^2$ and X classifying $> 10^{-4} W/m^2$. Flares in general develope in various temporally subsequent phases: preflare, impulsive, flash, and decay phase (Benz, 2002). In a large event, these phases may last 10 min., 1 min., 5 min., and one hour, respectively. And this solar phenomenon is represented across the spectrum by hard X-rays, microwaves, decimetric and metric radio waves, EUV, soft X-rays, and $H\alpha$ emission (Benz, 2002, Fig. 1.5).

The plasma in the coronal magnetic loops is heated by the flare energy up to 3×10^7 K which obviously indicates the flare as a coronal phenomenon. Solar flares are often accompanied by other dynamic processes, as said, like coronal mass ejections (CMEs), which are even more powerful than flares. Solar coronal structures as loops or prominences (bright gaseous features reaching outward from the solar surface) may get out of equilibrium and a CME is released into interplanetary space with bulk speeds of several hundred km/s. Another phenomenon related to solar flares is solar radio emission, the main topic of the following chapters.

By their appearance in the dynamic spectra (burst intensity displayed in a frequency versus time diagram) solar radio bursts are classified in Type II, III, IV, and V. These various types are signatures of specific solar processes and provide by their observations significant insight into the physics in the vicinity of the Sun.

4 Radio Emission of the Quiet Sun

4.1 Radio emission of the quiet Sun at decameter wavelengths

Solar atmosphere observations in the radio region are made within a broad frequency range: from the ionosphere transmission cutoff frequency of about 10 MHz ($\lambda = 30\,\mathrm{m}$) up to 300 GHz (submillimeter spectral region, $\lambda < 1\,\mathrm{mm}$). Different radiation wavelengths correspond to different layers of the Sun and solar atmosphere: millimeter waves to the lower chromosphere, centimeter to the middle and upper chromosphere, decimeter to the transition region, meter to the lower corona, and decameter to the upper corona. Multifrequency observations allow to determine the electron density, temperature and magnetic fields in the solar corona versus height above the Sun's surface. The radio sun during the minimum activity looks like an extended ($> 30'$) and rather homogeneous source whose size exceeds the solar radius. It is usually stretched equatorially because the solar atmosphere has a larger electron density on the equator than on the poles. This fact allows performing its diagnostics by investigating the solar radio continuum. In the absence of solar bursts, the noncoherent radiation of thermal plasma in the corona is the source of solar radio emission. The most favorable conditions for observation of the solar continuum radio emission appear during the solar activity minimum. At decameter wavelengths, this radiation is much weaker than the solar radio bursts (the nonthermal radiation mechanism), and to observe them simultaneously, the high sensitivity and large dynamic range of radio telescopes are required. In this case, the solar activity effects may influence the characteristics of solar atmosphere, and this latter can hardly be considered undisturbed.

Now, the solar radio image is investigated regularly at several radio-astronomy instruments. Some of these are specially designed for solar researches: the Nançay radioheliograph(France) (Leblanc and Le Squeren, 1969; Lantos and Avignon, 1975) operating within 150 MHz - 450 MHz, the Owens Valley Radio Observatory interferometer (USA) where the observations are made within 1 GHz - 18 GHz, and the Nobeyama heliograph (Japan) which measures at frequencies 17 and 34 GHz. The RATAN-600 radio telescope (Russia) performs solar observations within 1 GHz - 20 GHz, and the SSRT (Siberian Solar Radio Telescope, Russia) at frequency 5.7 GHz. In recent decades, the brightness distribution of thermal continuum has been investigated very much explicitly and with high resolution at millimeter and centimeter wavelengths. The progress made in observations at meter and decameter wavelengths is so far insignificant that may be caused by several reasons. First, this is the absence of radio telescopes with the sensitivity and spatial resolution characteristic of the instruments for higher frequencies. Moreover, the large intensity of terrestrial interfering signals of various nature, negative influence of the ionosphere (radiowave refraction, absorption, and scattering), high temperature of the galactic background noise essentially hinder the performance of precision investigation of astrophysical objects, the Sun including. During daylight hours, many of the listed factors aggravate. Very effective space missions for solar investigations (WIND, STEREO, etc.) successfully detect the sporadic solar radio emission at the maximum possible low frequencies (0.1 MHz - 16 MHz), but they cannot detect the continuum solar radio emission on account of the limited sensitivity (inasmuch as elementary antennas are used).

At decameter wavelengths, the most effective ground-based instruments remain so far the UTR-2 radio telescope (Ukraine) (Bazelyan et al., 1970), operating within 8 MHz - 32 MHz, and the Gauribidanur radio telescope (India), where the measurements at frequencies 30 MHz – 110 MHz are made. Introduction into service of some new large-area radio telescopes, for example, LOFAR (Low Frequency Array), LWA (Long Wavelength Array), GURT (Giant Ukrainian Radio Telescope), and NenuFAR (New Extension in Nançay Upgrading loFAR) is anticipated, though their construction is still in progress. Unfortunately, the Culgoora radio telescopes (Australia) and the Clark

Lake Teepee-Tee radio telescope (USA) (Cronyn and Erickson, 1965; Erickson et al., 1977; Kundu et al., 1977; Gergely et al., 1985) are made inactive. Now and then, for solar observation within 0.3 GHz - 22 GHz, the VLA (Very Large Array) telescope (USA) is used, while within l0 MHz - 70 MHz the Nançay Decameter Array (France) is in operation. This latter allows to observe only the spectral response of the solar radio burst activity. Here, it is noteworthy that the aforementioned instruments have different performances, and the observations are made at different time (by virtue of differing geographical locations). All this presents noticeable difficulties while comparing the obtained results. It should be kept in mind that the coordinated and/or simultaneous use of spaced low-frequency radio telescopes (with allowance for the visibility zone), which operate in coincident frequency bands, leads to an essential reliability and efficiency increase of investigations even under the conditions of negative influence of interfering signals and ionosphere.

Investigations of the quiet Sun continuum radiation at low frequencies, along with the observations in the high-frequency spectrum region, are the major sources of determination of the structure, electron concentration distribution, radiating layer height, coronal temperature and shape. The quiet Sun decameter wavelength radiation data are of particular interest as they enable determining the parameters of the solar outer corona at distances from 2 to 3 solar radii from the Sun's center. Roughly in this region of the solar atmosphere the solar wind originates whose nature is not yet fully understood.

Investigating the solar continuum radio emission, the observations with the URAN-2 radio telescope were made in summer seasons of 2008 - 2009 (Brazhenko et al., 2010), as well as those made with the UTR-2 antenna system in summer-autumn period of 2010 (Brazhenko et al., 2012a).

The observations of the quiet Sun by URAN-2 in 2008 - 2009 used a receiver system consisting of two double-channel superheterodyne receivers (whose intermediate frequency is 10.7 MHz and operating frequency band 200-300 kHz) capable of making measurements at two separate frequencies, for example 20 and 25 MHz, in two orthogonal polarizations (Brazhenko et al., 2010). The received signal is fed to a 10-digit analog-to-digital converter (ADC) comprising 4 identical signal conversion channels. Next, the interface unit permits to con-

tinuously insert into the computer the data arriving from the ADC with the stream reaching 4 Mb/s. The software developed for this signal recording complex accomplishes a number of useful functions, such as elimination of the receiver frequency response nonuniformity, received signal bandwidth reduction to 250 kHz, narrow-band interference filtering, etc.

4.1.1 Observations of the quiet Sun by URAN-2

Solar continuum radio emission was investigated with the URAN-2 radio telescope in summer months of 2008 and 2009. The measurements were simultaneously made at two frequencies, 20 and 25 MHz. The active regions on the solar disk were absent at those periods of observations. The URAN-2 array experimentally obtained data were represented in terms proportional to the antenna temperature T_A or visible flux density,

$$S_A = \frac{2kT_A}{\lambda^2}, \tag{4.1}$$

where k is the Boltzmann constant, and the wavelength λ at which the observations were made. The total visible flux density is determined by the equation

$$S = \int_{\Omega_\tau} S_A d\Omega, \tag{4.2}$$

where Ω_τ is the solid angle of URAN-2 beaming. At decameter wavelengths, the variations in the observed total flux density of solar radio emission are associated not only with the variations of solar activity, but also with the amount of attenuation of radio waves in the ionosphere, as well as with their refraction on ionospheric inhomogeneities. The average values of flux density decrease are usually considered while observing a powerful point source whose position on the celestial sphere and time of observation should be as close as possible to those of the measured object. As such a source, the well known radio source Taurus A (3Cl44) was selected. The obtained values of radiation flux density for this source are about 2870 Jy at 25 MHz and 3430 Jy at 20 MHz. This agrees well with the UTR-2 observed data and those obtained by Viner and Erickson (1975).

With the URAN-2 array, the long-term series of daily flux density values of the quiet Sun radio emission were recorded. A fragment of those observations is presented in Fig. 4.1, where some portions of two 10-minute scans can be seen. The noticeable difference between the flux density values of the solar continuum radio emission in the scans maxima is seen. We suppose that the time variations of radio emission flux density depend on the URAN-2 array phasing increment and asynchrony, rather than on variations of the quiet Sun radiation. This effect essentially decreases as the series of scans are subject to averaging. In the analysis of the observed results only those scans of the quiet Sun were considered which were not distorted by many short-term spikes with duration comparable to the scan length, and with intensity level either equal or higher than that of the undisturbed Sun.

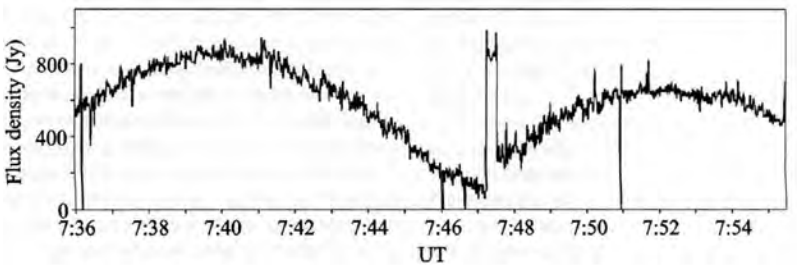


Figure 4.1: *Quiet Sun radio emission fragment recorded on July 13, 2008, with the URAN-2 at 25 MHz within 250 kHz bandwidth.*

During the 2008 - 2009 observation campaign, after the interfering signals removal procedure, more than 2500 samples of flux density of the solar continuum radio emission at 20 MHz, and almost 3200 samples at 25 MHz were obtained. The averaged values yielded 710 and 860 Jy for these two frequencies, respectively. Fig. 4.2a presents the data of the quiet Sun flux density measured by different instruments, including those observed with the URAN-2 array, for this latter shown by full points. The values obtained for the quiet Sun flux density at 25 MHz show to be somewhat less than those indicated in papers by Erickson et al. (1977) and Kundu et al. (1977). As

has already been noted, the URAN-2 array observations were made in the absence of active regions on the solar disk, whereas in the paper by Erickson et al. (1977), active regions are treated as such possibly capable of contributing to the obtained values. As can be seen from Fig. 4.2a, generally, the URAN-2 measurements are in good agreement with the data observed by other authors (Leblanc and Le Squeren, 1969; Lantos and Avignon, 1975; Bazelyan et al., 1970; Erickson et al., 1977; Kundu et al., 1977; Aubier et al., 1971; Ramesh, 2000; Abranin and Bazelyan, 1986; Borkowski, 1982; Fokker, 1966; Subramanian and Sastry, 1988). The solid line in this picture represents the linear dependence approximation (in log-log scale) over all points. As a result, the spectral index of the quiet Sun radio emission within the bandwidth of 20 MHz - 200 MHz is equal to -2.1±0.1, that is very close to the spectral index value for the long-wavelength blackbody radiation. This is explained by the fact that the source angular sizes grow with wavelength, while its brightness temperature drops at rather high altitudes.

The temporal variations of flux density of the quiet Sun radio emission are shown in Fig. 4.3. It can be seen that flux variations in 2008 (Fig. 4.3a) are much lower than in 2009 (Fig. 4.3b). We can conclude that fluxes of the quiet Sun change from month to month even in years of the minimum of solar activity.

4.1.2 Observations of the quiet Sun by UTR-2

The quiet Sun radio emission was investigated with the UTR-2 antenna system during September 4 - 6, 2010. Getting the scans of the continuum solar radiation, the five-beam mode of the UTR-2 array directional pattern was used. The middle (third) beam was directed toward the solar disk center over declination, and then turned away from this direction at 60 arcmin. The duration of each scan was 30 min. During this period of time, due to the Earth‘s rotation, the solar disk crossed the main lobe of the telescope directional pattern. For the indicated period of observations, more than twenty 30-minute scans were obtained. The measurements were made within the bandwidth 16.5 MHz - 33 MHz. Fig. 4.4 shows an example of amplitude-time profiles of a scan of the solar radio emission as observed along the solar equator direction for different frequencies. The flux density

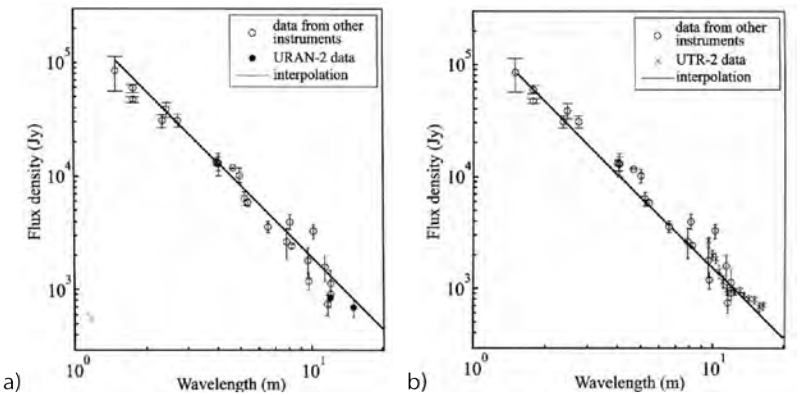


Figure 4.2: *Low-frequency subspectrum (meter and decameter wavelengths) of the quiet Sun radio emission. Circlets are the data from papers (Leblanc and Le Squeren, 1969; Lantos and Avignon, 1975; Bazelyan et al., 1970; Erickson et al., 1977; Kundu et al., 1977; Aubier et al., 1971; Ramesh, 2000; Abranin and Bazelyan, 1986; Borkowski, 1982; Fokker, 1966; Subramanian and Sastry, 1988), criss-crosses are UTR-2 data, full points are URAN-2 data, the solid line is the approximation of linear dependence ($\lambda^{-2.1}$) in the log-log scale.*

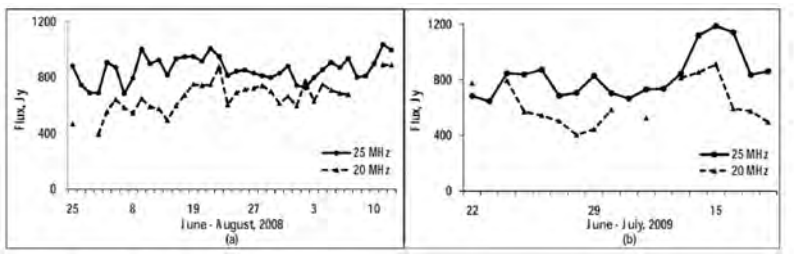


Figure 4.3: *The temporal variations of the quiet Sun fluxes in 2008 – 2009.*

values of the received radio emission were determined using the calibration by the known values of the noise generator spectral power, as well as through calculation of the UTR-2 array effective area in dependence of the Sun's position on the celestial sphere. The obtained profiles are well approximated by the one-dimensional Gaussian function. Note that the profiles visualize strong solar bursts as well. However, these bursts were observed rarely enough and did not noticeably distort the shape of recorded profiles which successfully discriminate them. The dynamic range of the DSP digital spectrum analyzer, used as a receiver-recorder unit, was quite sufficient to perform simultaneous observations of the solar continuum radiation and solar bursts. Fig. 4.2b represents the integral values of the undisturbed Sun radio emission flux density as observed with the UTR-2. Also, the results of other observations made at meter-decameter wavelengths are shown. Linear dependence approximation (in log-log scale) over all points with the least-squares method enabled the derivation of the spectral dependence of the quiet Sun radio emission flux density. As a result, the spectral index within the bandwidth 18 - 200 MHz is equal to -2.1±0.1 that coincides with the index value determined from the URAN-2 measurements.

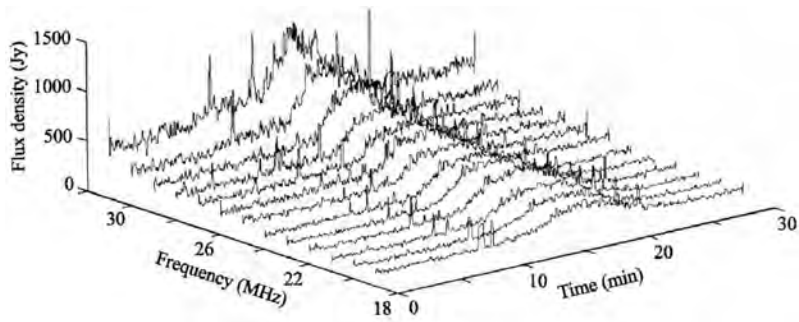


Figure 4.4: *Amplitude-time scan profiles of the quiet Sun's corona radio emission measured with the UTR-2 radio telescope on September 5, 2010. The time axis origin corresponds to 09:01:59 UT.*

Table 4.1 represents the average integral flux density of the quiet

Sun radio emission at 20 and 25 MHz calculated by means of the URAN-2 array observed data. For comparison, the UTR-2 array measured results are also shown. For the indicated frequencies, the UTR-2 measured flux density values are higher, caused by several factors. In the Table 4.1, the URAN-2 data are those annual average values of flux density of the quiet Sun continuum radio emission, whereas the UTR-2 data have been obtained for a much shorter period of time. Besides, in 2008 - 2009 the expected solar activity minimum occurred, however in 2010 the increasing phase of the 11-year cycle started. There were some small active regions on the solar disk on September 4 - 6, 2010, when these observations have been performed.

Table 4.1: *Average integral flux densities of the quiet Sun radio emission at 20 and 25 MHz*

Radio telescopes	year	Flux, Jy	
		20 MHz	25 MHz
URAN-2	2008	710	870
	2009	700	860
UTR-2	2010	800	950

Summarizing, using the URAN-2 and UTR-2 data, the spectral index was determined which within the frequency band 16.5 MHz - 200 MHz is -2.1±0.1. The quiet solar corona brightness temperature in this frequency band is noticeably lower than its electron temperature that denotes its partial transparency.

4.2 Sizes and brightness temperature of the quiet Sun at decameter wavelengths

4.2.1 Radio emission of the quiet Sun at 20 and 25 MHz – sizes and brightness temperatures

The large size and sectioned construction of the decameter radio telescope UTR-2 enabled the use as a local interferometer with baselines

between its sections from 225 m up to 1.6 km in N-S direction and up to 700 m in W-E direction. Interferometers with such baselines provide the opportunity to define the location of radio emission sources and their sizes if the latter are from units to tens of minutes. Such angular sizes are peculiar to the quiet Sun (Aubier et al., 1971; Kundu et al., 1977; Erickson et al., 1977; Bhonsle et al., 1979; Abranin and Bazelyan, 1986; Thejappa and Kundu, 1992; Sastry, 1994; Subramanian, 2004; Ramesh et al., 2006; Brazhenko et al., 2012a; Stanislavsky et al., 2013) as well as to the sources of Type III bursts (Abranin et al., 1976; Chen and Shawhan, 1978; Bhonsle et al., 1979; Abranin et al., 1980b; Suzuki and Dulk, 1985), Type II bursts (Chen and Shawhan, 1978; Bhonsle et al., 1979; Nelson and Melrose, 1985) and Type IV bursts (Gergely and Kundu, 1974; Chen and Shawhan, 1978) in the decameter wavelength range.

During the period from May 27 to June 2, 2014 there was the only powerful CME (Coronal Mass Ejection) which occurred on May 29. On other days, May 27, 28, 30, 31 and June 2, the activity of the Sun was minor, only separate weak Type III bursts were registered and this opened the opportunity to study the radio emission of the quiet Sun before and after a CME.

The results of the first interferometric observations of the quiet Sun at frequencies 20 and 25 MHz are presented in the following. Radio emission of the quiet Sun in a wide frequency band had been studied from the forties of the last century, mainly in the mm-, cm-, dm- and m-wavelength bands. For the first time the quiet Sun decameter radio emission was observed by the Arecibo radio telescope (Aubier et al., 1971). They found that fluxes were 3300 ± 500 Jy and 4000 ± 600 Jy at frequencies 29.3 MHz and 36.9 MHz, respectively. The sizes of the Sun in the equatorial plane were $70' \pm 10'$ and $53' \pm 5'$, the brightness temperatures $3.8 \cdot 10^5$ K and $5 \cdot 10^5$ K at these frequencies. In May-June 1976 and April 1977 (Kundu et al., 1977) observed the Sun by means of the radio telescope in Clark Lake at 26.3 MHz and found the fluxes, sizes and brightness temperatures of the quiet Sun radio emission to be equal to $1.6 \pm 0.4 \cdot 10^3$ Jy, $56.6' \pm 6'$, $4.7 \cdot 10^5$ K, respectively. Observations of the quiet Sun performed by Erickson et al. (1977) with this radio telescope in July-August 1977 gave fluxes $< 1.1 \cdot 10^3$ Jy, $1.5 \pm 0.3 \cdot 10^3$ Jy, $1.2 \pm 0.2 \cdot 10^3$ Jy, sizes $55'$, $50'$, $48'$ and brightness temperatures $5 \cdot 10^5$ K, $4.4 \cdot 10^5$ K, $2.6 \cdot 10^5$ K at frequencies

19 MHz, 25.8 MHz and 30.9 MHz, correspondingly. The average angular sizes of the quiet Sun in W-E and N-S directions obtained by the radio heliograph in Clark Lake in September 1986 (Thejappa and Kundu, 1992) equaled $64'$ and $53'$, while the brightness temperatures changed from $0.5 \cdot 10^5$ K to $2.5 \cdot 10^5$ K at 38.5 MHz.

Abranin and Bazelyan (1986) observing the Sun by the UTR-2 heliograph in 1976-1977 identified smaller fluxes (770 – 990 Jy) and sizes ($56' - 58'$) at frequency 25 MHz.

At frequency 34.5 MHz the quiet Sun was repeatedly studied with the radio telescope in Gauribidanur (India). Observations in August 1983 (Sastry, 1994) indicated that the diameter of the quiet Sun was 3–4 R_S (solar radius) and the brightness temperature changed from day to day in the range $1 \cdot 10^5 - 7 \cdot 10^5$ K. Subramanian (2004) got the angular size in the equatorial plane from $39'$ to $66'$ and brightness temperature from $1 \cdot 10^5$ K to $4.5 \cdot 10^5$ K during the observations in June-July 1986 and in May-June 1987.

In the years of the solar minimum 2008-2009 the radio emission of the quiet Sun was observed by the radio telescope URAN-2 (Poltava, Ukraine) (Brazhenko et al., 2012a). The obtained fluxes were relatively small and equaled 710 Jy and 870 Jy in 2008, and 700 Jy and 860 Jy in 2009 at frequencies 20 and 25 MHz, respectively. In September 2010 the quiet Sun was observed by the UTR-2 radio heliograph (Stanislavsky et al., 2013), which yielded fluxes of 763 Jy and 1094 Jy and (W – E) × (N – S) sizes of $60' \times 50'$ and $58' \times 42'$ at the same set of frequencies.

We see that for the periods of deep minimum of solar activity and for the years of its increasing phase the measured fluxes, sizes and brightness temperatures differ significantly. One can say that these parameters of the quiet Sun are non-stationary.

Radio telescope UTR-2 and its interferometers

In the interferometric observations the spectral analyzers tuned to frequencies 20 and 25 MHz with frequency width 250 kHz were in use.

Due to the fact that the sections of UTR-2 can be acquired independently the interferometer scan can be shaped with different baselines (Fig.2.2). For solar observations, baselines between neighboring sec-

tions (225 m), over one section (450 m), and over two sections (675 m) of W-E and N-S arms were used. In the interferometric method the size of radio emission source is defined from analysis of the so-called visibility function (Thompson et al., 2001). Fig.4.5 shows the visibility function γ for different sizes of sources ($\theta = 60$, 30, 15, and 7 arcmin) via interferometer bases (L) at frequency 25 MHz according to

$$\gamma = \exp\left[-\left(\frac{\pi\theta L}{2\lambda\sqrt{\ln 2}}\right)^2\right], \tag{4.3}$$

where θ is the angular size on the half flux, λ is the wavelength, at which observations are carried out. It is seen that the sources with an angular size from some minutes to tens of minutes can be measured by interferometers of UTR-2.

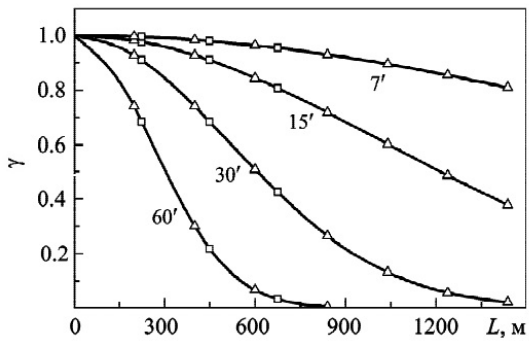


Figure 4.5: *Dependence of visibility function for Gaussian sources of different angular sizes via baseline of interferometer.*

Observations

Observations were carried out from May 27 to June 2, 2014 by 10 minutes scans at angles ± 2 hours from culmination. For the calibration the radio source 3C144 was used. So after every 2 solar scans the interferometer beam was directed to the calibration radio source 3C144 for one scan record.

From May 27 - 30, 2014, solar radio emission was recorded by interferometric means consisting of W-E sections with baselines 225 m, 450 m, and 675 m. From May 31 to June 2, the interferometers consisted of N-S sections with the same set of baselines. Average visibilities were derived from the scans close to local noon without any interferences.

These values did not significantly differ from day to day, so the average visibilities for May 27, 28, 30 and 31, and June 2 are presented in Fig. 4.6.

Assuming Gaussian distributions of the quiet Sun brightness the curves were found in the observational data according to Equation (4.3). Corresponding sizes of the quiet Sun in W-E and N-S directions at frequencies 20 MHz and 25 MHz are summarized in Table 4.2. These sizes are close to those obtained earlier with the Clark Lake radio telescope (Kundu et al., 1977). At the same time heliograph measurements give slightly larger sizes in both directions (Abranin and Bazelyan, 1986; Stanislavsky et al., 2013). Any discrepancy in size can be caused by its dependence on year and even month of observation as well as on the activity of the Sun. If we suppose that sizes of the quiet Sun do not change significantly during a week then the compression ratio ($\theta_{\rm north}/\theta_{\rm west}$) was 0.89 and 0.86 at 20 MHz and 25 MHz (van de Hulst, 1947).

Measured fluxes of the quiet Sun were calibrated by the source 3C144 whose flux is well known in the decameter range and is 3000 Jy at frequency 25 MHz (Bobeiko et al., 1979). The average flux per day was defined in the scan nearest to the local noon. Fig.4.7 illustrates the fact that the fluxes before and after a CME were practically the same.

Table 4.2: *Sizes and fluxes of the quiet Sun at 20 MHz and 25 MHz according to observations on May 27 – June 2, 2014.*

	W-E direction		N-S direction	
Frequency, MHz	Size, min	Flux, Jy	Size, min	Flux, Jy
20	$55' \pm 4$	1050 ± 150	$49' \pm 3$	1100 ± 230
25	$50' \pm 3$	1480 ± 130	$42' \pm 2$	1570 ± 190

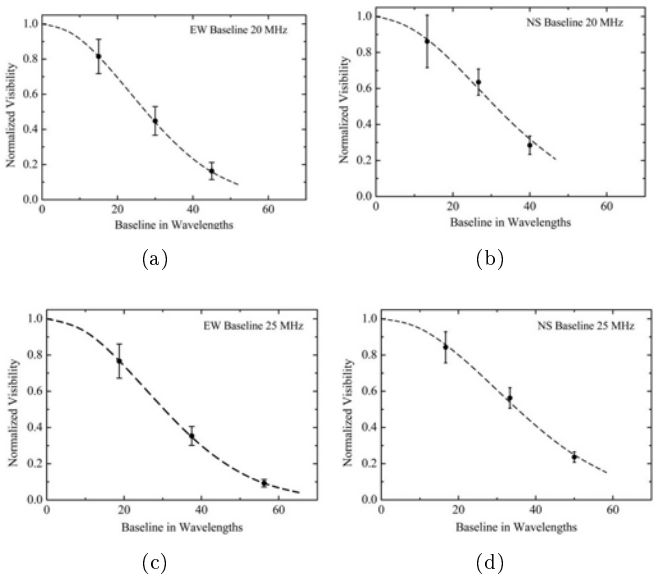


Figure 4.6: *Visibility functions of the quiet Sun at 20 MHz and 25 MHz in W-E (May 27, 28, and 30, 2014) and N-S (May 31 and June 2, 2014) directions.*

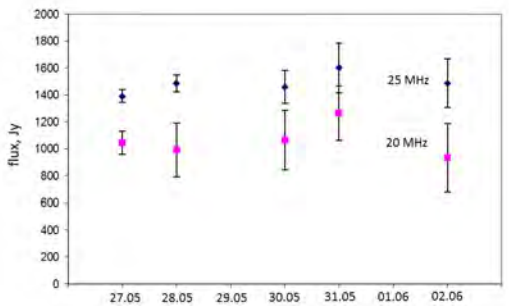


Figure 4.7: *Fluxes of the quiet Sun at frequencies 20 MHz and 25 MHz from May 27 to June 2, 2014.*

Interpretation of the observations

The brightness temperature of the quiet Sun is defined by (Aubier et al., 1971)

$$T_b = 5.5 \cdot 10^{29} \frac{\lambda^2 S}{\theta_W \theta_N}, \tag{4.4}$$

where S is the flux (in Jy), θ_W, θ_N are diameters (in minutes) in equator and polar directions and λ is the wavelength (in m). Using the obtained average fluxes and sizes at frequencies 20 MHz and 25 MHz we get the brightness temperatures of the quiet Sun as $4.8 \cdot 10^5$ K and $5.5 \cdot 10^5$ K at these frequencies. The temperatures derived by the other authors (Abranin and Bazelyan, 1986; Thejappa and Kundu, 1992; Subramanian, 2004) are noticeably lower than the temperature of the coronal plasma, which usually is supposed to be $T_e = 10^6$ K. Such difference can be caused by scattering of electromagnetic waves on the density inhomogeneity of coronal plasma (Aubier et al., 1971). We also consider that processes like scattering should be involved in order to understand the observable parameters of the quiet Sun, first of all at decameter wavelengths because this radio emission escapes

from high in the corona where scattering effects are more pronounced (Aubier et al., 1971; Abranin and Bazelyan, 1986). With respect to the obtained sizes, it is worth pointing out that these sizes are close to the heights at which the local plasma frequency is equal to the corresponding observed radio emission frequency following the Baumbach-Allen model (Fig. 4.8).

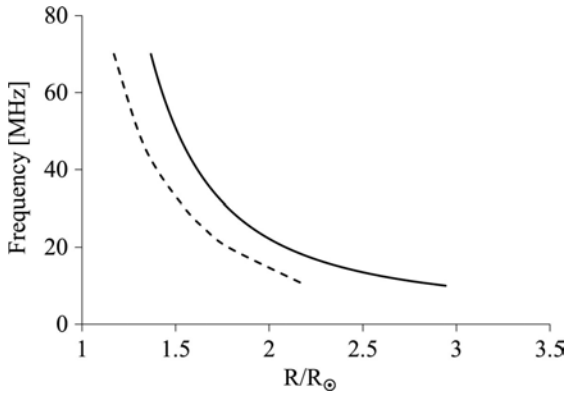


Figure 4.8: *Baumbach-Allen (dashed) and Newkirk (solid) models in dependence of radii of the quiet Sun according to the observations presented here.*

Assuming that radio emission of the quiet Sun escapes from the heights in accordance with the barometric equation (Mann et al., 1999) then the density distribution will follow the Newkirk-like law

$$n(r) = n_0 10^{3.2R_S/r}, \tag{4.5}$$

where $n_0 = 6.9 \cdot 10^4$ cm^{-3}, and r is the distance from the Sun. The power index 3.2 corresponds to the plasma temperature $T_e = 1.9 \cdot 10^6$ K. Such temperature can be reasonable taking into account that the Sun was yet in an active phase in 2014 and the temperature of the coronal plasma could be higher than usually accepted. So it is very important to regularly measure the sizes of the Sun in the decameter range for the definition of the temperature of coronal plasma at heights $0.5R_S - 2R_S$ (height measured from the solar surface).

In summary, interferometric observations of the quiet Sun with the

UTR-2 radio telescope have shown that this method can be used to obtain quiet Sun parameters such as flux, sizes and brightness temperature at heights of $0.5R_S - 2R_S$. From this point of view it is of current interest to regularly observe the quiet Sun in the decameter range. During the first observations in interferometric mode at the radio telescope UTR-2 we can state that:

- Gaussian distribution of the quiet Sun intensity is a good approximation,
- brightness temperatures of the quiet Sun are $T_e = 4.8{\cdot}10^5$ K and $T_e = 5.5 \cdot 10^5$ K at 20 MHz and 25 MHz, correspondingly, and they are smaller than the temperature of the coronal plasma,
- the obtained sizes of the quiet Sun at 20 MHz and 25 MHz are close to the heights of corresponding local plasma frequencies in the Baumbach-Allen solar corona,
- the compression ratio of the quiet Sun is about $0.85 - 0.9$ in the decameter band, and
- on the days before and after a CME the radio fluxes of the quiet Sun are practically the same.

5 Type III Bursts

5.1 Introductory remarks

Type III bursts are the most studied component of sporadic radio emission of the Sun. These bursts are observed in the wide frequency band from 1 GHz to 20 kHz. They drift from high to low frequencies (frequency drift rate is negative) with decreasing drift rate of some hundreds of MHz/s at high frequencies down to some kHz/s at low frequencies. The durations of Type III bursts are from a fraction of a second to some minutes. The fluxes of Type III bursts change within very wide limits, from some s.f.u. to 10^6 s.f.u., and these bursts are frequently observed in the form of pairs. It is considered that these pairs are harmonic pairs, the first component as the fundamental radio emission, and the second component as the second harmonic of radio emission. The ratio of frequencies is about factor 2 at simultaneous time. The polarization of the fundamental component is not high, only 10 % - 20 %. At the same time the polarization of the second harmonic is essentially higher, up to 80 % and even more. Recently it is considered that electron beams are responsible for Type III bursts. Their densities are considerably smaller than the density of coronal plasma and their velocities are in the range of the speed of light. Fast electrons propagating through coronal plasma along open magnetic field lines generate Langmuir waves. These waves are transformed into transversal electromagnetic waves at the local plasma frequency and the double local plasma frequency, yielding radio emission at the fundamental and the second harmonic of Type III bursts. Heliographic and interferometer observations of Type III bursts show that the corresponding sources move outward of the Sun and their spatial sizes increase with increasing distance from the Sun. If electrons propagate into closed magnetic structures like arcs or magnetic loops, then their radio emission is registered as so-called U- and J-bursts. They differ from the usual Type III

bursts insofar as at a given frequency their drift rates very quickly decrease and at the turning point the drift rate gets zero. After that the burst drifts to higher frequencies (drift rate is positive). On the dynamic spectrum these bursts resemble the letter "U" if the region with positive drift is clearly registered, and resembling the letter "J" if this region is absent and the burst ends in the region with zero drift rate. As for usual Type III bursts there were harmonic pairs of U- and J-bursts. Time profiles of Type III bursts and their subclass of U- and J-bursts are smooth, i.e., they have no fine time structures. At the same time the so-called Type IIIb bursts are observed with fine frequency structures in the form of striae-bursts chains. The occurrence of such structures is connected with coronal irregularities through which the electrons are moving.

Common observational factors of Type III class of bursts (including ordinary Type III bursts, Type IIIb bursts, U- and J-bursts) are understandable from a physical point of view. These bursts require the presence of sources in the form of electron beams accelerated by solar flares. These electrons enter the coronal plasma by moving along open magnetic field lines (in the case of Type III and IIIb bursts) or in closed magnetic structures (in the case of U- and J-bursts). At each point along their path the electrons generate Langmuir waves l, which in the nonlinear processes $l + i = t + i$, $l + s = t$ and $l + l = t$ (where i is the ion, s is the sound wave, and t is the transverse wave) are transformed into electromagnetic waves at a frequency equal to the local or double plasma frequencies. The local plasma frequency decreases with distance because the coronal density decreases too, and this fact is manifested in the negative drift rate of bursts, tracks of Type III bursts directed from high to low frequencies. Observational data on the locations of bursts sources at a given frequency indicate the heights at which the corresponding bursts were generated. The frequency drift rate of bursts is defined both by the electron velocity and by the density gradients of coronal plasma in the case of Type III and Type IIIb bursts and density gradients into coronal arches for U- and J-bursts. Movement of electron beams in regions near the top of arcs leads to small drift rates of U- and J-bursts because of small density gradients in these regions. At the top of arcs the burst drift rate equals zero. Propagating toward the Sun after that the density into the arc increases and naturally the drift rate of U- bursts

increases, too. Considering that open magnetic field lines disperse with distance, it is expected that the size of the radio emitting sources also increases, which is confirmed by radio observations at different frequencies.

Despite an understanding of common factors of Type III bursts as well as Type IIIb , U- and J-bursts there are however some points, which are left unclear and are not commonly discussed, as listed in the following:

1. During flares, electrons are accelerated to different velocities, but according to drift rates at different frequencies, the velocities of the electron beams responsible for Type III bursts have mainly values of 0.2 c - 0.6 c. This seems strange, at least, because since accelerated electrons have different velocities, Type III bursts should be expected to have different drift rates. Moreover, bursts with low drift rates should be registered, presumably.

2. Contrary to the fact that electron velocities are within a narrow interval of values, the Type III fluxes are in a very wide range, the lowest fluxes are of some s.f.u. and the highest fluxes achieve values of 10^6s.f.u. The reservoir of energy is kinetic energy of accelerated electrons which is $E_b \approx m\nu_b^2$. The electron velocity does not change essentially from burst to burst. So we can admit that only the density of fast electrons mainly defines the burst fluxes. But estimates indicate that changes are in the limits $n_b \approx 10^{-3} - 10^{-6} n_c$ (n_c is the coronal density). We see that this can not provide the observed dispersion of Type III fluxes.

3. There is evidence that the positions of the fundamental and the second harmonic sources of Type III bursts are practically the same, identical at different frequencies. However, according to plasma theory, the second harmonic radio emission should escape from the highest altitudes. The same is true for the sizes of the fundamental and second harmonic sources of Type III bursts. Their sizes are practically the same, which contradicts plasma theory. The size of the harmonic source should be larger than that of the fundamental source.

4. The fundamental radio emission is thought to be confined within a narrow solid angle along the electron propagation, i.e. outwards from the Sun, due to refraction effects. Therefore, the fundamental radio emission should be observed from the central regions of the Sun. But there are many cases that have been recorded as limb events.

In this section, recent observations of Type III, IIIb bursts, U-, J-bursts and their harmonics in the decameter range by means of UTR-2, URAN-2 and GURT radio telescopes and spectrometer have been yielded in a wide frequency band. Due to the unique capabilities of these radio telescopes, with a frequency band of ground-based radio telescopes 8 MHz - 32 MHz for UTR-2 and URAN-2, and 8 MHz - 70 MHz for GURT, and due to high sensitivity, high frequency-time resolution, high dynamic range, and the opportunity to carry out observations over a long time practically every month during several hours, these observations are of extraordinary quality. The frequency bands of the radio telescopes allow to study the properties of Type III bursts, which are generated at heights $0.5R_S - 2.5R_S$ (measured from the solar surface) that is very high in the solar corona. The observations enable the registration of the weakest and more powerful events simultaneously with a frequency resolution of 4 kHz and time resolution of 10 ms and even better.

It is shown that such parameters as duration and frequency drift rates of powerful bursts (more than 10^3 s.f.u.) do not differ from the weakest Type III bursts. We conclude that neither velocities nor spatial sizes of sources of these bursts determine the values which govern Type III fluxes. Some phenomena discussed in this section have been observed for the first time. Type III bursts with a fine time structure were registered in the decameter range. Sometimes Type III bursts consist of sub-bursts with durations of 1 s (durations of usual decameter Type III bursts change from 5 s - 6 s at 30 MHz to 12 s - 16 s at 10 MHz), which have different drift rates, higher, lower, or equal to those for parent bursts. Furthermore, Type III bursts were found with a jump, changing frequency drift rate at some frequency. They were called "dog-leg" Type III bursts. Maximum drift rates of usual decameter Type III bursts are not higher than 4 MHz/s - 5 MHz/s. But sometimes fast Type III bursts have been observed with

drift rates of about 40 MHz/s.

Given that the velocity of electrons responsible for ordinary Type III bursts is about 0.2 c - 0.6 c, the electrons generating fast Type III bursts should have velocities close to the speed of light. In rare cases we have observed Type III bursts that sometimes change the sign of the drift rate. To explain both types of Type III bursts, it is sufficient to consider that the group velocity of the generated radio emission can be lower, higher or equal to the electron velocity in the region of generation. Since the group velocity is defined by the plasma temperature, the registration of such bursts indicate regions of different temperature of the coronal plasma and can be a kind of diagnostic of it.

In the decameter wavelength range there are many IIIb-III pairs where the first component (Type IIIb burst) is the fundamental radio emission and the second (Type III burst) is the second harmonic. Since the first component has a fine frequency structure and the second does not, it is doubtful that they are harmonically related. Reasons for and against the harmonic character of the pairs components have been presented on the basis of examples of such Type IIIb-III pairs observed in different months of 2012. However, in 1970 some theoretical theories were published suggesting that trios of Type III bursts could exist in addition to the fundamental and second harmonic pairs.

The first interferometer observations of Type III bursts were conducted out by the UTR-2 radio telescope at frequencies of 20 MHz and 25 MHz. These first observations revealed that the sizes and positions of Type III sources can reliably be obtained at different frequencies providing the opportunity to follow motion and evolution of Type III bursts at heights from 0.5 to 2.5 solar radii above the solar surface. In the decameter range U- and J-bursts are not frequently observed. Corresponding magnetic arcs can have large sizes in the order of some solar radii. Like the harmonic IIIb-III pairs there are observed Jb-J bursts, in which the first component has a frequency fine structure as Type IIIb bursts. For the first time a harmonic pair of U-bursts was observed with UTR-2 and GURT radio telescopes for which the delay time between the fundamental and the harmonic components was measured. Moreover, the second harmonic reached the Earth earlier than the fundamental following the plasma mecha-

nism of radio emission. The delay time enables the derivation of the plasma temperature in the top of the corresponding arc.

5.2 Fast Type III bursts

Fast Type III bursts (they are called Type III-like bursts) were observed in 1959 at frequencies 500 MHz - 950 MHz (Young et al., 1961; Mel'Nik et al., 2008). Their drift rates were sometimes higher than those for usual Type III bursts at these frequencies. Moreover, sometimes drift rates became even infinite or changed the sign, getting positive. Till the year 2000 such bursts were observed only at frequencies higher than 100 MHz. Bursts durations were restricted within the range 0.3 s - 3 s, only a quarter part of usual Type III bursts durations. These bursts had fluxes not exceeding 100 s.f.u. In 2002 Type III-like bursts (Fig.5.1, upper panel) were registered by the radio telescope UTR-2 at frequencies 18 MHz - 30 MHz for the first time in the decameter band. In 2003 - 2004 such bursts were observed with the UTR-2 telescope also at frequencies 10 MHz - 30 MHz. A remarkable number of Type IIIb-like bursts (Fig.5.1, lower panel) has been registered for the first time, and properties of decameter Type III-like and Type IIIb-like bursts have been observed in 2002 and 2004. The whole number of analyzed bursts exceeded 1000 bursts.

Decameter Type III-like and Type IIIb-like bursts have drift rates which change from 4 to 20 MHz/s (Fig. 5.2, upper panel). The burst observed on August 18, 2002, had the maximum drift rate of 42 MHz/s. Most Type III-like bursts have durations of about 1 s - 2 s (Fig. 5.2, lower panel) and these are significantly shorter than those for usual decameter Type III bursts. At frequencies 10 MHz - 30 MHz the durations of Type III-like bursts practically do not change with frequency, contrary to usual Type III bursts, where the duration decreases with frequency. Type III-like bursts fluxes do not exceed 100 s.f.u., but in rare cases they can be as high as 200 s.f.u.

The characteristic feature of these bursts is the fact that they are registered on days when active regions connected with them are placed near the central meridian (Fig.5.3). This property holds for five Type III bursts storms in 2002 - 2004: on July 13 - 17; July 24

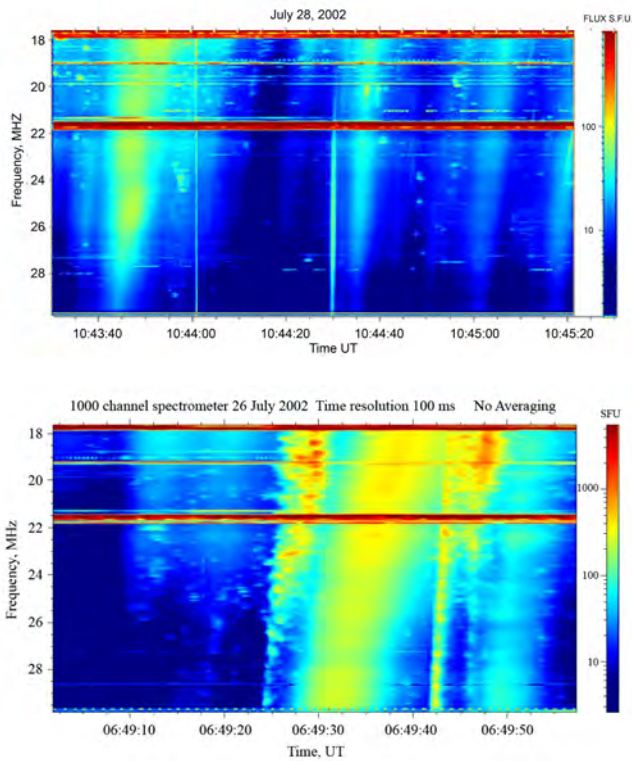


Figure 5.1: *Decameter Type III-like (10:44:30 UT) and Type IIIb-like bursts (06:49:42 UT) within a Type III bursts storm.*

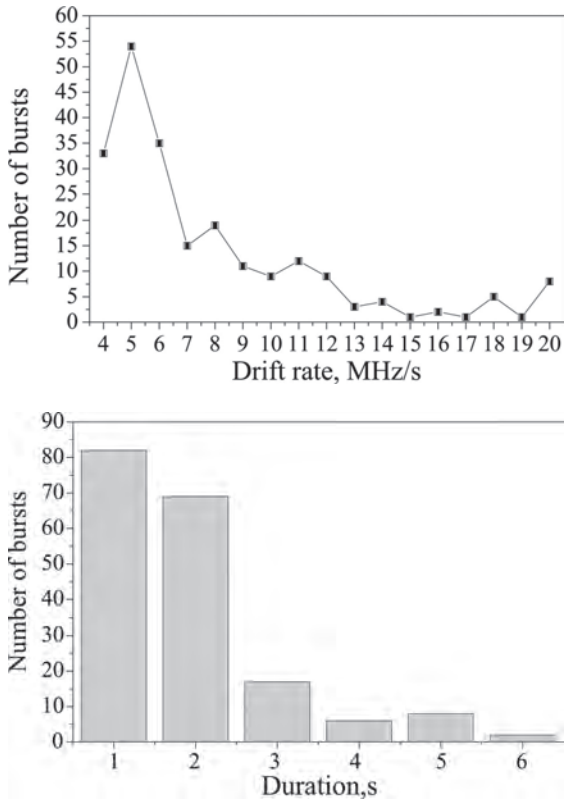


Figure 5.2: *Distributions of Type III-like bursts observed on July 24 - 30, 2002, of their frequency drift rates and durations.*

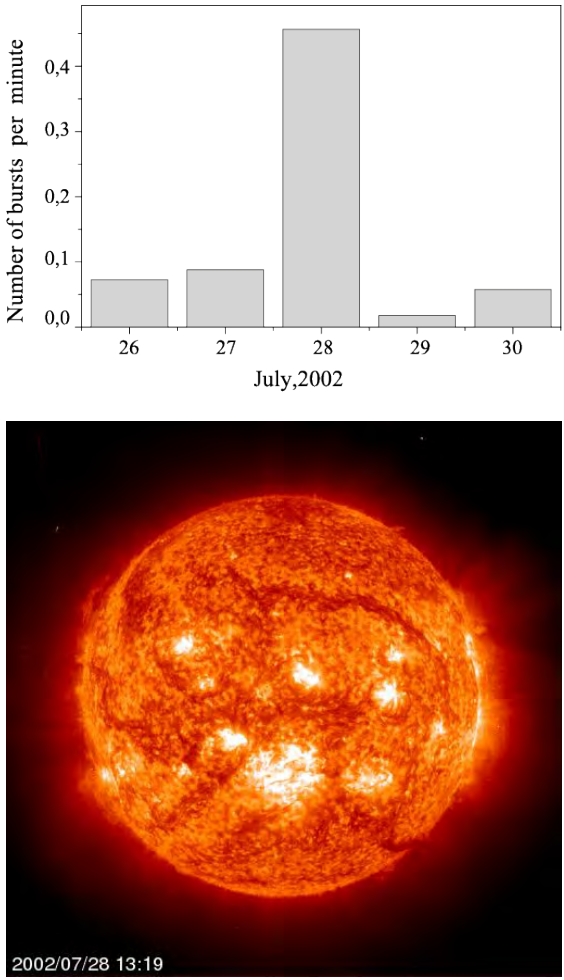


Figure 5.3: *Upper panel: The occurrence rate of Type III-like bursts for the storm event July 24 - 30, 2002. Lower panel: The location of the active region on the solar disk on 28 July 2002.*

- 30; August 16 - 20, 2002; July 1 - 6, 2003; and July 17 - 22, 2004. The cause of large frequency drift rates of these bursts may be the effects of propagation of electromagnetic waves from the sources to the observer, and that at small angles of line of sight the dependence of electromagnetic wave group velocity on the distance from the source is very important.

When the wave group velocity is close to the velocity of electrons (which generate electromagnetic waves) then the drift rate can be large and can even change its sign. For example in the case of small sizes of an electron beam, which is responsible for Type III burst radio emission and propagates under zero angle to the line of sight ($\alpha = 0$), then the difference of arrival times for electromagnetic waves generated by this beam at frequencies f_1 and f_2 from distances R_1 and R_2, correspondingly, is given by

$$\Delta t = \frac{R_{12}}{v_0} - \int_{R_1}^{R_2} \frac{dr}{v_{gr}(R_1, r)} + \int_{R_2}^{R_E} \left(\frac{1}{v_{gr}(R_2, r)} - \frac{1}{v_{gr}(R_1, r)} \right) dr, \tag{5.1}$$

where $v_{gr}(R, r) = c\sqrt{1 - \frac{\omega_{pe}^2(r)}{\omega_{pe}^2(R)(1+3v_{Te}^2/v_0^2)}}$ is the group velocity of electromagnetic wave generated at the distance R, $\omega_{pe} = 2\pi f_{pe} = \sqrt{e^2 n/(m\epsilon_0)}$ is the plasma frequency, v_{Te} is the thermal velocity, v_0 is the electron beam velocity. In Equation (5.1) the first term describes the time for the beam with velocity v_0 to bridge the distance between levels R_1 and R_2. The second term is the time for an electromagnetic wave to cover these distances and the third term is the difference of time required for electromagnetic waves with frequencies f_1 and f_2 to reach Earth from distance R_2. At $R_1 \to R_2$ and $f_1 \to f_2$ the drift rate df/dt at frequency $f_1 = f_2 = f$ is defined by

$$\frac{df(R)}{dt} = \frac{f_p}{2} \cdot \frac{\frac{1}{n}\frac{\partial n}{\partial R}}{\frac{1}{v_{gr}(R,R)} + \frac{Q \cdot R}{2c}\frac{1}{n}\frac{\partial n}{\partial R} - \frac{1}{v_0}}, \tag{5.2}$$

where Q is the value, which defines the model of the solar corona: For the Baumbach-Allen corona $Q = 4.57$ and for the Newkirk corona $Q = 1.49$. Terms of the sum in the denominator in Equation (5.2) are in amount close together for decameter band so there are cases when the denominator is small and as a consequence the drift rate can be large. At an altitude from which radio emission at decameter

wavelengths is emitted, the size of the electron beam is comparable with the solar radius, so for the derivation of correct values of drift rates of Type III bursts it is necessary to take into account the size of electron beams. Dividing the whole volume of the beam by small elementary volumes (Fig. 5.4) each of which radiate electromagnetic waves independently, then the resultant profile of radio emission reaching Earth can be derived. This profile is similar to that for Type III bursts. Knowing the time when the maximum of radio emission was achieved, the drift rates for Type III bursts could be obtained. Drift rates turn out to depend on the electron velocity and longitudinal angle α (Fig. 5.5). It can be seen that usual Type III bursts (with drift rates 4 MHz/s) are generated by electron beams with velocities $5 - 6 \cdot 10^9 cm/s$ and electrons with velocities $1.5 - 2 \cdot 10^{10} cm/s$ are sources of Type III-like bursts. Considering that an electron beam increases its size with propagation leads to a reduction of the effect of drift rate, whereas in the case of constant beam size to an increase (Fig. 5.6). So we conclude that usual Type III bursts are associated with increasing size of electron beams and Type III-like bursts are connected with electron beams of constant sizes.

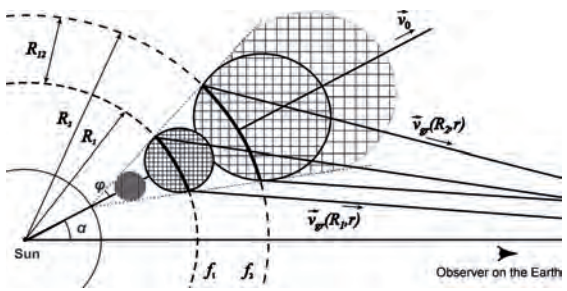


Figure 5.4: *Scheme of derivation of drift rates for radio emission of expanding electron beams.*

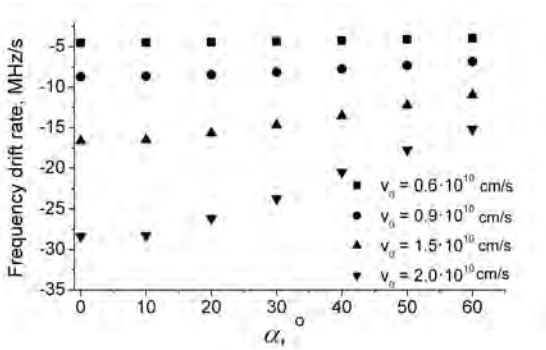


Figure 5.5: *Dependencies of Type III bursts drift rates on longitudinal angle α and velocity of electron beam v_0.*

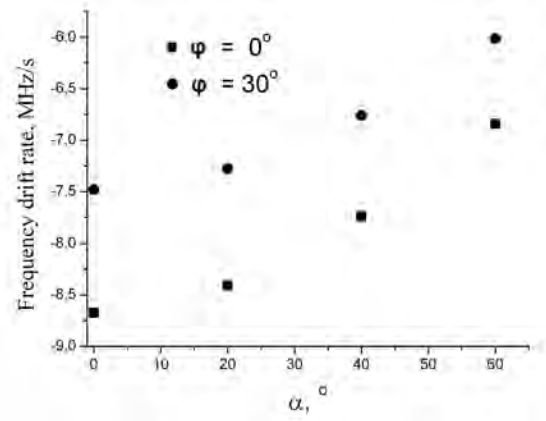


Figure 5.6: *Dependencies of frequency drift rate of Type III bursts on the expansion angle φ.*

5.3 Type III bursts with fine time structure

Type III bursts are generally considered to have no fine structure and their time profile is smooth with a fast rise and slow fall. The exception to this is the Type IIIb burst, which shows fine frequency structure in the form of chains of striae. There have been some attempts to find fine time structure at meter wavelengths (Raoult and Pick, 1980; Benz et al., 1982) based on the fact that meter-long Type III bursts start at frequencies where separate spikes have been observed. In 2001 - 2002, high-sensitivity, high-time-resolution observations of solar radio emission over a wide frequency band with the UTR-2 radio telescope registered Type III bursts with fine temporal structures (Mel'Nik et al., 2005b). During these observations more than 50 such bursts were detected. Type III bursts with fine structures were registered many times in the following years. In most cases the fine structures were in the form of sub-bursts with different drift rates. There are sub-bursts with higher drift rates than those of the parent Type III bursts (Fig. 5.7, upper panel). In this case the maximum drift rate of the observed sub-bursts was 12 MHz/s. Sometimes the drift rates of the sub-bursts are close to the drift rate of the parent Type III bursts. In other cases, these drift rates were only about 100 kHz/s (Fig. 5.7, middle panel). There are also individual cases where sub-bursts have positive and negative drift rates within the same Type III bursts as shown in Fig. 5.7 (bottom panel).

Mel'Nik et al. (2005b) reported that from time to time drift pairs and S-bursts were observed together with Type III bursts. This could be a superposition of these bursts and Type III bursts when radio emission radiated from different places reaches the observer simultaneously. Another interesting feature of Type III bursts with fine structure is the fact that such bursts are observed on days when active regions associated with these bursts are placed near the central meridian.

The explanation of fine structure of Type III bursts is connected to the assumption that electron beams responsible for Type III bursts, have also sort of fine structure. Rutkevych and Melnik (2012) proposed that the electron beam may have "pancake" structure. The regions with large densities (of size b) are interchanged with regions of low densities (Fig. 5.8, upper panel). As a whole such a beam prop-

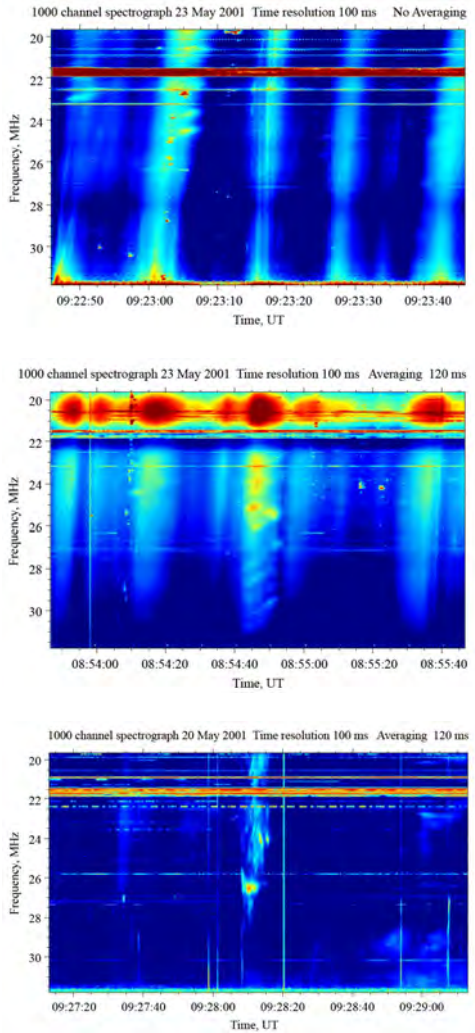


Figure 5.7: *Type III bursts with fine structures in the form of sub-bursts with large (upper panel) and small (middle panel) drift rates and with positive and negative drift rates simultaneously (bottom panel).*

agates with velocity $\boldsymbol{v}_0$. In this case, the profile of radio emission from such an electron beam is visualized in Fig. 5.8 (lower panel). When an electron beam moves straight on to the observer or at a small angle α to the observer then the profile consists of some sub-bursts (dotted line in Fig. 5.8, lower panel). This structure becomes less clear with increasing angle α. At the angle $\alpha_{cr} > \arcsin \frac{c}{v_0} \frac{b}{d}$ the fine structure practically disappears. In good agreement with observations is that at large longitude the Type III bursts with fine structure are absent. If "pancakes" are frozen into the beam their drift rates are the same as for the whole burst. If "pancakes" move with velocities different from the velocity of the beam as a whole, then the sub-bursts have different drift rates compared to that of the Type III burst.

5.4 Type IIIb

Solar Type IIIb bursts are observed in the wide frequency range from 200 MHz to 10 MHz (Benz et al., 1982; Bazelian et al., 1977; De La Noe and Boischot, 1972; de La Noe, 1975; Stewart, 1975). Type IIIb bursts were described in detail for the first time by De La Noe and Boischot (1972). They identified them as chains of short (t$\sim 0.6\,s - 1.2$ s), narrow-band ($\Delta f \sim 60\,kHz - 100$ kHz) striae bursts, which drifted slowly in frequency. Takakura and Yousef (Takakura and Yousef, 1975) considered Type IIIb bursts as the precursors of normal Type III bursts analyzing observations at 80 MHz. They demonstrated that the sizes of striae-bursts sources and Type III bursts are almost identical. In the decameter frequency range Type IIIb bursts were studied by Bazelian et al. (1977) and Abranin et al. (1978). They observed Type IIIb bursts only at fixed frequencies 6.25 MHz, 12.5 MHz and 25 MHz. It was concluded that Type IIIb bursts are formed by narrow-band ($\Delta f \sim 100$ kHz) and short (t~ 1 s) striae bursts. Takakura and Yousef (1975) suggested that Type IIIb bursts are generated by electron beams, which propagate through non-uniform plasma. In the following an analysis of Type IIIb bursts in the frequency band from 18 MHz to 30 MHz during Type III bursts storm in July 2002 is presented.

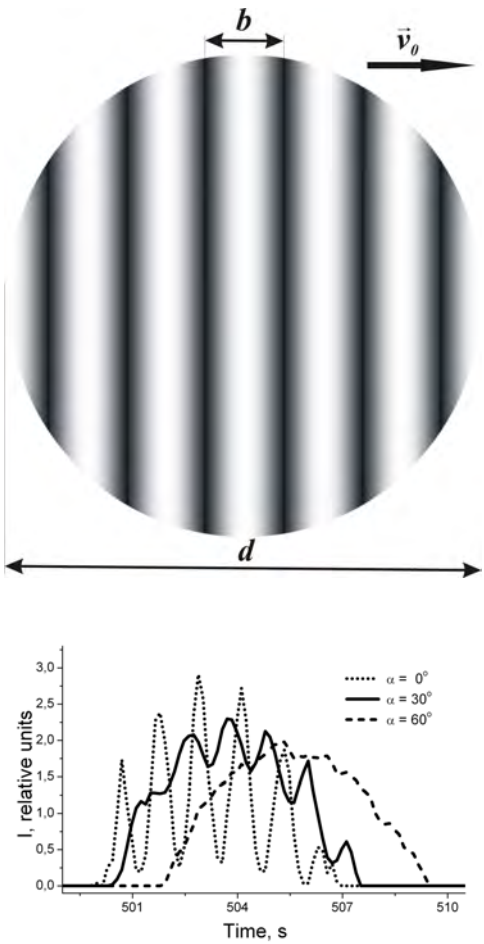


Figure 5.8: *Electron beam of size d consisting of a sequence of large density "pancakes" of size b (upper panel) and the time profile of radio emission intensity from such a beam in dependence of longitudinal angle α (see Fig.5.4).*

5.4.1 Observations

Solar radio observations by the UTR-2 radio telescope (Kharkiv, Ukraine) were carried out since 1970. In the late 1990ies the radio telescope was equipped with a new spectrometer, DSP. It made observations in a wide frequency band of 12 MHz with the frequency resolution of 12 kHz and a time resolution of 20 ms, 50 ms or 100 ms possible. In the present section we consider Type IIIb bursts, which were observed during the decameter storm on July 10 - 18, 2002. In the Fig. 5.9 an example of Type IIIb bursts together with Type III bursts is shown. The main parameters for some tens of Type IIIb bursts, such as number of striae in a burst, striae durations, their frequency widths and fluxes, and frequency drift rate of Type IIIb bursts were obtained. Every Type IIIb burst consists of more than 35 striae bursts in the whole frequency band from 18 MHz to 30 MHz (Fig. 5.9). The time profile of striae is similar to a typical Type III burst with fast rise and slower fall, but their durations were shorter than those for normal Type III bursts. In the majority the frequency profiles were symmetrical.

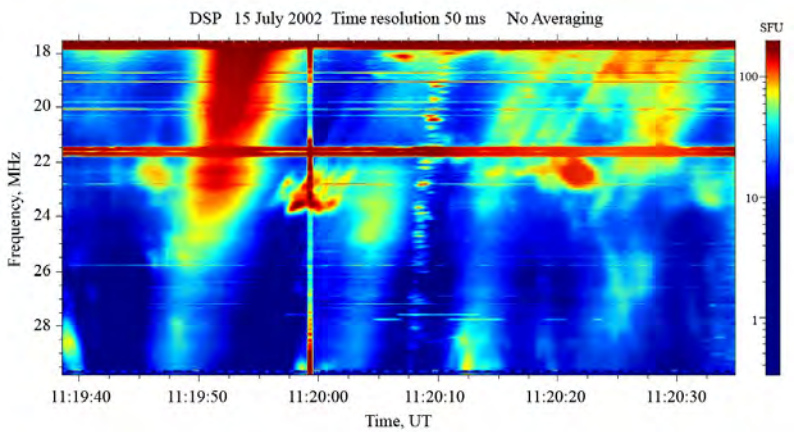


Figure 5.9: *An example of Type IIIb burst (11:20:10 UT) together with Type III bursts (11:19:50 UT; 11:20:00 UT; 11:20:13 UT; 11:20:25 UT) in the frequency range from 18 to 30 MHz.*

In Fig. 5.10 histograms of striae distributions on their duration and frequency width are presented. Fig. 5.10 (top) shows the maximum number of striae within the interval from 1 s to 1.4 s for a single Type IIIb burst, the average duration is about 1.2s. The striae distribution on frequency width (Fig. 5.10, bottom) shows that the maximum number of striae varies from 40 kHz to 80 kHz. The average bandwidth is 50 kHz. It is interesting to note that the minimum of striae duration is observed, when the active region N249 (Fig. 5.11) associated with the decameter radio activity is located near the central meridian. Parameters of the Type IIIb bursts (number of striae in a burst, flux and frequency drift rate) apparently depend on the position of the active area on the solar disk (Fig. 5.12).

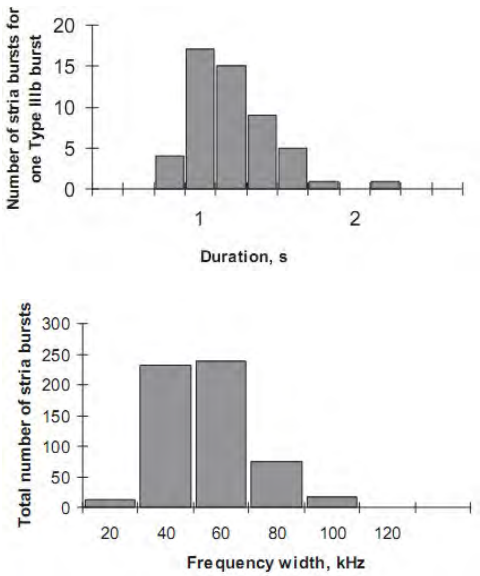


Figure 5.10: *The striae distributions on their durations (top) for a single Type IIIb burst and on their frequency widths (bottom) for all Type IIIb bursts observed on July 15, 2002.*

Analyzing these dependencies we can conclude that the average number of striae in a burst (Fig. 5.12 a, b) and average value of the

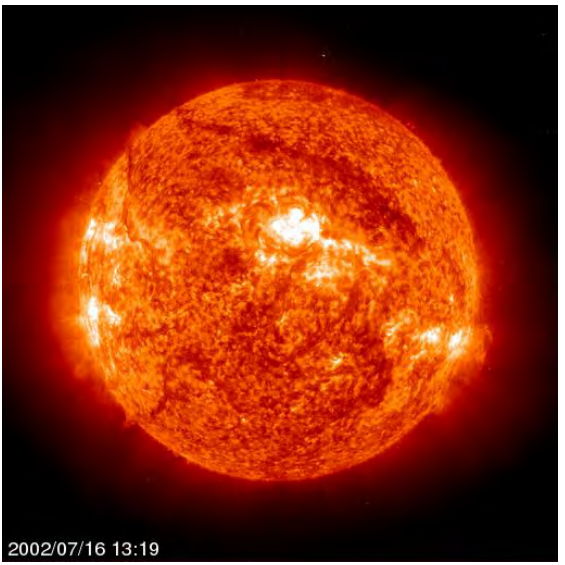


Figure 5.11: *The active region N249 associated with the decameter radio activity.*

flux (Fig. 5.12 c) depend on the day of observations, i.e. the position on the solar disk. When the active region is located on the east side of the solar disk, the average number of striae in Type IIIb burst is two times smaller compared to the case of position of the active region near the central meridian. The average flux however is increasing. At the same time the frequency drift rate of Type IIIb bursts (Fig. 5.12 d) is rather stable. Their average value is about 3 MHz/s. It was found that radio emission fluxes of striae do not exhibit any typical dependence on frequency, but fluxes have maximum values at frequencies 21 - 23 MHz, at higher frequencies however decreasing.

The important result is the dependence of burst parameters from the longitude of the associated active region which indicates the importance of propagation effects. In addition, the bandwidth seems to be defined by average parameters only of the coronal plasma (density, magnetic field, temperature).

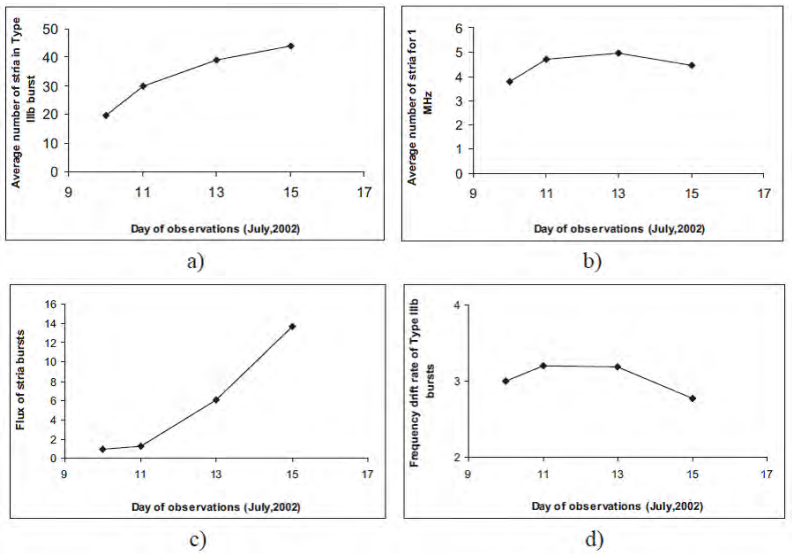


Figure 5.12: *Dependencies of average Type IIIb bursts parameters from the position of an active region on the solar disk: a) number of striae in a single Type IIIb burst; b) number of striae per 1 MHz; c) flux,* 10^{-21} W/m^2Hz*; d) frequency drift rate of Type IIIb burst,* MHz/s.

5.5 Powerful Type III bursts

Type III bursts at decameter wavelengths exhibit very different fluxes. The weakest Type III bursts observed at frequencies 10 MHz - 30 MHz, have fluxes of about of 1 s.f.u. (1 s.f.u. $= 10^{-22}$W/m^{2}Hz). The most powerful bursts however reach up to $10^4 - 10^5$ s.f.u. and in rare cases even 10^6 s.f.u. Drift rates and durations of Type III bursts do not differ as much. For most of Type III bursts the drift rates are in the range 2 MHz/s - 4 MHz/s and their durations are 4 s - 12 s. The exception is Type III-like bursts, whose drift rates can achieve 30 MHz/s and their durations are 1 s - 2 s. In the decameter wavelength range there are also bursts similar to usual Type III bursts, they are the so-called fiber-bursts, the fine structure of Type

IV bursts. Usual Type III bursts come out from the places, where plasma is not disturbed, but however radio emissions of fiber-bursts come out from the regions in the solar corona, where CMEs are passing. Melnik et al. (2010a, 2011a) noted that powerful Type III bursts with fluxes $> 10^3$ s.f.u. were observed beyond Type IV bursts. Thus, these are good examples for studying properties of usual Type III bursts. In Melnik et al. (2010a, 2011a) powerful Type III bursts with fluxes $> 10^3$ s.f.u. out of a sample of 400 bursts observed in July - August, 2002, were analyzed. Their maximum number was registered on those days when active regions associated with them were located at longitudes $40^\circ - 60^\circ$ to the West and to the East from the central meridian. Fig. 5.13 shows an example of such powerful Type III bursts against the background of usual Type III bursts.

The interesting feature of these bursts is the fact that the dependence of drift rates df/dt on frequency f is linear: $|df/dt| \approx A \cdot f$ (df/dt in MHz/s and f in MHz). Moreover, such linear dependence is not only valid for average drift rates of bursts for different days (Fig. 5.14), but also for single bursts. The coefficient A does not essentially change from burst to burst and from day to day and is in the range $A = 0.09\,\mathrm{s}^{-1} - 0.12\,\mathrm{s}^{-1}$ (Melnik et al., 2011a). Note that this dependence is flatter than that for usual Type III bursts ($df/dt \propto f^{1.84}$) in a wide frequency band (Alvarez and Haddock, 1973). The derived linear dependence means that at those altitudes, from which radio emission at decameter wavelengths is emitted, the density of the coronal plasma should follow the exponential law $n(r) \propto e^{-ar}$, where $a = 2A/v_s$ with v_s as the velocity of high energy electrons responsible for Type III bursts. It turns out that in such a corona the dependences of drift rates on frequency for the first and the second harmonics are the same. It is thus possible to distinguish harmonic radio emissions of Type III bursts on their drift rates. The example for this case we see at the Fig. 5.15, on which two identical harmonically connected Type III bursts are shown.

The durations of powerful Type III bursts (Fig. 5.16) are decreasing with frequency as for usual Type III bursts (Suzuki and Dulk, 1985). But this dependence is not as steep as given in Equation (5.3)

$$D \approx 220/f \tag{5.3}$$

(D in s and f in MHz) indicated by Suzuki and Dulk (1985). The

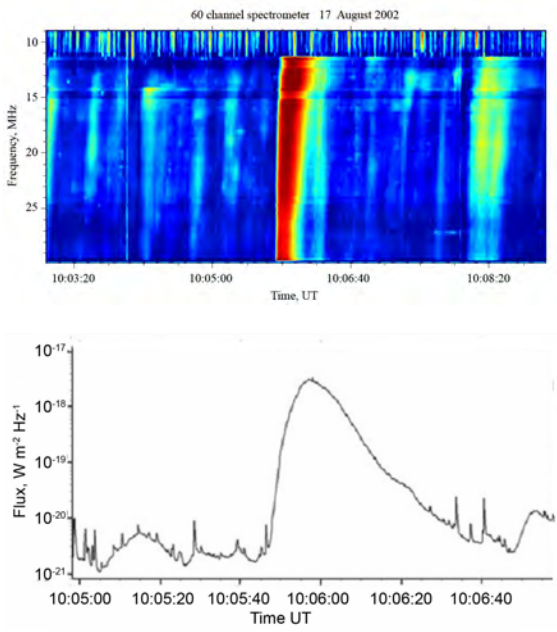


Figure 5.13: *A powerful Type III burst (10:05:50 UT) within a Type III bursts storm (top) and profile of this burst at frequency 12.5 MHz (bottom).*

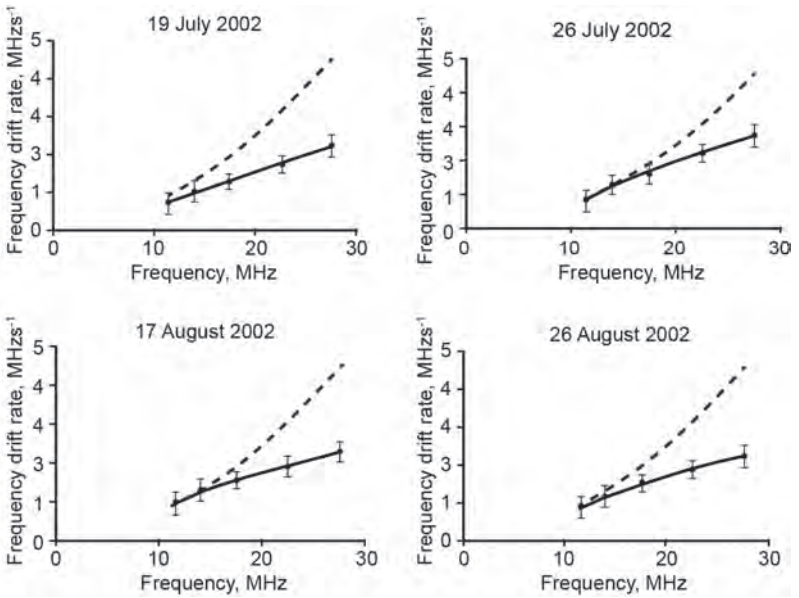


Figure 5.14: *Dependence of drift rate on frequency for powerful Type III bursts for different days. The solid line represents observational data, the dashed line represents the Alvarez-Haddock dependence.*

observational data are close to the dependence proposed by Elgaroy and Lyngstad (1972)

$$D \approx 60 \cdot f^{-2/3}. \tag{5.4}$$

In the paper by Rutkevych and Melnik (2012) (see Figure 5.17) it was shown that the durations of Type III bursts were defined by the sizes of electron beams, which generate these bursts. In the case of constant sizes their burst durations do not change with frequency. But if the size of electron beams is increasing with distance, and if the angle of extended φ (see Fig. 5.4) is of about 30°, then the duration via frequency dependence is close to Equation (5.4). If the angle φ is larger, then this dependence will be steeper (Rutkevych

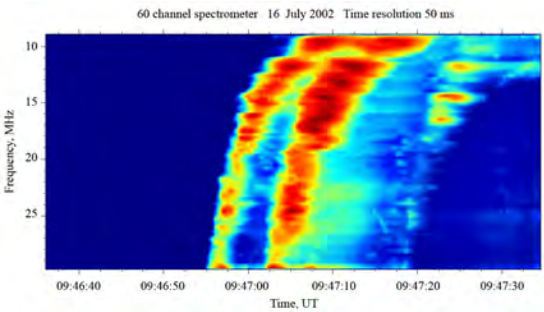


Figure 5.15: *Harmonic pair of two powerful Type III bursts observed on July 16, 2002.*

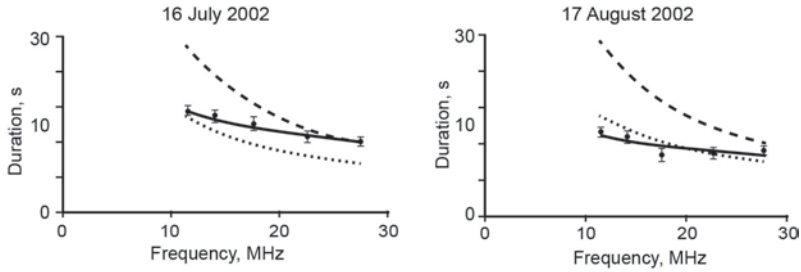


Figure 5.16: *Duration of powerful Type III bursts versus frequency for 16 July (upper panel) and 17 August (lower panel) 2002 (the solid lines represent observational data, the dashed and the dotted lines represent empirical dependencies (Eqs. (5.3) and (5.4)), respectively).*

and Melnik, 2012). So knowing the durations of observed bursts at different frequencies we can deduce in which way the beam is moving in the coronal plasma and changing its size.

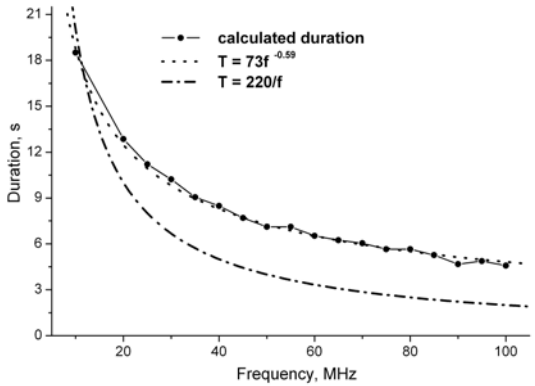


Figure 5.17: *Calculated dependence of duration on frequency (solid line) in comparison with empirical dependences (Eqs. (5.3) and (5.4)) according to results of Rutkevych and Melnik (2012).*

5.6 Type III bursts with changing sign of drift rate

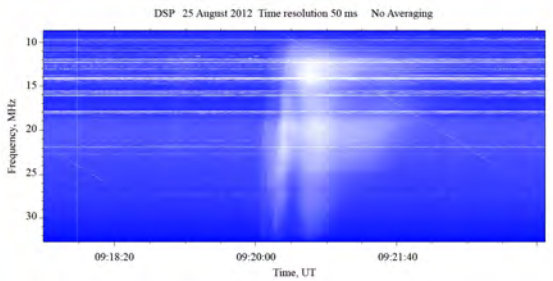
Type III bursts can change the sign of their drift rate from negative to positive and vice versa (Melnik et al., 2013, 2015), and this may happen more than once. These particular Type III bursts were observed simultaneously by the radio telescopes UTR-2, URAN-2, and NDA (Nançay Decameter Array) in the frequency range 8–41 MHz. The negative drift rates of these bursts are similar to those of previously reported decameter Type III bursts and vary from -0.7 MHz/s to -1.7 MHz/s, but their positive drift rates vary in a wider range from 0.44 MHz/s to 6 MHz/s. Unlike inverted U-bursts, the tracks of these Type III bursts have C- or inverted C- shapes. Our basic explanation of the positive drift rate of these Type III bursts

differs from the common assumption that positive drift rates of Type III bursts are connected with an electron beam propagation toward the Sun (Suzuki and Dulk, 1985). We propose that, even if electron beams are moving outward from the Sun, they may generate Type III bursts with positive drift rates if in some regions of the solar corona the group velocities of Type III radio emissions are lower than the velocities of the electron beams.

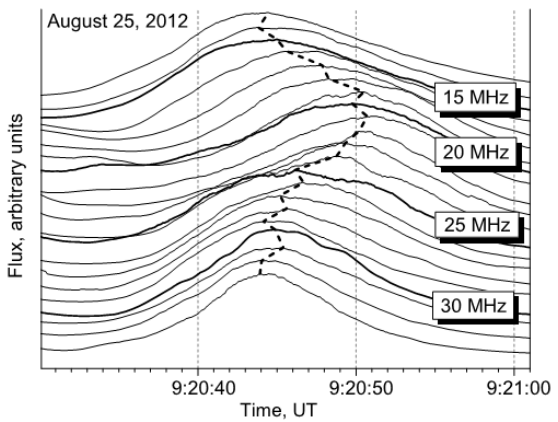
Type III bursts with an alternating drift-rate sign were observed by the Ukrainian radio telescopes UTR-2 (Kharkiv), URAN-2 (Poltava), and the Nançay Decameter Array (NDA, Nançay, France) during the summer observation campaign in 2012 (Melnik et al., 2015). At UTR-2 only four sections of the radio telescope were used. The two Ukrainian radio telescopes were equipped with digital spectral polarimeters. They enable the recording of radio emission in the continuous frequency band 8 MHz – 32 MHz. The frequency and time resolution of the DSP used here were 4 kHz and 100 ms. The spectrometer at NDA used for these observations had a frequency and time resolution of 12 kHz and 37 ms, respectively.

In the paper (Melnik et al., 2015) three Type III bursts with changing frequency drift-rate signs, observed on June 3, August 25, and 26, 2012, were discussed. The dynamic spectrum of one of them, registered on August 25, is shown in Fig. 5.18. The drift rate of its forefront was -3.6 MHz/s and 0.95 MHz/s in the frequency ranges 18 MHz – 32 MHz and 11 MHz – 18 MHz, correspondingly. In the frequency interval 21 MHz – 33 MHz the drift rate of its peak several times changed sign (Fig. 5.18b) with an average negative drift rate of about -1.7 MHz/s. At lower frequencies the drift rate also changed sign several times, but now the average drift rate is positive, 1.2 MHz/s. This Type III burst together with the preceding one resembles an inverted U-burst (Fig. 5.18a). However, this situation is considered to be accidental because all observed decameter U-bursts have a descending part which is essentially fainter than the ascending one (Suzuki and Dulk, 1985). Normal U-bursts have descending parts with positive drift rates. This means that the electron beam responsible for the descending part propagates toward the Sun.

A possible explanation for a change of drift rate might be the propagation of the radio emission that is generated by fast electrons in a coronal plasma. The frequency drift-rate of a Type III burst between



(a)



(b)

Figure 5.18: *a) Dynamic spectrum of the Type III burst with changing drift rate sign on August 25, 2012, at 09:20:44 UT; b) The time profiles of this Type III burst at different frequencies.*

frequencies f_1 and f_2 is equal to the ratio of frequency difference, $f_1 - f_2$, to the difference of radio emission arrival times at Earth, t_1 and t_2 (Fig. 5.19). As was shown by Mel'Nik et al. (2008), this time difference $t_1 - t_2$ is mainly given by the times needed for the electron beam and the electromagnetic wave to travel between the heights r_1 and r_2, at which the emissions at frequencies $f_1 = f(r_1)$ and $f_2 = f(r_2)$ were generated. The group velocity of the fundamental radio emission where it is generated may be much lower than the speed of light, so the time difference can be both positive and negative, depending on the electron beam velocity and the group velocity, and this defines the drift rate sign. Following Mel'Nik et al. (2008), a source moving with a constant velocity v_s at an angle α to the line of sight (Fig. 5.19) generates radio emission at frequency f with the frequency drift rate

$$\frac{df}{dt} \approx \frac{df}{dn}\frac{dn}{dr}\frac{v_s \cdot v_{gr}(r)}{v_{gr}(r) - v_s \cos\alpha}, \tag{5.5}$$

where $v_{gr}(r)$ is the group velocity of the radio emission, and $n(r)$ is the plasma density at the distance r from the Sun (Melnik et al., 2011a). When using Equation (5.5), we assume that $v_{gr}(r_1) = v_{gr}(r_2) = v_{gr}(r)$ is satisfied if the distance between points r_1 and r_2 is small compared with the sizes of the inhomogeneities that lead to the observed changes of Type III dynamic spectra. We also consider that the difference between travel times from points r_1 and r_2 to an observer is mainly defined by the distance $r_2 - r_1 \approx \delta r \cdot \cos\alpha$ traversed by the electromagnetic wave (Fig. 5.19) (Rutkevych and Melnik, 2012). For fundamental radio emission the frequency f equals the local plasma frequency $f = f_{pe} = \omega_{pe}/2\pi = \sqrt{e^2 n/(m\epsilon_0)}$ (e is the electron charge and m is its mass), and in this case, $df/dn = f/2n$. The source velocity v_s is assumed to be equal to $v_s = v_0/2$, where v_0 is the velocity of fast electrons (Mel'Nik et al., 1999).

In the plasma model of radio emission the fundamental radio emission (the electromagnetic wave t) appears at scattering of Langmuir waves by ions i, $l + i = t + i$ (Ginzburg and Zhelezniakov, 1958). In these processes the electromagnetic wave frequency equals the Langmuir wave frequency $\omega_t = \sqrt{\omega_{pe}^2 + k_t^2 c^2} = \omega_l = \sqrt{\omega_{pe}^2 + 3k_l^2 v_{Te}^2}$ (here k_t is the wave number of the electromagnetic wave, v_{Te} is the thermal velocity of electrons). From this equation, we conclude that

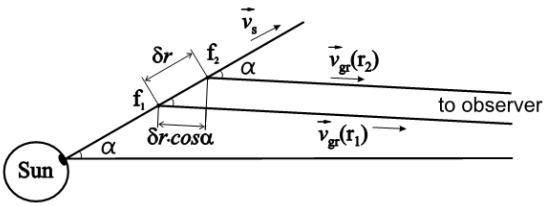


Figure 5.19: *Type III exciter propagating at an angle α to the line of sight.*

electromagnetic waves concentrate mainly at wave numbers $k_{t,0} \approx \sqrt{3}k_{l,0}v_{Te}/c$ and their group velocity $v_{gr} = \left|\frac{\partial\omega_t}{\partial k_t}\right|_{k_{t,0}} = k_{t,0}c^2/\omega_t$ is

$$v_{gr} = \sqrt{3}\frac{v_{Te}c}{v_0}. \tag{5.6}$$

Then the frequency drift rate in Equation (5.5) is positive for

$$v_{gr} < v_s \cos\alpha \tag{5.7}$$

if electrons move outward from the Sun, i.e. $dn/dr < 0$. Taking into account Equation (5.6), the condition in Equation (5.7) can be rewritten as

$$v_0 > \sqrt{\frac{2\sqrt{3}v_{Te}c}{\cos\alpha}}. \tag{5.8}$$

For electrons moving toward the observer ($\alpha = 0$) we find for the critical velocity v_0^* that

$$v_0^* = \sqrt{2\sqrt{3}v_{Te}c}, \tag{5.9}$$

which gives $v_0^* = 7 \cdot 10^9$ cm/s for a plasma temperature of $T_e = 2 \cdot 10^6$ K. If we assume that the source velocity remains constant while propagating through the coronal plasma, the observed Type III bursts with changing drift rate signs can be understood in the following way: Fast electrons with velocities lower than v_0^* generate Type III bursts with negative drift rates. When they enter the regions, in which the

plasma temperature is low enough for $v_0 > v_0^*$, the fast electrons generate Type III bursts with a positive drift rate (within the frequency band of 18 MHz –32 MHz for the Type III burst observed on August 25, 2012). When they enter high-temperature regions in which $v_0 < v_0^*$, the Type III bursts will again display negative drift rates (within the frequency band of 18 MHz – 32 MHz for the same burst). Thus the observation of Type III bursts with a change in the drift-rate sign means that the corresponding electron beams pass through regions of different temperatures.

In addition to normal Type III bursts (Suzuki and Dulk, 1985) and fast Type III bursts (Mel'Nik et al., 2008) Type III bursts with changing sign of their drift rates are observed in the decameter range. In this waveband such bursts are rare, while in the decimeter range such Type III bursts are common. The nature of these phenomena in the decimeter and decameter bands may be different. Even assuming that decimeter Type III bursts with changing drift rate signs result from the simultaneous propagation of fast electrons toward and away from the Sun, the explanation of decameter Type III bursts encounters difficulties. Because both the fluxes and the drift rates of these unusual decameter Type III bursts are similar to those of standard Type III bursts, we suggest that the change in drift rate sign in these bursts is related to the properties of the plasma through which the electrons are propagating. If the velocity of the source is less than the group velocity of Type III radio emission, bursts with negative drift rates are observed. Otherwise, Type III bursts have positive drift rates. When these velocities are approximately equal, fast Type III bursts are recorded. Thus, from this point of view, all types of decameter Type III bursts – standard, fast and with changing signs of the drift rates – can be understood. Moreover, because the critical velocity for sign change is defined by the plasma temperature, we can determine the heights of regions of different temperatures.

5.7 "Dog-leg" Type III bursts at the decameter wavelengths

Type III bursts were first identified by Wild and McCready (1950). Since that time these bursts were intensively studied by many scien-

tists (see, e.g., Wild and Smerd (1972); Solar Radio Group Utrecht (1974); Suzuki and Dulk (1985); Mel'Nik et al. (2008); Pick and Vilmer (2008); Melnik et al. (2011a); Reid and Ratcliffe (2014); Melnik et al. (2015)) in different frequency bands (from 1 GHz to some tens of kHz). All authors interpret these bursts as radiation produced near the electron plasma frequency f_{pe} and/or near its harmonic $2f_{pe}$ by electron beams moving along open magnetic field lines with superthermal velocities $\approx 0.3c$, where c is the speed of light.

According to all existing corona models (Allen, 1947; Newkirk, 1961; Abranin et al., 1990; Mann et al., 1999) the coronal plasma density monotonically decreases with distance from the Sun. As a result the frequency of radio emission of Type III burst (taking into account plasma emission mechanism) should monotonically decrease with time, forming the dynamic spectrum of well known appearance.

Summarizing many observational results, Alvarez and Haddock (1973) have proposed an empirical dependence of the frequency drift rate on frequency for Type III bursts in a wide frequency band

$$\frac{df}{dt} = -0.01 f^{1.84}, \tag{5.10}$$

where frequency f is in MHz.

Taking into account the dependence of the Type III bursts half-power duration on frequency (Equation (5.3)) proposed by Suzuki and Dulk (1985) we can calculate the idealized dynamic spectrum of the Type III burst. The result of calculation is shown in Fig. 5.20a. Cairns et al. (2009) suggested the model where solar bursts form a straight line on the $1/f - t$ plane. For the calculated spectrum (Fig. 5.20a) this is verified as shown in Fig. 5.20b.

Observations show that in the vast majority of cases real dynamic spectra of Type III bursts are very similar to the calculated spectrum shown in Fig. 5.20a. Nevertheless, observations carried out at the radio telescope UTR-2 in 2002 - 2006 in a wide frequency range discovered rare cases when Type III bursts have unusual dynamic spectra with a kind of jump point, where the drift rate changes stepwise. From the specific appearance of the dynamic spectra of such Type III bursts we may call them "dog-leg" Type III bursts. To reliably distinguish these "dog-leg" Type III bursts from other Type IIIs the dependence of the drift rate on frequency as well as $1/f - t$

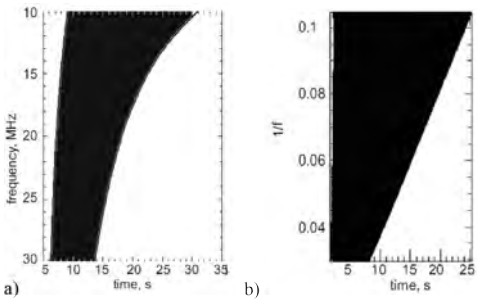


Figure 5.20: *Modeled Type III burst dynamic spectrum (a) and* $1/f - t$ *spectrum (b).*

spectra for each candidate has been analyzed in the frequency range 10 to 30 MHz.

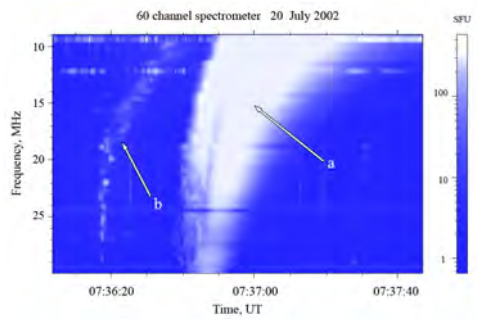


Figure 5.21: *Ordinary Type III burst (a) and dog-leg Type IIIb burst with knee-point at 19 MHz (b).*

5.7.1 Observations

As mentioned above ordinary Type III bursts are characterized by the frequency drift rate monotonically decreasing with time. An example is the burst (a) in Fig. 5.21. Observations show that Type III bursts sometimes demonstrate an unusual shape in the dynamic spectrum with a kind of jump point. A corresponding example of such

a burst is shown in Fig. 5.22. One can clearly see that at around 15 MHz the drift rate of the burst is rapidly decreased. To prove the reliability of the knee-point detection an additional analysis of the $1/f - t$ dynamic spectrum (Fig. 5.23a) and drift rate vs frequency dependence (Fig. 5.23b) of this burst has been performed. According to Cairns et al. (2009) Type III bursts form a straight line on the $1/f - t$ plane. In our case it is clearly seen that the discussed burst consists of two segments of a straight line with different slopes connected around $1/f = 0.065/\mathrm{MHz}$ ($f = 15\,\mathrm{MHz}$). Another evidence of the knee-point existence can be found on the drift rate dependence on frequency (Fig. 5.23b).

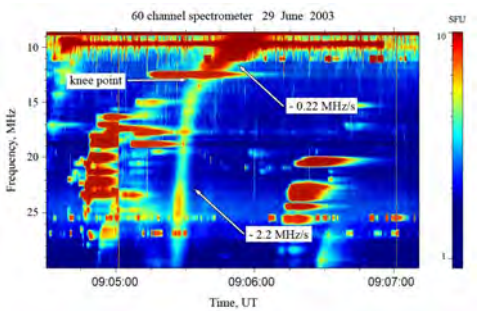


Figure 5.22: *Dog-leg Type III burst observed on 29 June, 2003.*

From 30 MHz down to 15 MHz the drift is monotonic, but at frequency 15 MHz the drift rate decreases step-wise.The majority of knee-points were found at frequencies below 20 MHz as can be seen on the distribution in Fig. 5.24. The fact of knee points absence at frequencies below 13 MHz (Fig. 5.24) does not mean that they were not observed. We just excluded those cases from consideration because they were too close to the lower frequency of the receiver recordings and we could not reliably conclude whether it was dog-leg, U- or J-burst.

The drift rate jump at the knee point in some cases reached an order of magnitude (see for example Fig. 5.23). In order to statistically analyze the value of this jump we used k_D and k_V parameters. If $D_1 = (df/dt)_1$ is the frequency drift rate before the knee point and $D_2 = (df/dt)_2$ is the frequency drift rate after the knee point then

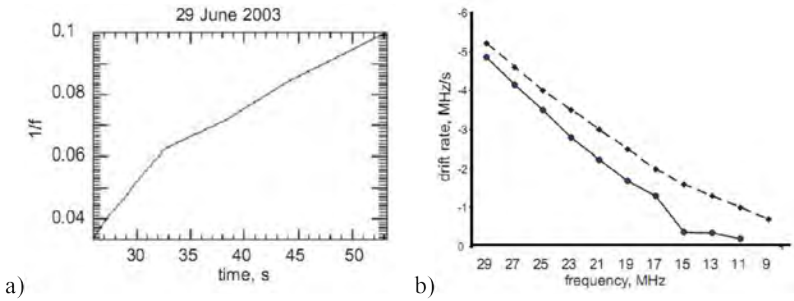


Figure 5.23: *Dog-leg burst on the $1/f - t$ plane (a) and its drift rate dependence on frequency (b). Here the UT in the left picture is 9h 06m + seconds on the time axis. The dashed line in the right picture represents the Alvarez and Haddock (1973) dependence (Equation (5.10)). The full line represents observational data.*

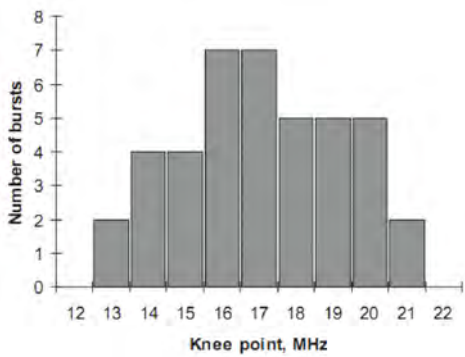


Figure 5.24: *Knee point frequency distribution.*

$k_D = D_1/D_2$. For instance, the k_D value for the burst in Fig. 5.22 equals 10. The k_D parameter distribution for 41 bursts registered in 2002 is show in Fig. 5.25a. According to the plasma generation model the frequency drift rate is defined by the fast electron velocity (under the conditions of known coronal density profile). Thus the value of the jump at the knee point can also be expressed in terms of the source velocity jump. If ν_1 is the source velocity before the knee point and ν_2 is the source velocity after the knee point then $k_V = \nu_1/\nu_2$. The k_V parameter distribution for the same set of bursts is shown in Fig. 5.25b.

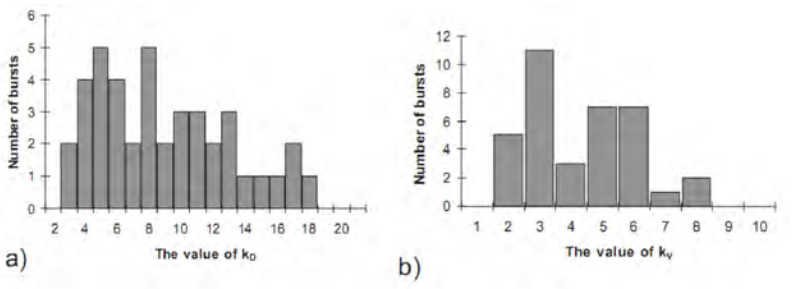


Figure 5.25: *a) Distributions of the jump values at the knee point: drift rate jump k_D, and b) source velocity jump k_V.*

5.7.2 Interpretation of the observations

The observable frequency drift rate of Type III burst df/dt (MHz s^{-1}) is defined by the equation

$$\frac{df}{dt} = \frac{df}{dn}\frac{dn}{dr}\nu_s \cos\phi, \tag{5.11}$$

where f is the radio frequency, n is the plasma electron density, r is the distance from the Sun, ν_s is the linear source velocity and ϕ is the angle between the electron beam direction and the plasma density antigradient. Apparently, the monotony of the drift rate dependence on time is predetermined by the monotony of all factors in the Equation (5.11). Consequently, the jump in the frequency dependence of the drift rate can be caused either by the jump in the dn/dr factor

(due to coronal inhomogeneity along the path of the superthermal electrons), or by the jump in the ν_s factor (due to a sudden electron deceleration), or by a sudden change in the electron beam direction. In fact, it is rather difficult to explain such large jumps in the drift rate jumps by the stepwise change of only one factor. For example, to obtain a drift rate jump of an order of magnitude, the electrons moving along the density antigradient would have to slow down by a factor of 10 or be deflected by about 80° from the initial direction almost instantaneously. Thus, the effect is probably caused by the combination of parameter jumps in all factors of Equation (5.11) or in other words, it may be the result of aggregate effects of plasma inhomogeneity, magnetic field structure change and variation of the electron beam parameters. According to an estimation the sizes of regions where such sudden changes take place do not exceed 30 000 km. Our observations show that the electrons responsible for the dog-leg Type III bursts generation are in general slower than 0.3 c (the speed of ordinary Type III electrons). This fact is well illustrated by the electron velocity distribution shown in Fig. 5.26. Thus, an initial deflection of the electrons away from the antigradient direction may be a possible explanation. One of the possible regions in the corona where such inhomogeneities can occur is the coronal streamer region.

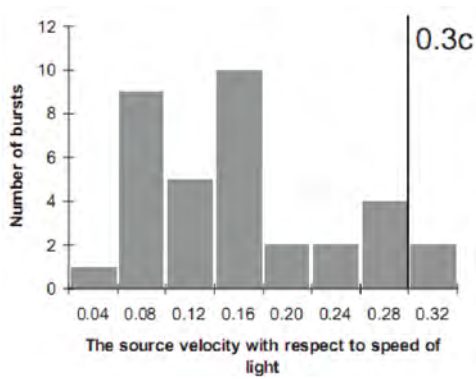


Figure 5.26: *Distribution of the initial velocities of electrons responsible for the dog-leg Type III bursts generation*

5.8 Decameter Type IIIb-III pairs

The existence of harmonic IIIb-III pairs (so-called fundamental-harmonic pairs) was established many years ago. The frequency ratio of harmonic to fundamental averages 1.8:1, with a range from 1.6:1 to 2:1. Fundamentals have high polarizations up to 70% - 80% with an average value of 35%. The polarization of harmonics is essentially smaller, in average only 11%. Burst durations of fundamentals are some times shorter than durations of harmonics, 6 times shorter than for harmonics at 38 MHz. Drift rates of decameter fundamentals and harmonics are similar and mainly equal to 2 MHz/s - 4 MHz/s. Altitudes and apparent source sizes of fundamentals and harmonics are practically the same and both increase with wavelengths. In such a way the diameter of radiated regions are $6'$, $11'$, and $20'$ at 169 MHz, 80 MHz, and 43 MHz, correspondingly. Radio fluxes of Type III bursts and their brightness temperatures also increase with wavelengths and change in the wide ranges from 10 s.f.u. to 10^4 s.f.u. for fluxes and from 10^7 K to 10^{12} K for brightness temperature in the meter band. Only in 10% of all harmonic pairs the fundamental is a Type IIIb burst. In these cases, IIIb-III pairs have properties as III-III pairs except for the fine frequency structure of Type IIIb bursts in the form of striae-bursts. Decameter IIIb-III pairs observed in July-August 2002 were discussed in Melnik et al. (2011c). Their main properties were the same as for fundamental-harmonic pairs. The frequency ratio was close to 2. The frequency drift rates of Type IIIb bursts were larger than those for Type III bursts in IIIb-III pairs and durations of Type IIIb bursts were 4-5 times shorter than Type III bursts durations. According to Abranin et al. (1976, 1978) sizes and locations of Type IIIb bursts and Type III bursts were practically the same. So the average size of sources for both Type IIIb and Type III bursts was equal to $30'$ at 25 MHz. Heights of sources of Type IIIb and Type III bursts in the solar corona have been in the range from $1.75R_S$ to $2.22R_S$.

In contrast to the harmonic character of IIIb-III pairs, one hypothesis is that the Type IIIb bursts were the precursors of the Type III bursts (Benz et al., 1982), which were generated by electrons with higher velocities than those of electrons responsible for the following Type III burst. This hypothesis is supported by the fact that the

drift rates of Type IIIb bursts are larger than the drift rates of Type III bursts. The fact that the heights and sizes of Type IIIb and Type III bursts are virtually identical supports this hypothesis.

From the very beginning, one of the difficulties of the IIIb-III harmonic character was the fine frequency structure of Type IIIb bursts and the absence of such structure at Type III bursts. The fine frequency structure of Type IIIb bursts manifests itself as a serious problem. As early as in the first paper (Takakura and Yousef, 1975), in which Type IIIb bursts have been considered, Takakura and Yousef proposed that electron beams propagating through coronal plasma with an inhomogeneity generate radio emission in the form of inhomogeneity structures - striae. This idea was developed in papers by Kontar (2001b), Kontar and Pécseli (2002) and Loi et al. (2014). Kontar (2001b) could numerically show that there were regions where the level of Langmuir waves generated by electron beams was higher or lower depending on variations of coronal density through which these electrons are passing. As a result, radio emissions from different regions will have different intensities and, in principle, some fine frequency structure can be obtained. Returning to the harmonic character of IIIb-III pairs there is the question why, if these pairs are harmonic, a Type III burst does not exhibit such a fine frequency structure? Recently Loi et al. (2014) have numerically shown that propagating through the plasma with Kolmogorov turbulence an electron beam can generate fundamental radio emission in the form of Type IIIb bursts and generate the second harmonic with a smooth profile like Type III bursts. But the durations of both the fundamental and harmonic appear to be practically the same. However, the difference both in durations and in frequency drift rates of Type IIIb bursts and Type III bursts has not been discussed at all.

The problem concerning the identical sizes and the same heights of Type IIIb and Type III bursts can be resolved in the model of ducts. Also, an interesting idea was proposed by Eremin and Zaitsev (1985). They considered the situation that the fundamental with frequency f propagating through the solar corona split into two Langmuir waves of half frequencies $f/2$ in the place where the local plasma frequency $f_{pe} = f/2$ and after that they coalesce again in the electromagnetic wave with the frequency f. This is also where the harmonic of frequency f is generated when fast electrons arrive. As a result, the

secondary fundamental and the harmonic come from the same place.

Thus, there is evidence for the harmonic character of IIIb-III pairs, as well as properties that are contradictory.

5.8.1 Observations

In order to clarify a possible harmonic connection between Type IIIb and Type III bursts in IIIb-III pairs, we analyzed the properties of such pairs observed by the URAN-2 radio telescope in April, June and September 2011. We processed 143 (April), 106 (June) and 56 (September) IIIb-III pairs registered during storms of such bursts.

Some examples of such pairs are shown in Fig. 5.27. As seen striae-bursts, from which Type IIIb bursts consist of, locate irregularly along Type IIIb bursts. There are rather noticeable gaps between them and sometimes striae-bursts tightly appear. Type IIIb bursts have larger radio fluxes than Type III bursts in the IIIb-III pairs. For April 3, 2011, and June 5, 2011, average fluxes of Type IIIb are 4 - 5 times larger than those for Type III bursts in the whole frequency band from 10 MHz to 32 MHz. For September 5, 2011, fluxes of both Type IIIb bursts and Type III bursts are practically equal at all frequencies. The flux-frequency dependences follow the power-law $I \propto f^{-\beta}$ with $\beta \approx 0.8$, 0.6, 1.0 for April 3, June 5 and September 5, respectively. Maximum fluxes slightly exceed 10^3 s.f.u. and minimum fluxes are about 10 s.f.u.

Average drift rates, durations and polarizations of Type IIIb and Type III bursts in IIIb-III pairs are presented in Table 5.1.

Table 5.1: *Frequency drift rates (one day averages), durations and polarizations of Type IIIb bursts and Type III bursts at 16 MHz for April 3, June 5 and September 5, 2011*

	Type IIIb			Type III		
	drift rates, MHz/s	duration, s	polarization, %	drift rates, MHz/s	duration, s	polarization, %
April	2.5	2	50.3	1.9	11.8	11.4
June	4.0	1.2	59.6	2.4	8.6	11.1
Sept	2.2	1.9	31.8	1.5	9.4	12.2

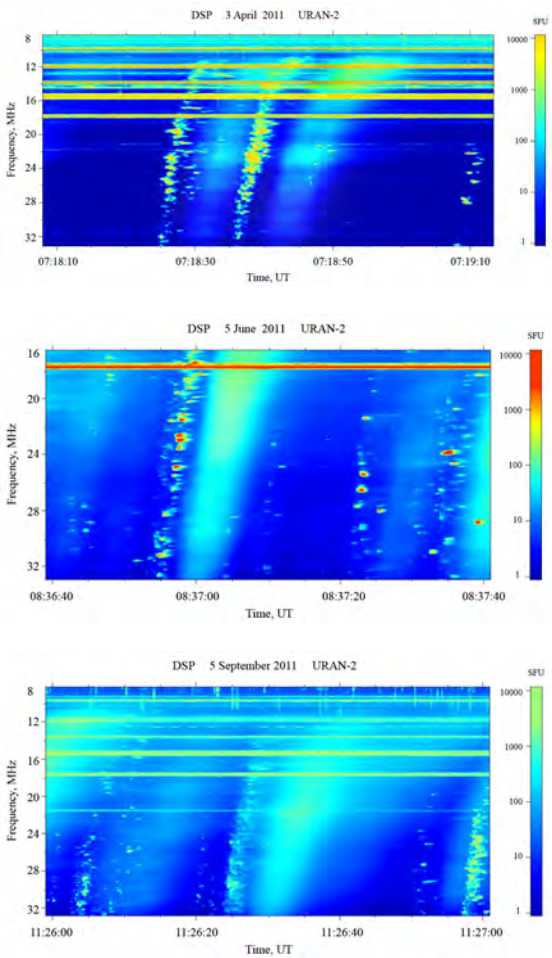


Figure 5.27: *Dynamic spectra of IIIb-III pairs observed on April 3 (top), June 5 (middle), and September 5, 2011 (bottom).*

Drift rates of both Type IIIb and Type III bursts are increasing with frequency (Fig.5.28). Moreover, drift rates of Type IIIb bursts are larger than those for Type III bursts at all frequencies. The drift rate-frequency dependence can be approximated by the equation

$$\frac{df}{dt} \approx -Af, \tag{5.12}$$

where the coefficient A is listed in Table 5.2 for some days of April, June and September 2011. Apparently this coefficient does not essentially differ for bursts in IIIb-IIII pairs. Moreover, these coefficients are practically the same for bursts in April and June, however larger compared to the bursts in September. The coefficient A is inversely proportional to the inhomogeneity size of the plasma region, from which radio emission escapes. With an electron velocity of $0.3\,c$ the inhomogeneity size $a = \left|\frac{1}{n}\frac{dn}{dr}\right|^{-1} = v_s/2A$ equals $a \approx 3 \cdot 10^{10}$cm for the coefficient $A = 0.16$. In September the inhomogeneity size is twice as large.

Table 5.2: *Coefficient A for components IIIb-III pairs for different days of observations*

	A, [1/s] Type IIIb bursts	A, [1/s] Type III bursts
03.04.2011	0.17	0.18
05.06.2011	0.16	0.18
05.09.2011	0.08	0.11

Durations of Type IIIb bursts and Type III bursts are decreasing with frequency (Fig. 5.29). Durations of Type IIIb bursts changed from 1 s at 16 MHz to 0.8 s at 32 MHz for April 3 and June 5 and changed from 1.6 s at 16 MHz to 1.2 s at 32 MHz for September 5. Type III bursts in IIIb-III pairs as well as usual Type III bursts have durations about 12 s at 16 MHz and 5 s at 32 MHz (Mel'Nik et al., 2005b). Note that durations of Type IIIb bursts are essentially smaller than durations of Type III bursts. In the context of the harmonic connection of these bursts in IIIb-III pairs, it is very difficult

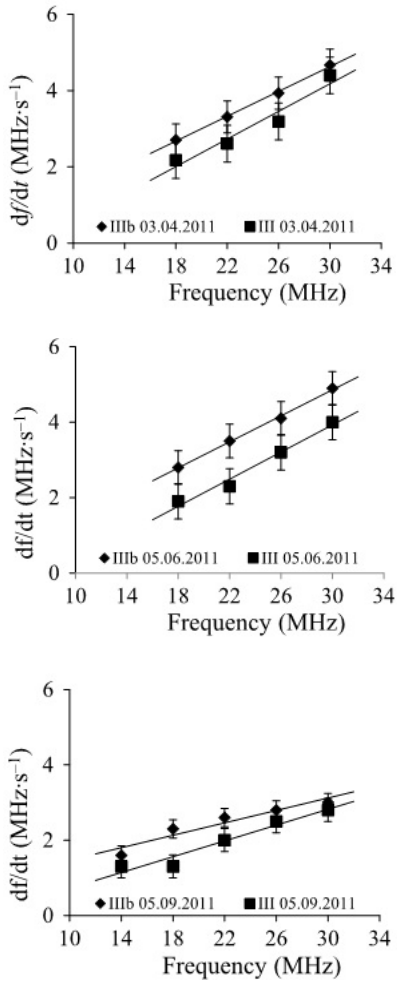


Figure 5.28: *Drift rate dependencies of Type IIIb bursts and Type III bursts on frequency for different days.*

to explain such a difference. In fact, if both bursts are generated at the same location, their durations should be similar. Moreover, the frequency dependence of the durations for Type IIIb bursts and Type III bursts should also be similar. However, the situation is different. Usually, frequency dependencies of burst durations are approximated by the power function (Elgaroy and Lyngstad, 1972; Suzuki and Dulk, 1985; Melnik et al., 2011a,c; Rutkevych and Melnik, 2012).

$$\tau \approx f^{-\alpha} \tag{5.13}$$

Power exponents α for Type IIIb bursts and Type III bursts are summarized in Table 5.3.

Table 5.3: *Power exponent α for Type IIIb bursts and Type III bursts in IIIb-III pairs for different days of observations*

	Type IIIb, α	Type III, α
03.04.2011	0.9	0.5
05.06.2011	0.7	1.1
05.09.2011	0.3	1.0

Polarizations of Type IIIb bursts exceed significantly those of Type III bursts (Fig. 5.30). Polarizations of Type III bursts are practically constant over their durations. At the same time polarizations of Type IIIb bursts achieve their maxima very quickly after the beginning of the bursts, then polarizations decrease regularly. So any polarization maximum is always preceding the flux maximum for all Type IIIb bursts (Fig. 5.31).

5.8.2 Discussion

The property of polarization with respect to intensity for Type IIIb bursts can be understood in the frame of the plasma mechanism of fundamental radio emission. The plasma mechanism is considered as such that the fundamental is generated due to the conversion of Langmuir waves (l) into electromagnetic waves (t) in processes of scattering on ions (i) by $l + i = t + i$ without changing frequency

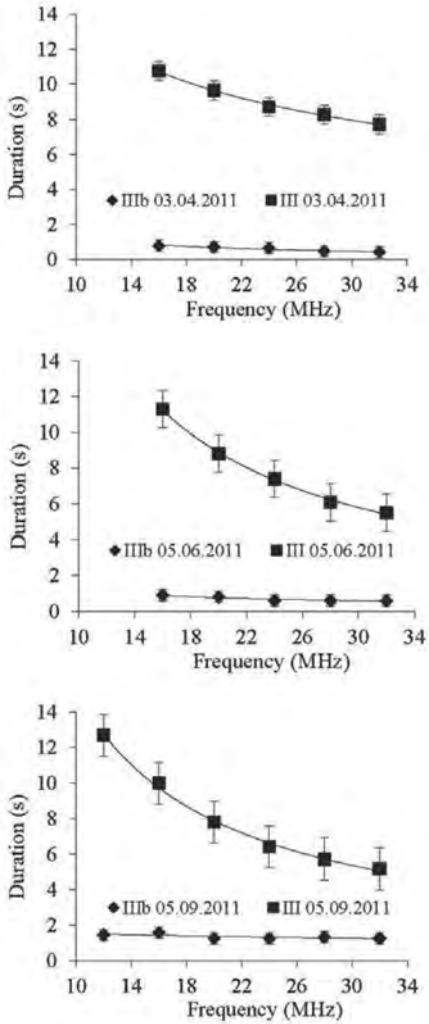


Figure 5.29: *Duration dependencies on frequency for components of IIIb-III pairs on frequency for April 3 (a), June 5 (b) and September 5 (c), 2011.*

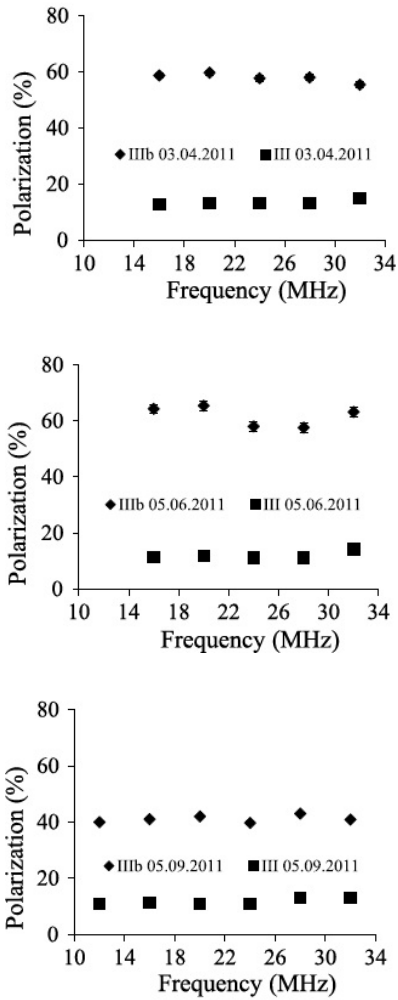


Figure 5.30: *Polarization dependencies of components in IIIb-III pairs on frequency for April 3 (top), June 5 (middle) and September 5 (bottom), 2011.*

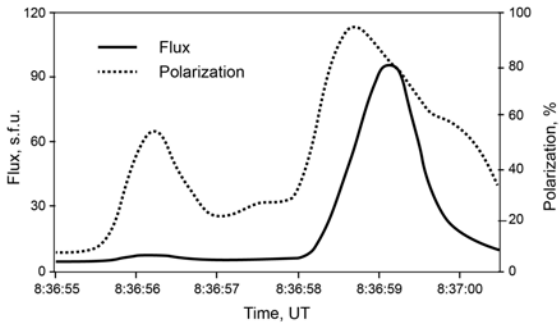


Figure 5.31: *Flux (solid curve) and polarization (dotted curve) profiles for a Type IIIb burst observed on June 5, 2011.*

$\omega_l = \omega_I$ (ω_l is the frequency of Langmuir waves and ω_I is the frequency of electromagnetic waves). Electron beams moving with velocity $v_s \approx 0.3c$ through coronal plasma generate Z-waves (which are Langmuir waves in the plasma without magnetic fields) with the wave number $k \geq \omega_{pe}/v_s$ ($\omega_{pe} = \sqrt{e^2 n/(m\epsilon_0)}$ is the plasma frequency). Mainly Z-waves are concentrated at minimum wave number $k_{min} \approx \omega_{pe}/v_s$ (Mel'Nik, 1995; Mel'Nik et al., 1999). There are a few of them at greater wave numbers up to $k_{max} \approx \omega_{pe}/v_{Te} \approx 1/r_{De}$ ($r_{De} = \sqrt{\epsilon_0 k_B T_e/(e^2 n)}$ is the Debye radius with ϵ_0 as dielectricity constant, and k_B as Boltzmann constant). As seen from Fig. 5.32 Z-waves with wave numbers from $k_{min} \approx \omega_{pe}/v_s = 0.05/r_{De}$ up to k^* are transformed into O-waves and only waves with wave numbers $k > k^*$ are emerging into X-waves. So the number of O-waves will be significantly larger than X-waves and as a consequence polarization of the fundamental will be considerable and its sign will coincide with O-waves. The wave number k^* at a given plasma frequency is determined by the electron cyclotron frequency $k^* \approx 1/(v_{Te})\sqrt{\omega_{Be}\omega_{pe}/3}$ ($\omega_{Be} = eB/m$ is the electron cyclotron frequency), in other words by the magnetic field. So, e.g., with the magnetic field $B = 1$ G the wave number k^* is $0.18/r_{De}$. In principal knowing the spectral density of Z-waves and having measured the polarization of fundamental radio emission of Type IIIb bursts it is possible to derive the magnetic field at the place of radio emission. The fact that polarization maxima of

Type IIIb bursts are achieved just at the beginning of the bursts but not at their flux maximum can also be understood. It was shown in Mel'Nik et al. (1999) that at the moment of the first arrival of fast electrons in a certain place the spectral energy density of Langmuir waves is centered at large phase velocities or small wave numbers. Langmuir waves with large wave numbers are practically absent. For this reason all Langmuir waves are transformed into O-waves and as a consequence polarization will be high. With ongoing time the number of Langmuir waves with large wave numbers increases. As a consequence the number of X-waves, in which these Langmuir waves are transformed, will also increase and thus burst polarization will decrease. Such behavior of Type IIIb bursts is visible in Fig. 5.31.

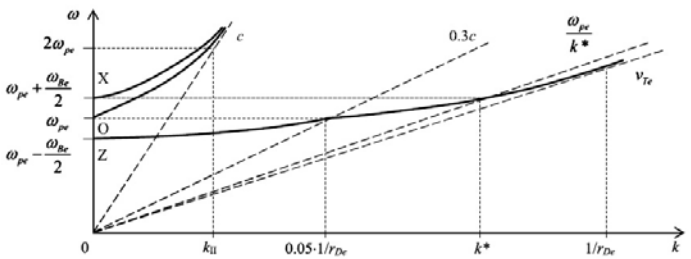


Figure 5.32: *Dispersion curves for X-, O- and Z- waves for plasma in a magnetic field.*

The second harmonic of radio emission appears in the processes of coalescence of two Z-waves (Mel'Nik and Kontar, 2003). In this respect the frequency of formed waves, either X-wave or O-wave, equals the double local plasma frequency $\omega_{II} \approx 2\omega_{pe}$. The wave number of formed waves equals $k_{II} \approx \sqrt{3} \cdot \omega_{pe}/c$ and does not depend on the wave numbers of Z-waves. So the numbers of formed X-waves and O-waves are defined by the probabilities of transformation of Z-waves into X- and O-waves (Zlotnik, 1981). Because these probabilities are not very much different the number of X-waves and O-waves are not noted distinction and as a result the polarization of the second harmonic is not high (Zlotnik, 1981).

In summary, the properties of decameter IIIb-III pairs can be considered to be such that Type IIIb bursts are the fundamental and

Type III bursts are the second harmonic. This is supported by the fact that the frequency ratios of the IIIb-III components are close to 2. As a consequence of harmonic character of the components the frequency drift ratios are also close to this value 2. Important evidence for the harmonic structure of IIIb-III pairs is the high polarization of Type IIIb bursts, and the small polarization of Type III bursts. It also explains the maximum polarization before the flux maximum for Type IIIb bursts and the larger frequency drifts of Type IIIb bursts compared to Type III bursts.

The presence of Type IIIb fine structure in the form of striae-bursts and its absence at Type III bursts can be interpreted by small-scale inhomogeneities of the coronal plasma (Loi et al., 2014). One open question still concerns the different durations of the IIIb-III components, e.g. what is the cause of the different physical phenomena that define these durations. Obviously, IIIb-III pairs are harmonic components, since most observational evidence supports this.

5.9 Trios

5.9.1 Trio of Type IIIb and Type III bursts

As mentioned above the second harmonic can appear due to coalescence of two Langmuir waves. But even a third harmonic can appear. This third harmonic radio emission can occur at the tripled plasma frequency by coupling of the three Langmuir waves $l + l + l \rightarrow t_{III}$, (where t_{III} is the third harmonic electromagnetic wave), or by coupling of the two Langmuir waves and transverse wave of the t_I harmonic $l + l + t_I \rightarrow t_{III}$, or by coupling of the Langmuir wave and the second harmonic electromagnetic wave t_{II}, $l + t_{II} \rightarrow t_{III}$ (Zlotnik et al., 1998).

Observations of three harmonics of U-bursts (Mel'Nik, 1991) and Type II bursts (Kliem et al., 1992; Zlotnik et al., 1998; Dorovskyy et al., 2007) do exist, but observation of three harmonics of Type III bursts are apparently rare. Detection of such events would be important in favor of the plasma mechanism of Type III bursts.

Here, examples of trio Type III and IIIb bursts observed by the UTR-2 and URAN-2 radio telescopes in 2011 - 2012 are discussed (Brazhenko et al., 2013). Their drift rates, durations, polarizations,

and frequency ratios of the components are studied with the aim of establishing their harmonic property.

Spring, summer, and autumn observational sessions in 2011 and 2012 yielded 27 triplets (Fig.5.33) by URAN-2 in the frequency band 8 MHz - 32 MHz. Frequency and time resolutions were 4 kHz and 100 ms, correspondingly. Some regularities have been found in the structure of the triple Type III bursts. In most cases the first component was a burst of Type IIIb. The second and the third components were a Type III burst as well as Type IIIb burst. The most frequently registered combination was IIIb-IIIb-III.

All components of all registered triple bursts drift from high to low frequencies. Absolute values of the frequency drift rates vary from 1 to 5 MHz/s. Such values refer to Type III bursts as well as to Type IIIb bursts.

Fig. 5.34 shows the dependence of the average drift rate of registered triple bursts on frequency. Drift rates of the different components in a triple burst structure are almost equal at the same frequencies. The average difference is about 10 %. But the average drift rate of the first component is higher than that of the other components. And there is a trend that the drift rate of the second component is slightly higher than of the third component.

The drift rate dependence on frequency can be approximated by a linear function as given by Equation (5.12), where A changes for different bursts from 0.05 to 0.2 s^{-1}. These values are close to those which were obtained for powerful Type III bursts. From Equation (5.12) follows the exponent density distribution near some distance R_0 from the Sun (Melnik et al., 2011a)

$$n = n_0 \exp \frac{-2Ar}{v_s}. \tag{5.14}$$

Supposing that the coronal density is governed by the Boltzmann distribution

$$n = n_0 \exp G\frac{\mu_0 \tilde{M_S} m_p}{r k_B T}, \tag{5.15}$$

we can derive an equation which is similar to Equation (5.12)

$$n = n_0 \exp G\frac{\mu_0 \tilde{M_S} m_p}{k_B T}\left(\frac{2}{R_0} - \frac{h}{R_0^2}\right). \tag{5.16}$$

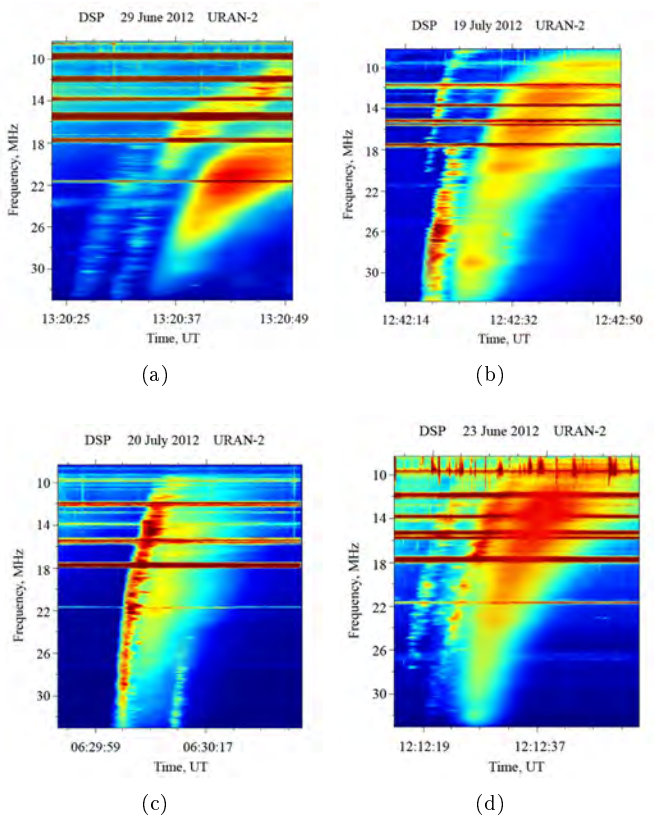


Figure 5.33: *Examples of the dynamic spectrum of the triple Type III bursts, registered by the radio telescope URAN-2. Panels (a), (b) and (d) show triplets with the first and second components of Type IIIb bursts, the third component is presented by a diffuse Type III burst. Triplet on the panel (c) consists of Type IIIb burst, Type III burst and Type IIIb burst.*

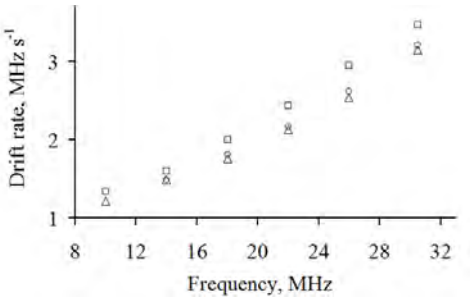


Figure 5.34: *Dependence of the average frequency drift rate of the triplet components on frequency. Markers represent absolute values of the drift rate of the components, averaged upon all registered triplets at the corresponding frequency bandwidths. The first, second and third components are marked by square, circle, and triangle, correspondingly.*

Here, G denotes the gravitational constant, μ_0 is the permeability constant, $\tilde{M_S}$ is the solar mass, m_p is the proton mass, and h is the height.

Comparing Eqs. (5.12) and (5.16) allows to find the plasma temperature in dependence of the value A (see Table (5.4)).

Table 5.4: *Estimation of the temperature in the solar corona at different heights (in solar radius R_S) with respect to maximum and minimum values of the coefficient A (see Equation (5.12)) under the assumption of the Boltzmann distribution.*

	$A_{min} = 0.05$ s^{-1}	$A_{max} = 0.2$ s^{-1}
$1.8R_S$	$5.5 \cdot 10^6$ K	$1.4 \cdot 10^6$ K
$2.0R_S$	$4.5 \cdot 10^6$ K	$1.1 \cdot 10^6$ K
$2.2R_S$	$3.7 \cdot 10^6$ K	$0.9 \cdot 10^6$ K

The maximum values of A give reasonable temperatures of the coronal plasma, their minimum values lead to overestimated temperatures.

The duration of the triplet component, which is presented by the Type IIIb burst, is about 0.3 s - 2 s at frequencies 28 MHz - 32 MHz, and it is increased up to 1 s - 3 s at frequencies 8 MHz - 12 MHz. No obvious dependence in the position of the component within the triplet is found. Therefore we may suggest that any duration difference of the triplet components presented by the same type of burst is not defined by their position within this triplet. The same dependencies can be found at Type III bursts. The duration increases from 3 s - 7 s at the interval of 28 MHz - 32 MHz up to 9 s - 12 s at frequencies 12 MHz - 16 MHz. Such durations are typical for the standard Type III bursts and Type IIIb bursts (Brazhenko et al., 2015b).

Fig. 5.35 shows average durations of the triplet components. The first component (squares) exhibits a shorter duration because in most cases it is a Type IIIb burst, which has a shorter duration than a Type III burst at the same frequency. Durations of the second (circles) and the third (triangles) components are approximately the same because they both can be Type IIIb and Type III bursts with equal possibility.

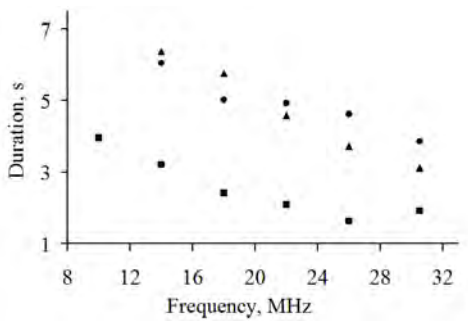


Figure 5.35: *Dependence of the average duration of the triplet components on frequency. Markers represent duration of the components, averaged upon all triplets without distinguishing the types of bursts at the corresponding frequency bandwidths. The first, second and third components are marked by square, circle, and triangle correspondingly.*

The instantaneous frequency ratio of the harmonic radiation is 1:2:3 according to the plasma emission mechanism.Because the bursts were not clearly distinguishable at low frequencies due to noise and ionospheric effects, we could not measure the instantaneous frequency ratio of the components of all the triple bursts recorded. We extrapolated the traces of the bursts at low frequencies considering their behavior at high frequencies, in order to estimate the frequency ratio. We analyzed different time dependencies of the flux peaks. The best model was exponential:

$$f = C \exp(-bt) \tag{5.17}$$

Solving Equation (5.16) with respect to $f(t)$ we obtain Equation (5.17). As an instantaneous frequency ratio we accept an average of the values calculated in the time interval where frequencies of the triplet components lie in the interval 8 MHz - 32 MHz. Fig. 5.36 shows observed flux peaks and interpolated tracks of the triplet components. Frequency ratios of flux peaks of the third and the first components are f1 : f3 = 1 : 2.7, of the third and the second components f2 : f3 = 1 : 1.5 and of the second and the first components f1 : f2 = 1 : 1.8. The frequency ratio of the second and the first components is the same as in the observed harmonic pairs. The obtained frequency ratio of the triplet components (f1 : f2 : f3 = 1 : 1.8 : 2.7) differs from the frequency ratio of the emission at the first, the second and the third harmonics (f1 : f2 : f3 = 1 : 2 : 3). Under the assumption that triplet components are harmonics we can explain this difference due to distinction in the initial group velocity of the harmonic radiation. In other words, this difference does not appear in the source region but occurs along the path to the observer.

The polarization of Type IIIb bursts is high, reaching up to 60 % - 70 %. The degree of circular polarization of the component, appearing as Type III burst, is lower, up to 30 % - 40 %. The polarization of the first component of the triple burst is higher than that of the other components. Moreover, there is a trend that polarization of the second component is higher than that of the third one if these components are of the same type.

The high polarization of the first harmonic and the low polarization of the second harmonic agree with observations and theoretical models.

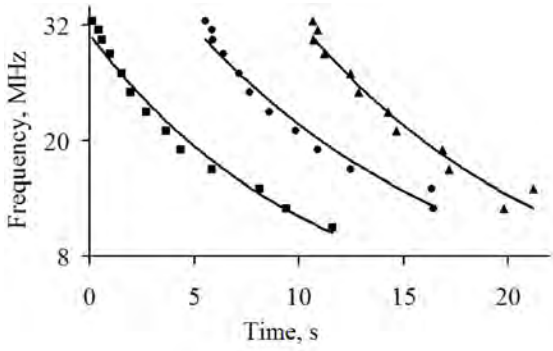


Figure 5.36: *Model of the "average" triple Type III burst. Markers represent time of the flux peaks from the onset of the event at the corresponding frequency bandwidths, averaged upon all observed triplets. The first, second and third components are marked by square, circle and triangle, correspondingly. Solid lines are interpolated tracks of the triplet components.*

Summarizing, the parameters of triple Type III bursts and their components provide evidence of both proof and disproof of the harmonic structure of the triplets. Main point is the absence of the fine structures in the form of striae of the Type III bursts and shorter durations of the Type IIIb bursts. Both facts can be interpreted as evidence of different sources of the components presented by different types of bursts. On the other hand, they may result from the inhomogeneity structure of the source (Takakura and Yousef, 1975).

The frequency ratio of the triplet components, which is close to 1 : 2 : 3, exhibits the harmonic structure of the triple Type III bursts. The average values obtained (less than 2 and 3), can be explained by the different group velocities of the harmonics as they propagate to the observer. Polarization measurements also indicate the harmonic relationship of the triplet components. High polarization of the first component is evidence of fundamental emission, and low polarization of the second and third components is typical of emission on the second and third harmonics. As shown, the drift rates of the harmonics

at the same frequencies are almost identical, the differences do not exceed the measurement accuracy. Therefore, we can assume that this observation feature confirms the harmonic relationships of the triplet components.

5.10 Spatial sizes and heights of Type III radio emission at the decameter wavelengths

5.10.1 Sizes of Type III sources and heights of their radio emission at frequencies 20 and 25 MHz

A number of observations have been performed to define the sizes of different solar burst sources in the decameter wavelength range from 12.5 MHz to 40 MHz (Weiss and Sheridan, 1962; Erickson, 1963; Malitson and Erickson, 1966; Gergely and Kundu, 1975; Abranin et al., 1976; Chen and Shawhan, 1978; Dulk and Suzuki, 1980; Abranin et al., 1980a). Heliographic and interferometer methods were used for those observations. According to some authors Type III bursts had core-halo structures, others did not find such structures. Sizes of cores, if detected, were about $10'$ and sizes of halos were up to $40'$ at different frequencies. The small sizes, $15'$, were revealed at 40 MHz and the largest ones, not more than $40'$, at 12.5 MHz. At intermediate frequencies the sizes were from $15'$ to $30'$ mainly. In some of these observations the solar distance location of radiation was defined, in the range $1.75R_S - 2.5R_S$ at frequency 40 MHz and in the range $1.55R_S - 2.9R_S$ at frequencies 25 MHz, 26.3 MHz and 30 MHz. It was found that radio emissions of the discussed Type III bursts predominantly occurred at the second harmonic of the local plasma frequency.

The results of interferometer observations of Type III bursts by the radio telescopes UTR-2 and URAN-2 on May 29 and June 2, 2014, are discussed in the following (Melnik et al., 2017b). The radio telescope UTR-2 (Braude et al., 1978) worked in the interferometer mode at frequencies 20 and 25 MHz and the radio telescope URAN-2 (Brazhenko et al., 2005) observed the solar radio emission in the

standard spectrographic mode in the frequency band 8 MHz - 32 MHz.

Observations

The bases 225 m, 450 m and 675 m between sections of West-East arm on May 29 and the bases 208 m, 416 m, 624 m, 885 m, 1301 m and 1509 m between the sections of North-South arm on June 2, 2014, were used in the interferometer mode of observations by the radio telescope UTR-2 (Fig. 2.2). Single Type III bursts and their groups were observed together with a Type IV burst on May 29, 2014 (Fig. 5.37). Eight most powerful Type III bursts registered on May 29 were chosen for the analysis (Fig. 5.38). On June 2, however, there was practically sort of quiet Sun in the frequency band 8 MHz - 32 MHz with an additional single weak Type III burst at 06:59 UT.

The dynamic spectrum of solar radio emission in the frequency range 8 MHz - 32 MHz from 9:00 to 12:00 UT on May 29, 2014 (Fig. 5.37) corresponds to the time interval of the interferometer operating mode of UTR-2 on this particular day.

The main parameters of the discussed Type III bursts are given in Table 5.5 (25 MHz) and Table 5.6 (20 MHz). All Type III bursts registered on May 29 had fluxes from 10^2 to 10^3 s.f.u. The Type III burst observed on June 2 was weaker with a flux of about 10 s.f.u.

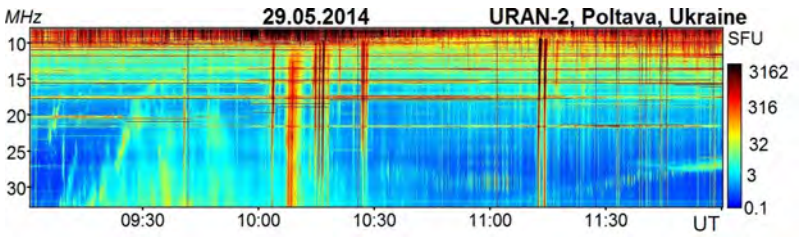


Figure 5.37: *The dynamic spectrum of solar radio emission from 9:00 to 12:00 UT on May 29, 2014, recorded by the URAN-2 radio telescope.*

The frequency drift rates of discussed bursts between 20 MHz and 25 MHz are less than those of standard decameter Type III bursts at

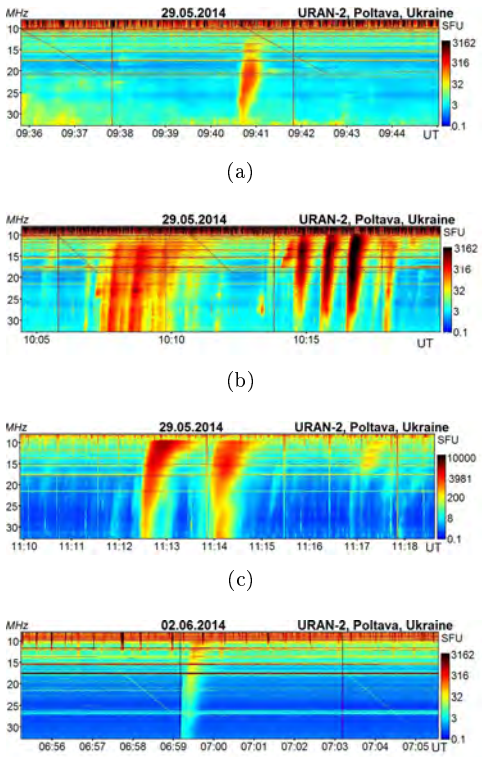


Figure 5.38: *Type III bursts observed by the radio telescope URAN-2 on May 29 (a), (b), (c) and on June 2, 2014 (d).*

these frequencies, only 1−2 MHz/s. Such drift rates are characteristic to decameter Type III bursts at lower frequencies (Melnik et al., 2011a; Brazhenko et al., 2015) if radio emission happened at the fundamental harmonic.

The burst durations τ at frequencies 20 MHz and 25 MHz are in the range 11 s - 17 s and only the burst at 9:41 UT was slightly shorter. Again such durations are more typical for bursts at low frequencies (Brazhenko et al., 2015).

The polarization degree of all analyzed Type III bursts does not exceed 11%. It indicates that these bursts seem to be generated at the second harmonic of the local plasma frequency (Dulk and Suzuki, 1980; Brazhenko et al., 2015).

Sizes of Type III are defined by the visibility function (Thompson et al., 2001)

$$\gamma = \exp\left[-\left(\frac{\pi\theta L}{2\sqrt{\ln 2}\lambda}\right)\right], \tag{5.18}$$

where θ is the angular size, λ is the wavelength at which observations were carried out, and L is the interferometer base length (Fig. 5.39). The derived sizes are presented in Tables (5.5) and (5.6). In most cases Type III source sizes are in the ranges $24' - 27'$ and $20' - 22'$ at frequencies 20 and 25 MHz, respectively. The sizes of two bursts at 10:07 UT and 10:08 UT at 25 MHz are visibly larger compared to others. We associate this feature with a high degree of background radio emission in the form of Type IV burst (Fig. 5.37) that enlarges the effective sizes of bursts. At the same time the level of radio emission at 20 MHz is not so high, and as a consequence, the effective sizes of bursts at this frequency do not differ very much. The sizes of the Type III burst at 6:59 UT at both 20 and 25 MHz (Fig. 5.38) are larger compared to those of Type III bursts observed on May 29. Notice that in the last case Type III electrons moved in the equatorial plane, the measured sizes in West-East direction are prolonged sizes of electron beams d (Fig. 5.40). However, the measured sizes of Type III burst source on June 2, 2014, in North-South direction are transverse sizes l. So we can conclude that transverse sizes are larger of prolonged sizes of Type III bursts at frequencies 20 and 25 MHz. Maybe this is a common property, but to be sure statistics of measured Type III sizes need to be increased.

Following the theory of Type III bursts fast electrons propagating

through the solar corona generate radio emission at the local plasma frequency, so any electron beam with velocity v and prolonged size d radiates electromagnetic waves for the duration $\tau = d/v$. Measuring this duration τ and the prolonged size d one can derive the velocity of the electron beam $v = d/\tau$ responsible for this burst. We see (Tables (5.5, 5.6)) that these velocities at both frequencies are in the range 0.2 c - 0.3 c (c is the speed of light). These values are in good agreement with the generally accepted theory for Type III bursts.

Supposing that the transverse sizes do not significantly differ from the longitudinal sizes, the brightness temperatures (Aubier et al., 1971) for different Type III bursts can be found by

$$T_b = 5.5 \cdot 10^{29} \frac{\lambda^2 S}{\theta_W \theta_N}, \tag{5.19}$$

(S is the flux given in $\mathrm{Wm^{-2}Hz^{-1}}$, θ_W, θ_N are diameters in minutes in equatorial and polar directions and λ is the wavelength in m). The obtained temperatures vary from $2.1 \cdot 10^9$ K to $4.5 \cdot 10^{10}$ K for Type III bursts observed on May 29, 2014. Such brightness temperatures are characteristic for the induced processes of transformation of Langmuir waves to electromagnetic waves (Mel'Nik and Kontar, 2003). The observed Type III burst on June 2, 2014, had brightness temperatures below 10^9 K at both frequencies. It means that this burst was generated in spontaneous processes (Mel'Nik and Kontar, 2003).

With regard to distances of Type III sources this parameter is defined by the phase differences of signals coming to different sections of the interferometer

$$\sin \Delta\theta = \frac{\Delta\varphi\lambda}{2\pi L}, \tag{5.20}$$

where $\Delta\theta$ is the angular distance, $\Delta\varphi$ is the phase difference, λ is the wavelength and L is the interferometer base length (Thompson et al., 2001). Sources of Type III bursts at 20 and 25 MHz were located from $45'$ to $49'$ and from $39'$ to $43'$ from the solar center, respectively. Assuming that electron beams propagating in a Newkirk corona we found that at these distances the local plasma frequencies were two times smaller than the frequency of Type III radio emissions. This is in favor of radio emission of these Type III bursts at the second harmonic, in concurrence with polarizations, drift rates and durations

Table 5.5: *Parameters of Type III bursts at 25 MHz (May 29 and June 6, 2014).*

time UT	flux s.f.u.	drift rate MHz/s	duration s	polarization %	size arcmin	velocity c	distance arcmin	brightness temp. K
09:41	170	-1.2	7	-11	14	0.29	50	$7.5 \cdot 10^9$
10:07	230	-0.9	13	-6	29	0.33	39	$2.4 \cdot 10^9$
10:08	270	-1	14	-6	28	0.29	39	$3.0 \cdot 10^9$
10:14	120	-2.5	12	-6	22	0.27	41.5	$2.1 \cdot 10^9$
10:15	500	-1.6	11.3	-9	22	0.28	43	$8.9 \cdot 10^9$
10:16	1000	-2.5	13	-9	22	0.25	41.5	$1.8 \cdot 10^{10}$
11:13	710	-0.9	10.6	0	20	0.28	42.5	$1.5 \cdot 10^{10}$
11:14	260	-0.9	13.5	0	21	0.29	41.5	$5.1 \cdot 10^9$
06:59	6	-2	12	0	27	-	-	$7.0 \cdot 10^7$

Table 5.6: *Parameters of Type III bursts at 20 MHz (May 29 and June 6, 2014).*

time UT	flux s.f.u.	drift rate MHz/s	duration s	polarization %	size arcmin	velocity c	distance arcmin	brightness temp. K
09:41	170	-1.2	11	0	16	0.21	55	$8.0 \cdot 10^9$
10:07	255	-0.9	14.4	-4	26	0.26	49	$4.7 \cdot 10^9$
10:08	316	-1	17.5	-1	27	0.23	49	$5.4 \cdot 10^9$
10:14	600	-2.5	14.5	-5	27	0.27	47	$1.0 \cdot 10^{10}$
10:15	1150	-1.6	12.3	-6	25	0.3	45.5	$2.3 \cdot 10^{10}$
10:16	2600	-2.5	16.7	-7	27	0.24	44.5	$4.4 \cdot 10^{10}$
11:13	2090	-0.9	12.5	-5	24	0.28	47	$4.5 \cdot 10^{10}$
11:14	790	-0.9	16	-5	23	0.21	46	$1.8 \cdot 10^{10}$
06:59	18	-2	14	0	29	-	-	$2.6 \cdot 10^8$

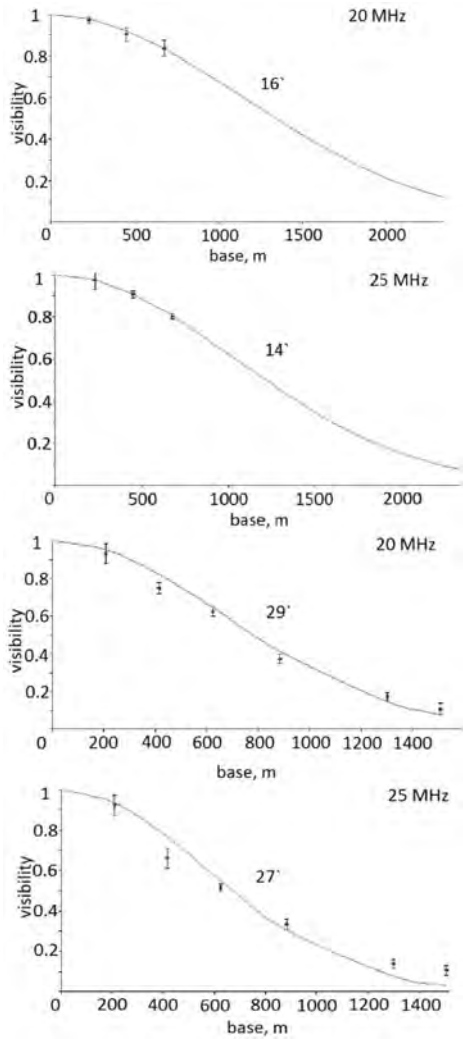


Figure 5.39: *Visibility functions for Type III bursts observed at 9:41 UT on May 29 (a, b) and at 6:59 UT on June 2, 2014, at frequencies 20 and 25 MHz (c, d).*

of the discussed bursts. Slightly higher altitudes for Type III burst at 9:41 UT may indicate that corresponding electrons propagate through the corona with temperature higher than $1.4 \cdot 10^6$ K (see, for example Mann et al., 1999).

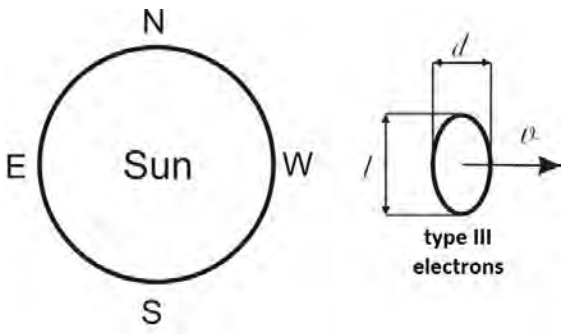


Figure 5.40: *Sketch for Type III electrons propagating in the equatorial plane with velocity $\vec{v}$ outward of the Sun.*

Conclusions

The first interferometer observations of the solar radio emission by the UTR-2 radio telescope demonstrated that size and construction are very appropriate for the determination of Type III source sizes and their distances. Measured visibility functions for Type III sources had practically Gaussian distributions, which were defined only by size, i.e., the sources did not show any core-halo structure. (This statement needs to be confirmed on more statistical samples.) At both frequencies 20 and 25 MHz Type III sources had prolonged sizes between $20'$ and $30'$. The velocities of electron beams responsible for Type III bursts had values of $0.2c$ - $0.3c$ in agreement with Type III bursts theory. Brightness temperatures of Type III bursts with fluxes $10^2 - 10^3$ s.f.u. are in the range $10^9 - 5 \cdot 10^{10}$ K which corresponds to the induced processes of Type III bursts generation.

5.11 Inverted U- and J-bursts

Solar U-bursts are so named because of the shape of their dynamic spectra, which resemble an inverted "U" on the frequency - time plane. Previously U-bursts were classified as separate type of solar sporadic radio emission by Maxwell and Swarup (1958) at the meter wavelengths. Later they were registered also at lower frequencies (Stewart, 1974). Leblanc and Hoyos (1985) specified that in the frequency range 25 MHz - 75 MHz the turning frequencies of U-bursts were mainly between 25 and 30 MHz. Aschwanden et al. (1992) stated that at frequencies of up to 1.4 GHz these bursts were extremely rare. Stone and Fainberg (1971) have observed U-bursts at frequencies 0.7 MHz - 5 MHz.

The main distinctive feature of U-bursts is their dynamic spectrum consisting of two branches: ascending and descending. The ascending branch has a rather fast frequency drift from high to low frequencies. In fact the ascending branch resembles Type III bursts. By analogy to Type III bursts the U-bursts are interpreted within the frame of plasma mechanism of radio emission generation, which is connected to beams of sub-relativistic electrons moving along magnetic field lines. While the frequency drift rate of the Type III bursts depends on frequency as given in Equation (5.10) (Alvarez and Haddock, 1973) in a wide frequency band, the U-bursts do not follow this law. Their drift rates decrease much faster, when approaching the so-called turning frequency. At the turning frequency, the negative drift rate becomes zero and then changes its sign to positive, forming a descending branch of the burst. Now the commonly accepted point of view is that the decrease of the drift rate and sign reversal are the result of the electron beam deflection, when moving along closed magnetic field lines in solar magnetic loops.

The velocity of electrons responsible for the U-bursts is constant and equals approximately $0.1c$–$0.2c$ (Aschwanden et al., 1992; Fokker, 1970), which is slightly less than the velocities of electrons associated with Type III bursts. Regarding frequencies at which U-bursts are observed, the possible heights of magnetic loops can vary from $0.2\,R_S$ (where R_S is the solar radius) (Aschwanden et al., 1992) up to approximately $35\,R_S$ (Stone and Fainberg, 1971).

Type U-bursts are less common than usual Type III bursts (As-

chwanden et al., 1992). Normally U-bursts are observed as single events and less often as groups of bursts. The group usually consists of up to ten bursts with a total duration of about 2 - 3 minutes. At the same time, the groups of allied Type III bursts may last over several hours and even days.

There were U-burst clusters where the turning frequencies of all bursts in the cluster remained unchanged along the cluster. Assuming that all bursts in the group were generated by electron beams moving along the same magnetic loop, this fact indicates that the coronal loops in this case were stable in time. In other groups, the turning frequency decreases sequentially from one U-burst to the next. Such groups have received the name of "drifting U-bursts" (Leblanc and Hoyos, 1985). If all drifting U-bursts of one group are associated with one coronal loop, one can speak about the turning frequency drift, defined in Smith (1970) as "TFD" (Turning Frequency Drift), which characterizes the velocity of the coronal loop lift in the solar corona.

U-bursts with a well developed dynamic spectrum are rarely observed. The descending branches of the bursts are usually weak, diffuse, or even absent. This effect can either be the result of the different efficiency of the interaction of the electron beam with the plasma when propagating towards the Sun and when propagating outwards (Fokker, 1970), or because of misfocusing of the beam due to "expansion" of a guiding magnetic pipe (Caroubalos et al., 1973), or owing to electron beam scattering on inhomogeneities created by a streamer at the top of the loop (Abranin et al., 1980b).

The bursts are usually called J-bursts, when only an ascending branch is visible (Fokker, 1970).

Occasionally, harmonic pairs of U-bursts have been observed. Stewart (1974) noticed that the harmonic ratio in such pairs varies from 1.4 up to 2.2 and in most cases is less than 2.

U-bursts at the decameter wavelengths are usually associated with Type III and Type II bursts, and at the meter wavelengths also with Type I bursts (Smith, 1970). Leblanc and Hoyos (1985) noticed that U - burst groups were mainly observed during 50 minutes before or after the Type II bursts and corresponding CMEs, in the frequency band 25 - 75 MHz (Leblanc and Hoyos, 1985).

In 2003 - 2004 more than 50 U- and J-bursts were registered by the UTR-2 radio telescope in the frequency band 10 MHz - 30 MHz.

It was the first case of ground-based observations of U-bursts with turning frequencies between 10 and 25 MHz proving the existence of coronal loops as high as 3 solar radii. From these bursts only 7 have been identified as U-bursts. Two of them are presented in Fig. 5.41. The turning frequencies of the U-bursts being analyzed are practically uniformly distributed over the range from 10 MHz to 22 MHz (Fig. 5.42). There was a small tendency of a number of bursts to decrease towards higher frequencies. Approximately 90% of all analyzed U-bursts had turning frequencies below 24 MHz.

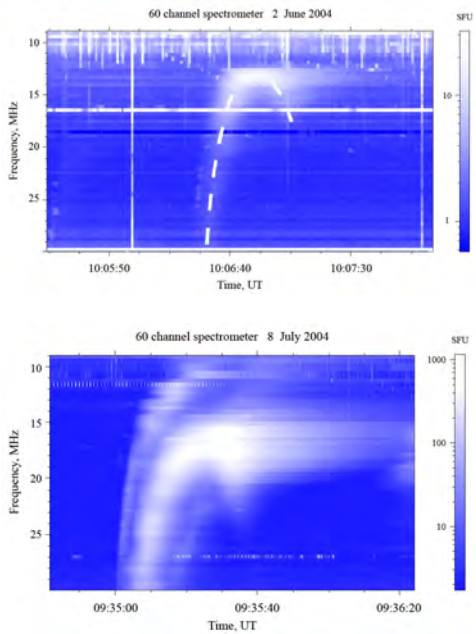


Figure 5.41: *Examples of U-bursts with developed descending branches observed in the decameter range on June 2, 2004 (upper panel) and July 8, 2004 (lower panel).*

The temporal and frequency characteristics of the ascending branches of U- and J-bursts far away from the turning point were very close to those of usual Type III bursts. Their durations varied from 1.5 s

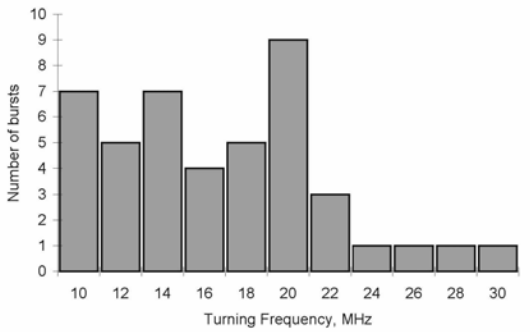


Figure 5.42: *The distribution of U- and J-bursts on turning frequency.*

up to 13 s with an average value of 6 s, and the absolute values of their frequency drift rates were about 1.8 MHz/s - 4.5 MHz/s, which in total corresponds to the characteristics of the Type III bursts in the decameter wavelengths band (drift rates 2 MHz/s - 4 MHz/s, durations 4 s - 10 s) (Abranin et al., 1980b, 1990).

Among all registered U-bursts in two cases the absolute values of drift rates of ascending and descending branches at fixed frequency were approximately equal (both cases on August 15, 2004), in two cases the ascending branch drifted twice as fast as the descending one (both cases on June 2, 2004), and in the remaining three cases (July 8, July 16 and August 29, 2004) the situation was inverse.

Type U- and J-bursts provide a unique possibility to estimate the actual width of the magnetic tube of the loop owing to zero drift rate area in the spectrum (the top of the loop). Under the assumption of the plasma emission model the spectral width of the top of the loop is defined by the linear width of the magnetic tube at its highest position, where the time delay between the radio emissions at different frequencies does not provide an effect onto the instantaneous spectral width of the burst (unlike in the case of ordinary Type III bursts). Due to the high quality of the obtained dynamic spectrum it appears to be possible to detect the spectral widths of the top of the loop for all observed U-bursts. The spectral width of the top of the different U-bursts varied from 1.5 MHz to 3 MHz. It corresponds to linear

widths of the top of the loop from 0.09 to 0.18 solar radii or from $6.3 \cdot 10^9$ cm to $1.3 \cdot 10^{10}$ cm in the Newkirk model.

It should be noted that, while U-bursts were exclusively observed as isolated events, the J-bursts occurred both as isolated events and in groups of 3 - 4 bursts within a group. A group of three drifting J-bursts was registered on June 26, 2004 (Fig. 5.43). The spacing between the bursts in the group was not a stationary value: the second burst was observed 90 s after the first, and the third - 70 s after the second one. The bursts in the group were very similar in structure. This could be confirmed by superposition of the contour (spectral shape) of the first burst (12:10:30 UT), and then superimposed over the second and third burst of the group (Fig. 5.43).

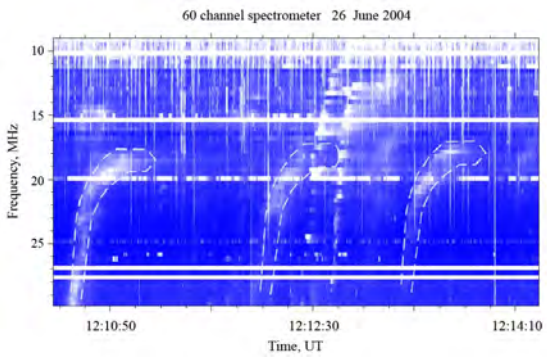


Figure 5.43: *The group of J-bursts observed on June 26, 2004.*

An essential feature of this J-bursts group is its unusual TFD ("Turning Frequency Drift"). It is known that TFD of drifting J-bursts is very close to the frequency drift rate of Type II bursts and corresponds to the linear velocity of the CME in the corona (600 km/s - 700 km/s) (Leblanc and Hoyos, 1985). The observed group had a TFD of about -2 kHz/s. Within the frame of the plasma emission model such frequency drift rate corresponds to the source linear velocity of only 60 km/s, which is an order of magnitude less than the velocities of the shock waves and CME. As shown in Dorovskyy et al. (2010a) observations by LASCO confirmed this conclusion in general.

In a few cases harmonically related pairs of J-bursts were found. Several authors have observed this phenomenon in the frequency band 25 MHz - 200 MHz (Stewart, 1974; Leblanc and Hoyos, 1985). It should however be marked that in the mentioned papers only F-H pairs of ordinary J-bursts were discussed. As was reported in Dorovskyy et al. (2010a,b) the J-bursts harmonic pairs, which were analogous to well-known Type IIIb-III pairs, were observed, too. In such a pair the fundamental component consisted of a chain of narrow-band striae bursts, while the harmonic component did not have fine frequency structure. The examples of such Jb - J pairs are shown in Fig. 5.44. The observations of harmonically related pairs of U - and J-bursts are undoubtedly of interest for the study of harmonic structure of solar radio emission in general. When studying the harmonically related Type III bursts, which have high frequency drift rates, the difference in group velocities of the fundamental and harmonic radiation or radio wave "ducting" effects in the corona may result in a time delay between elements of the harmonic pair, and, therefore, may cause errors in the definition of the actual harmonic ratio. In this sense F-H pairs of U- and J-bursts give true ratios in the points of turning frequencies. The instantaneous frequencies ratio of the F- and H- components of J-bursts pairs is between 1.5 and 2 and in most cases was less than 2 which meets the data given by Stewart (1974). Averaging of the harmonic ratio obtained from the analysis of 6 J-bursts pairs leads to a value of 1.8. The duration of the fundamental component is in the range of 1.5 s - 3.8 s with an average value of 3 s obtained from the analysis of 10 bursts. The harmonic component had longer durations - from 6 s up to 13 s with an average value of 9.3 s (statistics of 23 samples). All these values were derived in U-bursts dynamic spectra far away from the turning point.

The frequency drift rates of U- and J-bursts at frequencies far off the turning point also were close to those of Type III bursts. At 25 MHz the average value of the drift rates of F- and H- components counted -4.5 MHz/s and -1.8 MHz/s, respectively. And according to Abranin et al. (1980b, 1990) the Type III bursts drift rates at the decameter wavelengths vary from -2 up to -4 MHz/s, and durations from 4 to 10 s.

In very few cases (Dorovskyy et al., 2010a,b) unusual and complex

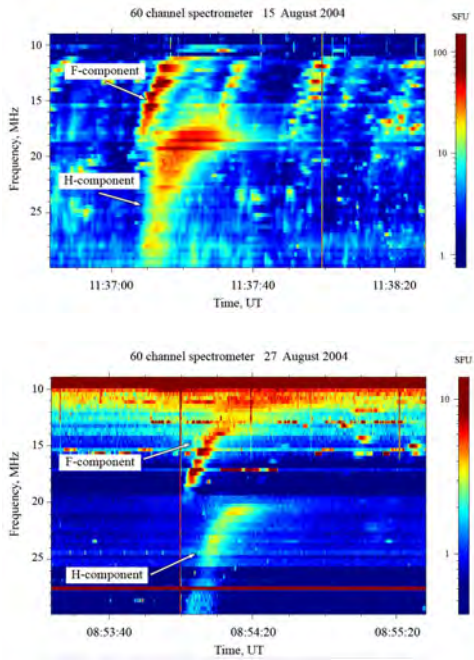


Figure 5.44: *The harmonic Jb-J pairs observed on August 15 (upper panel) and August 27, 2004 (lower panel).*

Type U bursts were observed. One of them was registered on June 2, 2004 at 11:46 UT (Fig. 5.45 upper panel). At 30 MHz the burst looked like a usual Type III burst with the drift rate of approximately -3 MHz/s and duration of 8.2 s. But at lower frequencies this burst "splitted" into at least two separate U-bursts with turning frequencies 23 MHz and 18 MHz and one burst, which could be either a Jb - burst with a turning frequency below 10 MHz, or the usual Type IIIb burst. Though there were no heliographic observations in this frequency band, such an event cannot be considered as a simple superposition of several separate bursts. Caroubalos et al. (1973) have assumed that U- and J-bursts are generated near the neutral plane of streamers. They assumed that depending on the electron injection area, solar bursts of different shapes could be formed: Usual Type III bursts (electrons are injected into the open magnetic field lines areas), U-bursts (electrons are injected into closed magnetic field lines areas), or combined Type III and Type U-bursts (electrons are injected into an area covering both open magnetic field lines and magnetic loops). A similar idea can be applied to explain the split U-burst generation (Fig. 5.45 upper panel) with the specific note that in this case the injection area covers open and several closed magnetic lines. Another interesting case took place on July 14, 2004 at 7:53:20 UT. This composite burst resembled several nested U-bursts (Fig. 5.45 lower panel). At 20 MHz the frequency drift rate of an inward loop equals -0.6 MHz/s (point 1) and + 1.5 MHz/s (point 2). The ascending and descending branches of the burst were characterized by high absolute frequency drift rates, up to 6 MHz/s. Dorovskyy et al. (2010a,b) demonstrated that loops with heights up to 1.5 R_S correspond to decameter U-bursts with a turning frequency of 14 MHz if the radio emission of these bursts was a fundamental one.

5.12 Observations of the solar U-bursts harmonic pair with new radio telescope GURT

Recent observations of solar U-burst harmonic pair in the frequency range 10-70 MHz have been performed by the radio telescope UTR-2

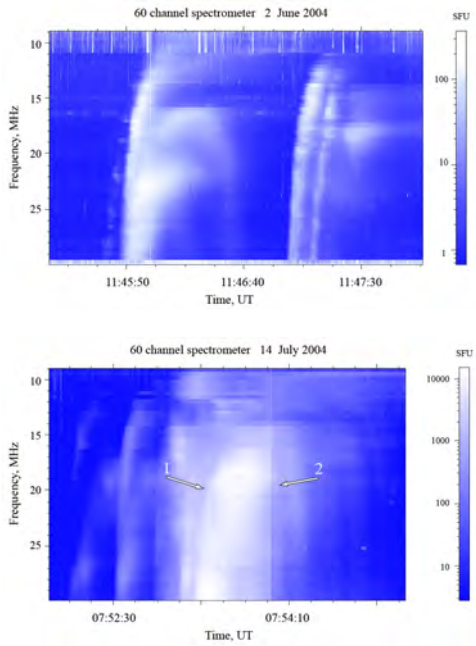


Figure 5.45: *Complex events: splitting group of U-, J-bursts (upper panel) and nested U-bursts (lower panel).*

and by the recently built first section of the new Giant Ukrainian Radio Telescope (GURT). The extended frequency range of the new telescope provides a higher probability in the detection of harmonically connected pairs. Particular focus is laid on the interpretation of the time delay between the harmonic (H) and fundamental (F) components of the burst, which appeared to be as large as 7 s. It is rather difficult to estimate the F-to-H mutual delay using Type III harmonic pairs since they have smooth spectra lacking any specific "reference markers". U-bursts do have such reference markers - the U-bursts turnover points. The explanation of the delay is based on the difference of group velocities of H and F waves during their travel inside high, hot and dense coronal loops.

The discussed U-bursts harmonic pair was observed on August 8, 2012, by one section of the new Giant Ukrainian Radio Telescope (GURT), currently being built near the existing radio telescope UTR-2 (Kharkiv, Ukraine). (Dorovskyy et al., 2013). The section is a square active antenna array consisting of 5 rows and 5 columns oriented along the East-West and North-South directions, respectively, or 5×5 cross-dipoles (Fig. 5.46). The individual dipoles are spaced by 3.75 m from each other along both rows and columns. All dipoles are mounted at 1.6 m above the ground and oriented at 45° to the meridian. Main parameters of this section are presented in Table (5.7).



Figure 5.46: *General view of the GURT section.*

Table 5.7: *Technical characteristics of the GURT section.*

Frequency band, MHz	10 - 70
Dimensions of one section, m	18.75×18.75
Beam width at frequency of 40 MHz, deg	20×20
Beam steering angle, deg	± 70
Elevation of the Galactic background temperature above the antenna amplifier temperature, dB	> 9
Dynamic range, dB	> 90

The dynamic spectrum of the discussed U-bursts pair is shown in Fig. 5.47.

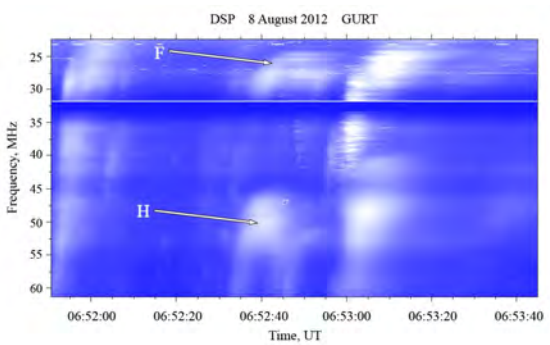


Figure 5.47: *The dynamic spectrum of the fundamental (F) and the harmonic (H) components of the U-burst recorded on August 8, 2012.*

The parameters of the recorded U-burst harmonic pair (August 8, 2012) are shown in the Table (5.8).

Table 5.8: *Parameters of the U-burst components of August 8, 2012.*

	Fundamental	Harmonic
Half-flux duration[1], s	7 ± 0.2	5 ± 0.2
Frequency drift rate[1], MHz s^{-1}	-2.2 ± 0.3	-4.2 ± 0.5
Turnover frequency[2], MHz	25.5 ± 0.1	51.2 ± 0.3
Turnover time[2], UT	$06^h52^m45.2 \pm 0.2^s$	$06^h52^m38.3 \pm 0.5^s$

[1] measured at frequencies 30 and 60 MHz for F and H components, respectively
[2] measured using differential (in time) dynamic spectra not shown in the text

These two solar U-bursts were harmonically connected because:

- the ratio of the turning frequencies of the bursts was close to 2;
- the ratio between the drift rates of the corresponding parts of the ascending arms of the burst harmonic components were also close to 2 by analogy with normal Type III harmonic pairs;
- the two bursts were morphologically similar, with a well-defined time of the frequency turnover (Dorovskyy et al., 2015b).

The most interesting fact which needs additional explanation is the time delay of the fundamental emission of 6.9 s.

In our opinion, the observed delay between the turning points of the fundamental and harmonic components of the U-burst was determined by the difference in their group velocities while they travel inside a magnetic loop containing plasma of increased density and temperature. The loop which may be associated with the burst was observed by the STEREO/COR2-A coronagraph (see Fig. 5.48).

Analyzing the daily Sun charts and sunspots and their magnetic fields for that date and also using the magnetic field extrapolation technique available at the SDO website, we can reasonably suppose

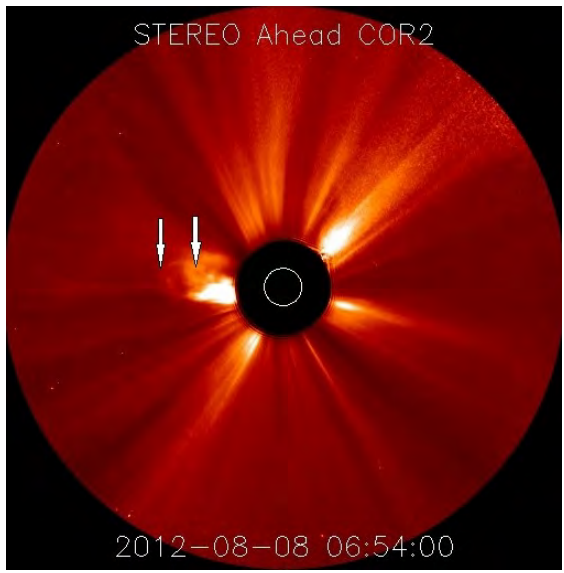


Figure 5.48: *Loop structures (marked with arrows) in COR2-A image.*

the existence of magnetic field lines connecting the active region NOAA11537 with NOAA11538 or NOAA11540 forming corresponding coronal loops. Furthermore, it is known that coronal loops with heights of several solar radii are closely connected with solar transient events, such as CMEs. We assume that the observed high coronal loops could arise due to a CME which appeared in the LASCO-C2 field of view at about 5:48 UT according to the SOHO-LASCO CME catalog. To fit the observed U-bursts turnover frequencies and the apparent loop height, we suppose that the loop should hold plasma of increased density with regard to the ambient corona. Dense plasma inside the loop means that the time delay is formed while both F and H waves travel from the source to the loop boundary along the line of sight because outside the loop, the group velocities of both waves are all close to the speed of light.

We suppose that plasma confined by the magnetic field inside the loop follows the barometric density distribution (also known as Boltzmann equation for density) (see, e.g., Mann et al., 1999). Also constant plasma temperature all over the loop is assumed.

In general, time needed for the electromagnetic wave to travel from the source to the loop boundary can be calculated as

$$t = \int_{R}^{R_1} \frac{dr}{v_{gr}(R, r)}, \tag{5.21}$$

where R is the height of the source in the corona (or the height of the loop for turnover frequency), R_1 is the height of the loop boundary, r is the current distance of the EM wave from the source and v_{gr} is the group velocity of the EM wave. Finding the group velocities of the fundamental and harmonic waves from their dispersion equations and solving the integral we get

$$\left(\frac{R}{R_S}\right)^2 \frac{v_{Te}}{c}\frac{v_0}{c} = 0.082 \text{ if } v_0 < 4.6 v_{Te} \tag{5.22}$$

$$\left(\frac{R}{R_S}\right) \frac{v_{Te}}{c} = 0.094 \text{ if } v_0 > 4.6 v_{Te}, \tag{5.23}$$

where R_S is the solar radius, v_{Te} the electron thermal velocity, v_0 the suprathermal electrons velocity, and c is the speed of light.

Under the assumption that the observed U-burst originates from high coronal loops ($R = 4R_S - 6R_S$), using Eqs. (5.22) and (5.23), we can formulate the restrictions on the plasma temperature shown in Table (5.9):

Table 5.9: *Inside the loop plasma temperature restrictions*

Conditions	$v_0 < 4.6v_{Te}$		$v_0 > 4.6v_{Te}$	
	$R = 4\,R_S$	$R = 6\,R_S$	$R = 4\,R_S$	$R = 6\,R_S$
T, °K	$> 6.5 \cdot 10^6$	$> 2.9 \cdot 10^6$	$> 3.3 \cdot 10^6$	$> 1.45 \cdot 10^6$

From Eqs. (5.22) and (5.23) it is clearly seen that the higher loops contain colder plasma. Knowing one of these parameters, we can define the other if the time delay between the F and H components is known. From the STEREO/COR2-A the height of the associated loop roughly equals $4.5R_S$. Assuming $v_0 \approx 0.3c$, we can estimate the temperature inside this loop as $\sim 3.2 \cdot 10^6$ K. Under the obtained conditions, the plasma inside this loop should be about 20 times denser than the ambient coronal plasma (Dorovskyy et al., 2015b).

During the first observations performed by the new radio telescope GURT, a U-burst harmonic pair with abnormally large relative time shift was registered. It was shown that the delay of about 7 s cannot be achieved using existing models and standard corona parameters. In our opinion, the above delay arises due to the different group velocities of the pair components when they move across the magnetic loop towards the observer. The essential property of the proposed model is that the temperature and density of the plasma held by the coronal loop are much higher than those of the surrounding corona. As long as the frequency of the fundamental component at the generation point is close to the local plasma frequency, its group velocity is much less than that of the harmonic one. Thus while traveling across the loop, the fundamental component lags. Using the value of the time delay of the fundamental component in the U-burst harmonic pair, we can determine the plasma temperature of the corresponding loop plasma. For the given harmonic pair, the temperature inside the loop may reach several million degrees (Dorovskyy et al., 2015b).

6 Type II Bursts

6.1 Solar Type II bursts at frequencies 10 MHz - 30 MHz

It is known that solar Type II radio bursts are associated with shock waves propagating through the solar corona. Wild and McCready (1950) first reported observations of these bursts. Such shock waves can be generated by flares or/and coronal mass ejections (Nelson and Melrose, 1985; Klassen et al., 1998; Claßen and Aurass, 2002). When coronal shock waves propagate into interplanetary space, they may generate solar Type II bursts observed below 1 MHz (Lengyel-Frey and Stone, 1989). Consequently, solar Type II bursts are observed in a wide frequency range, from meter wavelengths up to kilometer and even more. With the launch of the spacecraft ISEE, Ulysses, and WIND, the experimental study of these bursts was enlarged in frequency from a few tens of kHz to some MHz. However, it should be noted that till the beginning of the year 2000 the solar Type II radio burst ground-based observations in the decameter band at frequencies from 10 MHz to 30 MHz have been practically not existing (however, see Leblanc et al., 1998). This situation was connected with the absence of corresponding radio telescopes and adequate back-end facilities. In spite of comparably large intensities of these radio phenomena ($>$1 s.f.u.$= 10^{-22}\mathrm{Wm}^{-2}\mathrm{Hz}^{-1}$) it is very important to use large radio telescopes, necessary for the increase of both signal-to-noise ratio (with the aim of their identification and analysis), and of signal-interference ratio (due to a lot of interference in the decameter range). Investigations of fine frequency-time features demand also large antenna arrays with high performance, and high dynamic range back-end instruments.

Until 2000 the radio astronomy observations at the world largest decameter radio telescope UTR-2 have been carried out only at a few

discrete frequencies, unable to distinguish the solar Type II bursts with confidence. However, by the beginning of 2000 the facilities at the radio telescope UTR-2 have been extended and improved. From that year 2000 the observations were conducted by means of the DSP (digital spectropolarimeter described in Kleewein (1997)) in the continuous frequency band of 12 MHz and by a 60-channel spectrometer from 10 to 30 MHz. This allows it to be possible to identify slow drift bursts and to obtain their fine frequency–time structure by means of a high spectral resolution with high sensitivity of the corresponding equipment. The first Type II burst observed by the radio telescope UTR-2 is shown in Fig. 6.1.

This event was observed on May 11, 2001 (Fig. 6.1a). We see that the burst drifts from 32 MHz to 23 MHz with the rate $df/dt \approx -0.07\,\mathrm{MHz\,s^{-1}}$. Its characteristic feature is an irregular cloudy structure with the maximum radio flux $S = 2 \cdot 10^{-21}\,\mathrm{W\,m^{-2}Hz^{-1}}$ at low frequencies (23 MHz), whereas at higher frequencies (32 MHz) its flux is $S = 4.7 \cdot 10^{-21}\,\mathrm{W\,m^{-2}Hz^{-1}}$. The DSP can distinguish the fine structure of the received burst (Fig. 6.1a). It consists of fast drift bursts (constituents) with duration $\tau \approx 1\,\mathrm{s}$ and flux $S = 2 \cdot 10^{-21}\,\mathrm{W\,m^{-2}Hz^{-1}}$. The values of their drift rates are close enough but not equal (from $df/dt \approx -0.8\,\mathrm{MHz/s}$ up to $df/dt \approx -2.5\,\mathrm{MHz/s}$). Moreover, there are some components (07:10:40–07:10:50 UT and 07:11:20 – 07:11:40 UT) with positive (from lower to higher frequencies) drift $df/dt \approx 2 - 3\,\mathrm{MHz\,s^{-1}}$. The full duration of constituents defines the frequency band of the Type II burst. It equals $\Delta f \approx 1 - 3\,\mathrm{MHz}$. We can discern also a band splitting at frequencies 24 MHz (7:11:40 UT) and 27 MHz (7:10:50 UT).

On July 6, 2002, a solar Type II burst (Fig. 6.2) was registered at 9:48:00 UT and represented four cloudy bright lanes. They follow one after another at intervals 2 min – 3 min at a fixed frequency (or $\Delta f \approx 5\,\mathrm{MHz}$ in frequency domain at a fixed instant of time). It can be assumed that the first two lanes correspond to band splitting of the fundamental emission, and the two others are band splitting of the harmonic emission. The frequency drift of each lane is $df/dt \approx -0.03\,\mathrm{MHz\,s^{-1}}$. Their frequency bandwidth is about $\Delta f \approx 2{-}3\,\mathrm{MHz}$. In fact, the enhanced brightness regions have a fine structure in the form of fast drifting Type III-like bursts (with a drift rate df/dt from ≈ -0.6 up to -1.5 $\mathrm{MHz\,s^{-1}}$) specifically distinguishable on the DSP

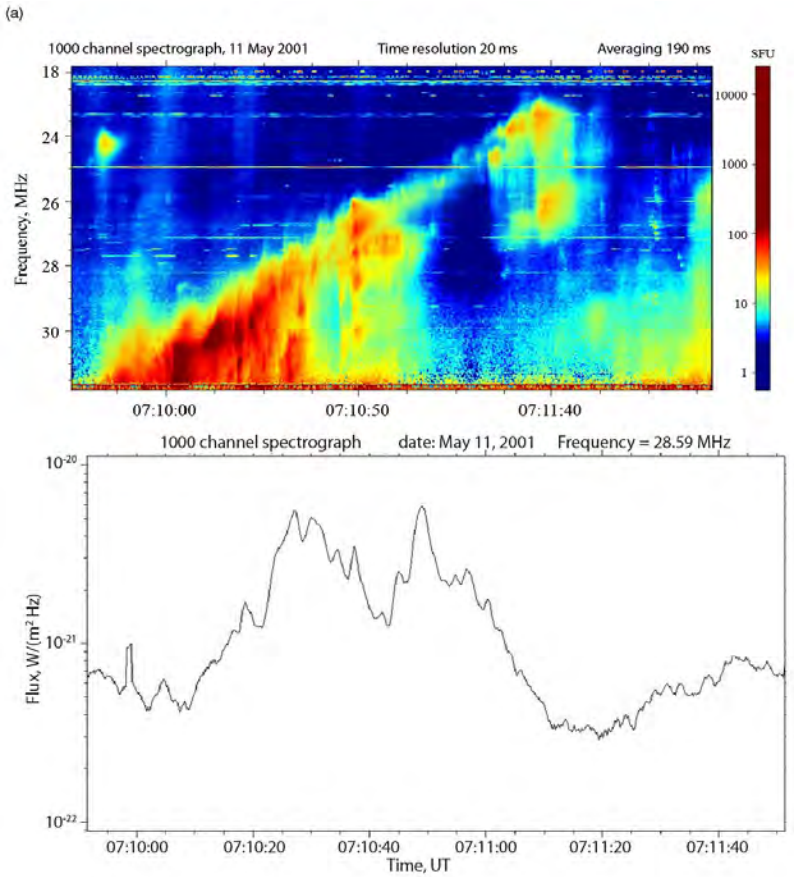


Figure 6.1: *(a) Type II burst as observed by the radio telescope UTR-2 (Kharkiv, Ukraine) with DSP (digital spectropolarimeter). Fine structures in the form of Type III-like bursts with positive and negative drifts are seen. (b) The time profile of the Type II burst at frequency 28.59 MHz. The radio emission flux increase at 7:10:30 UT and 7:10:50 UT corresponds to two lanes of the burst.*

spectra (Fig. 6.1b). As in the case of the Type II burst (May 11, 2001), the lifetime of these sub-bursts defines the frequency band of bright lane components. The sub-burst flux is $S = 10^{-19}\mathrm{W\,m^{-2}\,Hz^{-1}}$ and is comparable with the Type III burst flux (Fig. 6.2, at 9:52:00 UT) at the corresponding frequencies.

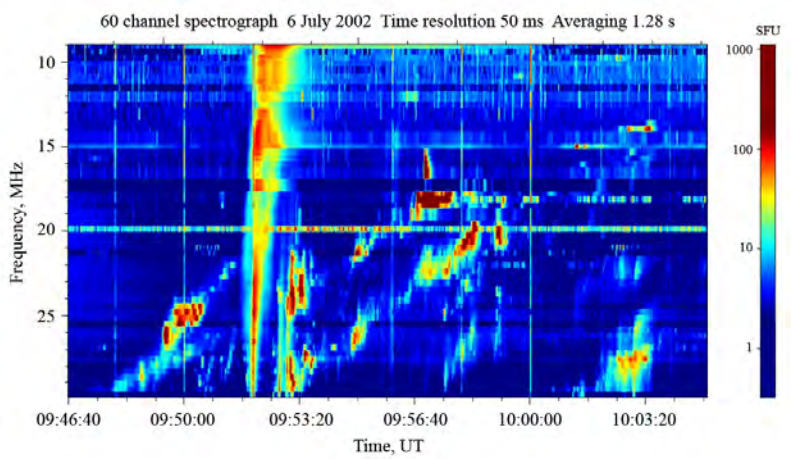


Figure 6.2: *Type II burst with band splitting of fundamental and harmonic emission observed by the 60-channel spectrometer. At 09:52:00 UT a Type III burst is visible.*

The herringbone structure is a distinct property of solar Type II bursts (Dulk and McLean, 1978). On July 7, 2002, (Fig. 6.3) we observed such a Type II burst. It began at about 11:43:20 UT and its track can be seen until 12:03:00 UT. The Type II burst has a waving backbone with an average drift rate equal approximately to zero. The herringbone structure sub-bursts (lifetime $\tau \approx 5\,s - 6\,\mathrm{s}$) drift with the rate $df/dt \approx 1.5\,\mathrm{MHz/s}$ towards higher frequencies and with the rate $df/dt \approx -0.5\,\mathrm{MHz/s}$ to lower frequencies. The maximum flux of the sub-bursts yields $S \approx 3.7 \cdot 10^{-19}\,\mathrm{W\,m^{-2}Hz^{-1}}$ at 11:49:20 UT. These sub-bursts cover a frequency band of about 10 MHz. Very likely, we observe the fundamental emission near 10 MHz with the radio emission maxima at 11:44:10 – 11:45:50 UT, 11:46:40 – 11:50:00 UT and 11:51:40 – 11:55:50 UT.

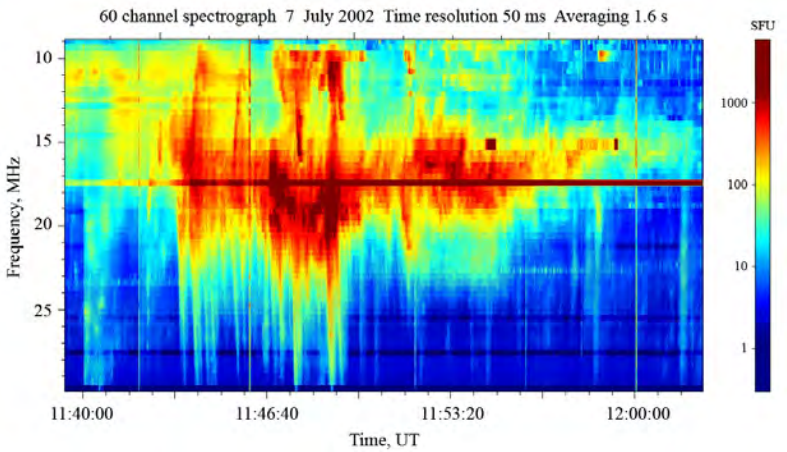


Figure 6.3: *Type II burst with herringbone structure and waving backbone. Fundamental radio emission of this Type II burst is probably visible close to 10 MHz.*

Decameter Type II bursts as well as the Type II bursts observed in other frequency bands, like meter and kilometer, have frequency drift rates up to hundred times less than those for Type III bursts. Their simultaneous frequency band is sufficiently narrow, 2 MHz – 10 MHz. The irregular radio emission of such a burst looks like a cloudy structure on a frequency versus time representation. Decameter Type II bursts also consist of drifting bands with typical frequency splitting $\Delta f/f \approx 0.1$ (Mann, 1995). Both fundamental and harmonic components of Type II bursts are obviously observed in the decameter range. The radio emission flux of the bursts varies between $10 - 10^3$ s.f.u.

Due to the density inhomogeneity of the solar corona the radio radiation which is assumed to be plasma emission, is originating from the outer corona in the frequency range 10 MHz – 30 MHz. Mann et al. (1999) described a density model of the corona and interplanetary space. It is based on a special solution of the Parker (1958) solar wind equation and agrees very well with observations from the low corona up to 5 AU. In the outer corona, where the solar wind is very slow, the radial behavior of the electron number density n_e can

be expressed by

$$n_e(r) = n_s \exp[\frac{A}{R_S}(\frac{R_S}{r} - 1)], \tag{6.1}$$

with $A = \tilde{\mu} G M_S m_p / k_B T$ ($\tilde{\mu}$ = mean molecular weight; G = gravitational constant; M_S = mass of the Sun; m_p = proton mass; k_B = Boltzmann constant; T = temperature; R_S = solar radius and $n_S = 5.14 \cdot 10^9\,\mathrm{cm}^{-3}$). $A/R_S = 13.83$ is found for the temperature of 10^6 K, which is typical in the outer corona. Then the plasma levels of 30, 20, 10 MHz correspond to radial distances of 1.78, 2.08, 2.94 R_S measured from the center of the Sun, respectively. A magnetic field of 0.5 G is usually expected in the corona at a distance of 2 R_S (Mann, 1995), leading to a typical Alfvén speed of 450 km s^{-1} at this distance. Here, the Alfvén speed is defined by $\nu_A = B/(\mu_0 n m_p)^{1/2}$, where the full particle number density n is related to the electron number density by $n = 1.92\, n_e$ (B = magnetic field induction). As already mentioned, the radio radiation is generally assumed to be emitted near the local electron plasma frequency $f_{pe} = 1/(2\pi)(e^2 n_e/m_e \epsilon_0)^{1/2}$ (e = elementary charge; m_e = electron mass; ϵ_0 = dielectric constant). Then, the drift rate df/dt of a signature in a dynamic radio spectrum is related to the velocity of the corresponding radio source ν_s by

$$\frac{df}{dt} = \frac{f}{2}\frac{1}{n}\frac{dn_e}{dr}\nu_s \cos\theta, \tag{6.2}$$

where θ is the deviation angle from the radial direction. Adopting the density model (Equation (6.1)) in Equation (6.2), the radial shock speeds ($\cos\theta = 1$) of 880 km s^{-1} and 580 km s^{-1} have been deduced from the drift rates of the events on May 11, 2001, and July 7, 2002, respectively. These speeds are higher than the CME velocities, 580 km s^{-1} and 280 km s^{-1} (see SOHO/LASCO CME Catalogue). This can be understood if the harmonic components of Type II bursts were observed in both cases. The July 7, 2002, Type II burst with herringbone structure was accompanied by a fast CME. The latter had a velocity of 1340 km s^{-1} according to the SOHO/LASCO CME Catalogue.

As is well known (McLean et al., 1985), in the radial direction (along the plasma's gradient) the shock velocity is higher than in other directions.

The fine-structure features of decameter Type II bursts

All the observed Type II bursts consist of short bursts with fast frequency drift (some MHz s^{-1}) close to the frequency drift of Type III bursts in the decameter range. Linear velocities of the latter range from 0.1 c – 0.3 c. Taking into account that the duration of Type III-like bursts equals $\Delta t \approx 1$ s, the longitudinal size of electron beams associated with these bursts is $\Delta l \approx (3-10) \cdot 10^9$ cm. It is important to emphasize that such fine structures are present not only in the bursts with herringbone structure, but also in the ordinary Type II bursts. They imply that electrons are accelerated on the shocks by separate beams (evidently with different velocities depending on the frequency drift rate of the sub-bursts) rather than as a whole. Moreover, since the frequency drift rate of the sub-bursts can be both positive and negative, this means that electron beams are moving in different directions off the bow shock, which is propagating away from the Sun. The presence of two lanes is usually connected with regions on each side of the shock front (Dulk and McLean, 1978). In our case the density jump calculated from the lane frequency splitting should be equal to $\Delta n \approx (1-2) \cdot 10^6$ cm^{-3}.

From the above-mentioned observations it follows that sub-bursts have smooth tracks (Fig. 6.1). This means that the beams propagate through plasma with almost uniform density (without any jump). These emission regions are located very probably on one side of the shock wave rather than on different sides (for example, inside a single so-called SLAMS: Short Large Amplitude Magnetic Field Structure, see Claßen and Mann (1998)). In this interpretation the reason (or cause), as to why electrons emit in two different plasma regions, remains unclear. Another significant question arises as to why electron beams disappear to pass these regions. One of the several possible explanations of the fact lies in the radio emission conditions of these beams. If the radiation mechanism is believed to occur via plasma waves, we can suppose that the level of plasma waves (Langmuir and ion-sound waves) will expand in these regions. They increase the effectiveness of transformation processes of Langmuir waves, generated by electron beams, into transversal waves. The spatial size of regions where electron beams radiate, for the coronal model such as of Mann et al. (1999), is equal to $\approx 0.1\, R_S$.

With regard to the burst with the herringbone structure (July 7, 2002), it propagates almost perpendicular to the density gradient. Consequently, the corresponding shock wave is perpendicular. From the backbone width the shock wave spatial width is derived as $\approx 10^9 - 10^{10}$ cm. If we suggest that electrons are accelerated to the same velocities in both directions towards the Sun and away from the Sun, and the non-uniformity of the coronal plasma density is equal on both front sides ($(dn/dr)_{upstream} \approx (dn/dr)_{downstream}$), then one of the possible explanations of the differences of drift rates towards higher and lower frequencies observed in the July 7, 2002, event can be connected with an electron motion under different angles to the density gradient in front and behind the shock front which moves with the velocity $\vec{V}_{shock}$. One can suppose that before the front (Fig. 6.4) electrons move along a density gradient that coincides with the antiparallel direction of magnetic field lines $\vec{B}_1$. Owing to the change of the direction of magnetic field $\vec{B}_2$ behind the shock front (Akhiezer et al., 1974; Zaitsev et al., 1998) electrons do not move along the density gradient but rather along the magnetic field lines $\vec{B}_2$, so the drift rates must be smaller, see Equation (6.2). If this scenario is correct then this provides a way to find a change of magnetic field lines on the shock front proceeding radio emission.

Type II bow-shock intersection of the coronal structure

Since the Type II burst (July 7, 2002) has an almost zero drift rate, most likely it is generated by the shock moving perpendicular to the coronal density gradient (angle between $\vec{V}_{shock}$ and $\vec{B}_1$ is almost 90°). The backbone waving in frequency can be interpreted as an intersection of the coronal structure by the shock. The frequency maxima of the backbone structure correspond to the shock passage through coronal streamers. When we observe frequency minima, the shock moves outside streamers. Assuming that the radio emission is harmonic, the transverse size between streamers is equal to $0.3R_S$. Then the streamer width is about $0.1R_S$, and the difference between the streamer density and the density beyond the bounds of the streamer is $\approx 6.3 \cdot 10^5\,\mathrm{cm}^{-3}$.

Observations of solar decameter Type II bursts, now for the first time recorded by the UTR-2 radio telescope, indicate that these

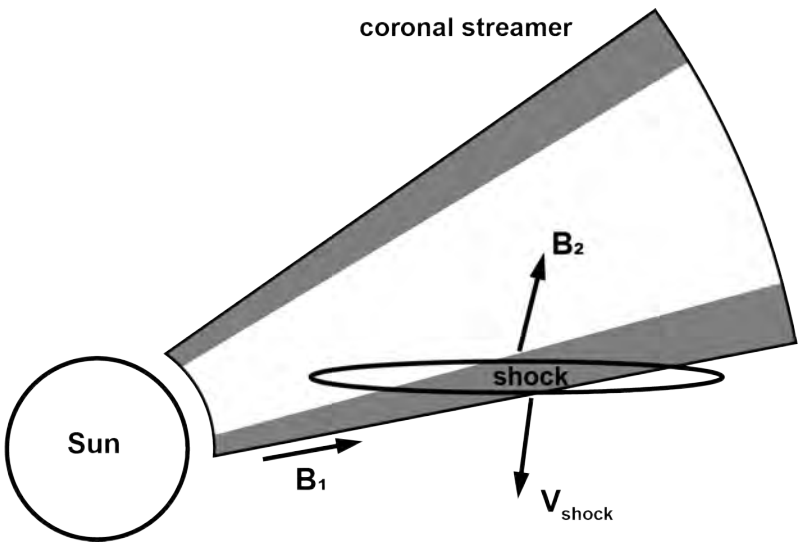


Figure 6.4: *Schematic sketch of shock movement through the solar corona with streamers.*

bursts show the following properties: slow frequency drift (0.1 MHz/s at decameter wavelengths), narrow simultaneous frequency band of radio emission (2 MHz – 3 MHz), band-splitting (3 MHz – 5 MHz at decameter range), cloudy structure, herringbone structure, fundamental and harmonic radio emission, high intensity of radio emission (from 10 to 10^3 s.f.u.).

The interesting and important feature of the decameter Type II bursts is that they have a fine structure in the form of Type III-like bursts. The drift rates of these sub-bursts are close to the ordinary Type III bursts velocity, but their duration is essentially shorter. According to previous results (Abranin et al., 1990), the duration of decameter Type III bursts is about 4 s – 10 s, whereas the duration of sub-bursts is ≈ 1 s. Furthermore, the ordinary Type III bursts propagate over large distances, and sub-bursts cover only 10^{10} cm. According to Suzuki and Dulk (1985), the duration of Type III bursts decreases inversely with frequency. The meter-wave observations show that the duration of Type III-like bursts is 0.2 s – 0.4 s (Slottje, 1982; Zlobec and Thejappa, 1987; Zlobec et al., 1993).

These results reveal that the duration trend (inversely proportional to the frequency) found for Type III bursts is valid mainly for Type III-like bursts, too. From the constant slope of sub-burst tracks (which intersect and form two lanes of increasing radio emission) it follows that these regions seem not to be separated by the shock front with a sharp density drop. The availability of sub-bursts with simultaneous positive and negative frequency drifts reveals that electrons are accelerated on the shock in both directions – to the Sun and away of the Sun. In our opinion some increased level of the Langmuir and ion-sound turbulence probably characterizes the band splitting regions. The Type II burst with the herringbone structure is associated with perpendicular shock waves that intersect streamers with a transverse size of 0.1 R_S and an internal density of $6.3 \cdot 10^5\,\mathrm{cm}^{-3}$.

6.1.1 Study of the decameter Type II bursts with rich fine and superfine structures

Coronal Mass Ejections (CMEs) are class of events that play a key role in space weather physics. One of the CME signatures in the radio band are Type II bursts. It is currently accepted that Type II bursts

are generated by sub-relativistic electrons accelerated at the front of the shocks driven by CMEs (Mann and Klassen, 2005) in processes known as plasma emission mechanism. Type II bursts are observed in wide wavelength ranges from decimeter (dm) through meter (m) and decameter-hectometer (DH) up to kilometer (km) wavelengths. The study of Type II bursts in the DH band is of increased interest since these bursts are connected with shocks driven by CMEs of extremely high kinetic energy, thus being potentially the most geoeffective events (Gopalswamy et al., 2005).

Observations

A Type II burst with extremely rich fine and superfine structure was observed on June 7, 2011, by two ground-based Ukrainian radio telescopes UTR-2 and URAN-2 in the frequency band 9 MHz - 32 MHz (Dorovskyy et al., 2015a). In addition, it was also recorded by spaceborne radio telescopes (STEREO mission) in the frequency band from 3 to 16 MHz. The Type II burst itself was part of a more complex and large-scale event which apparently was initiated by the solar flare (GOES X-ray class M2) which occurred at 06:20 UT near the NOAA11226 active region (22°S 52°W).

The dynamic spectrum of the whole complex event observed by URAN-2 and UTR-2 radio telescopes on June 7, 2011, is illustrated in Fig. 6.5a. The event started at 06:29 UT with a sudden increase of the radio emission continuum by almost five orders of flux magnitude in the whole frequency range covered by the radio telescopes. The continuum jump is marked with 's'. About 1.5 min later a group of powerful Type III bursts was recorded. Finally, the Type II burst with peak fluxes reaching 10^6 s.f.u. started at 06:34:00 UT and lasted for about half an hour.

For the present Type II burst the average drift rate is about -25 kHz/s within the frequency bounds of 16 MHz – 25 MHz which corresponds to the radial component of the shock front velocity near 600 km/s. Hereinafter all radial velocities are given on basis of the Newkirk's corona model. At the same time the instant absolute drift rates of separate parts of the backbone sometimes exceed 100 kHz/s. Three full oscillations of the backbone between 6:41 UT and 6:57 UT can be seen, whose periods are 530 s, 230 s, and 150 s, respectively.

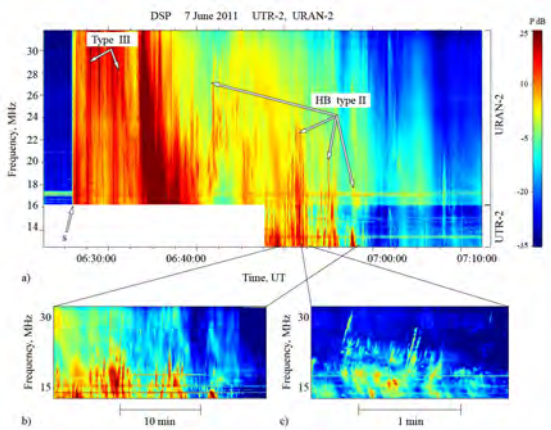


Figure 6.5: *Dynamic spectra of the whole event (a), the wavelike backbone (b), and separate HB (herringbone) sub-bursts (c).*

The magnitude of these oscillations along the frequency axis was on average 10 MHz (Dorovskyy et al., 2015a).

The continuation of the burst to frequencies below 12 MHz was recorded by the spaceborne STEREO/Waves radio receivers. The total frequency drift rates along the low-frequency part of the dynamic spectrum (Fig. 6.6) were -8 kHz/s at 6 MHz and -3 kHz/s at 3 MHz. These drift rates correspond to the radial velocities of 550 km/s and 400 km/s, respectively.

Discussion of the observations

High frequency and time resolutions of the ground-based backend instruments allowed for a detailed statistical analysis of the main parameters of the herringbone (HB) structure sub-bursts to be conducted. During the life-time of a Type II burst about 300 separate sub-bursts were identified, 200 of which with negative frequency drift rates (forward sub-bursts) and the remainder with positive drift rates (reverse sub-bursts). The basic parameters of the sub-bursts, such as the frequency drift rate and the duration, appeared to be distributed in a relatively narrow range. The distribution of these sub-bursts by

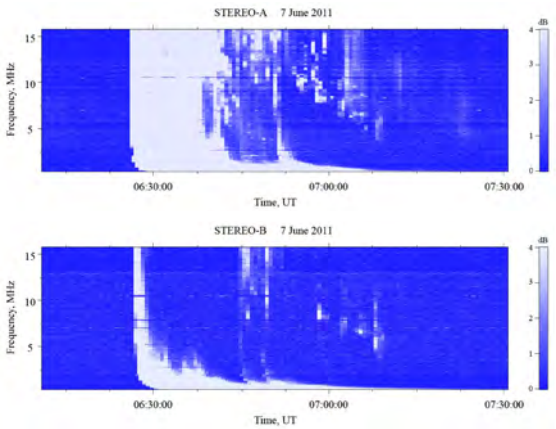


Figure 6.6: *Type II burst from STEREO-A (top panel) and STEREO-B spacecraft (bottom panel).*

the absolute value of the drift rate is shown in Fig. 6.7a. The corresponding distribution of reverse sub-bursts is shown in Fig. 6.7b.

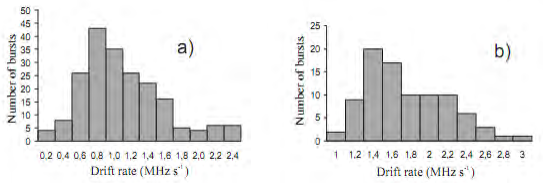


Figure 6.7: *Distributions of the frequency drift rates of the forward (a) and reverse (b) HB sub-bursts.*

The HB structure was observed over a wide frequency range. Therefore, it is of interest to study the frequency dependence of the absolute drift rates of the sub-bursts. These dependencies were approximated by a power law equation separately for forward (Equation (6.3)) and

reverse (Equation (6.4)) HB sub-bursts.

$$\frac{df_f}{dt} = 0.01 \cdot f^{1.73} \tag{6.3}$$

$$\frac{df_r}{dt} = 0.088 \cdot f, \tag{6.4}$$

where $\dot{f}_f$ and $\dot{f}_r$ are the absolute values of the drift rates (in MHz/s) of forward and reverse HB bursts, respectively, and f is the frequency in MHz.

The dependence for the forward HB sub-bursts is very close to that derived for Type III bursts by Alvarez and Haddock (1973) while the reverse sub-bursts reveal linear dependence.

The distribution of the HB sub-bursts by their instant durations is shown in Fig. 6.8. Roughly speaking these distributions are similar. The only difference is the average duration of the forward (2.3 s) and reverse (1.9 s) sub-bursts. Both values are substantially smaller than typical durations of Type III bursts (Dorovskyy et al., 2015a).

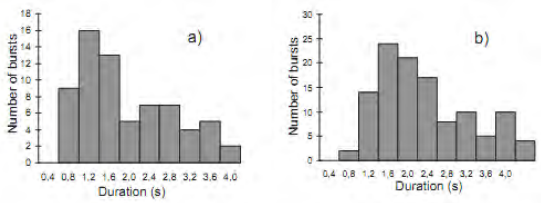


Figure 6.8: *Distributions of the instant durations of the forward HB sub-bursts (a) and the reverse HB sub-bursts (b).*

The average degree of circular polarization of both types of sub-bursts was 50 %, in some cases reaching as high as 80 %. Importantly, the direction of circular polarization of forward and reverse sub-bursts appeared to be the same, with left-handed circular polarization observed in all cases. The polarization of the preceding powerful Type III bursts was much lower (20 % – 30 %) and in the opposite sense.

High frequency resolution of the experiment enabled the definition of a "second order fine structure" of the HB sub-bursts. This fine structure (Fig. 6.9) has the appearance of a quasi-periodic (in

the frequency domain) chain of narrow-band sub-bursts. The bandwidths of these sub-bursts were 30–60 kHz and the frequency spacing between neighboring sub-bursts was 60 kHz – 120 kHz. As a rule the narrow-band sub-bursts showed no clear drift rate while in rare cases slight positive drift rates of 100 kHz were observed (Fig. 6.9d).

Data obtained from Solar Dynamics Observatory (SDO) onboard SOlar Heliospheric Observatory (SOHO) show that the discussed complex solar burst was the result of the M2 solar flare, near the active region NOAA11226 which was located in the South-West part of the solar disk (22° S, 52° W). This flare was accompanied by a Coronal Mass Ejection (CME) registered by SOHO/LASCO-C2 coronagraph and Solar TErrestrial Relations Observatory (STEREO) coronagraphs. Using data of COR1 coronagraphs onboard the STEREO Ahead (A) and Behind (B) spacecraft it is comprehensable that the CME driven shock reached the heliocentric height of 1.7 R_S (R_S solar radius) with a local plasma frequency of 30 MHz at about 06:30 UT.

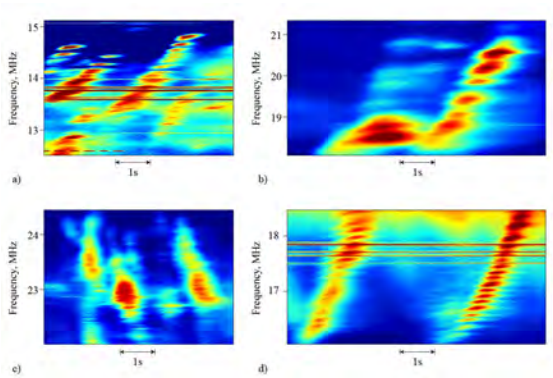


Figure 6.9: *Frequency fine structures of the HB sub-bursts.*

This time (06:30 UT) corresponds to the onset of the Type II bursts at 30 MHz. It was possible to retrieve the true absolute velocity and direction of CME propagation from sky plane images of the CME obtained from three different coronagraphs located along the Earth's orbit at about 90° angular separation. The sky-plane component of the CME velocity obtained from the STEREO-A spacecraft was

found as 1200 km/s and that from the SOHO spacecraft 1550 km/s. Solving simple trigonometric equations the absolute CME velocity of 1950 km/s was obtained and the direction of about 52° Westward from the observer's line-of-sight was determined. Apparently the obtained angle coincides with the longitudinal position of the active region NOAA11226 and proves the previously supposed association between the CME and the active region (Dorovskyy et al., 2015a).

As can be seen from the data analysis, the linear velocity of the shock obtained from coronagraphic observations is at least three times higher than the radial velocity of the radio source derived from the frequency drift rate of the burst (1950 km/s versus 650 km/s). In our opinion, if the source of the Type II bursts was located at the flank of the shock rather than at the forehead, this discrepancy could occur. Indeed, the drift rate of the bursts is determined by the radial component of the total linear velocity of the source, as given in Equation (6.2). Taking into account the above derived direction of the CME propagation it is possible to conclude that the Type II burst may originate from the Eastern flank of the shock, which moves non-radially ($\approx 50°$ to the density gradient) towards the Earth.

The wavelike oscillation of the HB Type II backbone can occur when CME flanks intersect dense coronal streamers. In the case discussed, it is assumed that the source moves at an angle of about 50° to the CME forehead direction and intersects at least three inhomogeneous regions, most likely streamers. The magnitude of the backbone oscillations in this case is determined by the ratio between the plasma density inside the streamer and the surrounding coronal plasma density. Thus 10 MHz oscillation magnitude corresponds to the density deviation of $5 \cdot 10^6$ cm^{-3}. Judging from the periods of the oscillations the linear distance between neighboring streamers are $0.5R_S$, $0.2R_S$, and $0.15R_S$. Since these distances are determined at the heliocentric heights of about $2R_S$ the corresponding angular separations between the streamers are $\approx 10°$, 15°, and 25°. Then the transverse dimensions of the streamers at these heights vary from $0.1R_S$ to $0.2R_S$ (Dorovskyy et al., 2015a).

The frequency range over which a separate HB burst extends is rather narrow, compared with Type III bursts. For the observed burst this frequency range varied from 2 to 10 MHz. Taking into account the source velocity derived from the HB bursts drift rates,

the linear dimensions of the area where the emission originates, is between $3 \cdot 10^9$ cm and $2 \cdot 10^{10}$ cm (or $0.05R_S$ and $0.3R_S$). It is commonly assumed that the linear velocities of the electrons generating the forward and the reverse HB bursts are approximately equal. The difference between the mean values of the absolute drift rates of these two populations are more likely caused by different conditions behind and in front of the source position. This fact may also play a role in the difference of the drift rates (Equations (6.3) and (6.4)).

6.2 Type II burst with herringbone structures

Solar Type II radio bursts are manifestations of the Coronal Mass Ejection (CME) movement through the solar corona and interplanetary space, and they originate from the shock formed ahead of a CME. The CMEs, in turn, are the most effective drivers of the space weather changes. Though Type II bursts are observed in a wide frequency range, the bursts detected at meter and decameter-hectometer wavelengths are believed to be connected with the potentially most geoeffective CMEs (Gopalswamy et al., 2005). The geoeffectiveness of the CME is mainly defined by its mass, velocity and direction. The velocity of the CME can be detected in three ways: by coronagraph observations in visible light, by the frequency drift rate of Type II bursts and by the speed of the Type II source displacement. The first method provides correct results for CMEs which propagate close to the sky plane, but this is not applicable for Earth-directed CMEs (when observing from Earth). This problem can be alleviated by means of multi-spacecraft observations such as those provided by the STEREO mission. In addition, multi-spacecraft observations also allow to define the direction of the CME movement. However, the accuracy of this method depends on mutual positions of the STEREO spacecraft with respect to Earth, and these positions are changing with time. The second method is indirect and is a model dependent one. In addition, it gives the radial component of the velocity vector and is inaccurate for CMEs which may move at a substantial angle to the density gradient. This method is especially effective in cases of Earth-directed CMEs. The third method deals with the spatial

displacement of the source of Type II bursts with time on the sky plane regardless of the chosen coronal density model, though it suffers from projection effects. It is also known that Type II bursts reveal a wide variety of morphological features, such as fundamental and harmonic emission, band splitting, a cloudy structure, a herringbone (HB) structure etc. (Nelson and Melrose, 1985; Mel'nik et al., 2004; Dorovskyy et al., 2015b). The interpretations of all these features are based on their spectral properties assuming some models of plasma distributions in the corona and the shock. For instance, the band splitting is attributed to the plasma emission from regions ahead (upstream) and behind (downstream) the shock (Vršnak et al., 2004), HB sub-bursts are manifestations of shock-accelerated electrons escaping from the shock towards and away from the Sun (Cairns, 1987). Measurements with a high time, frequency and spatial resolution may confirm or call these assumptions into question. Thus, the study of the spatial properties of the sources of Type II bursts may improve the quality and reliability of the space weather diagnostics and will lead to a better understanding of underlying physics as well.

Observations since 2011 of solar radio emission at the UTR-2 radio telescope are carried out in the interferometric mode, which provides the opportunity to estimate the sizes and locations of solar radio burst sources. The UTR-2 radio telescope consists of 12 separate sections, which can be configured in different ways. For the discussed observations, the sections were grouped into three separate antennas: North (N), West (W) and South (S) antenna with 4 sections in each, thus forming a local interferometer with two orthogonal baselines B1 and B2 each being 674 m long (see Fig. 2.2). These two baselines are inclined by 45° to the meridian.

Two spectropolarimeters DSP (Zakharenko et al., 2016) are used as a backend. These digital analyzers calculate complex correlation functions in an instantaneous frequency band of 10 MHz - 32 MHz for each of the two bases. The absolute value of the correlation function carries information about the size of the source via a visibility function, while the phase of the correlation function is determined by the source angular displacement.

On May 31, 2013, a complex and powerful Type II burst was observed by UTR-2, URAN-2 and NDA radio telescopes. The overall view of the burst is shown in Fig. 6.10. The whole event started

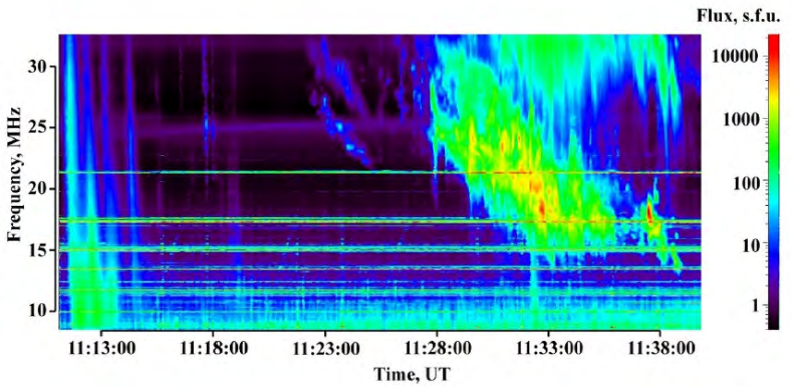


Figure 6.10: *Type II burst recorded on May 31, 2013, by the UTR-2 radio telescope.*

at 11:12 UT with a group of Type III bursts. In this particular case, these Type III bursts are the precursor of the following Type II bursts and coincide in time with a solar flare of class C1.1 above the active region NOAA11761 (S18E23). The Type II burst itself consists of two parts separated in time. The first part lasted from 11:22:30 UT till 11:25:30 UT and the second one from 11:28 UT till 11:39 UT. Both parts of the burst exhibit band splitting. The lanes were separated in frequency by 4.5 MHz and 6 MHz, respectively. The dynamic spectrum obtained by the NDA shows also the harmonic structure of the bursts (Fig. 6.11). The burst appeared to be bound both above at 65 MHz and below at 10 MHz, and displayed extremely intense maximum fluxes as high as 10000 s.f.u. at the frequency around 20 MHz. No sign of a Type II burst at lower frequencies was found by SWAVES receivers onboard the STEREO spacecraft. This Type II burst was apparently initiated by the CME recorded by the coronagraphs SOHO/LASCO-C2 at 12:12 UT (`https://cdaw.gsfc.nasa.gov/CME_list/`) and by STEREO-B/COR1 at 11:20 UT. For STEREO-A the CME was not visible.

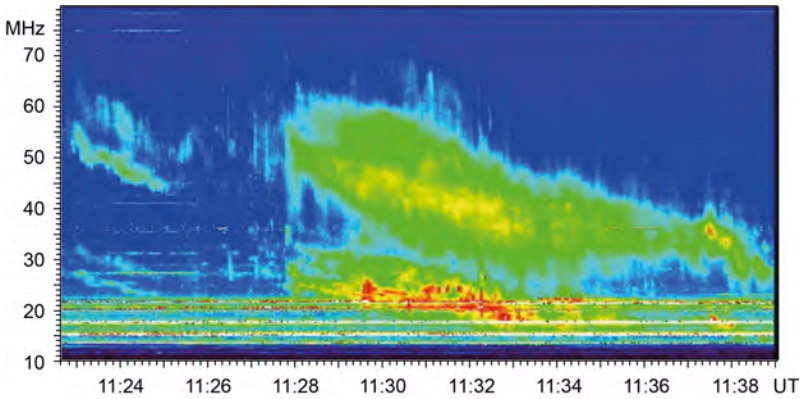


Figure 6.11: *Type II burst recorded on May 31, 2013, by the NDA radio telescope.*

6.2.1 Analysis and discussion

Determination of the direction and the speed of the CME propagation using optical data

The views of the CME from the different location of the spacecraft are shown in Fig. 6.12. The CME of interest is marked with white arrows. The bulk velocities of the CME measured from the SOHO and STEREO-B spacecraft were 280 km/s and 340 km/s, respectively. Taking into account the longitudinal positions of STEREO-A (138°) and STEREO-B (−141°) spacecraft, and the fact that this CME was not visible to the former, we may conclude that this CME propagated at an angle of $\sim 30°$ eastward to the line of sight from Earth with a velocity of about 340 km/s. In this case, the CME moved practically in the sky plane for the STEREO-B spacecraft and at $\sim 30°$ eastward to the line of sight from the SOHO spacecraft. For such a trajectory, STEREO-A could not observe the CME because it was completely behind the Sun.

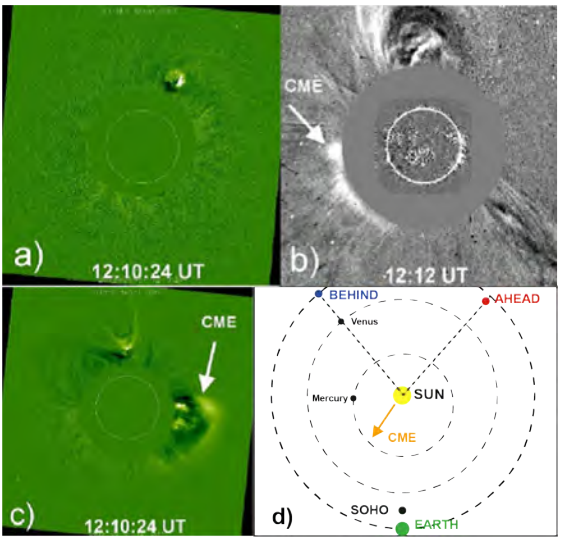


Figure 6.12: *Running difference images from STEREO-A (a), SOHO (b) and STEREO-B (c) spacecraft and the positions of the STEREO spacecraft on May 31, 2013 (d). The arrow in panels (b) and (c) points to the associated CME and in panel (d) marks the CME propagation direction.*

Determination of the CME speed via the frequency drift rate of the Type II bursts

It is well known that because of the plasma emission mechanism, the frequency drift rate of any burst depends on the corona density profile and the source velocity. For the current analysis, we apply the Newkirk (1961) corona density model. For the fundamental component of the discussed burst, the drift rate is not constant over the burst lifetime. In the beginning, the drift rate was about $-40\,\mathrm{kHz/s}$ corresponding to a radial velocity of about $800\,\mathrm{km/s}$. The tail of the Type II bursts had practically no drift. The radial velocity of the first part of the bursts is more than double to that of the CME speed according to coronagraph data. The possible reason of such a discrepancy is discussed in the following.

Using spatial properties of the Type II burst to retrieve CME parameters

The possibility to estimate the radio source sizes and positions using the UTR-2 radio telescope as an interferometer was shown by Shepelev (2015) and Melnik et al. (2017a). The size of the radio source in this case is determined by the visibility function Equation (4.3) (Thompson et al., 1986). Note that Equation (4.3) is only valid for sources with a Gaussian brightness distribution. In the case when the interferometer is composed of the elements of the same array (providing identical antenna parameters) the visibility function can be calculated as (Shepelev, 2015):

$$\gamma = \frac{P_c}{P_1 P_2}\,, \tag{6.5}$$

where P_c is the absolute value of the correlation function, and P_1 and P_2 are the respective powers received by the two antennas of the interferometer base. Using Eqs. (4.3) and (6.5) it is possible to get the source size along the direction of the baseline. The angular deflection of the source from the interferometer axis can be defined from the phase of the correlation function. Note that the phase analysis is quite sensitive to the accuracy of the antenna beam pointing as well as to the refraction effects in the ionosphere. Thus, the estimation of the source position with respect to the solar disc center is much less accurate than the estimation of the source displacements with respect to each other. For the current analysis, we assume the accuracy of the respective angular displacement measurement as about $1'$. The absolute angular position of the source with respect to the center of the Sun is not less than $8'$ (i.e. one axis tick in Figs. 6.13 - 6.16). Using the thermal radio emission of the quiet Sun as the reference point this can substantially increase the latter accuracy. Given that the angular size of the quiet radio Sun at frequencies around 20 MHz is roughly 1°, additional shorter baselines should be used, as planned in future. The spatial properties of the first part of the Type II burst, which manifests a well-distinguished band splitting, are shown in Fig. 6.13. An analysis has been performed on the spatial properties of the two lanes of the first Type II burst taken at the same moment in time. The source of the higher frequency lane is drawn in red, while the

lower frequency lane is marked with a blue color. The source sizes are almost equal ($14'$ and $16'$, respectively) and this leads to the effective brightness temperatures of these sources of $2 \cdot 10^{12}$ K and $4 \cdot 10^{11}$ K. The obtained sizes of the Type II bursts sources appear to be slightly smaller than the sizes of Type III bursts, measured by the same radio telescope with a similar method at the same frequencies (Melnik et al., 2017a). Former analysis of the spatial properties of the solar radio sources by the UTR-2 radio telescope were concentrated exclusively on the source size estimation (Shepelev, 2015; Melnik et al., 2017a).

These investigations are based on the amplitude of the cross-correlation function, which is less affected by the accuracy of the radio telescope pointing and the refraction effects. This most recent experiment was the first attempt to estimate the displacement of the source center using the phase of cross-correlation function at the UTR-2 radio telescope. From the analysis of the respective angular positions of the radio sources it is evident that the higher frequency lane is located closer to the Sun than the lower frequency lane. In addition, we must note that these two lanes have a different morphology as can easily be seen in Fig. 6.13 b. Obviously the higher frequency lane consists of "clouds" extended along the frequency axis (vertically), while the lower frequency lane is composed of exclusively horizontally stretched structures. These facts show that the sources of the two lanes are different; this is in favor of the upstream and downstream model of band splitting of Type IIs.

Now that we have mentioned the three methods for estimating CME displacements, it seems interesting to roughly compare the results obtained by each method. Let's take the Type II burst segment at 11:25 UT (Fig. 6.13) for such a comparison. At this time the heliocentric height of the nose of the CME according to the STEREO-B/COR1 image was $1.87\,R_S$. The frequencies of the upper and lower lanes of the Type II burst correspond to the heights of $1.76\,R_S$ and $1.88\,R_S$, respectively, assuming the Newkirk corona density model. And lastly, interferometric observations provide the projections of these heights to the sky plane equal to $1.6\,R_S$ and $1.7\,R_S$. It is evident that, considering the declared accuracy, the obtained values are of the same order of magnitude. The angular sizes of the sources appear to be much larger than their angular displacements thus making

accurate determination of linear velocity difficult. Using baselines of different lengths might improve the analysis in further experiments. In the same way we can investigate how the source of the lower-frequency lane moves in space with time. Apparently, the source moves away from the Sun (Fig. 6.14). The velocity obtained from this displacement is around 900 km/s. This velocity is very close to that obtained from the frequency drift rate and is much higher than the velocity provided by the coronagraphs. In our opinion, this discrepancy may possibly be connected with the migration of the radio source across the shock surface. Indeed, the obtained size of the radio source is much less than the size of the CME itself and thus the source may change its position at the shock with time causing the apparent increase of its velocity. By such an assumption the source may migrate from the flank of the CME toward its nose at the beginning of the Type II burst, where the velocities retrieved from the drift rate and from the interferometer are higher than those provided by the coronagraph. On the contrary, the source possibly migrates backwards towards the tail of the Type II burst where the burst has practically no drift. Another possible reason of the discrepancy could be an extremely irregular shape of the source that leads to errors in the detection of the source center position. Interferometry at the UTR-2 estimates the sizes and the locations only along the two baselines of equal lengths and thus is sensitive to the shape of the source. The current configuration of the UTR-2 radio telescope provides accurate estimations of the spatial parameters of the spherical sources with Gaussian brightness distribution.

The formation of the HB structure is generally attributed to the electron beams acceleration at the shock in two opposite directions (Cairns, 1987). Fig. 6.15 and 6.16 evidently illustrate the inward and outward movement of the sources of HB subbursts with opposite frequency drift signs. The velocities of these motions are about 0.3 c and are close to the Type III electrons velocity.

Polarization properties of the Type II burst

Data from the URAN-2 radio telescope makes it possible to measure the polarization of radio emission. For this particular burst (May 31, 2013), the fundamental HB sub-bursts reveal a high degree of circu-

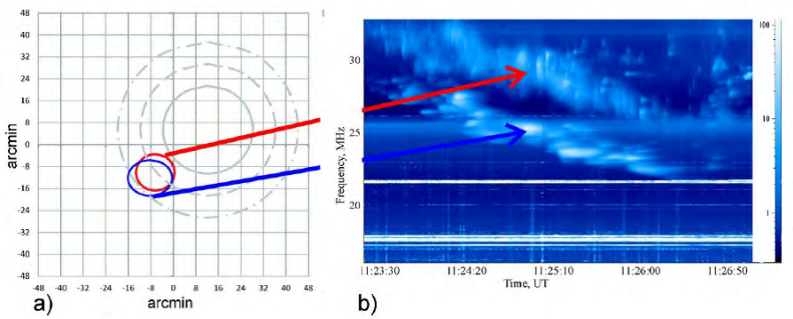


Figure 6.13: *The positions and sizes of the sources of Type II burst with band splitting (a) and the corresponding dynamic spectrum (b).*

lar polarization reaching as high as 70%. The harmonic counterparts are weakly polarized. This is in good agreement with the theoretical view, according to which the fundamental radio emission is the O-mode wave with almost 100% circular polarization, while the harmonic emission is a mixture of the O- and X-mode waves resulting in a much less polarization degree (Melrose, 1983). On the contrary, both the fundamental and the harmonic components of the first part of the Type II burst (without a HB structure) are completely unpolarized. This may indicate that the sources of different parts of Type II burst are located at different sites with different conditions.

6.3 Tadpoles - a new type of solar radio bursts

Type III-, Type II-, Type IV-bursts, large scale bursts in absorption, spikes, fiber-bursts, zebra-structures, Type IIIb bursts, sub-bursts of herringbone structures at the decameter wavelengths: All these bursts do not accompany all CMEs. Their appearance seems to be determined by the strength, velocity and mass of the CME. It is also essential at what angle the CME is observed.

In the following the results of solar observations on April 7, 2011,

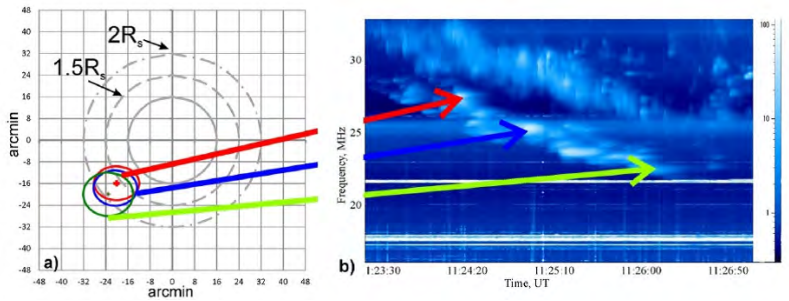


Figure 6.14: *Displacement of the Type II burst source with time (a) and the corresponding dynamic spectrum (b).*

by URAN-2 are considered. The new features of a hitherto unknown type of phenomenon associated with a CME were obtained due to the new registration equipment (DSP) and the possibility to measure the polarization of radio emission.

Observations

The active region NOAA1176 (Fig. 6.17(a)), which probably initiated the CME (appearance at 12:00 UT) (Fig. 6.17(b)), was located behind the solar limb at the longitudinal angle of about 135°. The CME velocity was more than 1000 km/s.

The flare under the active region NOAA1178 started at 11:16 UT and finished at 11:26 UT. The onset of the corresponding Type IV burst was at about 11:15 UT and continued over more than 2 hours (Fig. 6.18). Its maximum flux reached 10^2 s.f.u. and the polarization was in the range of 20 % - 40 %. This Type IV burst was registered also by the radio telescope in Nançay. Prior to this Type IV burst there was - in accordance with the standard model of Type IV burst (Melnik et al., 2008) - a group of Type III bursts (Fig. 6.19). Electrons responsible for the Type III bursts are accelerated in the flare and preceded the Type II and Type IV bursts. In the present case the Type II bursts were superimposed on the Type IV burst.

There were three Type II bursts (Fig. 6.20), each of them different, which in our mind were radiated by different parts of the spherical

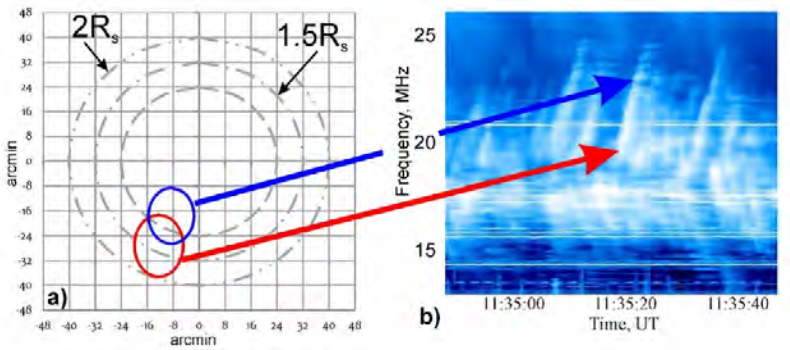


Figure 6.15: *Displacement of the reverse HB sub-bursts source with time (a) and the corresponding dynamic spectrum (b).*

shock (Fig. 6.21). The first Type II burst began at 11:22 UT and ended at 11:42 UT (Fig. 6.20, top). Its drift rate was not very high, only 10 kHz/s, that corresponds to a linear velocity of 300 km/s.

The first Type II burst comprises a sequence of tadpole-bursts. Every tadpole consists of a head and a tail. The frequency band of tadpoles were 2 MHz - 6 MHz and frequency drift rates of their tails were both positive and negative and as high as 4 MHz/s. The durations of tadpoles heads were about 4 s and durations of their tails were only 2s. Polarizations of tails were high, up to 20 % and higher, whereas the polarizations of tadpole heads were only 10 %.

The second Type II burst continued for 7 minutes, from 11:43 UT to 11:50 UT (Figures 6.20, bottom; 6.21). Its drift rate was 25 kHz/s, which corresponds to a linear velocity of 800 km/s in the Newkirk model of the solar corona. This value is close to the velocity of the shock front. It means that the second Type II burst is the radio emission of the shock regions, located near the front shock (Fig. 6.4). This burst also consists of tadpoles. Their characteristic property is their tails, directed from high to low frequencies. The head polarizations of these tadpoles are practically absent and tails polarizations reach values of 20 % - 40 %. Just to reiterate, the durations of heads are about 4 s and that of tails are 2 s. Head fluxes are about 10 times higher than those of tail fluxes. The frequency band of tadpoles is up

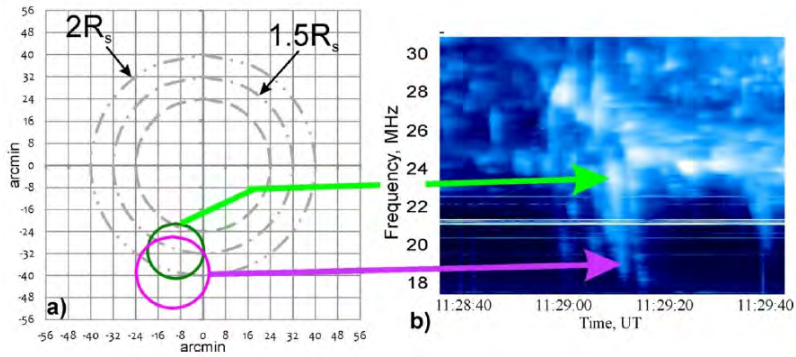


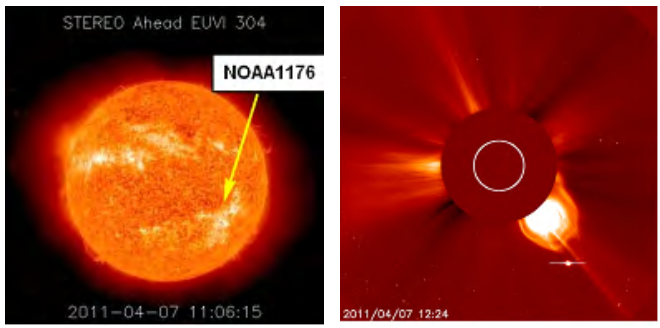
Figure 6.16: *Displacement of the forward HB sub-bursts source with time and the corresponding dynamic spectrum (b).*

to 10 MHz and characteristic drift rates of tails are about 1.4 MHz/s.

The third Type II burst continued for 7 minutes (from 11:52 UT to 11:59 UT) (Fig. 6.20, bottom). This burst had practically no drift rate. Thus, we can conclude that this burst was generated by the region of the spherical shock which propagated parallel to the solar surface (Fig. 6.4). Some of the tadpole tails of this Type II burst were directed towards high frequencies and others directed towards low frequencies. The frequency band of these tadpoles comprises 4 MHz and tail polarizations of these tadpoles reached 20 %.

All Type II bursts had second harmonics. In many cases the details of the first harmonics appeared again in the further harmonics. Fluxes of those harmonics were lower than those for the first harmonics. The same situation was observed with regard to polarization.

It can be assumed that tadpoles are connected with regions of electron acceleration at the shock. These regions can be regarded as the so-called SLAMS (Short Large Amplitude Magnetic Structures) proposed by Mann and Luehr (1994) as a sort of fine structure of shocks. In these regions of increased plasma density, the magnetic field is lower than in the surrounding plasma. Moving through the coronal plasma these regions lead to an effective acceleration of electrons at the SLAMS. Electrons captured in these regions radiate heads of the tadpoles and non-captured electrons propagating in the surrounding



(a) (b)

Figure 6.17: *The active region NOAA1176 (STEREO A) (a), and CME (SOHO) (b) associated with this active region.*

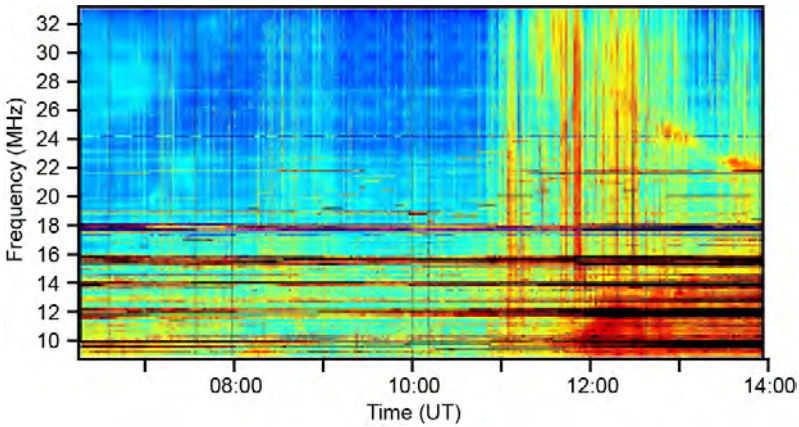


Figure 6.18: *The dynamic spectrum of radio emission on April 7, 2011.*

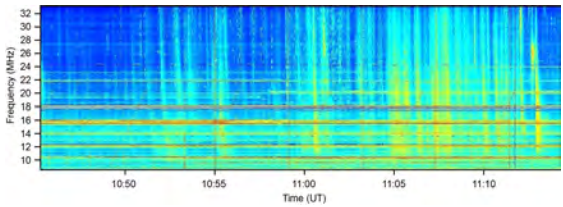


Figure 6.19: *Group of Type III bursts, which preceded Type II and Type IV bursts.*

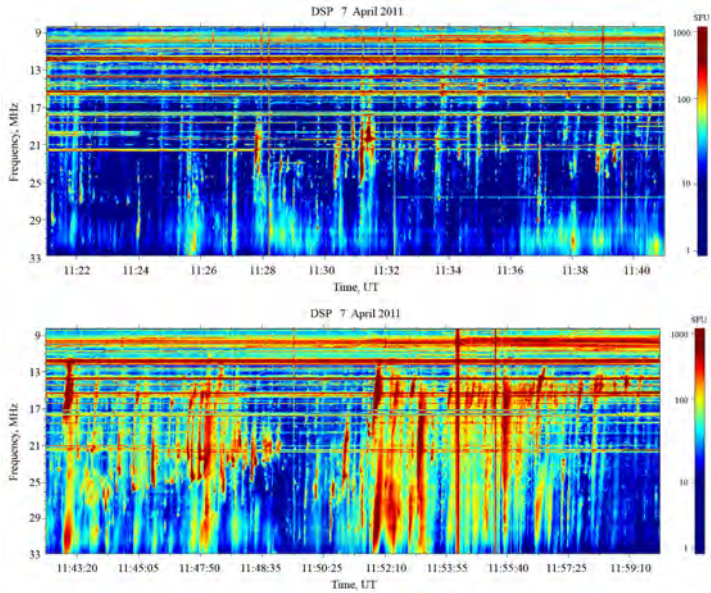


Figure 6.20: *The first Type II burst (top) and the second and the third Type II bursts (bottom) superposed on the Type IV burst.*

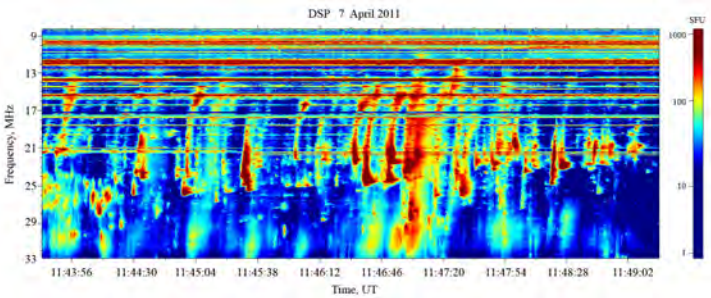


Figure 6.21: *Separate tadpoles of Type II burst with upward and downward tails.*

coronal plasma radiate tails of the tadpoles.

7 Type IV Bursts

7.1 Decameter Type IV burst associated with a behind-limb CME observed on November 7, 2013

Type IV bursts were classified as a separate type of solar phenomenon by Boischot (1957), distinguished in stationary and moving Type IV bursts (Stewart, 1985). Coronal arches and CMEs are considered responsible for the former and the latter, correspondingly. In the past Type IV bursts were observed only in the decimeter and meter ranges (Stewart, 1985). Regular observations of these bursts at frequencies 8 MHz - 32 MHz started during solar cycle 23 with the UTR-2 and URAN-2 radio telescopes performed by the wide frequency range 60-channel spectrometers and by the DSP (Digital Spectral Polarimeter) (Melnik et al., 2008). With the launch of WIND and later STEREO (Solar-Terrestrial Relations Observatory) A and B spacecraft high quality observations of Type IV bursts in the hectometer range became possible (Gopalswamy, 2011; Hillaris et al., 2016).

Several issues regarding the Type IV bursts remain as open questions: the mechanism of Type IV bursts generation, the places, from which radio emissions at different frequencies escape, the beaming of radiation of these bursts, their connections with Type II bursts and SEP (Solar Energetic Particle) events, among open topics (Stewart, 1985; Aschwanden, 2004; Gopalswamy, 2011).

The paper by Gopalswamy et al. (2016) considers in detail the event on November 7, 2013. At this day, a CME was ejected into a region behind the limb. It was accompanied by a Type IV burst observed by STEREO A and B from 10:40 UT to 11:50 UT and was not registered by WIND. The authors concluded that the directivity of the Type IV radio emission was narrow, about 60°, along its propagation path and that the observed Type IV burst was stationary and not moving.

This day the radio telescope URAN-2 (Poltava, Ukraine) carried out observations from 06:00 UT to 13:30 UT in the frequency band 17 MHz - 33 MHz. Starting from 10:22 UT and up to 10:44 UT this Type IV burst was registered by this radio telescope. Approximately at the same time this burst was also observed by the Nançay Decameter Array (NDA, Nançay, France) in the frequency band 30 MHz - 60 MHz.

In the following a possible source of this Type IV burst on the base of the results of observations by telescopes URAN-2, NDA, and by the spacecraft STEREO A and B and SOHO (Solar and Heliospheric Observatory) will be discussed.

7.1.1 Observations

In Fig. 7.1 the dynamic spectrum of solar radio emission from 10:17 UT to 11:01 UT in the frequency band 17 MHz - 33 MHz is shown. The Type IV burst began at approximately 10:22 UT and finished at 10:44 UT. There were also some Type III bursts prior to the Type IV burst. The Type IV burst and Type III bursts reached 30 - 40 s.f.u. and 100 s.f.u., respectively (Fig. 7.2) and the polarizations of these bursts were high, slightly below 40% for Type IV and up to 50% for Type III bursts. This supports the idea that both Type IV burst and Type III bursts are generated at the first harmonic of the local plasma frequency (Stewart, 1985). Type III bursts were rather diffuse with sub-bursts exhibiting positive and negative frequency drift rates of 2 MHz s^{-1} - 6 MHz s^{-1} (Fig. 7.3). Simultaneously the drift rate of Type IV burst front was about 30 MHz s^{-1}.

The NDA radio telescope observed the Sun on this day (November 7, 2013) too (Fig. 7.4). Its data demonstrates exactly the same set of bursts as recorded by URAN-2, but at frequencies 30 MHz - 60 MHz. A weak Type II burst with drift rate of about 250 kHz s^{-1} was addionally observed at frequencies 44 MHz - 64 MHz from 10:16 UT to 10:17 UT. At frequencies 28 MHz - 33 MHz this very weak burst (flux of about 10 s.f.u. and polarization more than 20%) was possibly observed near 10:19 UT (Fig. 7.2).

As reported by Gopalswamy et al. (2016) STEREO A and B registered the Type IV, Type III, and Type II burst approximately at the same period of time (Fig. 7.5) as the URAN-2 and NDA radio tele-

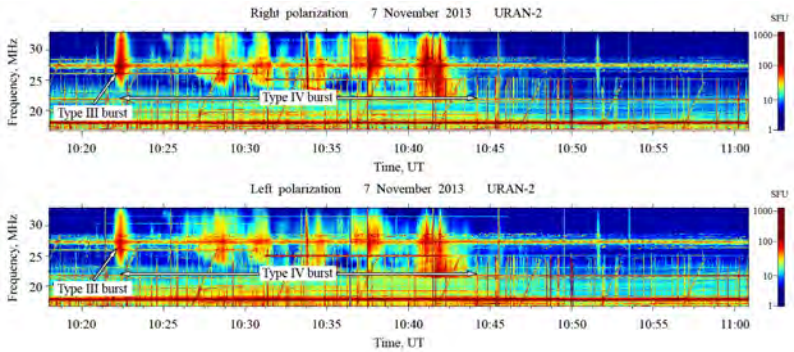


Figure 7.1: *Type IV burst and Type III bursts on November 7, 2013, according to URAN-2.*

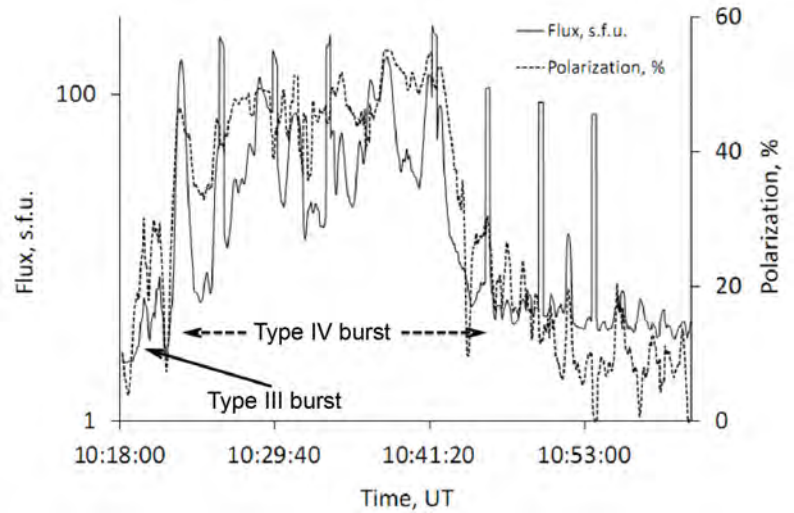


Figure 7.2: *The flux and polarization profiles of the Type IV and Type III bursts at 32 MHz.*

scopes, but shortly later. Gopalswamy et al. (2016) associated this event with a CME, which was initiated by an active region at the longitude E150 which appeared behind the limb as seen from the Earth. This CME propagated practically in the direction towards STEREO B (Fig. 7.6d) so it was registered by STEREO B as halo-CME. At the same time STEREO A registered this CME as a compact object with bright core and envelope (Fig. 7.6). The velocity of this CME was high, up to 2000 $\mathrm{km\,s^{-1}}$ (Gopalswamy et al., 2016). According to STEREO A and SOHO data the velocity of the CME core was only 550 $\mathrm{km\,s^{-1}}$.

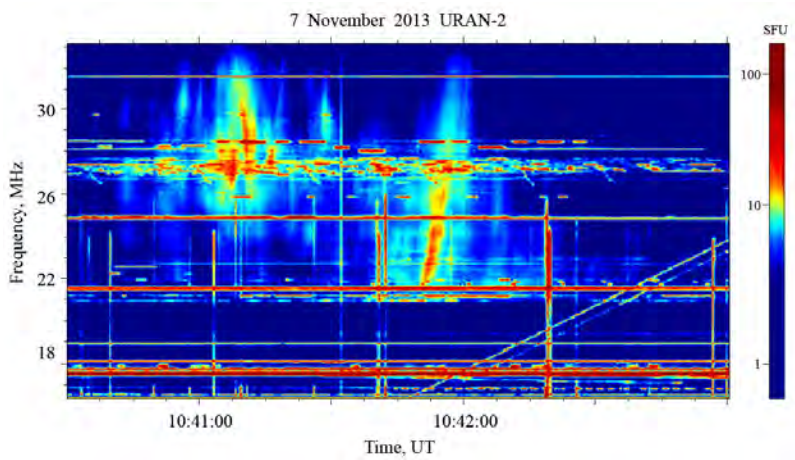


Figure 7.3: *Type III burst with fine structure in the form of sub-bursts with positive and negative drift rates.*

STEREO B observed the Type IV burst very clearly, but it was very weak in the observations of STEREO A due to the high viewing angle of about 60°. Despite approximately the same viewing angles, ground-based radio telescopes could register this Type IV burst due to their high sensitivity (Konovalenko et al., 2013). According to STEREO B this Type IV burst was observed mainly between 16 and 11 MHz from 10:50 UT to 11:30 UT. The fact that at low frequencies the burst was registered later than at higher frequencies indicates that this Type IV burst was moving. This is confirmed by the drift

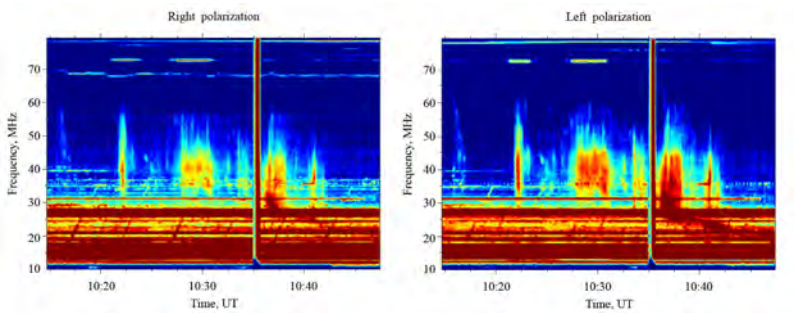


Figure 7.4: *Type IV, Type III, and Type II burst observed by the radio telescope NDA on November 7, 2013.*

of the front not only at frequencies 22-33 MHz but also at frequencies 11 MHz - 16 MHz. Its drift rate is about 6 kHz s^{-1} at frequencies 11 MHz - 16 MHz. Besides Type IV bursts, Fig. 7.5 shows Type III bursts having their counterparts at higher frequencies, but there are also Type III bursts at 10:18 UT and about 10:58 UT, which are absent in URAN-2 and NDA records. Both STEREO A and STEREO B observed Type II bursts, which drifted from 16 MHz to 3 MHz with a drift rate of about 8 kHz s^{-1}.

7.1.2 Interpretation of the observations

Both Type IV and Type III bursts are behind-the-limb and this raises the question about the locations of their sources and their association with the CME. The positions and sizes of the CME core (obtained from STEREO A data) at 10:22 UT and 10:28 UT, when the Type IV burst was observed in the frequency ranges 30 MHz - 60 MHz and 23 MHz - 60 MHz, are shown in Fig. 7.7.

Levels of local plasma frequencies 23, 30 and 60 MHz and the regions of occultation by the Newkirk solar corona (on this particular day November 7, 2013, there were active regions on the eastern limb) are given. From Fig. 7.7 we see that radio emissions at 23, 30 and 60 MHz can only escape towards the Earth from regions left to the lines f_{NK}=23, 30, 60 MHz, correspondingly. If we suppose that the source of Type IV burst is within the CME core (following Bain et al.

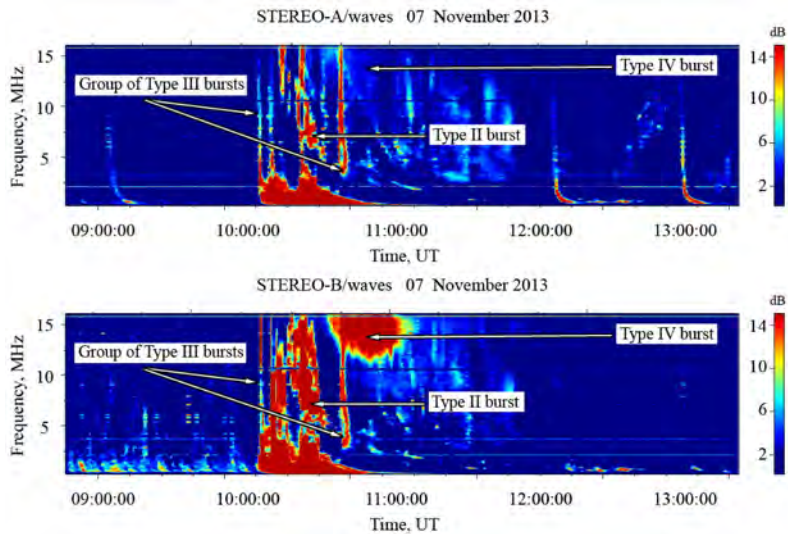


Figure 7.5: *Type IV, Type III, and Type II burst according to STEREO A and B.*

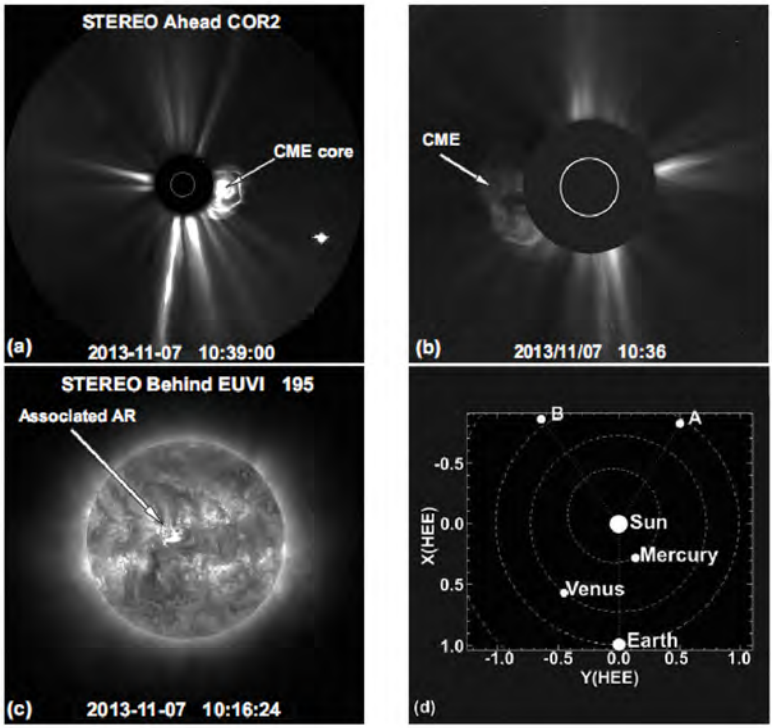


Figure 7.6: *CME according to STEREO A (a), and SOHO (b) and the active region responsible for the CME (c) and STEREO A and B close to the Earth orbit on November 7, 2013 (d).*

(2014)) then it is reasonable to suggest that the radio emissions at frequencies 23 and 30 MHz escape from the peripheral regions of the CME core and at frequency 60 MHz from its center. Assuming plasma mechanism of radio emission, then the densities in the center ($n_c = 4.5 \cdot 10^7\,\mathrm{cm}^{-3}$) and in the peripheral regions ($n_p = 1.3 \cdot 10^7\,\mathrm{cm}^{-3}$) of the CME core can be determined. If the density distribution in the core is exponential

$$n(r) = n_c exp(-\alpha r), \tag{7.1}$$

where r is the distance from the core center, then $\alpha = 2.5/R_S$ (R_S is the solar radius). At $r = 0.5R_S$ (the core radius at 10:22 UT) the density equals $n(r = R_S/2) = n_p = 1.2 \cdot 10^7\,\mathrm{cm}^{-3}$. For compensation of gas kinetic pressure $p = nkT$ at the core surface by the magnetic pressure $p_B = B^2/2\mu_0$ a magnetic field of 0.06 G with a plasma temperature in the core $T = 10^5$ K, and 0.21 G at $T = 10^6$ K are necessary. The density of the surrounding coronal plasma at distance $R = 2.8R_S$ equals only $n_p = 1.2 \cdot 10^6\,\mathrm{cm}^{-3}$ which is essentially smaller than the density in the core at this distance. Supposing that the size of the Type IV source was about 1 R_S at frequencies 22 MHz - 30 MHz we derive a brightness temperature of the Type IV radio emission at these frequencies $T_{br} \approx 10^9$ K. Such a high brightness temperature is difficult to explain by gyrosynchrotron mechanism (Stewart, 1985), however easily interpreted within the frame of the plasma mechanism (Stewart, 1985).

The mass of the CME core with the density distribution by Eq. (7.1) can be estimated as

$$M_{CME} = 4\pi \int_0^{R_S/2} m_p n(r) r^2 dr \approx 10^{16} g. \tag{7.2}$$

This value is in agreement with the SOHO data. (Due to expansion of the core the peripheral density decreases and this leads to the frequency drift of Type IV burst whose drift rate is defined by the equation

$$df/dt = \frac{f}{2n}\frac{dn}{dr}\frac{dr}{dt}, \tag{7.3}$$

where dr/dt is the velocity of the core expansion equal to 300 km s^{-1} according to STEREO A data. Taking into account the

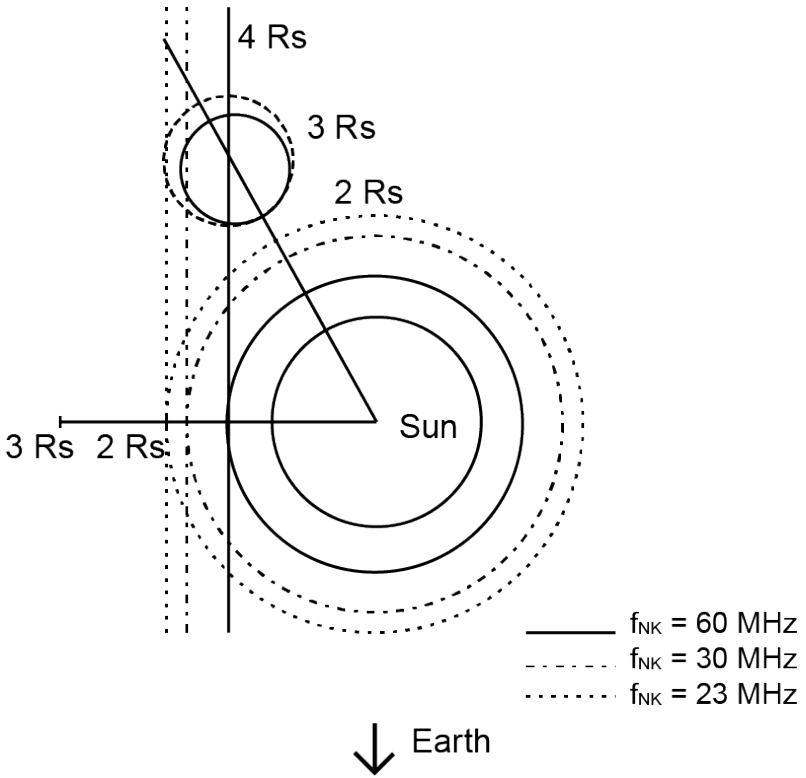


Figure 7.7: *Schematic positions of the CME core at November 7, 2013, 10:22 UT (solid line) and 10:28 UT (dashed line), the Sun and the Earth and levels in the solar corona, which corresponds to local plasma frequencies 23, 30 and 60 MHz* ($f_{\mathrm{NK}} = f_{\mathrm{Newkirk}}$).

inhomogeneity size $((1/n)(dn/dr))^{-1}$ the drift rate can be derived from Eq. (7.3), which is about $27\,\mathrm{kHz\,s^{-1}}$ in the frequency range 22 - 33 MHz, which is in good agreement with the observational results of URAN-2.

7.2 Decameter Type IV bursts observed in the years 2003-2006

During 2003 - 2006, the UTR-2 radio telescope registered 17 Type IV bursts. All observations were carried out by means of a 60-channel spectrometer. Each of the 60 channels had a bandwidth of 3 kHz and was set at some frequency within the range 8 MHz - 33 MHz. The channels were in average spaced by 340 kHz, but not regularly. A common consequence of appearance of Type IV bursts is outlined in the following. At first a group of strong Type III bursts appears, followed then by Type II bursts, then a Type IV burst follows. Such a sequence can be seen on July 13, 2004, (Fig. 7.8) as an example. But there are cases where a group of Type III bursts or Type II bursts are absent. Sometimes as, for instance, on July 23, 2005, a Type II burst is observed against a background of a Type IV burst (Fig. 7.9).

This "canonical" sequence is connected with the fact that during the flare, associated with CMEs and Type IV bursts, electron beams are accelerated to high energies and are injected into the coronal plasma, whereby electrons generate a group of Type III bursts at corresponding heights. Any absence of such precursors means that such accelerated electrons were absent (for example if a flare was strong), or that radio emission was not registered because of Type IV beaming, or that some shadowing regions are present (e.g., the solar corona, if the event is behind-limb). Type II bursts preceding Type IV bursts, this seems to be a radio emission of the shock which was initiated by a CME if its velocity is high enough. This radio emission can be emitted from different parts of the shock (nose and/or flanks). Thus it is not surprising that sometimes several Type II bursts with different frequency drift rates are observed. Sometimes Type II bursts were registered not only with two harmonics but also with three harmonics (Fig. 7.10).

The superposition of Type II bursts and Type IV bursts can be

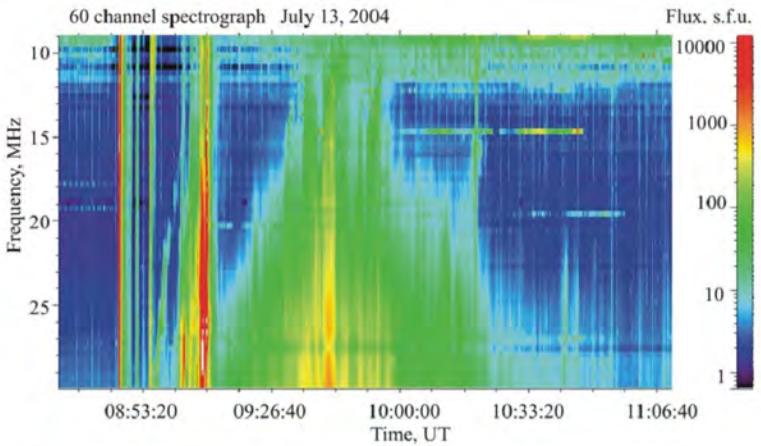


Figure 7.8: *Low frequency part of a Type IV burst with attendant Type III.*

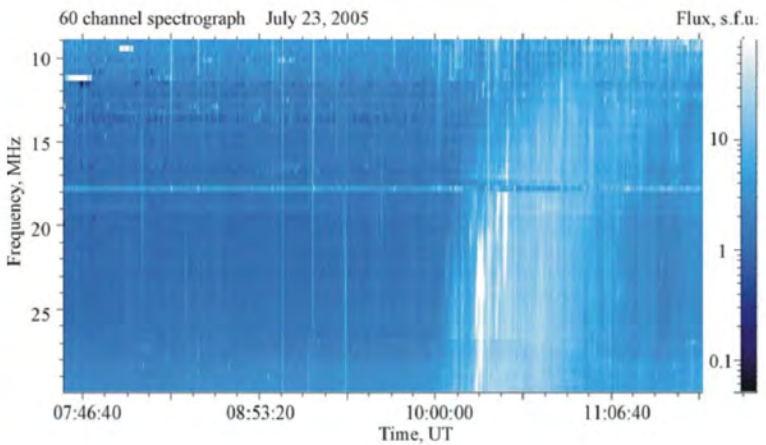


Figure 7.9: *Decameter Type II overlapped by Type IV burst.*

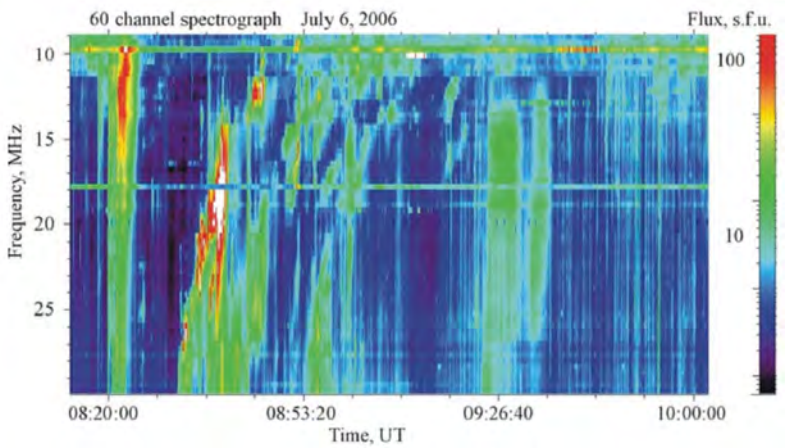


Figure 7.10: *Type IV burst on July 6, 2006.*

connected with the presence of a shock at the line of sight between a Type IV source and the observer, generating radio emission at the same frequency at the very same time. The Type IV source can be the CME core (in the case of a moving Type IV bursts) or coronal arcs (in the case of stationary Type IV bursts). The drift of the Type IV front is usually connected with the propagation of a CME into the coronal plasma and the radio emission frequency is equal to the local plasma frequency (following the plasma generation mechanism). But recently the hypothesis was stated that Type IV bursts may be emitted from the CME core, then the drift is caused by the expansion of the CME core during its movement.

The duration of Type IV bursts in the decameter range can essentially differ even at a single event (Fig. 7.8). The largest duration of decameter Type IV bursts can amount to several hours (Fig. 7.11). Such durations were also registered in the meter wavelength range (Fig. 7.12), but not only occasionally. In most cases, the durations are about 1-1.5 hours. It is still difficult to understand the cause of such long-term radio emission of Type IV bursts at different frequencies, since the plasma mechanism of generation demands a long-term generation of Langmuir waves. These Langmuir waves are incited by

electron beams but the source of such continuous electrons beams is still unclear.

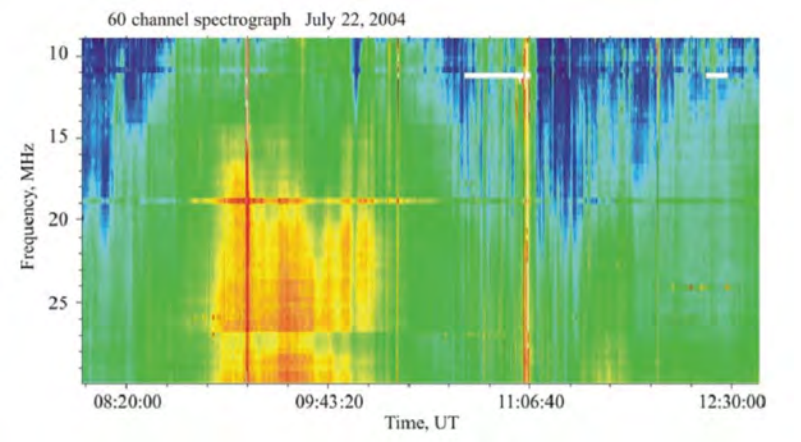


Figure 7.11: *Decameter Type IV burst (UTR-2 data).*

The front of a Type IV burst drifts from high to low frequencies (Figs. 7.8, 7.9) or has no noticeable drift (Fig. 7.11). Frequency drift rates range from 10 to some tens of kHz/s, their drift rates are slightly smaller than those of corresponding Type II bursts. The "back" of Type IV bursts can have positive (Fig. 7.8), or negative (Fig. 7.9) drift rates.

As a rule, Type IV bursts have fast-increasing and then slow-decreasing flux profiles (Fig. 7.13). Maximum fluxes reach 10^3 s.f.u. in rare cases. Generally the radio flux does not show a well-defined dependence of frequency. Long period oscillations of Type IV fluxes can occur (Fig. 7.13), which are caused by oscillations of radio emission sources. The polarization of Type IV bursts achieves a maximum value after a flux maximum and in most cases amounts to 40%. The corresponding polarization profile shows a slow increase and a fast decrease.

The fine structure of decameter Type IV bursts is mainly sort of Type III bursts-like with intermediate frequency drift rates. Figs. 7.14, 7.15 and 7.16 present different kinds of such bursts. Sometimes

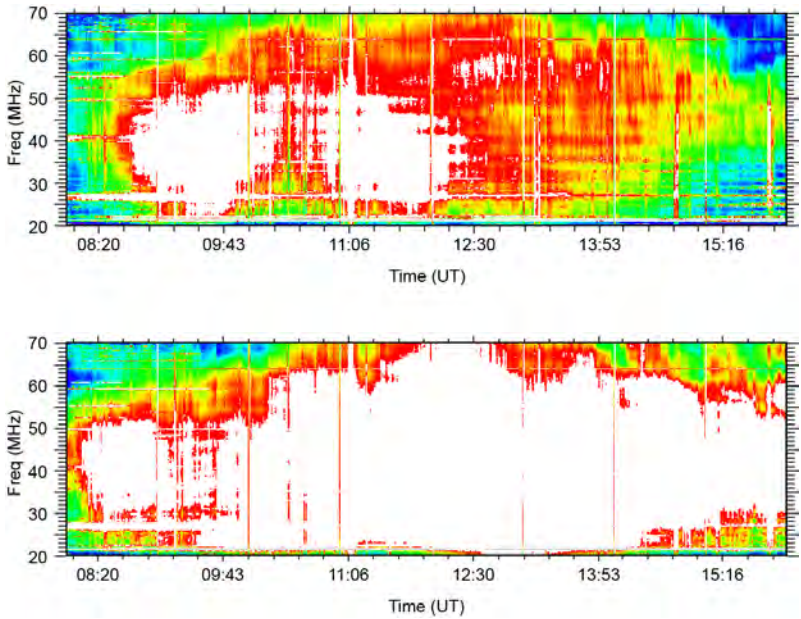


Figure 7.12: *Type IV burst at frequencies 20 - 70 MHz (NDA data).*

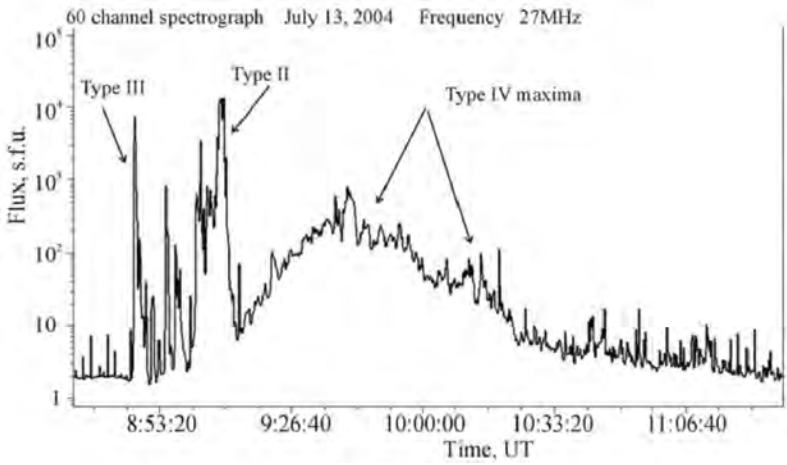


Figure 7.13: *Time profile of Type III-, Type II- and Type IV-burst.*

this fine structure appears in the form of fiber bursts (Fig. 7.14), sometimes it is smeared-out and exhibits some internal structures (Fig. 7.15). Sometimes these bursts are similar to Type IIIb bursts (Fig. 7.16). In rare cases some regions of Type IV bursts present continuum radio emission without any internal structure (Fig. 7.14).

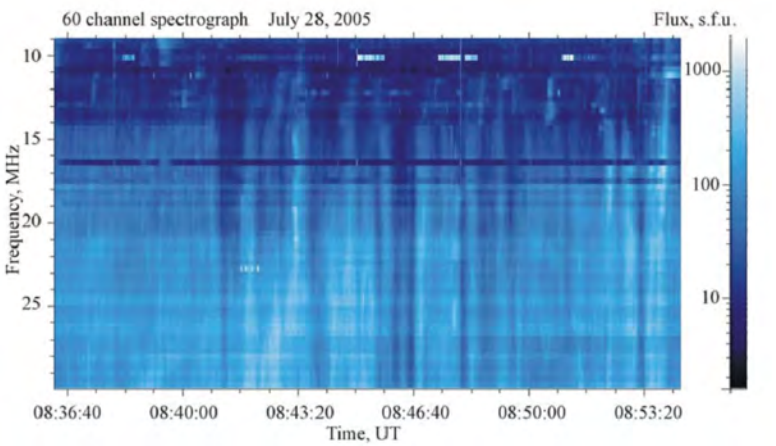


Figure 7.14: *Fine structure of Type IV burst in the form of fiber bursts with positive and negative drift rates in emission and absorption.*

Regarding fiber bursts their fluxes do not strongly differ from the parent Type IV burst, i.e. 10 - 1000 s.f.u. in most cases. Frequency drift rates of fiber-bursts are slightly smaller than those for standard Type III burst at corresponding frequencies and mainly equal to 1 MHz/s - 3 MHz/s, in some cases even smaller than 1 MHz/s. Sometimes drift rates can be even more than 3 MHz/s, but such cases are very rare. Durations of fiber bursts are in the frame of 10 s - 20 s and this is slightly longer than standard Type III bursts. In some cases, durations are in the range of 1 s - 2 s. Fiber bursts exhibit both negative as well positive drift rates. Moreover, fiber bursts were also observed in absorption (Figs. 7.17, 7.18), featuring both negative and positive drift rates. All this suggests that radio emission escapes from a rather non-homogenous plasma.

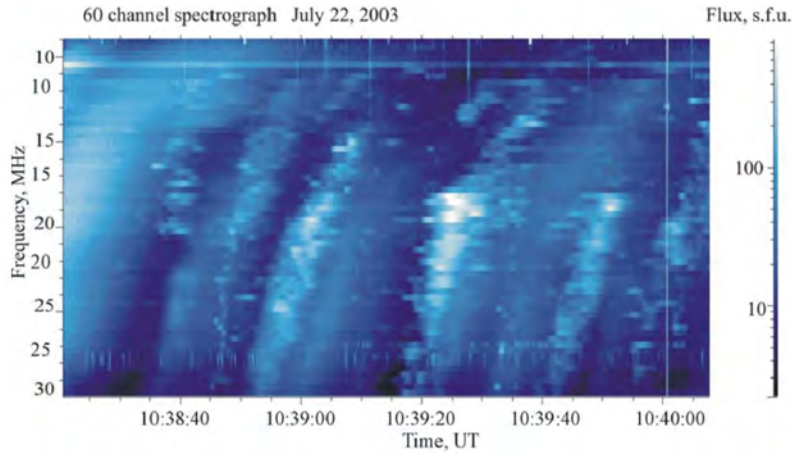


Figure 7.15: *Fragment of Type IV burst with fine structure.*

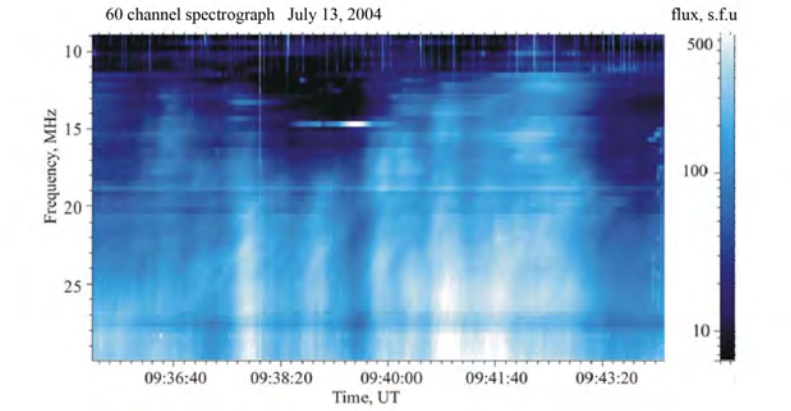


Figure 7.16: *Fiber bursts as a fine structure of a Type IV burst (July 13, 2004).*

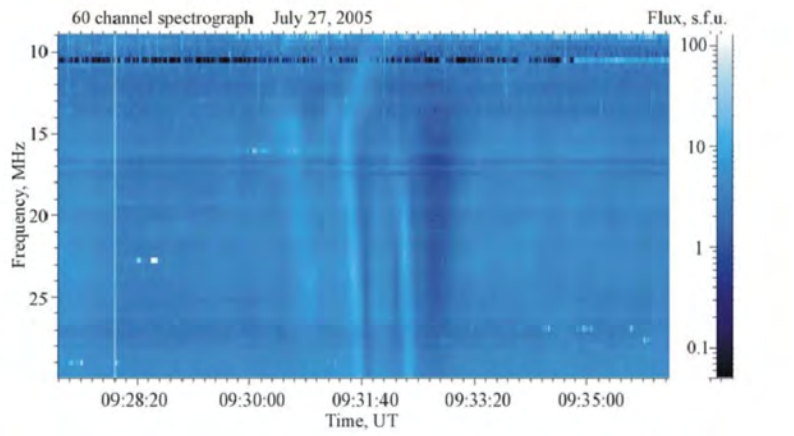


Figure 7.17: *Bursts in emission and absorption with positive drift rates.*

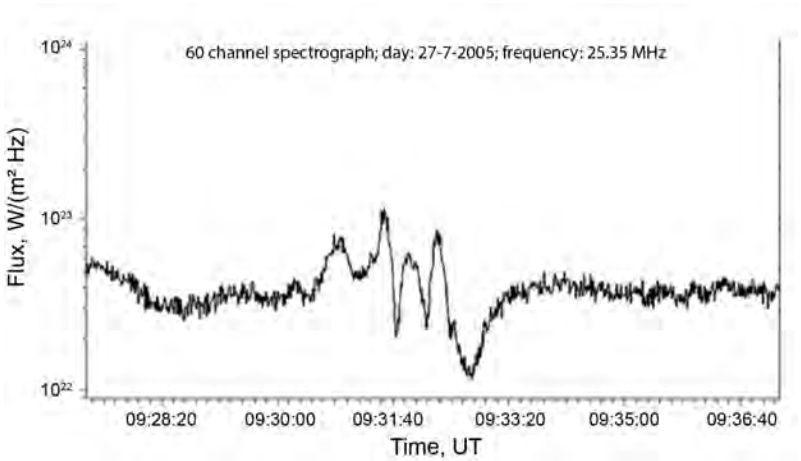


Figure 7.18: *Time profile of bursts in emission and absorption.*

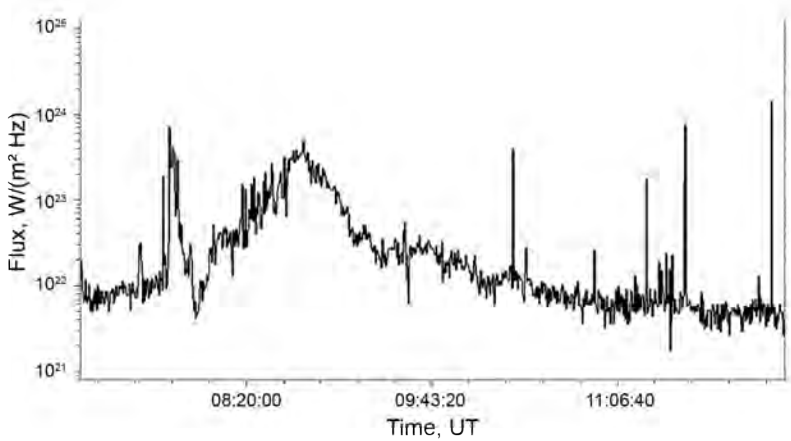


Figure 7.19: *Time profile of a Type IV burst.*

Sometimes Type IV bursts have large–scale bursts in absorption, lasting some minutes (Figs. 7.44, 7.45). In some cases such bursts appear after a group of Type III bursts at once and before a Type IV burst (Fig. 7.19).

On July 22, 2004, we observed a fingerprint fine structure (Figs. 7.26 and 7.27) of Type IV burst. Such episodes were from 8:10 UT to 11:40 UT. The distance between stripes of fingerprint was about 1 s - 2 s and for a given group this temporal distance is constant. The theory underpinning this sort of zebra structure will be discussed below.

7.3 Properties of decameter Type IV bursts

Among the recordings of 40 Type IV bursts observed by UTR-2 (Kharkiv, Ukraine) during 2002-2006, a very interesting Type IV burst was registered on July 13, 2004, at frequencies 10 MHz - 30 MHz. This event shows the most complete phenomena of the solar Type IV burst at decametric wavelengths (Melnik et al., 2008). Three sections of the radio telescope UTR-2 with a total area of 30000 m^2 and beam

size of $1^\circ \times 13^\circ$ were used for these observations. Registrations were carried out by the 60-channel receiver with a frequency resolution of 300 kHz and time resolution of 10 ms. The time profile at frequency 26.15 MHz of the July 13, 2004, event is shown in Fig. 7.20 with the following sequence: Type III bursts, bursts in absorption, Type II burst, and Type IV burst.

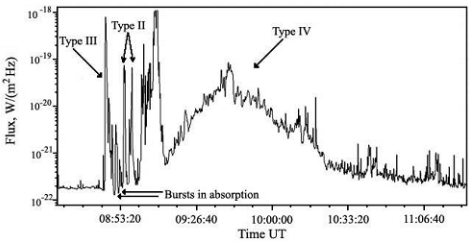


Figure 7.20: *Time profile of an event observed on July 13, 2004.*

On this July 13, 2004, four active regions (Fig. 7.21), which could be responsible for the Type IV radio emission and associated Type III and II bursts, were on the solar disc (85° and 40° to the East and 5° and 50° to the West from the central meridian). Decametric radio bursts observed at that day are associated with the active region N 121 [NOAA 10646], located 50° to the West from the central meridian.

For the purposes of statistical analysis we divided the whole frequency band from 10 to 30 MHz into the frequency sub-bands 10 - 13 MHz, 13 - 15 MHz, 15 - 20 MHz, 20 - 25 MHz, 25 - 30 MHz. We marked all the characteristics for every solar burst type on the average frequencies of each sub-bands.

On July 13, 2004, nine Type III bursts as precursors of the Type IV burst were observed. It should be noted, that one of these bursts was powerful with a flux of $1.6 \cdot 10^{-18}$ $\mathrm{Wm^{-2}Hz^{-1}}$ (Melnik et al., 2011a). Time profiles of these Type III bursts are not symmetrical, as can be seen in Fig. 7.22.

In the range of 10 MHz - 30 MHz all these bursts have negative frequency drift rates (drift from high to low frequencies). In Fig. 7.23 (top) it can be observed that most of the bursts have a linear drift rate dependence on frequency, but there are two irregular curves.

We assume that these two Type III bursts (at 08:53:04 UT and

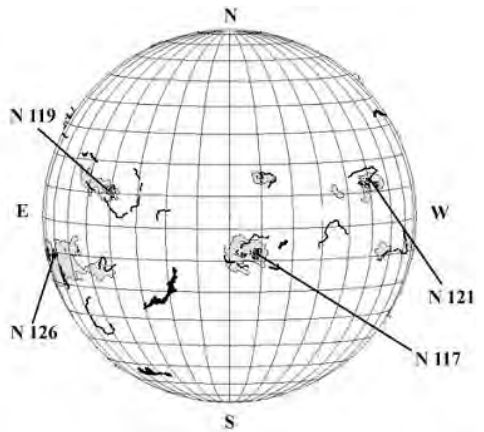


Figure 7.21: *Location of the active regions on the solar disc on July 13, 2004.*

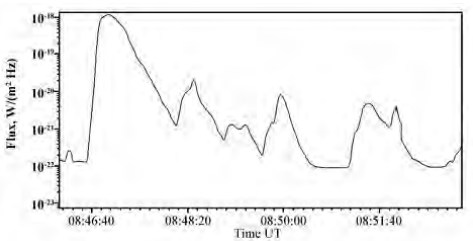


Figure 7.22: *Type III bursts (08:46:55 UT, 08:49:50 UT, 08:51:20 UT) time profiles at frequency 19.2 MHz.*

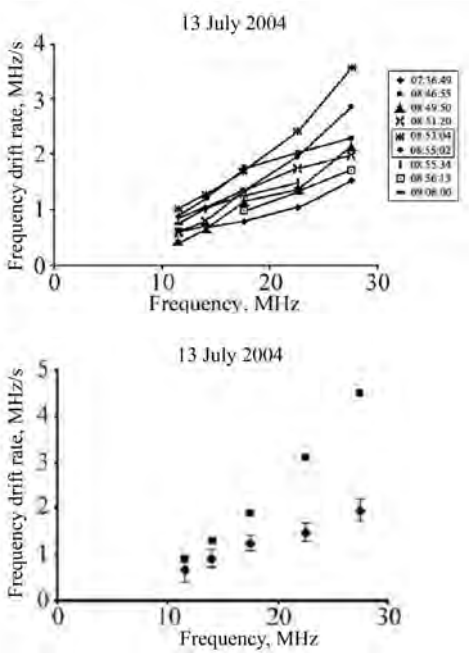


Figure 7.23: *Drift rate dependencies on frequency for individual Type III burst (top) and for average values (bottom) (dots represent observational data and squares represent data obtained by the empirical dependence* $df/dt = -0.01f^{1.84}$ *(Alvarez and Haddock, 1973)).*

08:55:02 UT) do not originate from the active region N121. Thus, these two bursts were excluded from statistical analysis. According to our observations Type III bursts have frequency drift rates in the range of 1 MHz/s - 3 MHz/s. The dependence of average drift rate on frequency for Type III bursts is shown in Fig. 7.23 (bottom). Attention should be paid to the difference between the derived and empirically obtained dependence. Drift rates are almost the same at frequencies 10 MHz - 15 MHz, but they considerably differ by a factor of about 2 at frequencies 20 MHz - 30 MHz. The duration of Type III bursts is within the range of 15 s - 20 s, which is higher than the usually found Type III burst duration (4 s - 12 s). The average duration dependence on frequency is shown in Fig. 7.24. After a group of Type III bursts two solar bursts in absorption were observed (at 08:50:53 UT and 08:52:40 UT). At the frequency 22.5 MHz the first burst had a duration of 32 s, and the second one of 19 s. In this range of 10 MHz - 30 MHz the drift rates were -1.5 MHz/s and -1.2 MHz/s for first and second burst, respectively.

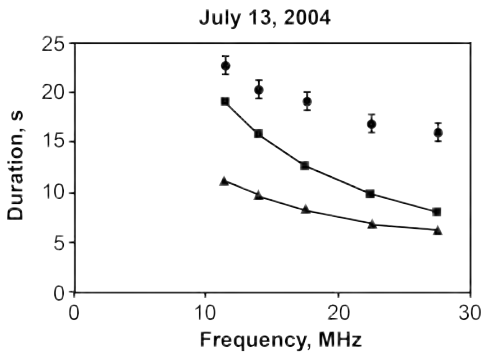


Figure 7.24: *The Type III bursts duration dependence on frequency (circles represent average observational duration values, solid line with squares represents $T = 220/f$ dependence (Suzuki and Dulk, 1985), solid line with triangles represents $T = 60 \cdot f^{-2/3}$ dependence (Elgaroy and Lyngstad, 1972).*

The Type II burst started at 30 MHz at about 08:56:10 UT and it

had two harmonics (Mel'nik et al., 2004). On July 13, 2004, observations of the Sun were carried out with the HiRAS (Hiraiso Radio Spectrograph) in the frequency range of 25 MHz - 2500 MHz. These observations were completed with the low-frequency observations by UTR-2. Due to these instruments the characteristics of the Type II burst could be determined in a wide frequency range. The frequency drift rate in the range of 10 MHz - 30 MHz for the fundamental component is -34 kHz/s, while for the second and the third harmonics these values are -58 kHz/s and -57 kHz/s, respectively. The Type II burst drift rate increases with frequency. The frequency drift rate values at higher frequencies for the fundamental harmonic of the Type II burst are much higher: in the range of 50 MHz - 100 MHz it is 256 kHz/s, while in the range of 100 MHz - 200 MHz it is 769 kHz/s.

Type II bursts are caused by shock waves. The leading edge of the CME corresponds to a shock wave, which was formed at about 08:46:00 UT according to our calculations. The linear velocity of the shock wave is 253 km/s at a distance of about 7 solar radii from the Sun (estimates were made using SOHO data). Calculations of the frequency drift rate of the fundamental component of Type II burst show that the velocity of the shock is 365 km/s at a distance of 1.5 solar radii. So apparently the shock was slowing down moving away from the Sun.

The Type IV burst observed on July 13, 2004, began at 09:11:00 UT and lasted for about 2 hours. It exhibited sort of fine structure in the form of drifting sub-bursts (so-called fiber bursts) (Melnik et al., 2010b). In the range of 10 MHz - 30 MHz the duration of the Type IV burst increases with frequency - about 30 min at 15 MHz, but at frequency 30 MHz it increases up to 2 hours 20 min. The drift rate of this burst measured at the forward edge is -15 kHz/s, the average flux value as 24 s.f.u. The frequency profile (Fig. 7.25) shows that the flux increases with frequency. The Type IV burst emission on this July 13, 2004, within the frequency band 20 MHz - 60 MHz was strongly polarized according to Nançay data. This Type IV burst was accompanied by a CME (Klecker et al., 2006) with a velocity of 713 km/s. According to the radio data we calculated a velocity of the CME using the Type IV burst leading edge. At the distance of 1.5 solar radii (at frequency 30 MHz) the velocity was determined as about 90 km/s.

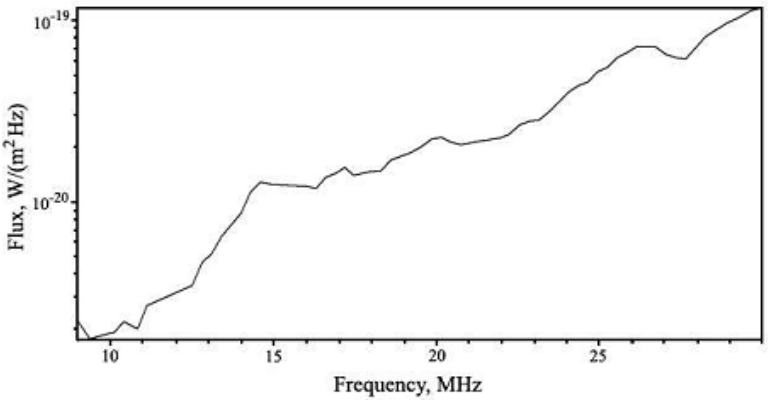


Figure 7.25: *The Type IV burst frequency profile, measured at burst flux maximum.*

Summarizing, the observational data in the wide frequency range (25 MHz - 2500 MHz) agree with low frequency (10 MHz - 30 MHz) observations. The event of July 13, 2004, enabled to determine the main properties of Type III bursts, bursts in absorption, Type II and Type IV burst. The velocity of the CME associated with this event using the decameter Type IV burst leading edge yielded 90 km/s. The shock wave velocity calculated from the fundamental component frequency drift rate of the Type II burst was found as 365 km/s.

7.4 "Fingerprint" fine structure of decameter Type IV burst

Decametric sporadic solar radio emission is known to have a great variety of spectral details (Mel'Nik et al., 2005b; Melnik et al., 2011b). It distinctly shows all five main types of bursts accompanying fast electrons or shock waves propagating through the solar corona, as well as the bursts induced by energetic electrons trapped in the coronal magnetic fields. The radio telescope UTR-2 in Kharkiv, Ukraine (Braude et al., 1978), has been used for more than 40 years for obser-

vations at frequencies of 10 MHz - 30 MHz. The application of a new back-end instrument with enhanced sensitivity, extended frequency range, and increased frequency resolution resulted in the detection of fine spectral details, which enables to get information about the physical conditions and processes in the upper corona.

In the following the fine structure in the dynamic spectrum, observed on July 22, 2004, will be discussed in more detail in terms of the Type IV continuum within the frequencies of 20 MHz - 30 MHz for one and a half minute (Melnik et al., 2008). In 2004, the solar radio emission was observed by only three sections of the UTR-2 radio telescope, with an effective area of 30000m^2 and an antenna pattern size of $1^\circ \times 13^\circ$. The signal was recorded by a 60-channel spectrometer with a frequency band of 3 kHz for each channel. The frequency spacing between the channels was 340 kHz, which means that the entire working frequency band from 10 MHz to 30 MHz was covered. The position of the frequency channels was chosen so as to eliminate interference. A linear interpolation was applied to fill the gaps between the channels. This 60-channel spectrometer provided a time resolution of 25 ms and a sensitivity of 10^{-23}W/(m^{2}Hz).

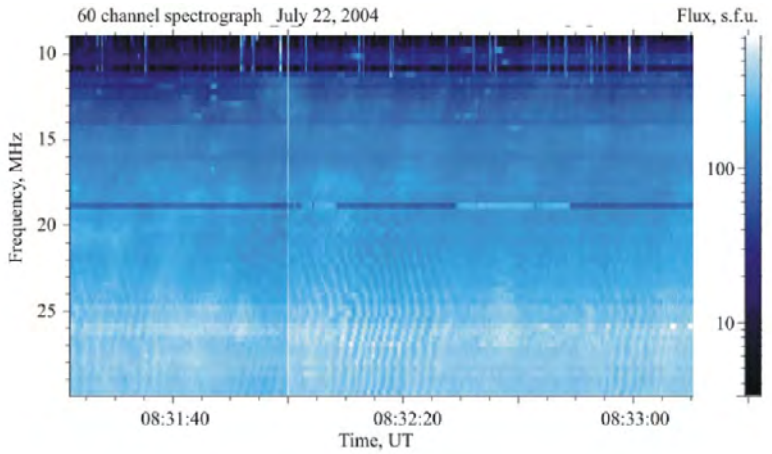


Figure 7.26: *Three groups of zebra patterns.*

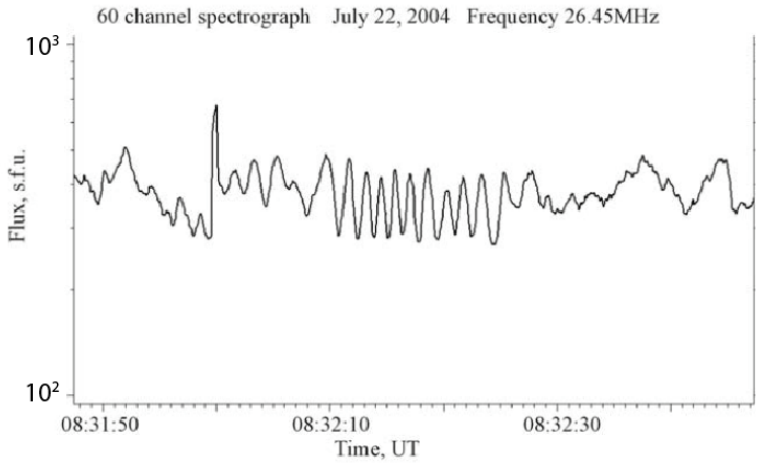


Figure 7.27: *Succession of stripes in zebra structure in emission and in absorption.*

Observations

The dynamic spectrum of the burst shown in Fig. 7.28 looks like a fingerprint, and in the following (Melnik et al., 2008), this term is used in the analysis. The fine structure as a system of quasi-harmonic parallel stripes drifting in time, or the so-called zebra pattern (ZP), is often observed in solar dynamic spectra at meter and decimeter wavelengths (see, for example, Aurass et al. (2003) and Chen et al. (2011), and reviews by Chernov (2006) and Zlotnik (2009)).

However, at first glance, the burst studied here can hardly be attributed to ZP. Instead, it does not show stripes of enhanced radiation equally spaced in frequency, but quasi-periodic bursts of enhanced radiation, namely fine structure in time, not in frequency domains. Thus, this cannot be considered as a typical ZP and be explained by the double plasma resonance (DPR) effect in a coronal trap. Nonetheless, as shown below, 'the fingerprint' is easily explained in the framework based on the DPR effect, and, finally, it really represents some type of usual ZPs.

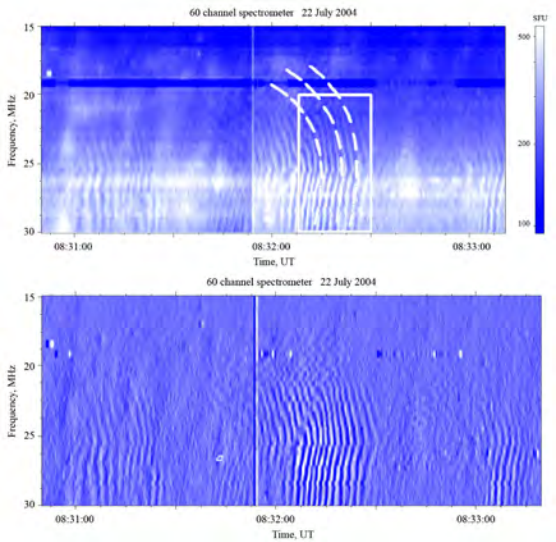


Figure 7.28: *Dynamic spectrum of the solar burst 'fingerprint' on July 22, 2004, (top) and its differential dynamic spectrum (bottom). The rectangle indicates the portion which is used for the numerical analysis. The dashed lines schematically show the form of the fine structure lines.*

On July 22, 2004, the observations of solar radio emission with the UTR-2 radio telescope were carried out from 08:00 UT till 12:40 UT. The dynamic spectrum and the time profile (at a frequency of 30 MHz) for the whole session are shown in Fig. 7.29. The enhanced radio emission observed between 08:40 UT and 10:15 UT is part of the Type IV burst, which apparently started before 08:00 UT and lasted after 12:40 UT. According to the Nançay Decametric Array data, this burst continued at least until 16:00 UT.

In the observed period of time, this burst had a main peak with a flux of $1 \cdot 10^3$ s.f.u. (solar flux unit; 1 s.f.u. $= 10^{-22}\mathrm{W}/(\mathrm{m}^2\mathrm{Hz}) = 10^4$ Jy) and two weaker peaks with fluxes of $2 \cdot 10^2$ s.f.u. As usual, the burst consisted of fine structure in the form of fiber bursts and zebra stripes. One of the peculiar properties is that the zebra stripes were observed in groups containing from 5 up to 38 separate stripes in each. About 20 groups were observed between 08:00 UT and 12:30 UT (Melnik et al., 2008).

Unlike the meter and decimeter zebra structure which is mainly periodical in frequency, the decameter zebra structure is periodical in time. The drift rates of these zebra stripes may have either negative or positive signs. Some stripes may have drift rates of both signs simultaneously. The most remarkable case of a decameter zebra structure is shown in Fig. 7.28. Nearly simultaneously with the onset of the Type IV burst, a partial halo CME was observed by SOHO/LASCO coronagraphs (Fig. 7.30b). The CME moved with a velocity of about 900 kms^{-1} presumably toward the Earth. It was most likely associated with the processes in the active region NOAA 10 652 (Fig. 7.30a), in particular, with flares at 07:00 UT and 08:00 UT, recorded by the GOES spacecraft in X-rays (see Fig. 7.30c). The CME moving through the coronal plasma and interacting with the high coronal loops that connect the active regions NOAA 10 652 and NOAA 10 653, appeared to be the source of the Type IV burst.

The data of available optical measurements did not provide definite information about the formation of the loop or trap configurations, which are necessary to form the nonequilibrium velocity distribution of electrons perpendicular to the magnetic field. However, it is quite possible that such loops existed in the upper corona and that in one of the loop conditions were established that are suitable for the DPR instability. The mere presence of the ZP on the decameter

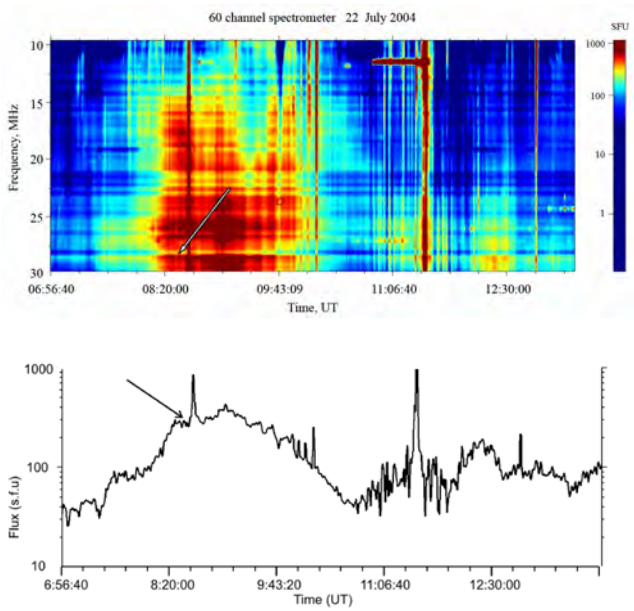


Figure 7.29: *Dynamic spectrum of the Type IV burst on July 22, 2004, (top) and its time profile at 30 MHz (bottom). The time corresponding to the discussed ZP is marked with arrows.*

dynamic spectrum unambiguously testifies the presence of the trap configuration in the source of the observed burst.

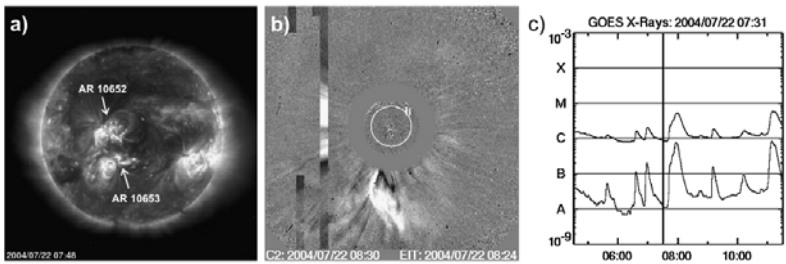


Figure 7.30: *Active regions in UV light observed by SOHO/EIT 191 (a), CME observed by SOHO/LASCO C2 (b), and X-ray flares observed by GOES (c).*

Theoretical explanation of "fingerprint" fine structure

As mentioned above, the 'fingerprint' fine structure discussed here does not look like a typical ZP slowly drifting in time and consisting of a number (sometimes several tens) of stripes of enhanced intensity at a given time. Nonetheless, it can be assumed that the bright stripes in Fig. 7.28 emerging in the DPR regions correspond to separate harmonics of the cyclotron frequency. These harmonics have the form of almost vertical arcs, shown by the dashed lines in Fig. 7.28. Here in that part of the event at about 08:32:00 UT, when the frequencies of the zebra stripes reached their minima, the spectrum resembled the usual ZP; the stripes had a mild positive frequency drift. However, the zebra stripe frequencies eventually started to increase sharply (fast positive drift, and its velocity grew with time), and simultaneously there appeared a low-frequency branch of the stripe with negative frequency drift, where the velocity also grew with time. At first glance, these two branches were not related to each other, but later they joined at a point with an infinitely large frequency drift. This means that they cannot be independent. Thus, an essential feature of the dynamic spectrum shown in Fig. 7.28 is the fast frequency drift of the zebra stripes and the reversal of the frequency drift within

the same harmonic. At each harmonic, there were two frequencies of enhanced radiation at a given instant of time. In Fig. 7.28, we consider in detail the portion of the spectrum indicated by a rectangle where the striped character is most clearly visible. Here the enhanced radiation appeared first at frequencies well separated from each other, then these frequencies get closer, and they merge and disappear at the point with infinite frequency drift. The model of the source should explain the different signs of the frequency drift.

We assume, however, that the electron number density changes with height in such a way that its gradient changes in a wide range from rather large values in the upper layers to smaller values in the lower layers. The assumed variations of the plasma frequency with height (coinciding with the electron number density in the source) are given in Fig. 7.31 (dashed lines).

Let's assume that at some time the radiating harmonics (with harmonic numbers $s-1$, s, and $s+1$) intersect the plasma frequency distribution only in the lower frequency part (Fig. 7.31a). Then three points will appear in the corresponding dynamic spectrum (Fig. 7.31d). When the magnetic field decreases with time, that is, three lines displaying harmonics move down in altitude (Fig. 7.31b), the DPR points will shift to higher frequencies and the usual ZP spectrum is formed with the weak positive frequency drift (as follows from Fig. 7.31a, here the ratio of the density gradient L_n and the ratio of the magnetic field gradient L_B is $L_n > L_B$). When the magnetic field proceeds to decrease and the DPR points shift to even higher frequencies, than the gradient of the electron number density increases, and so does the velocity of the frequency drift. The most important property of the model is that with further decrease of the magnetic field, the harmonics start to intersect the line $f_p(h)$ at two points; see in this context the moment t_2 (Fig. 7.31b).

Thus, there are always two points determining the zebra stripe within the same harmonic. In addition, in the high-frequency part of the zebra stripe the ratio of the gradients is opposite to that in the low-frequency part, that is, $L_n < L_B$. This means that the DPR frequencies decrease with the further decrease in the magnetic field, which provides the negative frequency drift. Therefore, in the dynamic spectrum the two branches of the harmonics will approach each other (Fig. 7.31e). Evidently, with further decrease in the mag-

netic field (Fig. 7.31c, moment t_3), the frequency separation between the DPR points decreases, the DPR points approach each other, and then the harmonic leaves the intersection region with the line $f_p(h)$, i.e. the harmonic curve no longer contains DPR points and disappears from the dynamic spectrum (Fig. 7.31f).

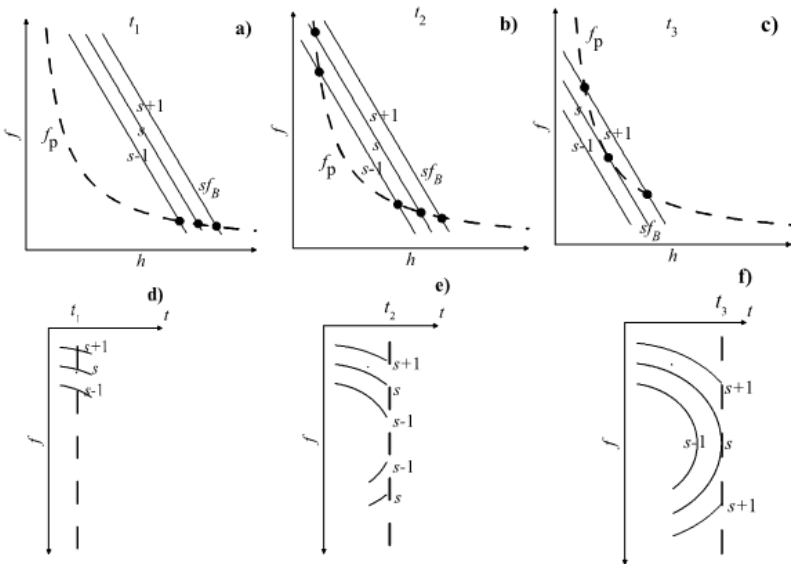


Figure 7.31: *Qualitative interpretation of the fingerprint structure as a set of quasi-vertical arcs. The top panel is the source model at three different times $t_1 < t_2 < t_3$; the electron number density remains constant, and the magnetic field decreases in time. The filled circles denote the DPR levels. The lower panel displays the dynamic spectrum with the zebra stripes corresponding to the times t_1, t_2, t_3.*

At the moment of touching the curves $f_p(h)$ and $sf_B(h)$, the velocity of the frequency drift is infinite. This is just the behavior of the zebra stripes in the observed spectrum in the selected portion of the fingerprint burst. The apparent almost vertical drift of the zebra stripes is due to the very similar values of the gradients of the magnetic field and electron number density. Thus, the quasi-vertical

arc-like ZP structure in the fingerprint event can be explained by the gradual decrease in the magnetic field in the source with electrons that are not in equilibrium in the transverse velocities (perpendicular to the magnetic field), under the condition that the harmonic with a given number has two DPR points at different heights. Herewith, the numbers of harmonics increase from the 'inner' to the 'outer' arcs.

From this argument it follows that the decrease of the magnetic field in time results in the appearance of 'descending' quasi-vertical arcs in the dynamic spectra. It can easily be seen that, if the magnetic field has increased in time, the harmonics would have moved upward, and the event would have developed according to Fig. 7.31 in the direction from (c) to (a) and from (f) to (d). In this case, the ascending arcs (with opposite convexity) would have been present in the dynamic spectrum.

The scheme given in Fig. 7.31 qualitatively illustrates the idea with which the observed details of the fine structure in the form of quasi-vertical arcs based on the DPR effect can be explained. However, to explain the fingerprint burst shown in Fig. 7.28 and to ensure that such a scheme can be realized under coronal conditions, it is necessary to propose a source model that can provide the observed numerical values of the zebra stripe frequencies and the velocities of the frequency drift under realistic conditions of the solar corona.

Discussion

Using the Newkirk model for the plasma density profile (Newkirk, 1961)

$$N = 4.2 \cdot 10^4 \cdot 10^{4.32 R_S/R}$$

and a model for the magnetic field

$$B = B_0(t)/(1 + h/7.95)^3,$$

a system of the cyclotron harmonics $s = 20 - 30$ can satisfactorily describe the observational situation (Fig. 7.32, upper panel). Moreover, assuming that the coronal density is constant in time then the magnetic field should decrease in time by 3% per second to meet the observational results with the model results (Fig. 7.32, lower panel).

A simultaneous change in the magnetic field over the entire height of the source implies that the observed zebra stripes as quasi-vertical arcs cannot be associated with any perturbation propagating along the loop in the corona. This is most likely due to some process involving the whole loop. The best candidate for such a process are nonlinear fast magneto-acoustic (FMA) oscillations of the magnetic flux tube, which are accompanied by compression and depression of the magnetic field. This idea is developed below.

As shown in Fig. 7.28 (bottom), the fingerprint burst discussed above was not a single event; there were at least three identical bursts that form a quasi-periodical sequence with a period of about 60 s. The close connection of the spectral parameters of three bright elements in Fig. 7.28 (bottom) (frequency band, stripe spacing, and frequency drift rate) implies that these bursts originated from the same source and were generated by the same process. According to the model, these elements are associated with the decrease in the magnetic field, and the magnitudes of the magnetic field should be approximately the same. Obviously, to start the decrease from the same values as in the previous element, the magnetic field needs to resume its initial magnitude.

In the dynamic spectrum such a process could result in the 'ascending' arcs with opposite curvature between the observed 'descending' arcs. But the spectrum under consideration only shows 'descending' arcs: when the magnetic field increases, the DPR instability weakens or disappears, and when the magnetic field decreases, the DPR instability is revived again. This effect can be understood under the assumption that it is due to the fast magneto-acoustic (FMA) oscillations of the magnetic flux tube.

FMA oscillations result in the periodic compression and depression of the magnetic field in the magnetic flux tube containing the source of the fingerprint burst as sort of a magnetic trap. When the tube is compressed, the mirror ratio decreases in the source, which results in a partial particle precipitation from the trap. In steps of the tube depression, the magnetic field in the source decreases, the local mirror ratio increases, and the fast electron number density increases again, leading to a revival of the generation process. We note that the weak 'ascending' arcs can be distinguished in Fig. 7.28 (bottom) at times before the appearance of the bright 'descending' stripes (at

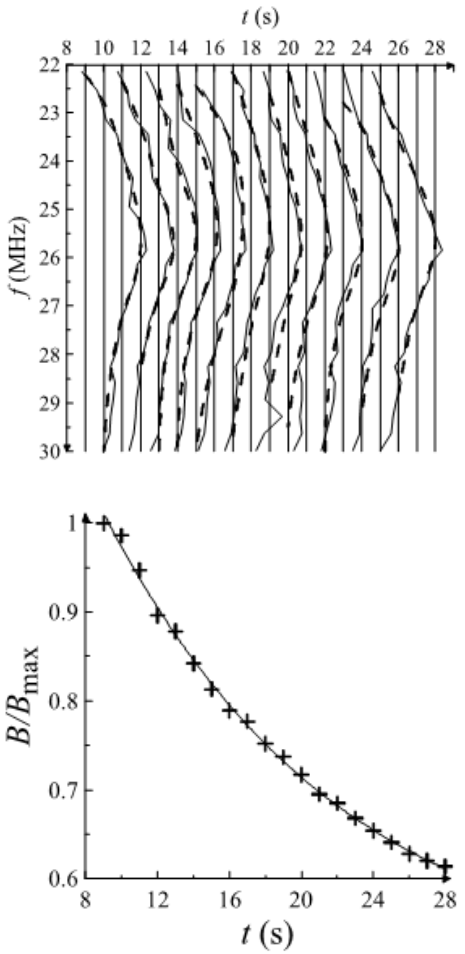


Figure 7.32: *Comparison of the observed spectrum (solid lines) (Fig. 7.28, beginning at 08:32:00 UT) with a calculated smoothed spectrum (dashed lines, upper panel) and the necessary magnetic field decrease in time explaining the observed spectrum.*

08:30:28 UT, 08:31:40 UT, 08:32:30 UT). This is also consistent with the assumption that FMA oscillations are the reason for the magnetic field change in the fingerprint source. Numerical estimations also confirm this idea. The period of the FMA oscillations is determined by the relation (Stepanov et al., 2012)

$$T = \frac{2.5r}{v_A}, \tag{7.4}$$

where r is the radius of the magnetic flux tube cross-section and v_A is the Alfvén velocity

$$v_A = \frac{B}{\sqrt{\mu_0 m_i n}} = c\frac{f_B}{f_p}\sqrt{\frac{m}{m_i}} \tag{7.5}$$

(m_i is the ion mass, n is number density). Since the Alfvén velocity only depends on the ratio f_B/f_p, in the DPR regions where $f_B/f_p = 1$, it remains constant and only depends on the harmonic number s:

$$v_A = \frac{c}{s}\sqrt{\frac{m}{m_i}}.$$

For the selected set of harmonics $s = 20 - 30$, the Alfvén velocity takes quite reasonable values $v_A \approx (2.3 - 3.5) \cdot 10^7$ cm/s. The oscillation period

$$T \approx \frac{2.5r}{c}s\sqrt{\frac{m_i}{m}}$$

for $s = 20 - 30$ is consistent with the observed value $T \approx 60$ s if the tube radius is $r \approx (5 - 8) \cdot 10^8$ cm, which does not contradict the known data about the coronal magnetic loop cross-section. The nonlinear character of the oscillations easily permits a significant change in the magnetic field strength with time, which is necessary to explain the fingerprint spectrum within the framework of the proposed interpretation. It should be noted that the FMA oscillations contain not only a change in the magnetic field, but also a change in the electron number density. However, the relative change in the electron number density can be neglected for low values of the plasma parameter β.

Summarizing, the presented model of the source is able to explain the details of the unusual frequency drift of the stripes of enhanced

intensity in the observed fingerprint spectrum within the framework of the DPR mechanism under quite reasonable physical conditions in the coronal magnetic trap. The necessary properties of the source model are, first, the close relationship of the gradients of the magnetic field and the electron number density (to provide few zebra stripes at a given moment), and second, the opposite signs of these gradients at the upper and lower parts of the source (to provide different signs of the frequency drift in the high- and low-frequency parts of the spectrum). Of course, the selected harmonic numbers, the proposed form of the electron number density distribution, and the height variations in the magnetic field cannot unambiguously be found from the observed spectral features. However, as shown above, the proposed model provides a quite good quantitative match of the observed and predicted model parameters of the fingerprint burst, and it provides reliable estimates of the physical conditions in the burst source.

7.4.1 Sub-bursts in emission and absorption

Solar Type IV bursts (Boischot, 1958; Stuart, 1985) are continuous radio emissions observed in the wide frequency range from 1 MHz to 500 MHz. They last from half an hour at high frequencies up to some hours at low frequencies. This type of radio emission is thought to be the result of the interaction of shocks with magnetic structures in the solar corona. Observations of such bursts at frequencies 10 MHz - 30 MHz were reported by Melnik et al. (2008). One of the main properties of these bursts is the existence of fine structure in the form of fiber bursts in every Type IV burst (Melnik et al., 2008; Chernov et al., 2007a). These bursts are observed both in emission and absorption. Fiber bursts have both forward (from high to low frequencies) and reverse frequency drift rates. The interesting peculiarity of them is the closeness of their parameters such as drift rates and durations to those of usual Type III bursts in the decameter range (Suzuki and Dulk, 1985). In the following the properties of Type IV fine structure observed in July 2002 during the passage of the active region N249 over the solar disk are presented.

Observations and results

Observations have been carried out with the radio telescope UTR-2 (Kharkiv, Ukraine) connected to the 60-channel radio spectrometer with a frequency and time resolution of 300 kHz and 100 ms, respectively. Type IV bursts were observed from July 11 through 17, 2002. The dynamic spectrum of one of these bursts is shown in Fig. 7.33.

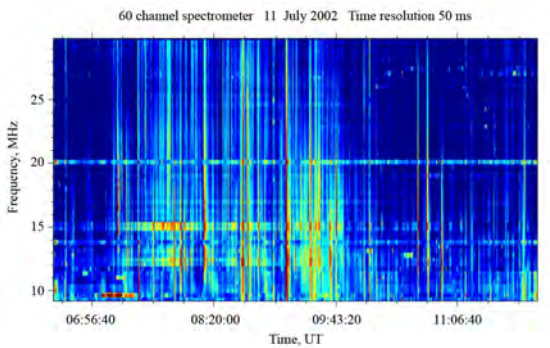


Figure 7.33: *Type IV burst observed on July 11, 2002, starting at about 07:00:00 UT and ending at about 10:00:00 UT.*

This event continued for only about 3 hours. The fine structure of this burst consists of a lot of fibers, following each other during all over this Type IV burst (Fig. 7.34). Fiber bursts in emission exceed the background of Type IV radio emission in intensity by a factor of 10 to 100. Since the number of such bursts is huge, statistically only about 200 bursts per day have been analyzed (in total more than 1200 fiber bursts for the period July 11 - 17, 2002). In addition, fibers in absorption were processed whose fluxes were significantly lower than the background level. Only those bursts with fluxes 7-10 times smaller than the background level have been considered and about 100 such bursts in absorption during this 7 day-period have been found.

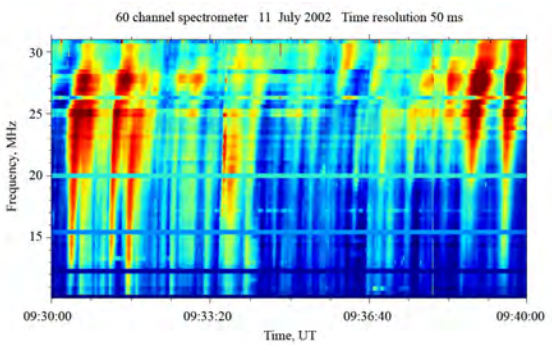


Figure 7.34: *A fragment of Type IV bursts. The train of fiber bursts in emission (red), succeeded by fibers in absorption (black).*

Frequency drift rates

One of the important parameters of bursts is the frequency drift rate. The drift rates of bursts both in emission and absorption are apparently comparable and changed from 1 MHz/s to 3 - 4 MHz/s, with higher drift rates at higher frequencies. Histograms of frequency drift rate may have two maxima at different frequencies, indicating that there are possibly two populations of electron beams, which generate these bursts. The dependences of drift rates on frequency are shown in Fig. 7.35. They are similar to those for usual Type III bursts, but not as steep. This may reflect the fact that the plasma, through which the fast electrons are moving, is more homogeneous compared to an average corona. The presence of bursts with positive and negative drift rates means that the corresponding electron beams propagate towards and away from the Sun, supposing the generation of radio emission by the plasma mechanism. Also bursts in absorption with positive and infinitive drift rates have been observed, but the data were insufficient for any statistical processing.

Duration of fiber bursts

The durations for both fiber bursts in emission and in absorption are remarkably constant for frequencies in the range from 10 MHz to

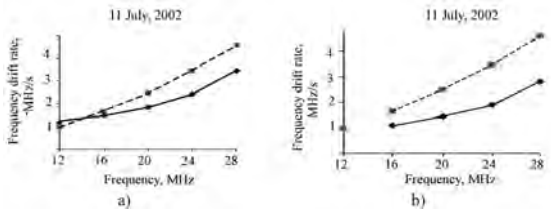


Figure 7.35: *Dependences of drift rates on frequency for fiber bursts in emission with forward (a) and reverse (b) drift rates. (Continuous line indicates observations, dashed line the Alvarez-Haddock dependence.)*

30 MHz (Fig. 7.36). But if bursts in emission have a duration of, e.g., about 6 s, the duration of bursts in absorption is longer, up to 20 s - 23 s. These values are close to those found for usual Type III bursts, but the latter exhibit a duration as a function of frequency. This means that, e.g., electron beams, which are responsible for fiber bursts, do not change their spatial sizes in the course of propagation through the plasma. The durations of fiber bursts in emission do not depend on the position of the corresponding active regions on the solar disk. However, such dependence is existing for bursts in absorption (Fig. 7.37).

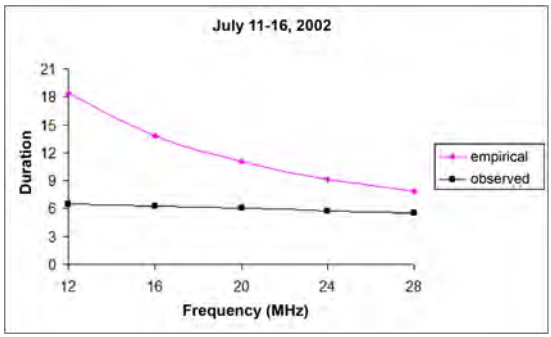


Figure 7.36: *Duration on frequency dependence (black line is observational data and pink line is 220/f dependence).*

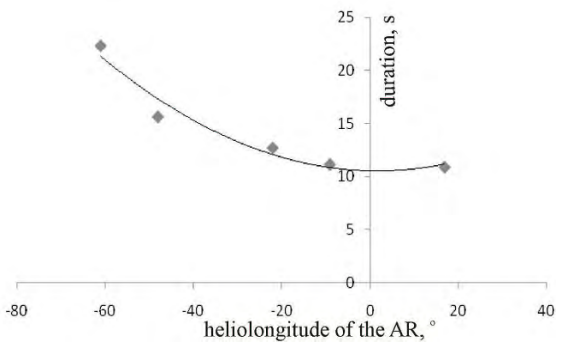


Figure 7.37: *Duration for fiber bursts in absorption in dependence on the position of active region on the Sun.*

Radio emission fluxes

The distributions of bursts on flux (approximately from 10 - 20 s.f.u. to 100 s.f.u.) is decreasing, the average flux is about 40 s.f.u. (Fig. 7.38) for all days of observations. This average value does not depend on frequency. From this we conclude that the electron beams, generated at the interaction of shocks and magnetic structures, may have approximately the same densities for all Type IV bursts. In the case of bursts in absorption, the physical quantity that characterizes these bursts is the ratio of the flux at absorption minimum to the background flux. We found no dependence of this ratio on frequency. We assume that the cause of bursts in absorption are fast electron beams, too. They may have such velocity distribution, which is suitable for the absorption of increased background Langmuir turbulence that manifest themselves. However, it is surprising that the parameters of these electron beams are approximately the same for all Type IV bursts.

7.5 Oscillations of Type IV bursts

Magnetohydrodynamic (MHD) waves and oscillations are ubiquitous in the solar corona (Nakariakov and Verwichte, 2005). The waves

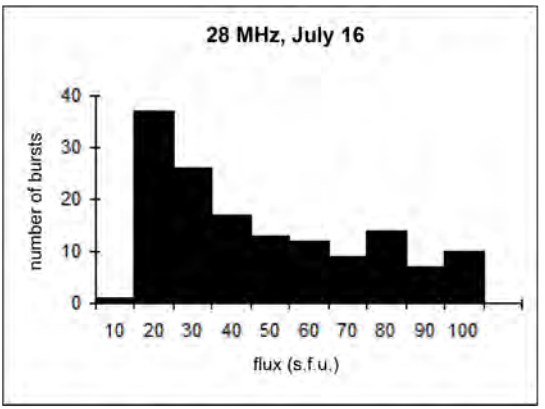


Figure 7.38: *Distribution of bursts on flux at frequency 28 MHz on 16 July, 2002.*

may heat the ambient plasma and accelerate solar wind particles (Aschwanden, 2004). Observations indicate the existence of almost all MHD modes (fast kink, fast sausage and slow magneto-acoustic waves) in the solar corona (Aschwanden et al., 1999; Nakariakov et al., 1999; Ofman et al., 1999; Nakariakov et al., 2003; Wang et al., 2003a,b; Wang and Solanki, 2004; Srivastava et al., 2008; Pascoe et al., 2009). Oscillations are mainly observed by imaging observations, but their spectroscopical indications are also possible. For example, purely incompressible torsional oscillation can be observed in coronal loops as periodic variation of spectral line broadening (Zaqarashvili, 2003). The observed MHD oscillations can be used to estimate plasma parameters in the solar corona using the known theoretical properties of MHD waves (Roberts et al., 1984). This method, the so-called coronal seismology (Nakariakov and Ofman, 2001), was effectively used to determine the magnetic field strength, stratification and other plasma properties and peculiarities of coronal loops (Arregui et al., 2007; Van Doorsselaere et al., 2007; McEwan et al., 2008; Andries et al., 2009; Verth et al., 2010; Arregui and Asensio Ramos, 2011), spicules (Zaqarashvili et al., 2007; Zaqarashvili and Murawski, 2007; Zaqarashvili and Erdélyi, 2009; Verth et al., 2011)

and prominences (Arregui et al., 2012, and references therein). The oscillations are mainly observed in the inner corona, where the intensity of EUV lines enables the detection of active region coronal loops. In the outer corona, the oscillations are not yet detected because of EUV line intensity decreases with altitude. Besides the EUV part of the spectrum, the solar corona can be observed in the radio frequency band, which is very useful to study the rapid oscillations of the solar atmosphere. High-frequency oscillations (< 1 min) are frequently detected in the radio observations (Aschwanden et al., 2004). According to Aschwanden et al. (2004) most of the reported oscillations fall in the frequency range of 100 MHz - 1000 MHz corresponding to the electron densities of $10^8 - 10^{10}\mathrm{cm}^{-3}$. Therefore, the radio emission originates from the inner corona and consequently the oscillations can be interpreted as fast sausage modes in short low-laying coronal loops (Nakariakov et al., 2003; Aschwanden et al., 2004; Pascoe et al., 2009). Long period modulation (5 min - 10 min) in the microwave range of > 1 GHz can be explained by the kink oscillations of coronal loops (Khodachenko et al., 2011). Recent high-resolution data obtained with the Nobeyama Radioheliograph show a frequency drift of 3-min oscillations, which can be explained by the dispersive evolution of upward propagating wave pulses (Sych et al., 2012).

Hence, radio observations are very important to study the plasma properties in the inner corona. On the other hand, radio observations in the frequency range of 10 MHz - 100 MHz are very useful to obtain information on the physics in the outer corona. Flare related activity at decameter wavelengths is manifested in a great variety of bursts: Type II-IV bursts, drifting pairs, S-bursts, spikes bursts in absorption etc. Some of them are continuations of the same bursts from decimeter and meter bands, such as Type III-, Type II-, Type IV-bursts, and spikes. There are some bursts, which are observed only in the long meter and decameter range, namely Type IIIb bursts, drifting pairs, S-bursts.

The plasma mechanism of radio emission generation is usually used for the explanation of these bursts (Ginzburg and Zhelezniakov, 1958). This mechanism has two stages. The first stage is the generation of Langmuir waves by fast electrons and the second stage is the emission of electromagnetic waves by these Langmuir waves. In this mechanism, the frequency of radio emission equals the local plasma

frequency or double local plasma frequency. Then the radio emission at a given frequency is originated in the plasma at a corresponding height above the solar surface.

In the following we focus on the decameter band (8 MHz - 32 MHz), therefore the radio emission at these frequencies is generated at heights $\geq 1R_S$ (R_S is the solar radius) above the solar surface depending on the density structure of the solar corona. Type IV bursts at decameter wavelength were first observed by the UTR-2 radio telescope during the observational campaign in 2002 - 2004 (Melnik et al., 2008). The duration of the bursts comprises 1.5 hours up to several hours and fluxes were $10 - 10^3$ s.f.u. Decameter Type IV bursts were usually accompanied by coronal mass ejections (CMEs), but sometimes there was no visible CME during the Type IV burst observation. Specific features of decameter Type IV bursts were fine structures in the form of fiber-bursts and oscillations of radio emission intensity. The longest periods of these oscillations were tens of minutes. It is suggested that the radio emission of Type IV bursts originates either in a coronal loop disturbed by the CME or in the "body" of the CME itself. Hence, the observed oscillations can be connected either with oscillations of the CME or the coronal loops. Oscillation in the intensity of Type IV bursts without any accompanied CME is probably connected to the coronal loop oscillations triggered by a solar flare. Then, the analysis of these oscillations allows to estimate the plasma properties in the coronal loops. Among decameter bursts there are also so-called inverted U- and J- bursts generated by fast electron beams, which propagate in high coronal loops (Dorovsky et al., 2010). Active region coronal loops may expand up to helmet streamers in the solar wind. Very long transequatorial loops, which connect the active regions in opposite hemispheres, may reach up to the height of one solar radius. Chase et al. (1976) presented the first observational indication of transequatorial loops. Later, Pevtsov (2000) presented 87 transequatorial loops by the analysis of Yohkoh satellite data between October 1991 and December 1998. The radio emission at 10 MHz - 30 MHz is originating from those heights, where transequatorial and/or active region loops are located. Consequently, the long-period modulation of emission intensity at these frequencies can be caused by the oscillations of these loops. In the following the observation of Type IV radio bursts from the large Ukrainian URAN-

2 radio telescope will be used for the seismological estimation of the magnetic field strength and other plasma parameters of coronal loops at heights of $\geq 0.2 R_S$.

7.5.1 Quasi-periodic variations of radio emission

During the time interval of 09:50 - 12:30 UT in April 14, 2011, a Type IV radio burst was detected and observed in the frequency range of $\sim$ 12 MHz - 32 MHz with the spectral resolution of 4 kHz and 100 ms by the radio telescope URAN-2 (Fig. 7.39). The polarization was high with about 40 % - 50 %. This radio burst was probably connected to a small C2.3 flare, which occurred in the active region AR 11190 (Fig.7.40). The flare started at 09:38 UT, reached the maximum phase at 09:44 UT and ended at 09:49 UT.

The dynamic spectrum of radio emission (Fig. 7.39) demonstrates that the variation of emission intensity has sort of a quasi-periodic behavior in time at all frequencies, which indicates that the physical parameters of the solar corona (density of energetic electron beams, local plasma density, magnetic field strength and/or direction etc.) undergo quasi-periodic variations. In order to understand the reason of the variations, one needs to estimate statistically significant periods in the time series.

Wavelet analysis was performed to study the temporal variation of emission intensity at different frequencies. Fig. 7.42 shows the wavelet spectrum of emission intensity during the interval 09:00 - 13:00 UT at four different frequencies, namely at 29 MHz, 25 MHz, 22 MHz and 14 MHz. It can be seen that mainly two periods, 23 and 34 min, were derived (Table (7.1)).

Quasi-periodic variations in the radio emission intensity can be caused by several physical processes. Energetic electron beams generated during the solar flare may excite Langmuir oscillations in the coronal loops, which then may emit the radio emission at the observed frequencies as Type IV burst. The variation of electron beam density may influence the amplitude of Langmuir oscillations and, in consequence, the intensity of radio emission. This requires the variation of the cross section of the coronal loop where the electron beam propagates. Therefore, the oscillation of magnetic tube cross section may lead to a quasi-periodic variation of beam density and conse-

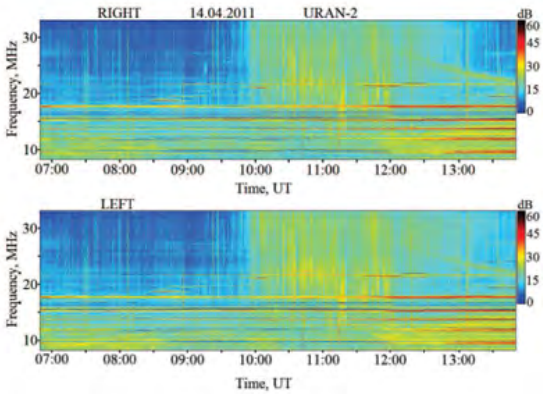


Figure 7.39: *Dynamic spectrum of radio emission (right- and left-hand polarization) observed by URAN-2 on April 14, 2011.*

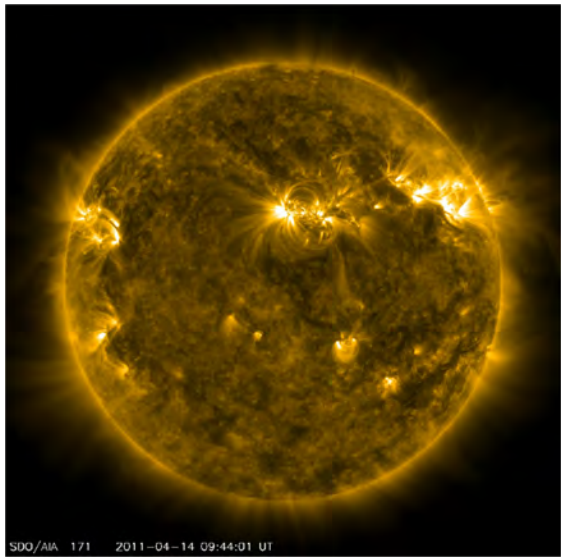


Figure 7.40: *Solar corona as seen in the 171 Å line at 09:44:01 UT in April 14, 2011, obtained by AIA/SDO.*

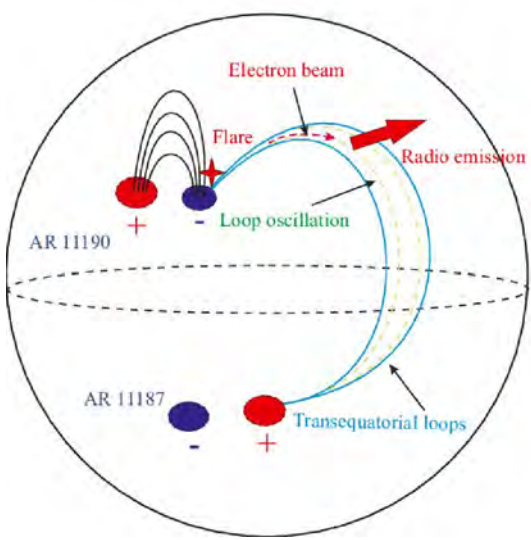


Figure 7.41: *Schematic picture of radio emission from a transequatorial coronal loop after a solar flare.*

quently to the variation of emission intensity. Any periodic variation of the angle between the magnetic field direction and the line of sight may also lead to the observed oscillation. Therefore, the transverse oscillation of the coronal loop can also be considered as a possible mechanism for the observed quasi-periodic variations.

A small C2.3 flare, which probably triggered the Type IV radio burst, occurred in AR11190. Fig. 7.40 shows the magnetogram of the solar disc at the photospheric level during the observed event, obtained by the Helioseismic and Magnetic Imager (HMI) (Schou et al., 2011) on board of Solar Dynamics Observatory (SDO) (Pesnell et al., 2012). The active region AR11190 is located at the central part of the northern hemisphere, while the active region AR 11187 is located just opposite in the southern hemisphere. Therefore, the two active regions could be connected by a transequatorial loop system. Transequatorial loops may connect two other active regions of the northern and southern hemispheres, namely AR 11186 and AR 11188. The distance between AR11190 and AR11187 is about 40°, which is $\approx 4.8 \cdot 10^5$ km, i.e. $0.7 R_S$. On the other hand, the distance between AR11186 and AR11188 is about 50°, which is around $\approx 6 \cdot 10^5$ km i.e. $0.86 R_S$. In the case of semi-circular shape, the transequatorial loops may reach up to $0.35 R_S$ in the first case and $0.43 R_S$ in the second combination of active regions. In the case of sheared magnetic arcade, the transequatorial loops may expand even much higher up to the observed heights.

The solar flare in AR11190 may excite energetic electron beams along transequatorial loops, which may trigger the Langmuir oscillations producing the observed radio emission. The solar flare may also trigger the MHD oscillations of transequatorial loops, which modulate the electron beams density leading to the observed quasi-periodicity in radio intensity.

The observed oscillation periods can be used to estimate the plasma parameters of the outer solar corona applying a theoretical oscillation spectrum of MHD waves in coronal loops. Corresponding analytical dispersion relations for MHD waves for straight homogeneous magnetic tubes was developed by Edwin and Roberts (1983).

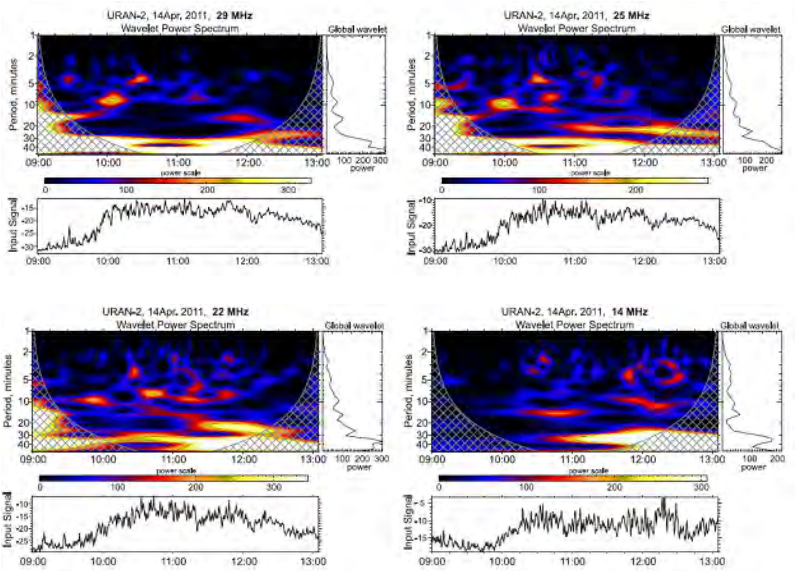


Figure 7.42: *Morlet wavelet power spectrum of emission intensity at 29 MHz (upper left panel), 25 MHz (upper right panel), 22 MHz (lower left panel) and 14 MHz (lower right panel) frequencies during 09:00 - 13:00 UT. Chrisscrossed areas outside the cone of influence (COI) indicate the regions where wavelet transform is not reliable.*

Table 7.1: *Oscillation periods at different frequencies of radio emission obtained by wavelet analysis*

29 MHz	25 MHz	22 MHz	14 MHz
47 min	40 min	-	-
33.5 min	34 min	31.5 min	34.6 min
-	23.4 min	23 min	-

We suppose that a transequatorial coronal loop (Fig. 7.41) is the source of Type IV bursts. The plasma density within the loop is assumed to be distributed according the Boltzmann law with a temperature of 1 MK with the bottom density three times larger than the Baumbach-Allen density outside the loop at the same height.

Since slow magneto-acoustic waves are probably not relevant for the interpretation of our observations, a zero plasma-β approximation was implemented taking into account small amplitude perturbations (Zaqarashvili et al., 2013). Using a Cartesian coordinate system (x, z), therefore the considered magnetic structure is rather a slab than a loop. A cylindrical magnetic tube makes the oscillation spectrum more comprehensive, but the slab model is also a good approximation. The equation governing the linear perturbations in the system can be written after Fourier analysis with $\exp(-i\omega t)$ as

$$\frac{\partial^2 u_x}{\partial x^2} + \frac{\partial^2 u_x}{\partial z^2} + \frac{\omega^2}{v_A^2} u_x = 0, \tag{7.6}$$

where u_x is the velocity perturbation, v_A is the Alfvén speed (Eq. (7.5)), and ω is the wave frequency. Eq. (7.6) accompanied by appropriate boundary conditions, represents a classical boundary value problem. We consider a straight dense coronal loop that is embedded in a rarified plasma. The low plasma-β condition in the solar corona implies that the enhanced hydrodynamic pressure due to the dense and hot plasma inside the coronal loop can easily be compensated by a very small difference in the magnetic field strength inside and outside the loop. Detailed analysis shows that kink modes of the first and the second harmonics correspond to periods 23 and 34 min. This leads to an Alfvén speed of $\approx$ 1000 km/s, in consequence with a plasma density of $4 \cdot 10^6 \mathrm{cm}^{-3}$ to a magnetic field of 0.9 G.

Summarizing, the Type IV radio burst, observed by the URAN-2 radio telescope on April 14, 2011, can be used as sort of a radio seismology of the outer solar corona ($\geq 0.2R_S$). Wavelet analysis at four different frequencies (29 MHz, 25 MHz, 22 MHz, and 14 MHz) shows the periodicity of 34 min and 23 min in the emission intensity. The periodicity may be caused by the first and second harmonics of vertical kink oscillations of a transequatorial loop system, which connects the active regions from Northern and Southern hemispheres. Using the theoretical properties of kink oscillations in longitudinally inhomogeneous coronal loops, an Alfvén speed inside the loop at the height of $1R_S$ was derived as ≈ 1000 km/s. The coronal loop seems to be thin (with width to length ratio of 0.1), longitudinally weakly inhomogeneous and dense ($\rho_0/\rho_e \geq 20$). An estimated magnetic field strength of the loop at the height of $1\,R_S$ above the solar surface yields 0.9 G. An extrapolation of this value leads to a magnetic field strength at the height of $0.1R_S$ as 10 G, which is in agreement with the estimation of Nakariakov and Ofman (2001).

7.6 Absorption bursts

Bursts are considered to be a signficant characteristic of solar activity because they are generally attributed to a sudden acceleration of particles from the Sun (Zheleznyakov and Zaitsev, 1970). Radio observations provide important information concerning physical conditions in the solar corona. Among the vast variety of solar bursts, some of them were detected as absorption events.

Absorption features visualized in solar radio spectra were first noted by Boischot et al. (1959) on the basis of single-frequency records. Wild et al. (1963) also mentioned the solar radio bursts in absorption. Slottje (1972) paid attention to sudden reductions in the intensity of Type IV radiation at frequencies of about 250 MHz. Kai (1973) described the Type II event of August 23 - 24, 1968, in which an absorption U-fold burst was visible at 80 MHz - 120 MHz. There is also a report on an enhancement and following decay of Type III emission (MacDowall, 1989). Aurass et al. (1993) noticed a Type II burst in absorption.

In the spectrum of the Type IV/II radio burst of July 18, 1994,

Klassen (1996) found a signature for a rare superposition of two counter-directed electron beams propagating into the surrounding open- and closed-field regions (cusp). They resulted in a reverse drifting absorption Type III burst appearing together with the negatively drifting emission Type III burst. Interesting observations of absorption bursts were represented by Sastry et al. (1983) at 34.15 MHz - 34.5 MHz. Their significant difference from the aforementioned observations is that they were not confined to any particular type of bursts such as Type IV or Type II. Gopalswamy et al. (1983) interpreted the reduction as the absorption of decameter radio continuum by a shock-generated ion-sound turbulence. The results of Ramesh and Ebenezer (2001) support a close temporal association between the absorption events and the corresponding flares accompanied by the onset of a "halo" coronal mass ejection (CME). Observations of decametric Type II bursts, recorded by the radio telescope UTR-2, show that such bursts in general keep the main ordinary properties well-known in other frequency ranges: slow frequency drift (<0.1 MHz/s at 10 MHz - 30 MHz), narrow simultaneous frequency band of radio emission (2 MHz - 3 MHz), herringbone structure, cloudy structure, band-splitting (3 MHz - 5 MHz), fundamental and harmonic radio emissions, high intensity of radio emission (10 - 1000 s.f.u.). Sometimes in the high corona the continuum radiation (Type IV), called FCII (flare continuum Type II), follows during or just after the Type II bursts (Leblanc et al., 2000). Their brightness temperature is approximately constant with frequency.

How can the absorption bursts be interpreted? Melrose (1974b,a) conjectured that the absorption is an inverse process of familiar plasma emission processes, for example, scattering of emission at ion-sound waves generated by electron beams. However, this approach has a number of difficulties, which are discussed by Melrose (1974b,a). Alternatively, other processes can be invoked to explain the appearance of an absorption drift burst. Zaitsev and Stepanov (1975), as well as Benz and Kuijpers (1976), considered the absorption bursts as a result of hot electrons being injected into the traps, which fill the loss cone and quench the instability.

Therefore, many studies have addressed this issue from both theoretical and experimental point of view, but a full understanding is still lacking. A new broad band observation of an absorption burst

at 9 MHz - 30 MHz is discussed in the following. Recall that the plasma levels of 30 and 10 MHz correspond to radial distances of 1.78 and 2.94 solar radii (according to the density model by Mann et al., 1999), respectively, from the center of the Sun. The radio data reported here were obtained on August 19, 2003, with the 60-channel spectrometer operating at the UTR-2 radio observatory near Grakovo (Braude et al. (1978), and from the Nançay Decameter Array (NDA) in the range 20 MHz – 70 MHz, as well as from the Wind WAVES instrument in the range 1 MHz to 13.8 MHz.

7.6.1 Observations and their analysis

On this day (August 19, 2003) the solar activity was moderate with two M-class flares from the Active Region 10431 (S13, L = 194). The GOES X-Ray Catalog (*http : //vso.nascom.nasa.gov/cgi − bin/catalog.pl*) indicates that one was impulsive (M21n) at 07:38 UT (S12W63) and the other (M2.7/2f) started at 09:45 UT (S10W57). Also, at 08:46 UT and 09:06 UT two C-class flares were observed. According to the CME catalog[1], at least six CMEs were registered on August 19, 2003. The observed times of their appearance are

04:30 UT southwestward, 388 km s^{-1}; ragged front disintegrates somewhat through C2

05:30 UT northwestward, 324 km s^{-1}; faint ragged front fades and disintegrates through C2

08:06 UT northeastward, 116 km s^{-1}

08:30 UT westward, 412 km s^{-1}; initially bright narrow loop front fades and resolves to multiple loops

09:30 UT northeastward, 300 km s^{-1}; ragged front follows extremely slow narrow loops along bright streamer

10:30 UT westward, 468 km s^{-1}; wide bright loop front with cavity and core.

[1] `http://cdaw.gsfc.nasa.gov/CME_list/UNIVERSAL/text_ver/univ2003_08.txt` and `ftp://lasco6.nascom.nasa.gov/pub/lasco/status/LASCO_CME_List_2003$`

Some of these events have radio emission traces in the data records of the telescopes UTR-2, and NDA, and by the WIND/WAVES instrument.

During continuum radiation (Type IV) one more Type II burst occurred with a sudden reduction in intensity at 11:16 - 11:21 UT depending on frequency. The absorption event lasted until 11:26 UT. It has a clear negative frequency drift. The time profiles of the absorption burst are characterized by the trailing edge being steeper than the leading edge.

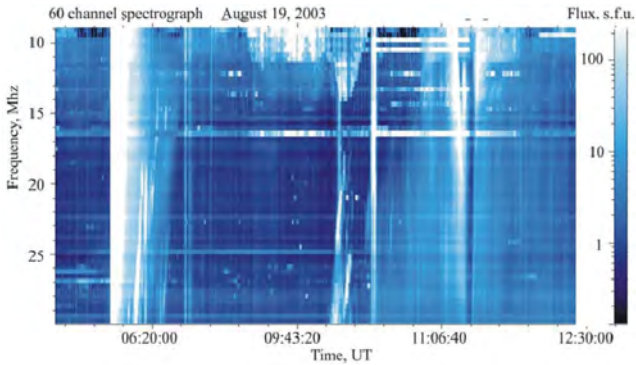


Figure 7.43: *Type IV burst (from 10:25 UT to 12:30 UT) with attendant phenomenon group of Type III- and Type II-bursts.*

The drift rate of the absorption burst was measured as $-0.119 \pm 0.008\,\mathrm{MHz\,s^{-1}}$ at the frequency range 1 MHz - 30 MHz. It is four times higher than the frequency drift rate of the corresponding Type II burst, which was about -0.03 MHz $\mathrm{s^{-1}}$. We see that the absorption structure intersects the underlying radio emission. Possibly, this implies that the absorber moved faster than the shock wave generating the Type II burst. In fact, the absorption feature seems to be superposed on the Type IV continuum, which usually represents rising (CME-associated) structures. From 14 to 9 MHz the frequency drift velocity for the absorption burst of August 19, 2003, distinctly dropped to -(0.02 - 0.03) $\mathrm{MHz\,s^{-1}}$. Against a background of the Type II burst, fine structures visualized in the form of fibers (in emission) with a drift rate nearly equal to -0.03 $\mathrm{MHz\,s^{-1}}$. In the absorption re-

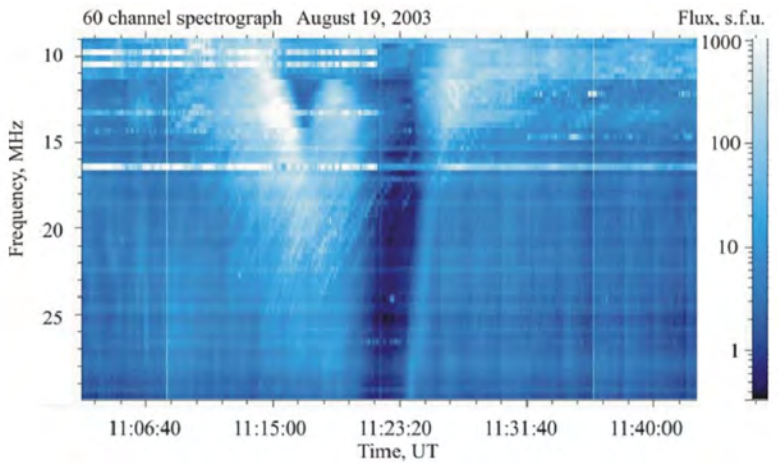


Figure 7.44: *Absorbing area (at low frequencies at 11:17 UT) and burst in absorption superposed on fiber bursts.*

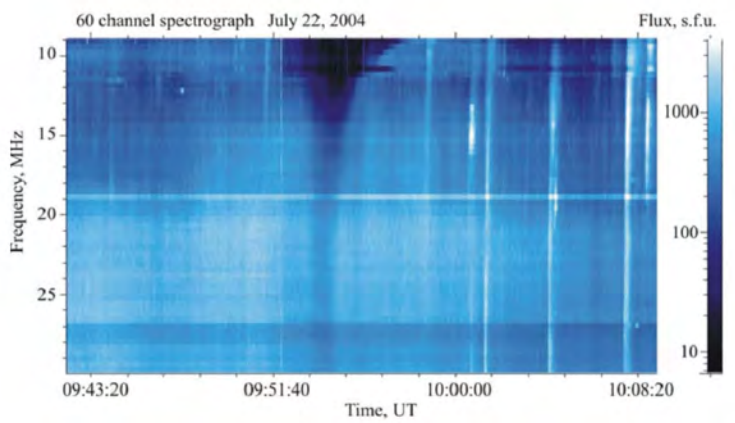


Figure 7.45: *Burst in absorption superposed on continuum radio emission of Type IV burst.*

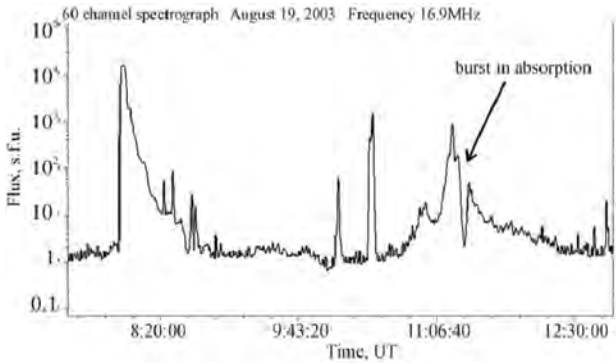


Figure 7.46: *Time profile of solar radio emission on August 19, 2003. The burst in absorption at 11:20 UT is clearly visible.*

gion they disappeared and appeared again on the background of the Type II emission after the absorption stopped. Most likely, they were traces in emission within the Type II burst rather than simply standard herringbones. As noted in the paper by Mel'nik et al. (2004), in the 10 MHz - 30 MHz frequency range the herringbone structure sub-bursts drift with a rate of about 1.5 MHz s^{-1} toward higher frequencies and with a rate of about -0.5 MHz s^{-1} to lower frequencies. Using the density model of Mann et al. (1999) and its interrelation with the velocity of the corresponding radio source (see details in Mel'nik et al. (2004) as an example), the radial velocity of the shock wave as it propagated into the solar corona can be estimated. The radial shock speed was about 640 km s^{-1} and the absorber moved with a velocity of about 2550 km s^{-1}. The absorber velocity is too high for the usual shock waves leading to Type II bursts, but it is extremely low for particle beams responsible for Type III bursts. Although surprising, such a value of the frequency drift occurs for some solar events observed in the decameter range. In particular, the radio event of May 2, 1998, (Chernov, 2004) shows a zebra-pattern structure consisting of numerous fragments of stripes ("main braid") with various frequency drifts. This main braid of fibers forms the low-frequency boundary of all the zebra-pattern fragments. Its frequency drift is about -0.13 MHz s^{-1} near 37 MHz. Assuming that the ra-

dio radiation was emitted near the local plasma frequency leads to a speed of an excitation agent, propagating in the outer layers of the corona, nearly equal to 2200 $\mathrm{km\,s^{-1}}$, whereas the frequency-drift rate of the zebra-pattern fragments were only -0.04 $\mathrm{MHz\,s^{-1}}$ corresponding to a velocity of about 700 $\mathrm{km\,s^{-1}}$. The source of the braid is associated with a shock front and is located in a narrow trap between the front and the leading edge of a CME. The zebra-pattern structure appeared probably because fast particles accelerated in the shock front were captured in this narrow trap.

The duration of the absorption changed with frequency. Between 20 MHz and 30 MHz it is approximately constant with the mean value of about 140 s, but from 20 MHz to 14 - 15 MHz it dropped to ≈ 86 seconds, and then it increased again. The measurement of duration was carried out with respect to a level that was twice as intensive as the absorption burst minimum for each profile. The theoretical analysis of Zaitsev and Stepanov (1975) shows that the duration of absorption bursts increases when the frequency decreases.

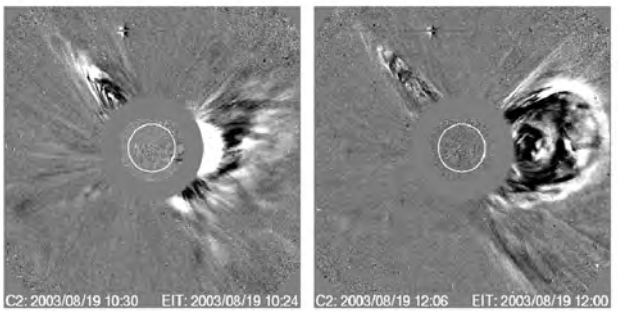


Figure 7.47: *Movement of West CME associated with the Type IV burst on August 19, 2003, according to SOHO data.*

7.6.2 Level of absorption

The maxima of absorption on the time profiles correspond to the most reduction of emission in intensity. How strong was it? We can compare the minimum power of the absorption burst with the

emission power of the quiescent Sun. According to the solar data (available at http://www.sec.noaa.gov from NOAA) on August 18, 2003, the solar activity was at low levels. Therefore, as a record of the quiescent Sun, the pre-flare period of the observation records on August 19 can be taken. Strictly speaking, the received emission contains not only the proper emission of the quiescent Sun, but also the galactic background emission. The ratio between their intensities can be estimated. So we obtain, at the frequency of ≈ 25 MHz, the intensity of the absorption burst at the valley of the absorption as $6.1 \cdot 10^{-20} WHz^{-1}$, with that of the galactic background plus the quiescent-Sun level of $3.5 \cdot 10^{-20} WHz^{-1}$ and a proper galactic background level of $2.7 \cdot 10^{-20} WHz^{-1}$. Then the brightness temperature of the galactic background determines as ≈ 26400 K. During the observation, the Sun was located in the sky region with a low (brightness) temperature of the galactic background. Consistent with Kraus (1966), the galactic background (brightness) temperature is expected to be around 27200 K, which agrees with the previous estimation. The frequency dependence of the minimum power of the absorption burst and the power of the background emission (from the quiescent Sun and the galactic background in sum) is represented in Fig. 7.48. It should be noted that the instrumental facilities at the UTR-2 radio observatory have a sufficiently high dynamical range, and therefore any receiver saturation was unlikely.

Alternatively, absorption processes in the terrestrial ionosphere could be invoked to explain the appearance of the absorption on the background of radio emission from the Sun. Most of the attenuation occurs in the ionospheric D region (50 - 90 km altitude) where the product of the electron density and the electron – neutral collision frequency attains a maximum. Much more significant changes to the electron density, and consequently the absorption strength, arise from solar X-ray flares (classic short-wave fade). However, no strong X-ray flares occurred between 11:00 UT and 12:00 UT on August 19, 2003, (from GOES data). Besides, we have found no reference to any extremely high absorption, owing to ionospheric effects (such as sudden ionospheric disturbances and short-wave fadeouts), during the observation time at 9 MHz - 30 MHz.

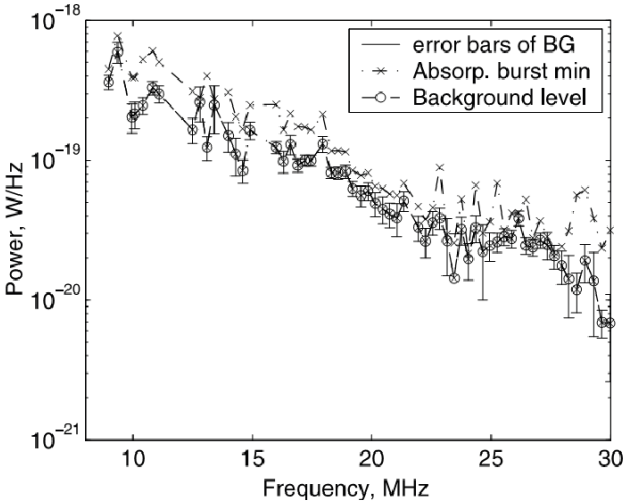


Figure 7.48: *Dependence of the absorption burst minimum and the background (BG) level on frequency. Here the BG level is the sum of emission contributions from the quiescent Sun and the galactic background.*

7.6.3 Size of absorbing region

To observe the almost full absorption, the cross section of the region should be certainly bigger than (or equal to) the source size of the Type II burst at 11:20 UT on August 19, 2003. Although no radio imaging instrument was available for the observations of this event, we can use the empirical dependence of log(size) = 0.76 - 0.86 log(f), given by Leblanc et al. (2000), for calculating the source size of a Type II burst from the burst frequency. In the frequency range 30 - 9 MHz the angular size increases from 0.3° to 0.9°. This enables the determination of the brightness temperature of the Type II burst associated with the absorption. It is approximately constant with frequency and nearly equals $1.5 \cdot 10^9$ K from 9 to 26.6 MHz. However, the simultaneous frequency band of the absorption burst (where it was present at the same time) exceeds 20 MHz. Most likely the longitudinal size of the absorber was more than one solar radius.

The following chain of processes responsible for the event of August 19, 2003, can be suggested: Fig. 7.47 shows "difference" images obtained with the Large Angle Spectroscopic Coronagraph (LASCO) onboard the Solar and Heliospheric Observatory (SOHO) at the appropriate time. As is well known, radiation of Type IV bursts (FCII) involves acceleration of electrons trapped in magnetic arcs, which can be stretched by CMEs. Consequently, the arcs extend to considerable heights in the solar corona. The appropriate CME evolution is shown in Fig. 7.47. Recall that the event was after the GOES M-class flare which started at 9:45 UT. From the height versus time plot in Fig. 7.49 it can be assumed that a piston shock wave propagated in the trace of the CME and that it was this shock wave as the source of the decametric Type II burst associated with absorption. In this case the electrons were accelerated by the Type II shock and became trapped in slowly expanding loops behind the front of the CME. The particles may then be subjected to further acceleration through interaction with magnetic turbulence. The shock wave traversed the loops at different heights. Their structure could have both open and closed magnetic field lines. The absorption burst resulted in the loss-cone instability in the system of "trapped and precipitating particles." The motion of the loops probably causes a negative frequency drift typical for the absorption burst. The CME at 9:30 UT also probably

contributed to the evolution, as the solar atmosphere was already disturbed when the CME at 10:30 UT was launched.

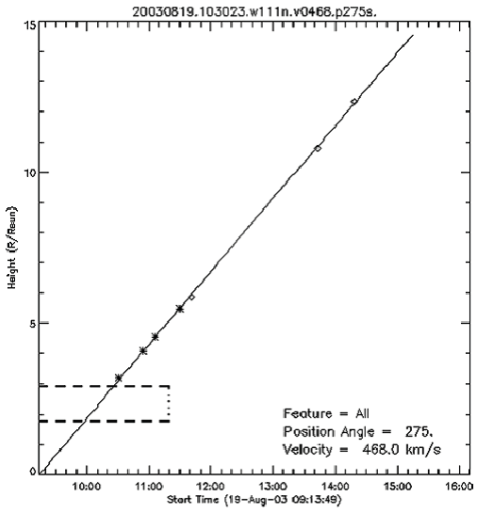


Figure 7.49: *Height versus time plot of the CME as shown in Fig. 7.47. The straight line is a linear fit to the data. The speed of the CME was measured by following its leading edge as a function of time. The upper dashed line at a height of 2.94 R_S corresponds to the frequency of 9 MHz; the lower dashed line at a height of 1.78 R_S corresponds to 30 MHz. The dotted vertical line indicates 11:20 UT. The height difference between the CME front and the absorption burst was almost 3R_S.*

8 Drift Pairs Bursts

8.1 Properties of decameter drift pairs

8.1.1 Drift pairs in the decameter range

Solar drift pairs bursts (DP) were observed as early as the late 1950s. Roberts (1958) was the first to mark them out in a separate class of solar radio phenomena. These bursts are associated with solar storms of Type III bursts. They consist of two short elements separated in time (of about 1 s - 2 s), which drift with typical absolute rates 2 MHz/s - 8 MHz/s from high to low frequencies – so-called "forward" drift pairs (FDP), and vice-versa – "reverse" drift pairs (RDP). de La Noe and Moller Pedersen (1971) pointed out that about 30% of observed DPs were FDPs and approximately 70% were RDPs. The drift rates of DP elements were the same and did not depend on frequency. According to de La Noe and Moller Pedersen (1971) DPs are observed exclusively at frequencies from 25 up to 70 MHz and their rate of occurrence increases toward lower frequencies. Another property of DPs is the constant time delay of the second element which equals 1 s – 2 s at all frequencies. Suzuki and Gary (1979) noted that both DP elements had the same sense of polarization, but their degree of polarization was different. They also provided the results of radioheliograph data, which demonstrated that the source positions were the same for both DP elements and coincided with the Type III source position. Sometimes there were bursts consisting of one element or even three elements (Ellis, 1969), and DPs with unusually high drift rates (de La Noe and Moller Pedersen, 1971; Thejappa et al., 1986). Another property regards the instantaneous bandwidth of an element $\delta f < 0.4$ MHz ("sharp") and "diffuse" ($\delta f \approx 1$ MHz) of DPs (Moller-Pedersen et al., 1978). Abranin et al. (1977) reported observations of DPs with a harmonic structure at 12.5 MHz and 25 MHz and noted that FDPs and RDPs were approximately equal in

amount of occurrence. For the study of DPs at low frequencies, where their number is expected to be a maximum, it is necessary to observe them by means of a radio telescope with a large effective area like the UTR-2 (Braude et al., 1978). At the beginning of the year 2000 this radio telescope was equipped with back-end facilities consisting of a digital spectral polarimeter (DSP, Kleewein et al., 1997) and a 60-channel spectrometer.

In the following UTR-2 observations of DPs in 2002 are analysed (Melnik et al., 2005) with regard to their main characteristics such as frequency drift rates, time delay between elements, element duration, and radio emission fluxes are listed. A possible mechanism of DPs formation is based on the interaction of Langmuir and magnetosonic waves generated by beam particles with velocities equal to the phase and group velocity of the magnetosonic waves.

Observations

A Type III bursts storm was observed in the period July 11 – 21, 2002. The complex active region No. 249 (according to the Pulkovo catalogue) moved from East to West and crossed the meridian around July 15 and 16. During this storm many DPs were observed with a maximum activity between July 13 – 15. On the other days, the rate of DPs occurrence was significantly smaller. This indicates that the emission pattern of the DP source is not wider than that of the Type III burst source. The relation between FDPs and RDPs was as follows: 109:89 on July 13, 186:123 on July 14, and 109:158 on July 15, respectively. Both the FDPs and RDPs were registered in the whole frequency range from 10 MHz to 30 MHz. An illustration of DPs activity is presented in Fig. 8.1.

In many cases both elements of one DP are sharply similar even at the level of fine structure (Fig. 8.2). One may assume that pairing occurs mostly due to time delay rather than to frequency shift, although sometimes a slight frequency shift ($\approx$ 200 kHz) takes place with the second element starting at a lower frequency than the first (Fig. 8.2).

The distribution of DPs over the frequency range (number of events at separate frequencies with the step of 1 MHz) is visualized in Fig. 8.3. Since one separate DP often extends over more than 1

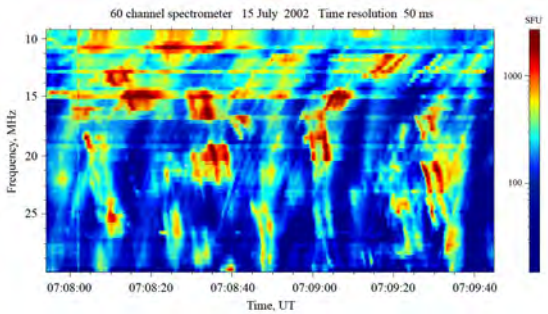


Figure 8.1: *Fragment of DPs storm on July 15, 2002.*

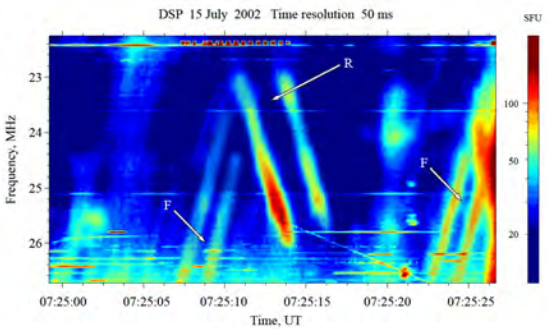


Figure 8.2: *The dynamic spectrum of the reverse DP (R) with sharply similar elements accompanied with forward DPs (F).*

MHz in frequency range, the values on the frequency axis in Fig. 8.3 correspond to the median frequencies of the bursts. It can clearly be seen that the FDPs appear to be almost uniformly distributed in frequency with a considerable fall just below 14 MHz. At the same time, the amount of RDPs decreases rapidly at frequencies below 25 MHz (Fig. 8.3). One of the most important characteristics of DPs is the frequency drift rate. It remains practically constant for a separate DP over the entire extending frequency range, unlike the Type III bursts, whose drift rate (slowly) increases with frequency. The values of drift rates and their dispersion are considerably different for FDPs and RDPs. The FDPs in majority have drift rates $|df/dt < 1|$ MHz/s with a maximum at $|df/dt < 0.8|$ MHz/s (Fig. 8.4), and low dispersion. The RDPs have a wide drift rate distribution with a maximum at 1.5 MHz/s.

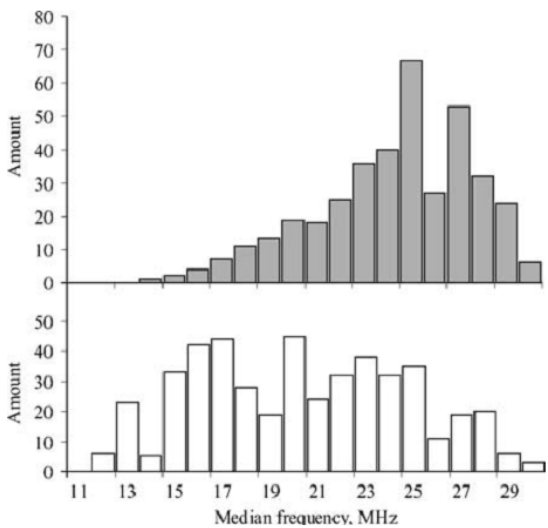


Figure 8.3: *Frequency distribution of FDPs (white columns) and RDPs (shaded columns).*

Also, it is important to note that the enormously high drift rates ($|df/dt > 8|$ MHz/s) were detected only for RDPs. On the other hand, only the FDPs were observed with anomalous low drift rates

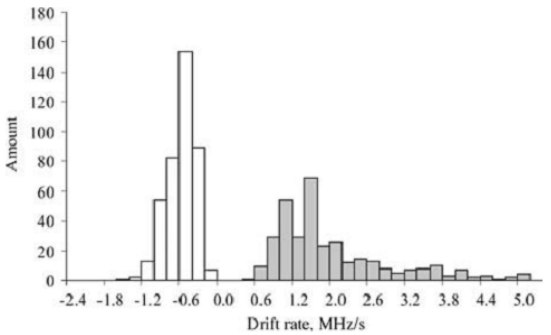


Figure 8.4: *Drift rates distribution of FDPs (white columns) and RDPs (shaded columns).*

($|df/dt \approx 0.3|$ MHz/s). As is seen from Fig. 8.4, the majority of both FDPs and RDPs have absolute frequency drift rates between 0.5 and 2 MHz/s.

According to the values of drift rate the linear velocity of the beam particles equals approximately $(1-2)\cdot 10^9$ cm/s, which is several times higher than the electron thermal velocity, and differs from both the shock waves speed and Type III electron velocities. The determination of the origin of this velocity may lead to the discovery of the nature of the DP phenomenon itself, which is not clear until recently.

Roberts (1958) and Ellis (1969) reported that DP drift rates were not connected with the central frequency of the DPs, though later de La Noe and Moller Pedersen (1971) noted that according to their observations there was a tendency of drift rates to increase with frequency. In Moller-Pedersen et al. (1978) the dependence of DPs drift rates versus frequency in the frequency range 20 MHz – 80 MHz for both positive and negative drifts was approximated by the equation

$$|df/dt| = |-0.17 \cdot f + 0.34| \tag{8.1}$$

The experimental data derived from UTR-2 observations yielded a drift rate versus frequency dependence, as shown in Fig. 8.5. We have approximated this dependence by a power law equation as follows:

$$df/dt = A \cdot (f/f_0)^B + C, \tag{8.2}$$

where df/dt is the drift rate in MHz/s, f is the median frequency of the burst, and f_0 is the normalization frequency, which in our case equals to the frequency at maximum of DPs occurrence, i.e. 25 MHz (Fig. 8.3). The least-squares approximation leads to coefficients as follows:

- for FDPs: $A = -0.5$ MHz/s, $B = 2.7$, and $C = -0.4$ MHz/s;
- for RDPs: $A = 2.3$ MHz/s, $B = 6.2$, and $C = 1$ MHz/s.

Thus, obviously both of these dependencies differ considerably from Eq. (8.1) introduced by Moller-Pedersen et al. (1978). We should note that Eq (8.2) with the above coefficients is valid only for the frequency range in which the measurements were carried out, i.e., 14 MHz $\leq f \leq$ 28 MHz.

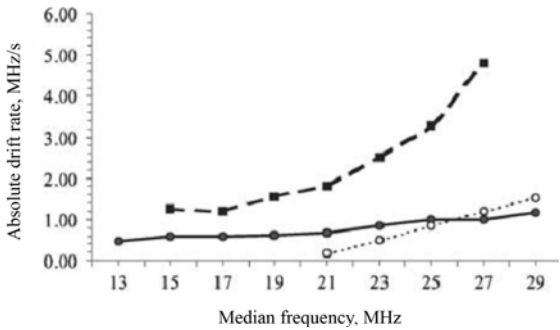


Figure 8.5: *The absolute drift rates vs. frequency dependence for FDPs (solid line), RDPs (dashed line), and the Eq. (8.2) given in Moller-Pedersen et al. (1978) (dotted line).*

One of the characteristic features of DPs is the constancy of delay time δT between DPs elements. The values of delay time vary from 1.4 s to 2.6 s with an average of about 1.7 s for FDPs and 2.0 s for RDPs. The delay time δT slowly decreases with frequency (Fig. 8.6).

The durations τ of DP elements, measured at the median frequency of the bursts, are approximately equal in the pair and are between 1 s and 1.5 s with an average value of 1.3 s, slightly decreasing with frequency (Fig. 8.7).

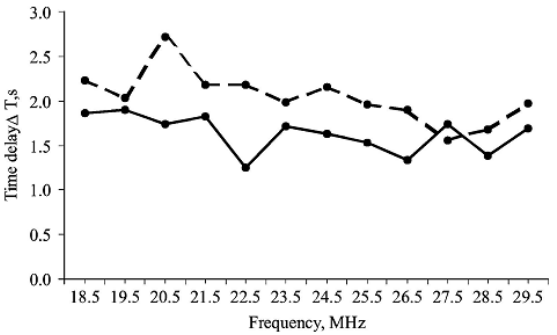


Figure 8.6: *Delay time δT vs. frequency dependence for FDPs (solid line) and RDPs (dashed line).*

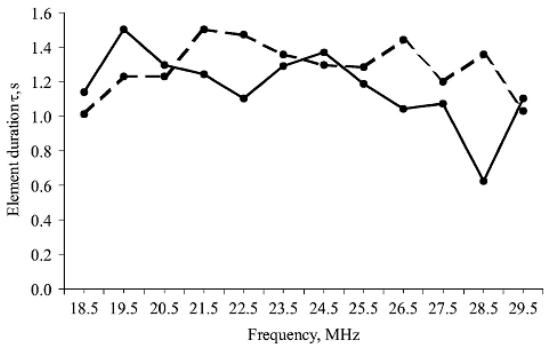


Figure 8.7: *The DP element duration τ dependence vs. frequency for FDP (solid line) and RDP (dashed line).*

The whole frequency range Δf over which DPs extend, varies from 0.9 MHz up to 10 MHz, with average values of 4 MHz and 3 MHz for FDPs and RDPs, respectively, which is in line with 1.5 MHz $\leq \Delta f \leq$ 8 MHz from de La Noe and Moller Pedersen (1971).

Most of the radio emission fluxes I of the observed DPs were moderate and vary from 5 s.f.u. to 100 s.f.u.. The averaged flux for RDPs (51 s.f.u.) is more than two times higher than for FDPs (22 s.f.u.) The fluxes of both types of DPs decrease with frequency, but for FDPs this decrease is monotonic, whereas the flux of RDPs sharply falls at 23 MHz – 25 MHz (Fig. 8.8). Also so-called "hook" bursts have been observed, first described by Ellis (1969), which are a combination of FDP and RDP when the end of one burst coincides with the beginning of the other (Fig. 8.9). This could be interpreted that both bursts are generated by the same source.

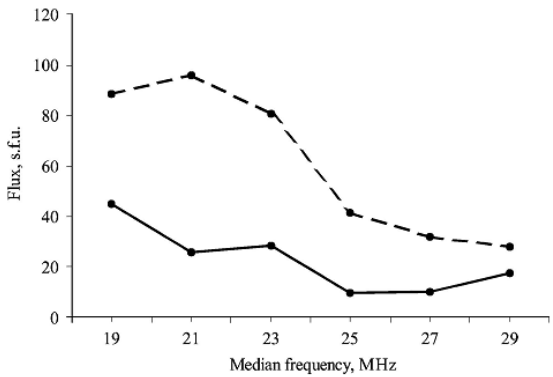


Figure 8.8: *The radio emission flux vs. frequency dependence for FDP (solid line) and RDP (dashed line).*

Some of the DPs exhibit fine structures, such as in the form of separate bright spots as presented in Fig. 8.10, with characteristic scales of 1 s and 400 kHz. Sometimes one DP element consists of sub-bursts, as shown in Fig. 8.11. The host DP has a frequency drift rate of 8 MHz/s while sub-bursts have an instantaneous bandwidth of about 400 kHz with a drift rate of -0.6 MHz/s.

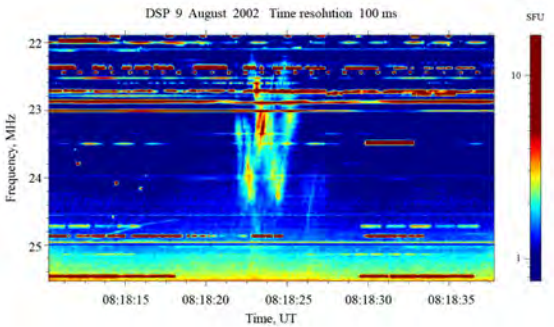


Figure 8.9: *The DP with cloudy fine structure.*

Interpretation of the observations

There is at present no satisfying theory of DPs explaining their main observational properties. Moreover, there is no theory preference on the cause of appearance of two DP components. The fact that the second observed component is time delayed may be explained by two identical waves generated at the place of the source and passing different ways to the observer. Such a situation is realized in the models with reflection from the underlying regions (Roberts, 1958) or from the walls of a duct (Melrose, 1982). Another possibility would be if two simultaneously generated waves belong to two different modes (Melnik et al., 2005). Then, due to differences in their group velocities, the observed time delay may arise.

In our opinion, the key property of the DPs is the value of their drift rates 1 MHz/s – 2 MHz/s. The corresponding linear velocity, derived from these drift rates and the Baumbach-Allen corona model, yields $(1 - 2) \cdot 10^9$ cm/s. Such a velocity, as was repeatedly noted, (see for example, Melrose, 1982), differs from the other characteristic velocities in the corona: electron and ion thermal velocities, Alfven velocity, Type II (Mel'nik et al., 2004) and Type III sources (Mel'Nik et al., 2005b) velocities. It should be emphasized that this velocity is close to the phase velocity of fast magnetosonic waves, for which it is equal to their group velocity. In fact from the dispersion law for

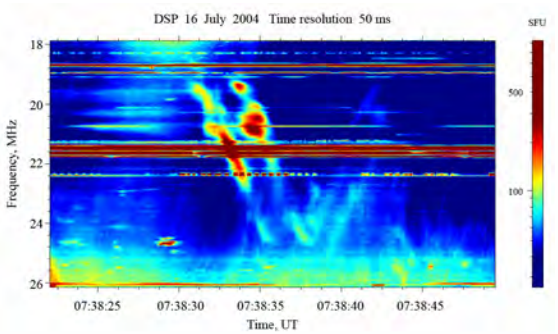


Figure 8.10: *Inverted "hook" burst with bright spots.*

these waves

$$\omega = \omega_{Be} \frac{k^2 c^2}{\omega_{pe}^2 + k^2 c^2}, \tag{8.3}$$

it can easily be derived that

$$v_{ph} = v_{gr} = \frac{\omega_{Be}}{2\omega_{pe}} \cdot c, \tag{8.4}$$

where ω_{Be} and ω_{pe} are the electron cyclotron and Langmuir frequencies, ω and k are the frequency and wave number of the fast magnetosonic wave, respectively, and c is the speed of light. For corresponding heights these velocities equal approximately $2 \cdot 10^9$ cm/s. Such fast magnetosonic waves may be excited by beam particles (electrons or ions) with the above velocities due to the Cherenkov resonance ($v_b = v_{ph} = \omega/k$, where v_b is the velocity of the beam particles). Moreover, having the same group velocity these waves are accompanying the beam and, as a consequence, they can obtain energy from resonant particles for a long period of time. Since drift pairs are closely associated with Type III storms (Melrose, 1982) it seems reasonable to assume that the drift pair radio emission may originate from the interaction between the aforementioned fast magnetosonic waves and Type III Langmuir waves which are independently excited by other, much faster ($v_b \approx 0.3c$) particle beams.

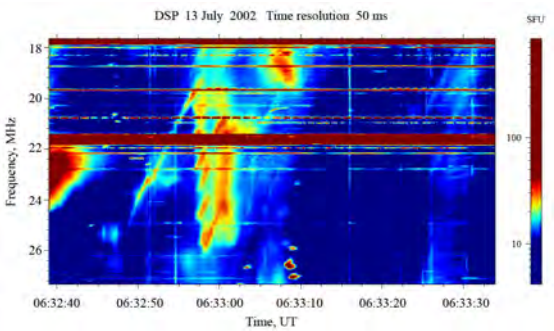


Figure 8.11: *The DP with fine structure in the form of sub-bursts.*

8.2 Polarization of drift pairs

One of the important parameters of drift pairs is the polarization of their components. Only few papers were devoted to this issue. According to the results of de La Noe and Moller Pedersen (1971) and Ellis (1969), the polarization degree of DP components is rather low. At the same time Suzuki and Gary (1979) and Dulk et al. (1984) stated that DPs polarization was about 50%.

The observations have been carried out from July 12 – 18, 2002. The investigated DPs were observed in the frequency range 20 MHz - 32 MHz at the radio telescopes UTR-2 and by URAN-2, and their polarizations were measured by the latter at 24.75 MHz (in a band of 10 kHz) during a Type III burst storm. These experimental data were of considerable interest because there was only one active region on the solar disk near the solar meridian.

As said the DP polarization was measured by URAN-2, however the bursts identification was performed by the dynamic spectra obtained at UTR-2. During the storm the left-hand polarized (LH) radio emission for all types of bursts was measured and the results of observations are given in Tab. 8.1.

The interdependency between the polarization degree of the first (P1) and the second (P2) DPs elements is shown in Fig. 8.12. Strong correlation ($r \approx 0.9$) between values of polarization degrees of the first and second elements is observed.

Table 8.1: *Average polarizations of components of RDPs and FDPs.*

Type	Number of bursts	Average polarization degree of first element P1, %	Average polarization degree of second element P2, %
RDPs	251	-29.1±0.9	-23.9±0.9
FDPs	251	-26.2±1.3	-27.7±1.7

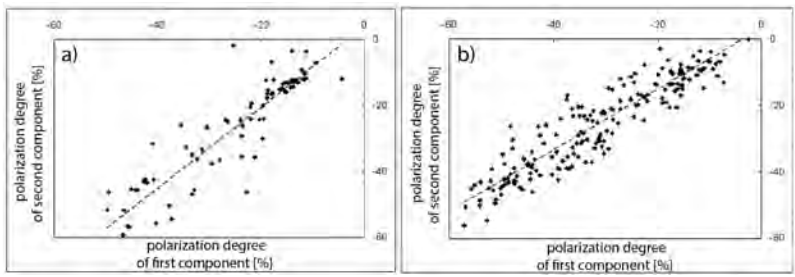


Figure 8.12: *Interdependency between the polarization degrees of the first (P1) and the second (P2) EPs elements for FDPs (a) and RDPs (b).*

The distribution of DPs by their polarization degree has two maxima, as it can be seen in Fig. 8.13. The first maximum – both for FDPs and for RDPs – is around the polarization degree of 10 % - 15 %. The second one is at $\approx$ 40% for FDPs and at $\approx$ 30% for RDPs. The longitudinal dependence of the average values of the DPs polarization degree obtained during the storm from July 12 to 18, 2004 is shown in Fig. 8.14.

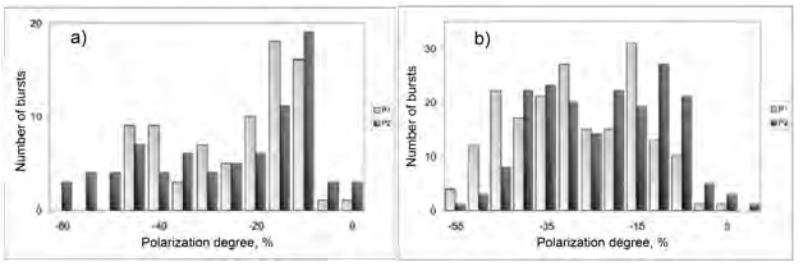


Figure 8.13: *The distribution of DPs by polarization degree: a) – FDPs, b) – RDPs.*

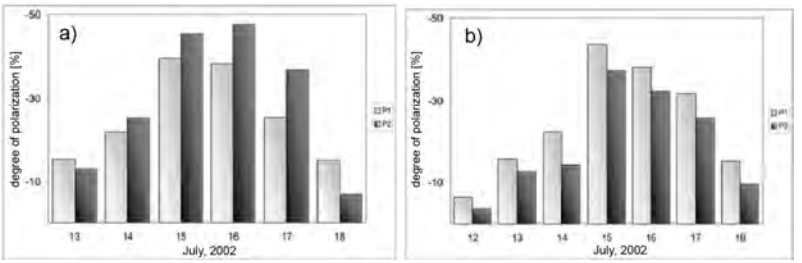


Figure 8.14: *The longitudinal dependence of the DPs polarization degree: a) – FDPs; b) – RDPs.*

Suzuki and Gary (1979) noted that for RDPs the polarization degree of the first element was higher, compared to the second one, and for FDPs, on the contrary, the polarization degree of the first element of the pair was lower. The observations of July 2004 also show that for 85% of RDPs the first element is more strongly polarized

(P1>P2) (see Fig. 8.14b and Fig. 8.15). The number of observations of FDPs for which P1>P2 and P1<P2 are approximately equal: 44% and 45%, accordingly. During four out of the six days from July 12 – 18, 2004, the polarization degree of the second element of FDPs exceeded that of the first element (Fig. 8.14a and Fig. 8.15).

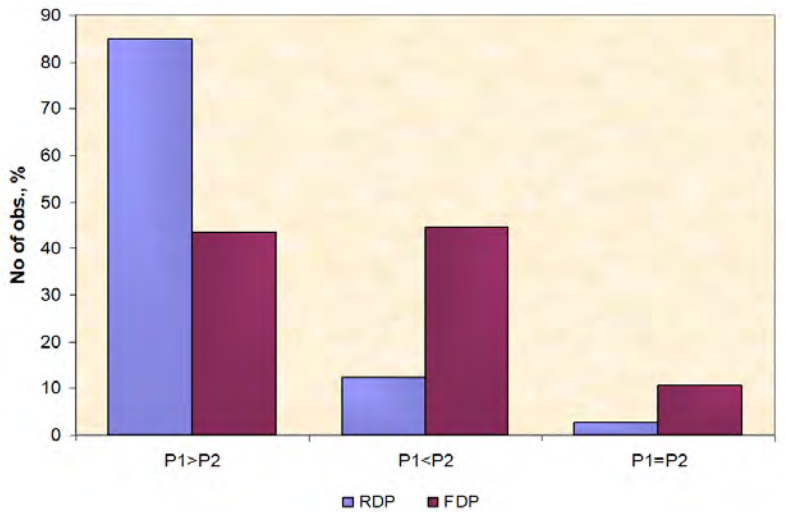


Figure 8.15: *DPs distribution by elements polarization.*

The investigation of DPs temporal structure reveals that for ≈ 80% of the bursts, the maximum value of the polarization degree of DPs elements is observed either at the front, or at the back of the burst. The maximum/minimum of the polarization degree very seldom coincides with the maximum of intensity of the burst.

Typical cases of time profiles of DP polarization degree are provided in Fig. 8.16. For more than half of FDPs, the maximum of polarization degree is found at the front of each pair elements. In other words, in both FDP elements, the maximum of polarization degree exceeds the maximum of intensity. With respect to RDPs, the most typical time profile of the polarization degree is different. The maximum of the polarization degree of the first element is found at its leading edge, and the maximum of polarization degree of the

second element – at the back edge of RDP. Such variant of time profile of polarization degree was observed almost for 70% of RDPs.

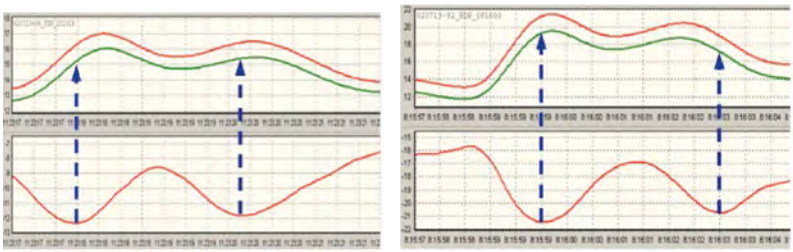


Figure 8.16: *The most typical DPs time profiles. Left panels: FDP burst at 11:23:18 UT on July 13, 2002. Top panels: time profile of "right" (green line) and "left" (red line) channels (dB above a level of background). Bottom panels: circular polarization degree, %. Right panels: RDP burst at 08:16:00 UT on July 13, 2002.*

9 S-Bursts

9.1 Properties of decameter S-bursts

Ellis (1969) first identified S-bursts as a special type of solar bursts in 1969. He referred to them as "fast drift storm bursts" because they appeared exclusively during storms in the form of bursts groups and reminded Type I (fd) fast drift burst storm according to the Elgaroy classification (Elgarøy, 1961). Later, McConnell (1980) called them S-bursts, where S meant "storm" or "short". Besides these bursts remind Jovian S-bursts by their structure in dynamic spectra.

S-bursts are observed in the frequency range 10 MHz - 80 MHz. At higher frequencies they are practically absent. The number of S-bursts increases at increasing frequency up to 23 MHz - 24 MHz (Ellis, 1969; Melnik et al., 2010c). These bursts disappear at lower frequencies (Fig. 9.1, Melnik et al., 2010c).

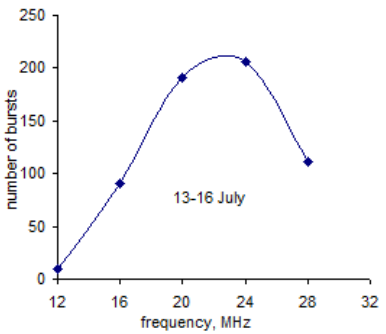


Figure 9.1: *Appearance rate of S-bursts at different frequencies on July 13 - 16, 2002 (Melnik et al., 2010c).*

A detailed analysis of S-bursts indicated that they are connected

with the position of associated active regions on the solar disk observed during the four days when the active regions are near the central meridian (Melnik et al., 2010c). Apparently the beam of S-bursts radio emission opens up to about $40° - 50°$. These bursts are observed in groups but sometimes appear as single bursts. One of the specific features of S-bursts is their appearance together with an increased activity of the Sun in the corresponding frequency range. This can be Type I-, Type III bursts, Type IIIb bursts, drift pairs with forward and reverse drift, etc. This feature was pointed out by different authors. This property can be very important for the understanding of the generation mechanism of S-bursts.

These bursts appear as narrow tracks, which drift from high to low frequencies with a noticeable drift rate dependence on frequency (Fig.9.2). This discriminates them from drift pairs, which have a constant drift rate for a single pair. There are few cases when S-bursts drift from high to low frequencies as noted by McConnell (1982). Such bursts are absent within the frequency range 10 MHz - 30 MHz.

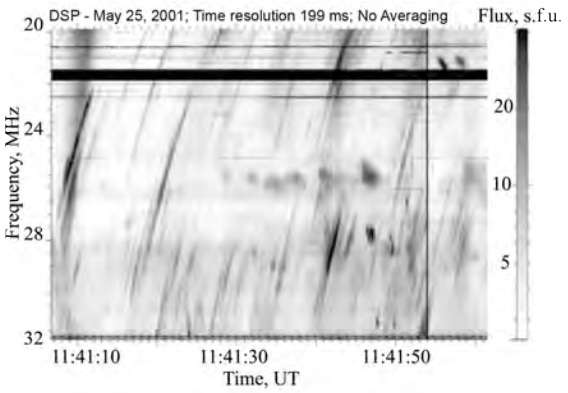


Figure 9.2: *Group of S-bursts above the background of decameter radio emission.*

The frequency band, in which single S-bursts have been observed, changed from 1 MHz - 2 MHz to 10 MHz - 12 MHz. This is wider than the frequency bands of drift pairs. It is interesting that the average frequency band exhibits sort of a jump when a corresponding active

region crosses the central meridian.

As to the S-bursts durations there are different data. According to Ellis (1969) their durations change from 0.2 s to 1.4 s with an average value of about 0.6 s in the frequency range 25 MHz - 80 MHz. But McConnell (1982) states only 50 ms and even shorter for that frequency range. Analyzing three S-bursts storms Dorovskyy et al. (2006) and Melnik et al. (2010c) got values, which were close to the durations found by Ellis (1969). Their average duration values were 0.35 s for the one storm and 0.4 s - 0.6 s for the other two storms. The durations did not display any frequency dependence. Besides, the durations were practically constant for all days of the given storms.

According to Ellis (1969), the instantaneous frequency width of S-bursts was about 30 kHz but this value was not confirmed by other observations. McConnell (1982) indicates 100 kHz at frequency 30 MHz and 500 kHz at frequency 80 MHz. At frequencies f $<$ 30 MHz the instantaneous frequency width is closer to McConnell (1980) results. The detailed analysis of frequency width dependence on frequency at frequencies 10 MHz - 30 MHz showed that this dependence was linear $\Delta f = A \cdot f$ (Fig.9.3) with a gradient of 0.02 for all analyzed storms and days. The coefficient A slightly changes from storm to storm but remains constant for a given storm. This may indicate that the frequency width is probably defined by physical processes in the place of generation, but not by effects of radio emission propagation in the solar corona.

A model proposed by Melnik et al. (2010c) explains some important properties of S-bursts observed at frequencies 10 MHz - 30 MHz in a consistent way:

- All S-bursts are observed over the background of other bursts such as Type III bursts, Type IIIb bursts and others in the decameter range.
- The linear velocities of S-bursts sources equal $5-9 \cdot v_{Te}$ (thermal velocity of electrons).
- The instantaneous frequency width of S-bursts linearly increases with frequency.

From the first point it follows that the sources of S-bursts move through a plasma with a rather high level of Langmuir turbulence.

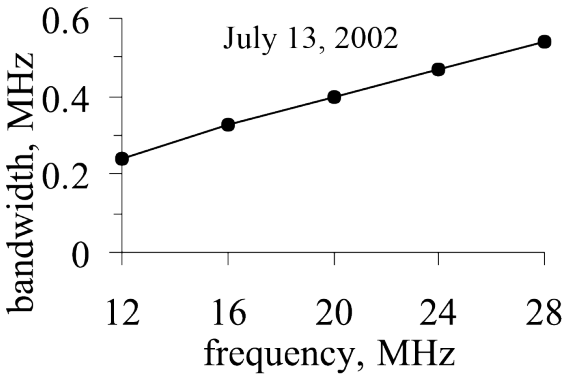


Figure 9.3: *Frequency width versus frequency for July 13, 2002 (Melnik et al., 2010c).*

The presence of such turbulence is obvious due to radio emission in the form of different solar bursts such as Type III, Type IIIb bursts, Type III-like bursts, drift pairs etc. The velocity of the S-bursts sources is well distinguished, because it is practically invariable and does not change over days or even months. However, some reasonable cause of such special velocity should be explained as well as a natural explanation should be given for the instantaneous frequency width of S-bursts following from the radio emission mechanism.

Let us suppose that sources of S-bursts in the form of particles, electron or proton beams are moving with a velocity $5 - 9 \cdot v_{Te}$ in a plasma with developed Langmuir turbulence. These beams are in resonance with fast magnetosonic waves, which have equal phase and group velocities. This equality of phase and particle velocity (Cherenkov's resonance) enables them to generate plasma waves. Due to the group velocity of these waves equal to the particles' velocity, the involved particles can generate these waves for a long period of time. As a result, a large amount of energy can be taken from the particle beam and gets accumulated in fast magnetosonic waves. In the course of interaction of these waves with Langmuir waves, they are transformed into electromagnetic waves, which are registered as S-bursts. From the dispersion equation for fast magnetosonic waves (see Eq. (8.3)), where k is the wave number of fast magnetosonic

waves, this specific velocity is given by Eq. (8.4).

This velocity is close to the required velocity for conditions in the solar corona. The fast magnetosonic waves m interacting with Langmuir waves l in processes like $l+m=t$ lead to electromagnetic waves t. Their frequency equals to $\omega_{Be}+\omega_H/2$, where

$$\omega_H = \left[1/2\left(\omega_{pe}^2+\omega_{Be}^2\right)+1/2\sqrt{\left(\omega_{pe}^2+\omega_{Be}^2\right)^2-4\omega_{pe}^2\omega_{Be}^2\cos^2\theta}\right]^{1/2} \tag{9.1}$$

is the upper hybrid frequency. In Eq. (9.1) θ is the angle between the vector of the magnetic field $\boldsymbol{B}$ and the wave vector of Langmuir waves $\boldsymbol{k}_l$. It can be expected that in the source regions of S-bursts generation the Langmuir waves of the background turbulence have a wide angular distribution. So, the waves with different directions of wave vector $\boldsymbol{k}_l$ can take part in the process $l+m=t$. As a result, the frequencies of electromagnetic waves t are enclosed in the frequency band

$$\Delta\omega = \omega_{es}(\theta_0)-\omega_{es}(0) = \frac{\omega_{Be}^2}{2\omega_{pe}}\sin^2\theta_0, \tag{9.2}$$

where θ_0 is the angular width of Langmuir waves spectrum. The Eq. (9.2) is derived in the approximation $\omega_{pe} \gg \omega_{Be}$. For the relative frequency width

$$\frac{\Delta f}{f} = \frac{\omega_{Be}^2}{2\omega_{pe}^2}\sin^2\theta_0 \tag{9.3}$$

the ratio of electron cyclotron frequency and plasma frequency depends on the angular width of background Langmuir turbulence. From Equation $\delta f = Af$ and (9.3) for the obtained coefficient values A the following equation holds

$$\frac{\omega_{Be}}{\omega_{pe}}\cdot|\sin\theta_0| = 0.19-0.23 \tag{9.4}$$

Eq. (9.4) defines the magnetic field in the place of S-burst generation at the frequency $f \approx f_{pe}$ for a given angular width of Langmuir turbulence. This turbulence is in excess of Langmuir waves after the passage of electron beams, which generate also other bursts simultaneously observed with S-bursts. At first this turbulence is anisotropic, approximately the same as was generated with quasi one-dimensional

electron beams. Wave vectors of these Langmuir waves are in the cones with angle $\theta_0 \approx 20^\circ$ along the direction of propagation of electrons (Zaitsev, 1974). After the passage of electron beams, a part of Langmuir waves are left over in a given place, for example in consequence of non-uniformity of coronal plasma (Kontar, 2001a). In the processes of scattering on plasma particles in processes $l + i = l + i$ the Langmuir waves become more isotropic. In the case of complete isotropy ($\theta_0 = 90^\circ$) the magnetic field is equal to 1.8 G. If the background Langmuir turbulence is partially isotropic (for example, $\theta_0 \approx 50^\circ - 60^\circ$) then the magnetic field equals 2 G. These values are obtained for the heights, at which radio emission at frequency 25 MHz is generated. Higher in the corona, the magnetic field decreases according to Eq. (9.4). Under the assumption that the angular width does not significantly change at heights corresponding to 10 MHz - 30 MHz, it follows that the ratio ω_{Be}/ω_{pe} remains practically unchanged at these heights. This means that the relation between magnetic energy and energy density of plasma $B^2/(2\mu_0 nkT)$ keeps constant and equals $1/50$. Substituting the derived value of magnetic field in Eq. $v_S = \omega_{Be}c/2\omega_{pe}$ we obtain $6 - 8\ v_{Te}$ for the velocity of S-bursts sources, well in agreement with the needed $5 - 9\, v_{Te}$.

Some models have been proposed for the explanation of the fringe phenomenon. Zhelezniakov and Zaitsev (1975) interpreted the lack of radio emission between fringes with the absorption of plasma waves at frequencies of multiple gyrofrequency. But such a model fails to explain the observed high number of fringes. The Faraday rotation could be an explanation of these fringes. However, the time profile of a fringe sequence should have a sinusoidal form, as, for example, for Jupiter S-bursts. But solar fringes do not exhibit such a form.

More realistic seems to be the model in which the S-burst source propagates through the plasma with a periodic structure in the form of, e.g., low frequency wave (McConnell and Ellis, 1981).

9.2 Groups of decameter S-bursts

Solar S-bursts are known to be the shortest bursts among all types of solar sporadic radio emission. Their duration is mostly shorter than 1 s with the shortest reported value of 20 ms (McConnell, 1982). These

bursts are observed exclusively at meter and decameter waves (Melnik et al., 2010c; Morosan et al., 2015). Due to their short durations and low intensity S-bursts can only be investigated by large ground-based radio telescopes equipped with high-resolution and sensitive back-end instruments, such as LOFAR, NenuFAR, LWA, UTR-2, etc.

The most recent study of S-bursts parameters was performed by Morosan et al. (2015). These authors have analyzed about 3000 individual S-bursts observed on July 9, 2013, by LOFAR tied-array in the frequency band 20 MHz - 80 MHz. They also obtained the image of the source.

On that particular day the UTR-2 and URAN-2 radio telescopes were also in operation. Thus, there was the possibility to supplement the above research with data obtained by other instruments at lower frequencies, namely from 9 MHz to 32 MHz.

9.2.1 Observations

On July 9, 2013, from 5:30 UT till 13:28 UT more than 1000 S-bursts were identified in the frequency band 9 MHz - 32 MHz. All S-bursts appeared to be very weak events with an average flux of about 10 s.f.u., and a minimum flux of 0.2 s.f.u., practically impossible to detect for small instruments. Using new antenna configuration as well as implementation of special processing methods allowed to retrieve S-bursts with fluxes below the quiet Sun background level.

Since 2010 the observations of solar radio emission with the UTR-2 radio telescope have been carried out in the interferometric mode. In this mode separate parts of the UTR-2 antenna array were used as points of local short-base interferometer. The configuration shown in Fig. 2.2 has been chosen as standard for the observations of sporadic solar radio emission.

In this scheme the Northern, Southern and Western branches of the UTR-2 radio telescope were used as the interferometer points. Thus, we get two 674 m long mutually orthogonal bases B1 (stretching from middle of North-branch to middle of West-branch) and B2 (stretching from middle of West-branch to middle of South-branch) inclined to the meridian by 45°. This configuration was originally used to determine the size and angular position of the sources of solar radio bursts. It was also used to distinguish weak, small-sized sources in

the background of the emission from more extended sources, such as the quiet Sun radio emission. The amplitude of the correlation function at the output of interferometer is proportional to the visibility function (Shepelev, 2015) as given by Eq. (5.18). Thus, the larger the source, the smaller its visibility function. This effect is clearly illustrated in Fig. 9.4.

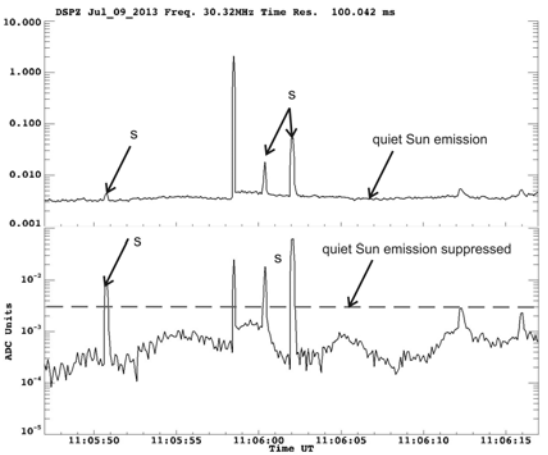


Figure 9.4: *Time profile of the emission received by the Northern antenna (top panel) and the profile of the correlator output (bottom panel) at frequency 30.3 MHz. The S-bursts are marked with 'S'.*

Using this technique more than 1000 individual S-bursts were identified in the frequency range from 9 MHz to 32 MHz, however, only some tens of S-bursts were registered by the LOFAR station (Morosan et al., 2015).

The essential feature of the observed S-bursts is their appearance in dense groups by 5 - 10 individual bursts separated in time by approximately twice the half-power duration of one burst.

There were few S-bursts that had the appearance of a solid line in the dynamic spectrum while drifting from its highest to lowest frequencies. The majority of them looked like dashed lines with a frequency width of one fragment varying from 0.5 MHz to 2 MHz

(Dorovskyy et al., 2016). Some examples of fragmented S-bursts are shown in Fig. 9.5.

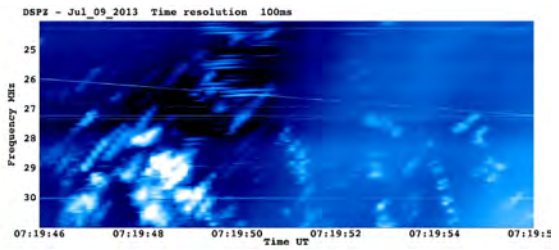


Figure 9.5: *Typical appearance of S-bursts on July 9, 2013.*

An interesting phenomenon occurred when the fragments of successive S-bursts of the group form kind of a chain drifting in frequency. More than 20 such chains were identified during the session. These chains have exclusively positive frequency drift rates varying from 1 MHz/s to 5 MHz/s and consisted of 4 to 16 elements. The frequency widths of the chains vary from 1.5 to 6 MHz. Such chains were never described before (Dorovskyy et al., 2016).

9.2.2 Analysis of observations

The distribution of the S-bursts observed by the UTR-2 radio telescope is not uniform. There is a strong tendency of the S-bursts occurrence rate to decrease towards low frequencies, as shown in Fig. 9.6. A power law approximation of this dependence yields

$$S = 0.0083 \cdot f^{2.95}, \tag{9.5}$$

where S is the number of S-bursts counted in the frequency bin of 2 MHz and f is the central frequency of the bin in MHz.

Two main parameters distinguish S-bursts from other types of solar radio emissions: the frequency drift rate, the duration, and their dependences on frequency.

Statistical analysis shows that the average drift rate of the observed S-bursts is $-1.57\,\mathrm{MHz}\cdot\mathrm{s}^{-1}$ and the average duration is 0.5 s. At the same time the most probable values of drift rate and duration equal

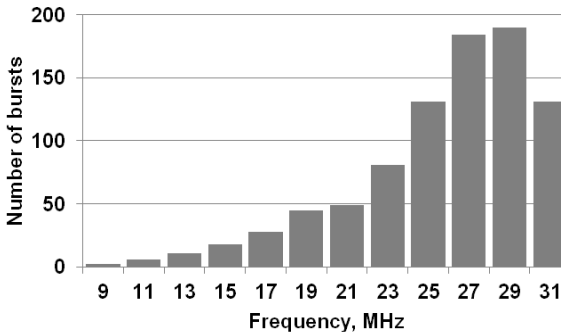


Figure 9.6: *Distribution of the S-bursts in the frequency range 9-31 MHz.*

$-1.2\,\mathrm{MHz}\cdot\mathrm{s}^{-1}$ and 200 ms, correspondingly. It is well known that the drift rate of the meter band S-bursts is proportional to the frequency with the power of 1.6 (McConnell, 1982).

The dependence derived from the data recorded on July 9, 2013, in the frequency range from 9 MHz to 32 MHz is close to that value, and is defined by the equation

$$\frac{df}{dt} = 7.4 \cdot 10^{-3} \cdot f^{1.65}, \tag{9.6}$$

where f is the frequency in MHz.

Fig. 9.7 shows the dependence of S-bursts duration on frequency, the analytical determination of this dependence is

$$\tau(f) = 58.1 \cdot f^{1.5}, \tag{9.7}$$

where τ is the duration in s.

Within the frame of plasma emission mechanism any frequency drift of the emission is the manifestation of its source movement in the corona. Negative drift rate corresponds to the outward movement, positive drift to the inward motion (i.e., towards the Sun). From this point of view, the observed positively drifting chains of negatively drifting S-bursts may be formed due to two kinds of movements simultaneously existing in one and the same region. The first is the

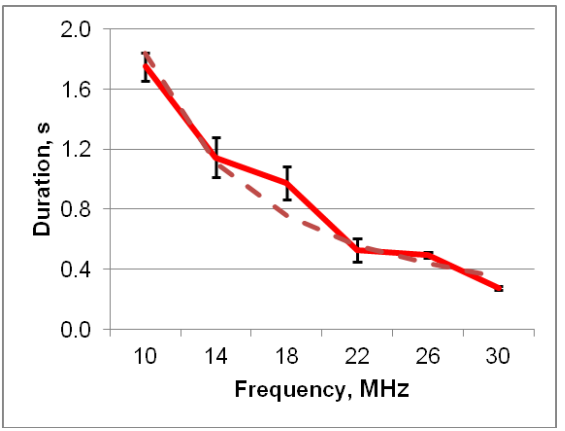


Figure 9.7: *Dependence of S-bursts duration on frequency (solid line) and its approximation (dashed line).*

movement of the supra-thermal electrons responsible for the generation of S-bursts with approximate velocities of $0.1c$ (c is the speed of light). The second motion may be due to some turbulence which provides the condition for an increased emission of the S-bursts. This turbulence moves towards the Sun with the same velocity of $0.1c$ (Dorovskyy et al., 2016).

The degree of circular polarization was high with the sense opposite to that of accompanying Type III and IIIb bursts. This may indicate that S-bursts emission is the fundamental one.

The analysis of optical data from the SOHO/SDO instruments shows that there were several Active Regions (AR) on July 9, 2013. Nevertheless, only AR NOAA 11785 produced five of the six C-class solar flares on that day. Therefore, it's reasonable to associate the S-bursts storm with this AR, whose heliolongitude was around 20° West.

10 Spikes

10.1 Decameter spikes

Elgarøy (1961) and de Groot (1960) were the first authors who categorized spikes into a special class of radio bursts. They referred to them as bursts with short duration (< 0.1 s) and narrow frequency bandwidth (1 % - 3 % of the observed frequency). Such bursts are observed in a wide frequency band from decimeter (as high as 5 GHz) to meter wavelengths. By analyzing all results of spike observations with different instruments reported by the various authors, the properties of spikes can be determined. Spikes are frequently observed in connection with other bursts, namely Type I-, Type III-, and Type IV bursts.

It has been noted that the spike duration decreases with increasing frequency (Benz, 1986). The instantaneous frequency bandwidth of the spikes increases with increasing frequency, in contrast to the duration of the spikes. The fluxes of spikes do not exceed 500 s.f.u. The polarization of spikes is circular and can be very high in individual cases, although the average value is only 25 %.

The duration of spikes is related to the rate of particle collisions in a plasma (Benz, 1986; McKim Malville et al., 1967; Tarnstrom and Philip, 1972b) because the spike durations and particle collision rates have similar values at different frequencies.

In the following the properties of spikes in the decameter range at frequencies 18 MHz - 30 MHz are discussed, as these bursts have been frequently observed with properties that are similar to those of spikes at higher frequencies.

10.1.1 Observations

Solar radio emission data were obtained by observations with the UTR-2 radio telescope and the back-end digital spectral polarimeter

(DSP) equipment. The observations with the DSP were performed at frequencies from 18 MHz to 30 MHz during about six hours around local noon each day in 2002. As discussed here, spikes were observed from July 27 to August 2, 2002. The frequency band from 18 MHz to 30 MHz was divided into 12 frequency intervals with 1 MHz width. In every frequency interval the average parameters of the spikes, such as their duration, frequency bandwidth, and the flux of spikes were determined. More than 2000 spikes were analyzed in total.

The decameter spikes look like a background for decameter Type III bursts, Type IIIb bursts, or other decameter activities (Fig. 10.1). Another feature of the spikes is that their duration and frequency bandwidth are in a narrow range, with durations near 1.2 s and frequency bandwidths in 50 kHz - 70 kHz intervals. We refer to these bursts as decameter spikes.

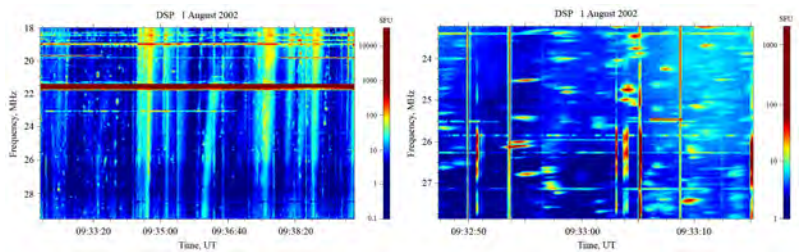


Figure 10.1: *The storm of spikes (left) and separate spikes (right) on August 1, 2002.*

The shortest measured duration of decameter spikes is 0.8 s, the longest is slightly more than 2.2 s. The duration dependence on the frequency presented in Fig. 10.2 for two different days agrees well with the collision time for a plasma with a temperature of 10^6 K. The durations of metric spikes are also close to the collision time for this temperature (Tarnstrom and Philip, 1972b). These dependencies are especially close at frequencies higher than 23 MHz - 24 MHz, and almost over the whole frequency band for July 31 and August 1 and 2, 2002. We may therefore assume that the plasma from which the radio emission of spikes is released, has a temperature of about 10^6 K. Thus decametric spikes may be used as a tool for determining the temperature at an altitude of 1 - 2 solar radii.

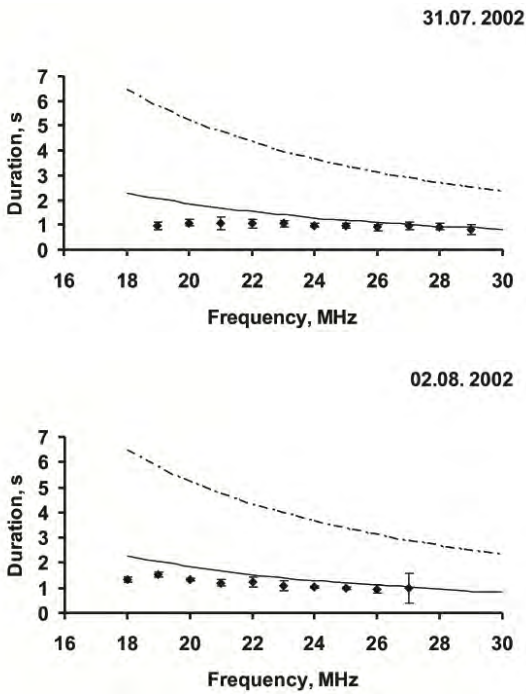


Figure 10.2: *Spike-duration dependencies versus frequency for July 31 and August 2, 2002. The collision time with a plasma temperature of* 10^6 *K (solid line) and* $2 \cdot 10^6$ *K (dashed-dotted line) is also shown.*

The average bandwidth of the spikes increases with frequency. The narrowest bandwidths are 40 kHz - 45 kHz at a frequency of 19 MHz, the highest values of the frequency bandwidth are found to be 90 kHz - 100 kHz at 29 MHz. The frequency-bandwidth dependencies on the frequency are shown in Fig. 10.3, when the Active Region 260 traversed the solar disk. These dependencies of the frequency bandwidth Δf on the frequency f can be approximated by the linear function:

$$\Delta f \propto A \cdot f. \tag{10.1}$$

The coefficient A equals $2 \cdot 10^{-3}$, $1.4 \cdot 10^{-3}$, $2.4 \cdot 10^{-3}$, $1.5 \cdot 10^{-3}$, $2.5 \cdot 10^{-3}$, $1.5 \cdot 10^{-3}$, $1.6 \cdot 10^{-3}$, respectively, for July 27 to August 2, 2002. As shown below, the bandwidth does not depend on the day of the observation, or precisely on the position of the active region on the solar disk. Further, the spike bandwidth does not depend on the effects of electromagnetic propagation in the solar corona, but is instead defined by the conditions at the place of spike generation.

The decameter spikes exhibit fluxes that are usually not higher than 500 s.f.u. In most cases, they are even below 100 s.f.u. The spike fluxes were about 200 s.f.u. at frequencies 18 MHz - 24 MHz and only 20 - 30 s.f.u. at frequencies 24 MHz - 30 MHz. Contrary to that, sometimes the spike fluxes are almost independent of the frequency, as observed on July 31 - August 2, 2002, ranging from 10 - 30 s.f.u..

10.1.2 Dependence of decameter-spike parameters on the location of active regions

The Active Region 260, associated with the analyzed spikes, appeared on the solar disk on July 20, 2002, and moved behind the Western limb of the Sun on August 3, 2002. Decameter spikes were registered from July 27 to August 2. This corresponds to positions of the active region from $20° - 30°$ to the East and $60° - 70°$ to the West from the central meridian, respectively.

The noticeable decrease in spike duration occurs for frequencies 19 MHz - 25 MHz on July 29 - 31, 2002. At higher frequencies (26 MHz - 29 MHz) the spike durations remain mainly unchanged, and

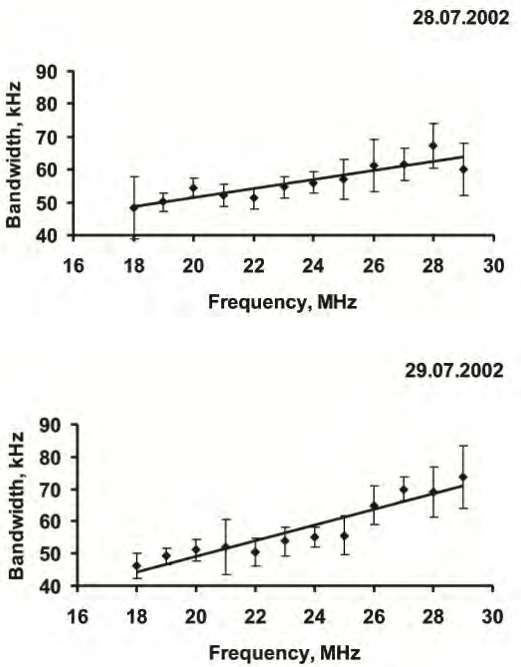


Figure 10.3: *The bandwidth dependencies versus frequency for spikes observed for July 28 and 29, 2002.*

apparently they do not depend on the position of the Active Region 260 on the solar disk. The shortest durations at all frequencies have been observed on July 30 when the active region was located $20° - 30°$ to the West of the central meridian. Regarding the frequency bandwidth dependence on the position of the active region on the solar disk, there is practically no change with the day of observations. The fact that the bandwidth does not depend on the position of the active region on the solar disk suggests that the bandwidth is defined exclusively by processes within the location of the spike radiation.

We assume that spikes are generated by fast-electron beams that are analogous to those associated with Type III electron beams, and in consequence we develop the ideas of Zhelezniakov and Zaitsev (1975) and Tarnstrom and Philip (1972a). The mechanism of radio emission for both Type III bursts and spikes is the same plasma mechanism, which consists of the generation of Langmuir waves by fast electrons followed by a transformation of these Langmuir waves into transverse waves. Because Langmuir waves in this region exist during a collision time $\tau_{coll} = T^{\frac{3}{2}}/100n$ (T is the plasma temperature, n the plasma density) (McKim Malville et al., 1967), we can conclude that the lifetime of the spikes is defined by the collisions.

We determine the frequency bandwidth of spikes associated with fast-electron beams by assuming that fast electrons of a beam propagate into some solid angle θ and generate Langmuir waves at the upper hybrid frequency (Eq. (9.1)) (Elgarøy, 1961). These waves are transformed into electromagnetic waves t in the processes $l+i = t+i$. The frequency of electromagnetic waves is approximately equal to ω_{pe}, and their frequency bandwidth is defined by

$$\Delta\omega = \omega_{uH}(\theta) - \omega_{uH}(0) \approx \frac{\omega_{Be}^2}{2\omega_{pe}} \sin^2\theta, \tag{10.2}$$

in the case of a small magnetic field $\omega_{Be} \ll \omega_{pe}$. As a result, for the relative frequency bandwidth we obtain Eq. 9.3.

Taking into account that the plasma density in the corona follows the Baumbach-Allen law $n \approx R^{-6}$ at altitudes from which radio emission at decametric wavelengths is emitted and that the magnetic field of the Sun is mainly a dipole $B \approx R^{-3}$, then the ratio ω_{Be}/ω_{pe} is almost independent of the altitude. Comparing Eqs. (10.1) and (9.3), we get

$$A = \frac{\omega_{Be}^2}{2\omega_{pe}^2} \sin^2 \theta. \tag{10.3}$$

From Eq. (10.3) we can derive the angle θ in which the fast electrons are confined. According to observations of decametric S-bursts (Melnik et al., 2010c), the magnitude of the magnetic field B equals about 2 G at heights from which the radio emission at decametric wavelengths escapes. Considering this value, the angle θ changes from 13° on July 28 to 18° on July 29 and July 31, 2002. We remark that these values of θ agree with the estimates of Zaitsev (1974) obtained for Type III electrons.

As stated above, the dependence of the decameter-spike duration on the frequency is very close to that for collision times, reminder that the spike duration is governed by particle collisions. If this is correct, then the temperature of the plasma at different heights can be determined by measuring the duration of spikes at the corresponding frequencies. The temperature is approximately equal to 10^6 K for July 27 to August 2, 2002.

In conclusion, we can state that decameter spikes registered at frequencies 10 MHz - 30 MHz seem to be the low-frequency continuation of meter spikes. The duration of decametric spikes, similar to metric spikes (Benz, 1986; McKim Malville et al., 1967; Tarnstrom and Philip, 1972b), may be explained by particle collisions in the plasma with a temperature of 10^6 K. Decametric spikes can be generated by electron beams similar to those that are responsible for Type III bursts, but with a lower density and smaller linear sizes than necessary for Type III bursts. In our model the frequency bandwidth of spikes is defined by the magnetic field and the angle in which the electron beam is confined.

10.2 Storm of decameter spikes

10.2.1 The storm of decameter spikes during the event of June 14, 2012

Spikes are solar radio bursts that are usually observed during high solar activity. Independently of the frequency band in which they

are observed, they have short durations and narrow frequency bandwidths when compared with other solar radio bursts.

Following Melnik et al. (2014b), the decameter bursts with short durations of about one second and narrow frequency bandwidths 50 kHz – 70 kHz chaotically located on the dynamical spectrum we call decameter spikes (Fig. 10.4). These morphological properties of the spikes make their identification simple and confident.

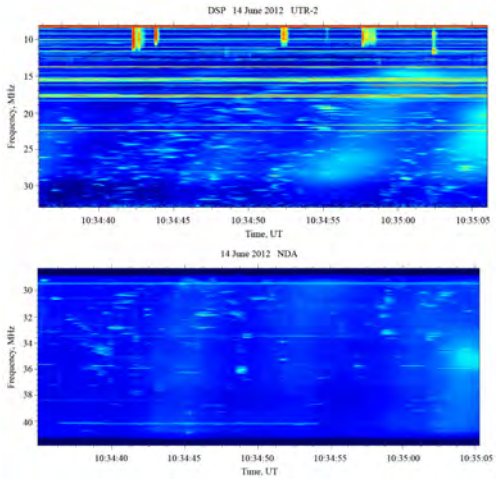
In the following the analysis of spikes simultaneously observed with the storm of Type III bursts and Type IV burst is presented. The studied event was observed in a continuous frequency band 8 MHz – 42 MHz on June 14, 2012, with the radio telescopes UTR-2, URAN-2, and NDA (Nançay Decameter Array, Nançay, France). Main parameters of the spikes (i.e. their durations, bandwidths, and fluxes) and their dependencies on the frequency are obtained.

Observations

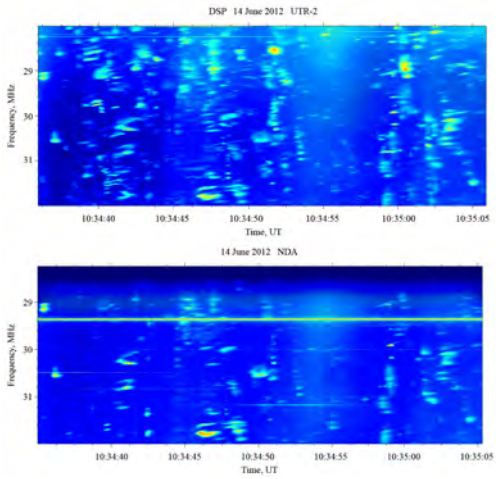
Operation of the UTR-2, URAN-2, and NDA radio telescopes provided the opportunity to conduct observations in a continuous frequency band ranging from 8 MHz to 42 MHz with an overlap in the bandwidth 28 MHz – 32 MHz (see Fig. 10.4). From these dynamical spectra it is clearly visible that the number of spikes in the frequency range 8 MHz – 32 MHz is significantly higher than in the range 28 MHz – 42 MHz. This is related to the fact that the UTR-2 radio telescope sensitivity is more than one order of magnitude higher than the sensitivity of the NDA radio telescope.

An interesting event was recorded on June 14, 2012, 04:45 – 16:00 UT. A storm of spikes was simultaneously observed with the storm of Type III bursts and a Type IV continuum (Fig. 10.5). This high activity is possibly related to the group of sunspots (NOAA 11504 – 11508) observed in the central part of the solar disk, South of the equator.

During the observations, the average flux of radio emission changed twice. Such variations of average flux can be related to changes of the coronal plasma parameters. Within the framework of the hypothesis that the durations of spikes are determined by the temperature of the ambient plasma and that their bandwidths are determined by the magnetic field in the ambient plasma, it was checked whether



(a)



(b)

Figure 10.4: *The dynamic spectrum in the frequency range 8 MHz – 42 MHz (a) and in the frequency range 28 MHz – 32 MHz (b). The upper panels correspond to the data obtained with the UTR-2 radio telescope and the lower panels to data obtained with the NDA radio telescope.*

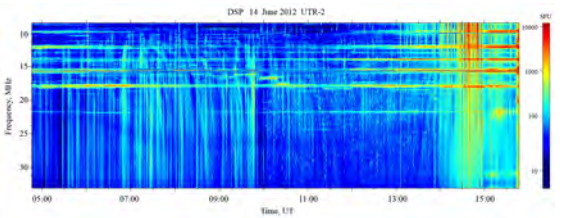


Figure 10.5: *The dynamic spectrum obtained with URAN-2 (full sunlit day of observations).*

the plasma parameters varied during the day. Hence, the observations were divided into three time intervals. A considerable number of spikes were analyzed for each time interval. For the first time interval, more than 500 spikes were measured, for the second time interval more than 800, and for the third interval more than 300 spikes. The spike parameters were measured manually using temporal and frequency profiles of the bursts.

As mentioned earlier, spikes have short durations in all frequency bands. In the majority of cases the temporal profiles of spikes are not symmetrical. The decay phase of the burst is somewhat longer than the rise phase. On such profiles at half maximum flux, the rise time $\tau_{rise} = \tau_r$, the decay time $\tau_{decay} = \tau_d$, and the total duration $d = \tau_r + \tau_d$ were measured. The majority of bursts have durations of 0.4 s – 1 s. The spikes durations decrease with the frequency increase. These variations of durations with frequency are clearly visible in Fig. 10.6, which displays the spike average duration dependencies versus frequency for the first (a), second (b), and third (c) time interval.

The average values of spike duration d, rise time τ_r, and decay time τ_d at one particular frequency differ from one interval to another during the day. Starting from certain frequencies (21 MHz – 22 MHz) the average values of durations, and as a consequence also the rise and decay times, decreased during the day.

No specific dependence of the decay time on frequency for the first time interval (Fig. 10.7a) could be found, similarly to the total-duration dependence in this interval (Fig. 10.6a). The dependencies for the second and third interval (Fig. 10.7b, 10.7c), however, can

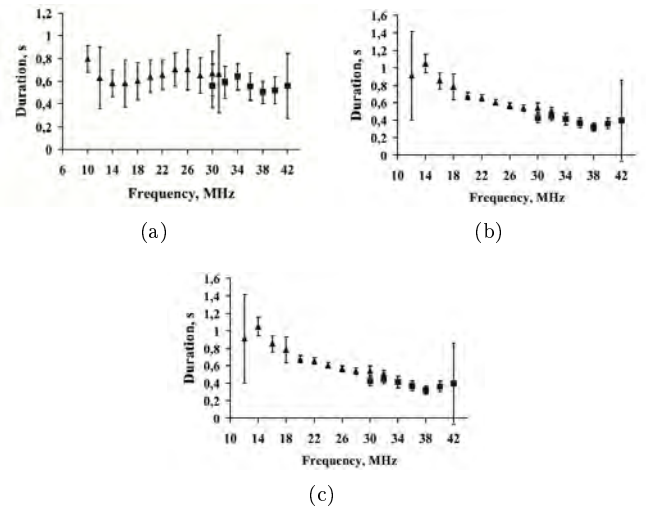


Figure 10.6: *The spike average duration versus frequency for the first (a), second (b), and third (c) temporal interval. The triangles correspond to data obtained with the UTR-2 radio telescope and squares to data obtained with the NDA radio telescope.*

be approximated by a power-law in the form of $\tau_d \propto f^p$ using the least-squares method. The power-law indices p are close to -1, having values of -1.01 and -1.05 for the second and third time interval, respectively. For comparison of dependencies and for further calculations we use the approximation $\tau_d = bf^{-1}$. The coefficient b for the second temporal interval is about 7.6 and for the third interval is approximately 6.4.

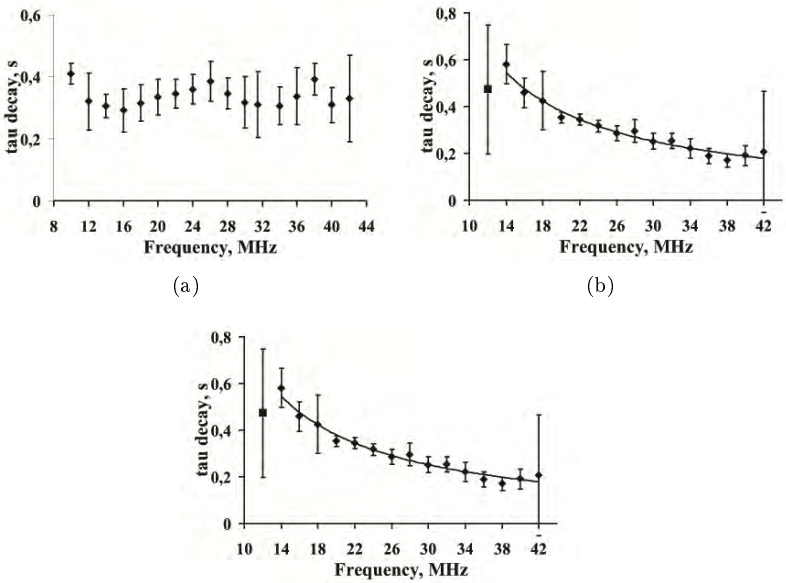


Figure 10.7: *The dependencies of average values τ_d on frequency for the first (a), second (b), and third (c) time interval.*

The decay time of spikes τ_d is comparable with the damping time τ_{coll} of Langmuir waves in a plasma. The damping time is determined by the temperature of the ambient plasma as follows:

$$\tau_{coll} = \frac{1}{n\sigma v_{Te}} \propto \frac{1}{\Lambda} \frac{T^{\frac{3}{2}}}{f^2}, \tag{10.4}$$

where n denotes the plasma density, σ is the transport cross-section, Λ is the Coulomb logarithm, v_{Te} is the electron thermal velocity, e is the electron charge, m is the electron mass, T is the temperature, and f is the frequency.

As a consequence, if $\tau_d \approx \tau_{coll}$, then, by knowing the spike decay time and using Eq. (10.4), we can estimate the temperature of the coronal plasma at the distance from the Sun which corresponds to each observing frequency

$$T = 8 \cdot 10^3 f^{4/3} \tau_{coll}^{2/3} \tag{10.5}$$

The obtained values and dependencies of the temperature versus the frequency for all temporal intervals are presented in Fig. 10.8.

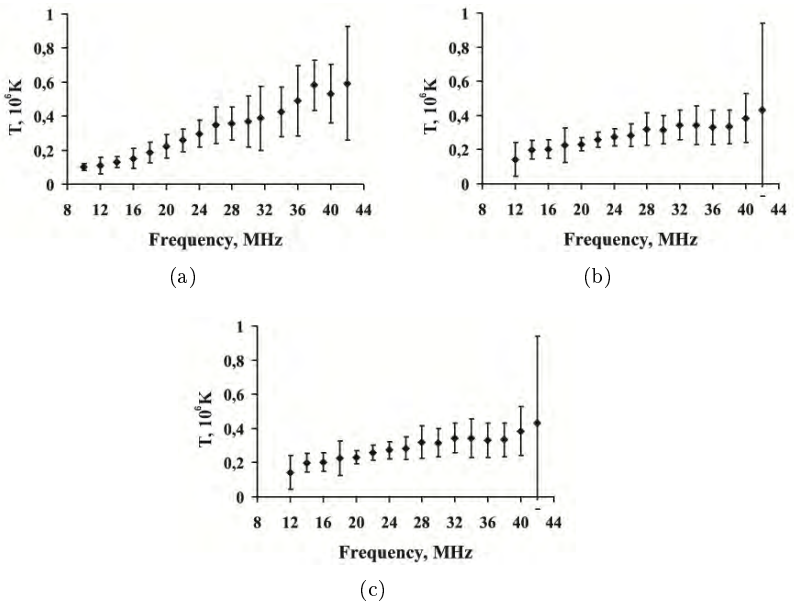


Figure 10.8: *The dependencies of the coronal plasma temperature on frequency for all three time intervals.*

The results indicate that the temperature T is rising when the

frequency is increasing, as can be expected. However, the values obtained for the temperature T are considerably smaller than the usually considered coronal plasma temperature (of the order of 10^6 K) at the distances corresponding to the decameter range. Therefore, the correspondence of the coronal temperatures obtained with the high-frequency spikes (362 MHz – 1010 MHz) (de Groot, 1960) and the low frequency spikes (8 MHz – 42 MHz) was investigated: The temperatures obtained in the present study are in good agreement with the temperatures found in (de Groot, 1960). We can conclude that if the decay time is defined by the particle collision time, then by knowing the duration of the spikes at different frequencies, we can construct a profile of the coronal temperature as a function of height above the solar surface.

Spikes have a narrow frequency bandwidth, which depends on the frequency. In contrast to the temporal profile, the frequency profile of spikes is symmetrical. The average value of the decameter spike bandwidth grows with the frequency, from 25 ± 5.8 kHz at frequency 11 MHz to 80 ± 17.2 kHz at frequency 40 MHz, which is approximately 0.2 % of the central frequency. The dependencies of the bandwidth on the frequency for all three time intervals are presented in Fig. 10.9.

These dependencies can be approximated by a linear function similar to Eq. (10.1). Based on the assumptions proposed by Melnik et al. (2014b), the angle θ in which the beam of electrons is confined can be obtained:

$$\theta = \arcsin \sqrt{2A} \frac{\omega_{pe}}{\omega_{Be}}.$$

If we assume that the magnetic field B is about 2 G at the distance that corresponds to the decameter range (Droege, 1977), then the angle θ changes from 12° to 17° for the observed values of A (Table (10.1)).

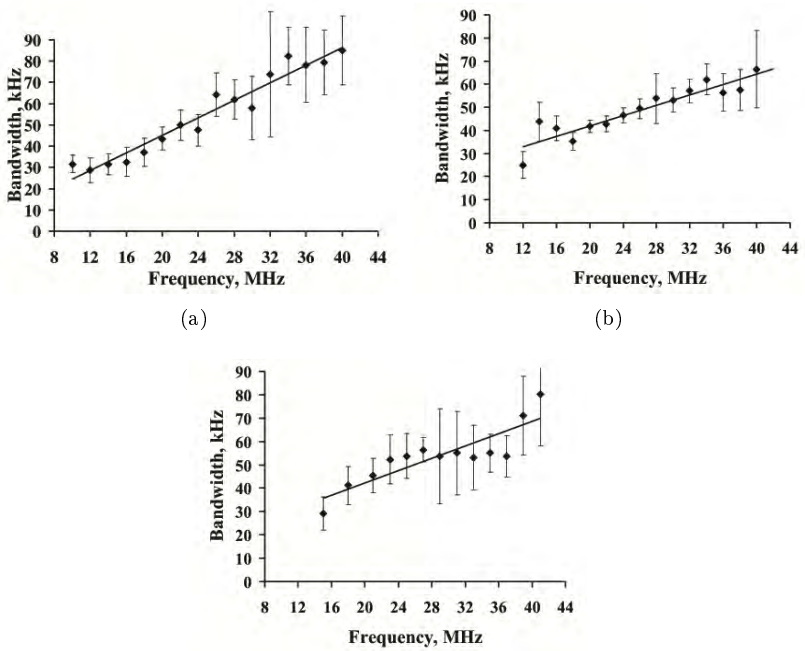


Figure 10.9: *The dependencies of the spike bandwidth on the frequency for all three time intervals.*

Table 10.1: *The values of coefficient of proportionality A and angle θ.*

	Temporal interval		
	I	II	III
A	$2.1 \cdot 10^{-3}$	$1.1 \cdot 10^{-3}$	$1.3 \cdot 10^{-3}$
θ	17°	12°	13°

We note that these values of θ agree well with the estimates obtained by Zaitsev (1975) and by Melnik et al. (2010c).

As mentioned, generally speaking, the decameter spike fluxes do not exceed 500 s.f.u. and in most cases they are even below 100 s.f.u. (Melnik et al., 2014b). The majority of bursts occur in the range from 20 s.f.u. to 100 s.f.u. with the largest number of bursts occurring with fluxes between $20 - 40$ s.f.u. The bursts with fluxes larger than 100 s.f.u. are rare. The maximum value of the flux registered on June 14, 2012, is 520 s.f.u. The estimated brightness temperatures of the decameter spike bursts have been in the range $10^9 - 10^{10}$ K.

Radio spikes are used not only as a tool for the determination of the coronal plasma parameters, but also for tracing the changes of the temperature T and the magnetic field B in the course of a particular day. According to the analysis outlined above, the coronal temperature decreases during the day of observation. As a matter of fact, during the first temporal interval the coronal temperature at the heights $3.3R_S - 1.6R_S$ (using Newkirk's empirical coronal model) was $\approx (0.1 - 0.6) \cdot 10^6$ K. During the second and third time intervals the temperature estimated at the heights $2.9R_S - 1.6R_S$ was found to be $\approx (0.2 - 0.43) \cdot 10^6$ K and $\approx (0.13 - 0.32) \cdot 10^6$ K, respectively.

The presented observations resulted in a linear increase of the spike bandwidth with the observational frequency. Assuming that the electron beam responsible for the generation of the spikes propagates within some average angle $\theta = 15°$ (Elgarøy, 1961), then the value of the magnetic field strength B varies in the range 1.6 G $-$ 2 G during the day. The comparison of temporal characteristics of decameter spikes studied herein with those characteristics of the high-frequency spikes (de Groot, 1960) indicates the consideration of the same family of solar radio bursts.

11 Unusual Solar Bursts

11.1 Caterpillar bursts

On June 3, 2011, unusual bursts were simultaneously observed by the URAN-2 (Poltava, Ukraine) and UTR-2 (Kharkiv, Ukraine)radio telescopes (Fig. 11.1) (Brazhenko et al., 2012b). The observed solar radio burst cannot be referred to any known type of the bursts in the decameter range (Mel'Nik et al., 2005b). The unusual burst was observed at around 12:10 UT at the frequencies from $\approx$ 16 MHz to $\approx$ 27.5 MHz.

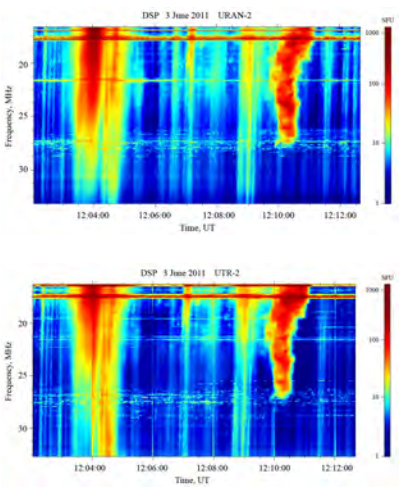


Figure 11.1: *Unusual burst in the form of a caterpillar (12:10:00 UT) observed by URAN-2 (a) and UTR-2 (b) in the course of a Type III storm on June 3, 2011.*

High frequency-time resolution of the radio telescopes exhibited a

complex fine structure of the unusual burst as shown in Fig. 11.2. The burst consists of 14 narrow-band stripes of different duration. Comparing this stripe structure with known striae fine features of Type IIIb bursts there are significant differences. In particular, the frequency bandwidth of the stripes of the unusual burst is about 300 kHz - 400 kHz whereas the striae of Type IIIb bursts in the decameter range have narrower bandwidth, only 50 kHz - 70 kHz (Melnik et al., 2010d, 2011c). The second difference is that individual striae of Type IIIb present a straight track whereas the stripes of this unusual burst looks like a serpentine. The "caterpillar" shows negative and positive frequency drifts simultaneously. In particular, the frequency drift rate of the burst is positive (about 500 kHz/s) at frequencies higher than 22 MHz and negative (- 100 kHz/s) at lower frequencies. These frequency drift rates are lower than those for Type III bursts but higher than the typical drift rates for Type II bursts in the decameter range (Mel'nik et al., 2004). The maximum flux of the unusual radio burst did not exceed 10^3 s.f.u.

The very interesting feature of the "caterpillar" is its strong cut-off at high frequencies. As shown in Fig. 11.1, the burst abruptly disappears at 27.5 MHz. At the same time there is no cut-off at low frequencies. This particular burst was also observed by STEREO significantly below 16 MHz (see Fig. 11.5).

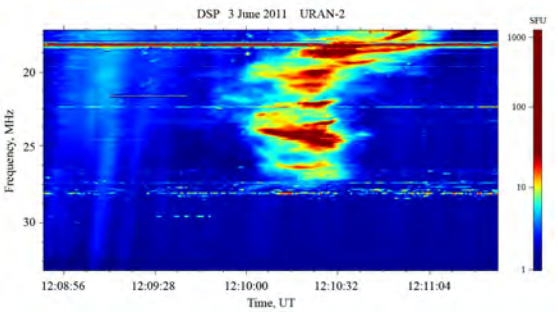


Figure 11.2: *Fine structure in the form of horizontal stripes is well visible in the high resolution radio spectra of the unusual burst observed by URAN-2.*

The time profile of the unusual burst at 26 MHz is shown in

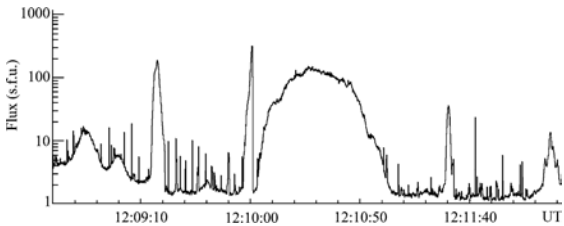


Figure 11.3: *Time profile of the unusual burst at 26 MHz.*

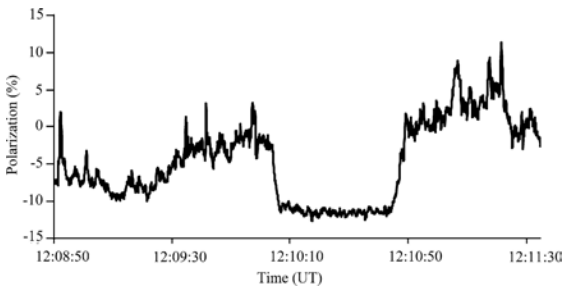


Figure 11.4: *Polarization of the unusual burst at 26 MHz according to URAN-2 observations.*

Fig. 11.3. Contrary to Type III bursts the time profile of the unusual burst had a bell-like shape. The full duration of the burst varied from 50 s at lower frequencies to 80 s at frequencies above 22 MHz. Such durations are significantly larger than the average durations of individual Type III bursts at decameter wavelengths, namely 6 s - 12 s (Mel'Nik et al., 2005b). Fig. 11.4 shows the time profile of the polarization measurements at a frequency of 26 MHz. The polarization degree of the caterpillar was practically constant and was ≈ -10 %. Such a degree of polarization is typical for the second harmonic of Type III bursts (Dulk and Suzuki, 1980). If the generation mechanism of the unusual burst is similar to those for Type III bursts, then the unusual burst was radiated at the second harmonic.

Additional to the ground-based observations also the data recorded by the radio experiment WAVES onboard the two STEREO spacecraft (STEREO-A and STEREO-B (Bougeret et al., 2008) have been analyzed. On June 3, 2011, the two spacecraft were located on the heliocentric orbits with an angular separation $\approx 180°$, i.e. on the opposite sides of the Sun (see Fig. 11.5b). The dynamic radio spectra recorded by STEREO-A and STEREO-B in the frequency range from 1 MHz to 16 MHz are shown in Fig. 11.5a. As can be seen, only STEREO-A observed the unusual burst at ≈12:10 UT. STEREO-B recorded only a group of Type III bursts at frequencies lower than 2 MHz at around 12:04 UT, which was also well visible at higher frequencies in the UTR-2 and URAN-2 spectra (see Fig. 11.1). Taking into account the positions of STEREO-A and STEREO-B (Fig. 11.5b) the source of the unusual burst was obviously situated on the West side of the Sun with respect to the Earth.

After the detection of the caterpillar (at 12:10 UT) two coronagraphs LASCO C2 and C3 onboard SOHO have observed three phenomena on the West side of the solar disk (Fig. 11.6). In particular, LASCO C2 recorded two successive ejections at 12:48 UT and 13:36 UT. The sizes of these two ejections were smaller than the typical size of coronal mass ejections (CMEs). At 12:48 UT there was also a jet at a latitude higher than those of the ejections (Fig. 11.6). According to UV images from SOHO (Fig. 11.7a) no active regions were detected on the West side of the solar disk. At the same time STEREO-A/EUVI observed two active regions NOAA 1224 and NOAA 1222 located at approximately $100°$ and $130° - 140°$ of Western longitude

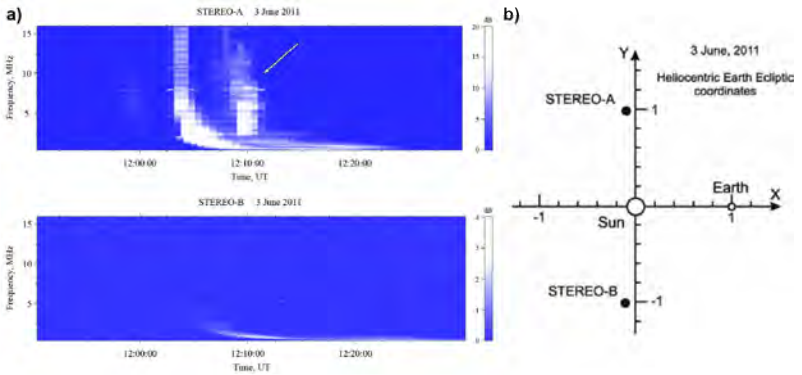


Figure 11.5: *Radio spectra obtained by WAVES experiment onboard STEREO-A and STEREO-B on June 3, 2011 (panel (a)). The unusual solar radio burst was observed only by STEREO-A (marked by an arrow). Panel (b) shows the positions of the spacecraft in the heliocentric Earth ecliptic coordinates.*

with respect to the central meridian (Fig. 11.7b). Since NOAA 1222 was on a lower latitude than the active region NOAA 1224 the former may have initiated two ejections while NOAA 1224 triggered the jet. Analyzing the dynamics of jets (Brazhenko et al., 2012b; Melnik et al., 2014a) the first jet was likely responsible for the unusual burst, which was radiated by the magnetic flux rope from the distance at frequency 22 MHz. This flux rope was connected with the active region NOAA 1222. The jet moved through the plasma of the solar corona. This source of fast electrons, propagated towards and away from the Sun. The first one generated the part of the unusual burst with positive drift rate and the other one radiated the part with negative drift rate. Radiation occurred at the second harmonic and this radio emission in particular might be coming from a behind-limb location (Fig. 11.8) (Melnik et al., 2012, 2014a).

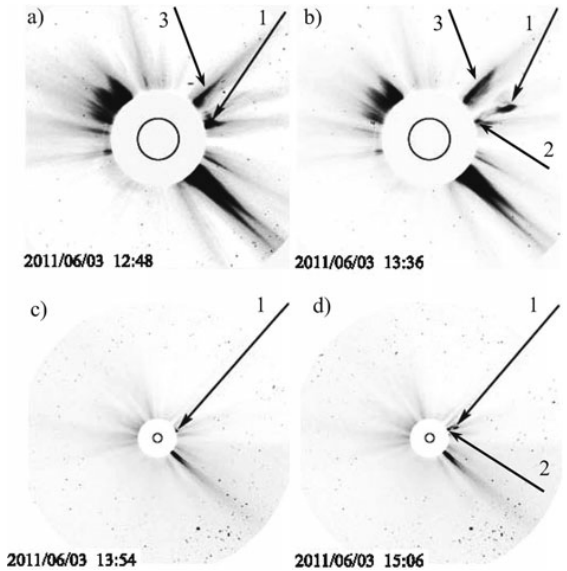


Figure 11.6: *Two ejections (1 and 2) and jet (3) observed by LASCO C2 ((a), (b)) and by LASCO C3 ((c), (d)) at the given moments of time.*

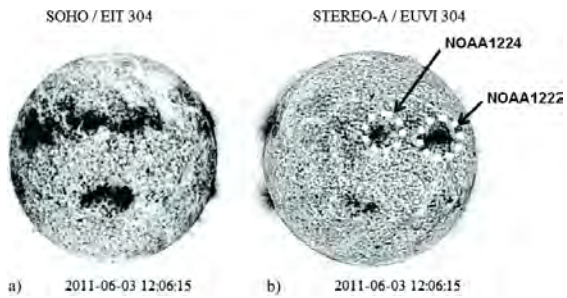


Figure 11.7: *The solar disk with active regions observed by SOHO Extreme ultraviolet Imaging Telescope (SOHO/EIT 304 Å) (a) and STEREO-A Extreme UltraViolet Imager (SECCHI EUVI) (b).*

11.1.1 Discussion

There is a possibility for the radio emission at the second harmonic of the local plasma frequency to propagate from a behind-the-limb region of the Sun towards the Earth. As outlined in the paper by Melnik et al. (2014a), the unusual burst seems to be generated at the second harmonic of the local plasma frequency. This follows from the low degree of polarization of the unusual radio burst which was about 10 %. Note that the fundamental radio emission is found with a higher degree of polarization (Type IIIb bursts have 60 % - 80 %) (Mel'Nik et al., 2005b).

Fig. 11.8 presents the scheme of such a propagation path. The radio source is located at a distance R_H from the solar center with the longitude α. The second harmonic can propagate towards the Earth if the distance R_1 is larger than the distance R_F from the Sun, which corresponds to the radial distance at which the local plasma frequency ω_F in the solar corona equals the double plasma frequency $\omega_H = 2\omega_{pe}$ at the place of generation of the second harmonic $\omega_H(R = R_F) = \omega_H(R = R_H) = 2\omega_{pe}$. Therefore, the condition for the observation of the behind-the-limb radio emission is

$$R_1 > R_F. \tag{11.1}$$

In the opposite case, when $R_1 < R_F$, the radio emission at the second harmonic cannot propagate towards the Earth. In the case of the Newkirk model (Newkirk, 1961) of the solar corona, $n = n_N 10^{4.32/r_n}$, where $n_N = 4.2{\cdot}10^4 \mathrm{cm}^{-3}$ and $r_n = R/R_S$, Equation (11.1) is satisfied when

$$R_H > \frac{2.16}{\log 2}\left(\frac{1}{\cos\alpha} - 1\right) R_S. \tag{11.2}$$

For the Baumbach-Allen model (Allen, 1947), $n = n_{BA}(1.55r^{-6} + 2.99r^{-16})$ with $n_{BA} = 10^8 \mathrm{cm}^{-3}$, we have

$$\cos\alpha > 2^{-1/3}. \tag{11.3}$$

For simplicity in the case of distances $r > 1.5$, we take into account only the first term, i.e. $n = n_{BA} 1.55 r^{-6}$. A similar result is obtained for the Leblanc model (Leblanc et al., 1998).

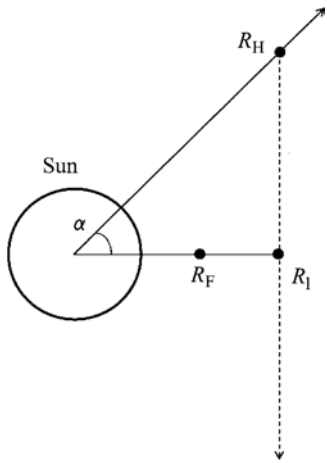


Figure 11.8: *Scheme of propagation of radio emission at the second harmonic $\omega_H = 2\omega_{pe}$ (at altitude R_H) in the direction towards the Earth (latitudinal plane).*

We can therefore define the regions in the "frequency-longitudinal angle" plane (Fig. 11.9), where the radio emission at the second harmonic can propagate toward the Earth. In the case of the Baumbach-Allen model the emission can be detected at the Earth if the source is at the longitudinal angle $\alpha < 37.5°$. Moreover, the radio emission can be observed in the whole frequency range (Fig. 11.9, to the left from the dashed line). If, however, the coronal density follows the Newkirk model, then the highest possible frequency (or the cut-off frequency) of the radio emission at the second harmonic detected at the Earth depends on the longitudinal angle α (Fig. 11.9, solid line). Therefore, in this case, the radio emission can be observed in regions to the left of the solid line in Fig. 11.9. This line is defined by

$$f^* = \frac{1}{2\pi}\left(\frac{e^2 n_N}{m_e \epsilon_0}\right)^{1/2} 2^{\cos\alpha/(1-\cos\alpha)}, \tag{11.4}$$

here e and m_e are the charge and mass of the electron.

Summarizing the unusual burst observed by radio telescopes UTR-2 and URAN-2 at frequencies 16 MHz - 27 MHz had the following

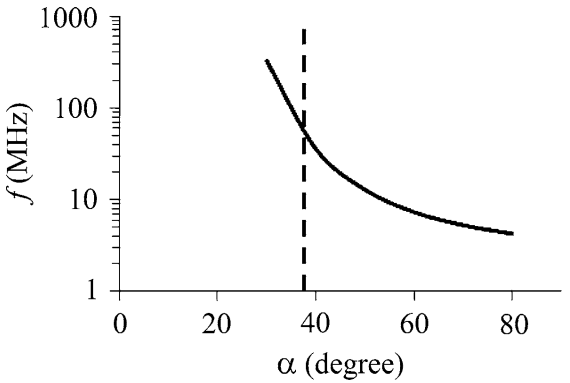


Figure 11.9: *Regions of propagation of the second harmonic radio emission to the Earth from the "behind-the limb" hemisphere in the Baumbach-Allen (dashed line) and Newkirk (solid line) models.*

properties:

1. Radio emission was emitted from a behind-the-limb region.
2. The burst had some unusual properties which are not typical for other known solar bursts. In particular,
   - the frequency drift rate was negative at low frequencies and positive at high frequencies;
   - the frequency drift rate changed in the range from 100 kHz/s to 500 kHz/s;
   - the burst disappeared at frequencies > 27.5 MHz, i.e. it showed a strong frequency cut-off effect;
   - the total duration of the burst (50 s - 80 s) was longer than that for the usual Type III bursts;
   - the burst had a fine structure in the form of stripes with frequency bandwidth 300 kHz - 400 kHz.
3. The polarization of the burst was about 10 %, which corresponds to the second harmonic of radio emission.

4. The radio flux of the burst attained 10^3 s.f.u.

5. The unusual burst was observed at a frequency as low as 1 MHz (STEREO/ WAVES data).

The following scenario of the generation of the caterpillar burst was proposed by Melnik et al. (2012) and Melnik et al. (2014a). The unusual burst was associated with the active region NOAA1222 which on June 3, 2011, started to be active at about 11:36 UT. The magnetic flux rope, which assumed to be associated with this activity, propagated radially with a velocity of about 500 km/s away from the Sun. At heights $R = 2.22R_S - 2.55R_S$ the magnetic flux rope accelerated electrons. Moving toward and away from the Sun these particles generated the radio emission which was observed as the unusual radio burst. The particles propagating towards the Sun produced the radio emission with a drift from low to high frequencies whereas particles moving away from the Sun generated the radio emission drifting from high to low frequencies. The velocities of the accelerated particles varied from $0.8 \cdot 10^9$ cm/s to $1.4 \cdot 10^9$ cm/s. At frequencies > 27.5 MHz the unusual burst was no longer observable because its radio emission could not propagate through the plasma of the solar corona towards the Earth.

11.2 New class of solar bursts with cut-off frequency

In the previous subsection, the unusual burst with a frequency cut-off, the so-called "caterpillar burst" (Melnik et al., 2014a), was discussed as it was generated in a behind-limb place. As shown in the following, the burst observed on June 3, 2011, was not an exclusive case, but was rather the representation of a new class of solar decameter bursts. From the model of caterpillar burst it follows that such bursts should appear more frequently in the decameter and hectometer ranges. Analyzing data of 2011 - 2014, obtained by the radio telescope URAN-2 in the frequency band 8 MHz - 32 MHz, representative examples of such bursts have been found (Brazhenko et al., 2015a). During the period of 2011 - 2014, 122 bursts with high-frequency cut-offs, similar

to the caterpillar burst registered on June 3, 2011, have been registered. Full durations of these bursts varied from 10 s to 250 s. These durations are much longer than those for the usual decameter Type III bursts. The average forward frequency drift rate (from high to low frequencies) was 0.9 MHz/s. This value is significantly lower than for typical decameter Type III bursts. In cases when these caterpillar bursts had also reverse drift rates (drifts from low to high frequencies) the drift rates were slightly smaller than those of typical Type III bursts. Most caterpillars had fluxes of 1 s.f.u. to 200 s.f.u. Some of these bursts had fine spectral structures in the form of stripes with a frequency bandwidth 250 - 500 kHz and small drift rates 20 kHz/s - 40 kHz/s. The polarization of most of the reported caterpillar bursts was in the range 10 % - 20 %.

Observations

The majority of caterpillar bursts had rather low fluxes (Fig. 11.10), contrary to decameter Type III bursts with fluxes of more than 10^3 s.f.u. (Melnik et al., 2011a). This fact can be explained having in mind that these bursts are generated in behind-limb regions of the solar corona and reaching Earth they need to pass a considerable thickness of coronal plasma suffering absorption and scattering. The observed number of caterpillar bursts increases with decreasing cut-off frequency (from 33 MHz down to 26 MHz) and the number of such bursts decreases at frequencies below 26 MHz (Fig.11.11).

The full duration of caterpillar bursts changed from 10 s to 250 s with an average value of about 40 s (Fig.11.12(a)). The half-flux duration was in the range 5 s - 100 s (Fig.11.12(b)) with an average duration of 15 s. These values are larger than those for usual Type III bursts at frequencies 10 MHz - 30 MHz.

The polarization of caterpillar bursts at the frequency of maximum flux is not high (Fig.11.13), practically all bursts had 10 % -20 % polarization. Assuming that the mechanism of radio emission of these bursts is the plasma mechanism then we can expect that the radio emission with low polarization occurs at the second harmonic. This is in line with the hypothesis that caterpillar bursts are generated in the behind-limb corona because only the second harmonic can reach the Earth from behind-limb regions. 28% of caterpillar bursts had

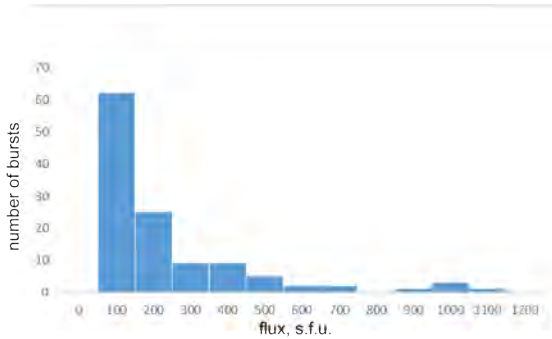


Figure 11.10: *Histogram of cut-off bursts observed in the years 2011 - 2014 by their maximum flux.*

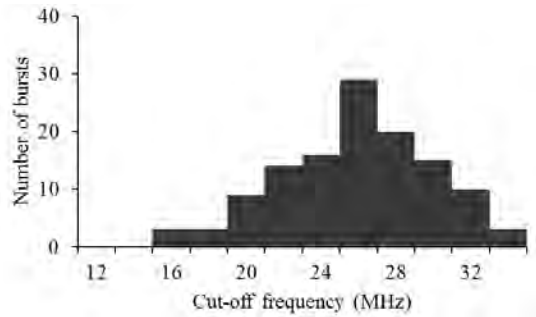
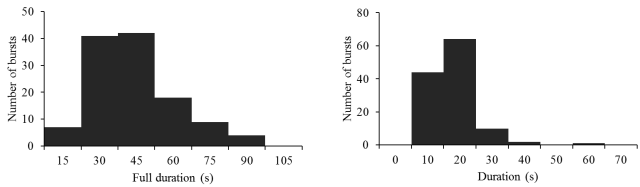


Figure 11.11: *Distribution of caterpillar bursts via cut-off frequency.*



(a) (b)

Figure 11.12: *Histograms of high-frequency cut-offs by their full (a) and half-flux (b) durations.*

a dynamical structure at which the frequency drift rate changed the sign. The average drift rates of the observed caterpillar bursts are 0.9 MHz/s and 1.3 MHz/s for forward and inverse drifting bursts, respectively. In both cases these values are smaller than the frequency drift rates of decameter Type III bursts.

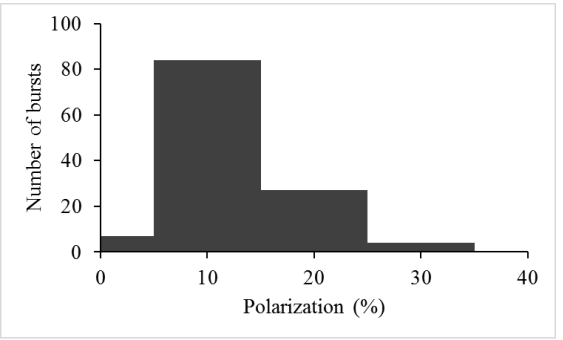
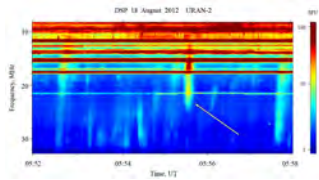
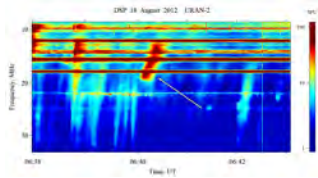


Figure 11.13: *Polarization of caterpillar bursts.*

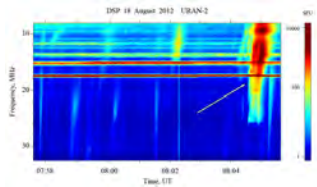
An interesting day with observations of caterpillar bursts was August 18, 2012, observed from 4:35 UT to 14:35 UT. Some of them are presented in Fig. 11.14. All the bursts had sudden cut-offs at high frequencies similar to the caterpillar burst observed on June 3, 2011 (Melnik et al., 2014a). At this day nine intense caterpillar bursts with fluxes $0.5 \cdot 10^2 - 4 \cdot 10^3$ s.f.u. (see Table 11.1, column 8) were registered together with several weaker ones which were difficult to analyze. The cut-off frequencies were different for each of the bursts and were in the frequency range 14.7 MHz - 26.3 MHz (column 6). The full durations of the bursts varied from 20 s to 90 s (column 2) which were larger than for usual decameter Type III bursts. Their half-flux durations were in the 9 s - 28 s range (column 3), which is two times longer than those for Type III bursts. Six out of nine observed caterpillar bursts (column 5) had changes of the sign of their drift rates from negative to positive ones. The remaining three bursts drifted from high to low frequencies with negative drift rates. The instantaneous start of bursts occurred at frequencies where the drift rates changed their signs. These frequencies were from 12.7 MHz to 18.8 MHz (column 7). Negative drift rates of these bursts were es-



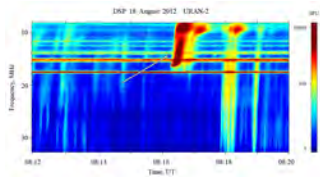
(a)



(b)



(c)



(d)

Figure 11.14: *Dynamic radio spectra of the caterpillar bursts observed on August 18, 2012, by the URAN-2 radio telescope. The analysed bursts are marked by arrows.*

sentially smaller than those for usual Type III bursts. The average value of negative drift rate for all nine caterpillar bursts is 0.55 MHz/s which is close to the drift rate of the burst observed on June 3, 2011 (Melnik et al., 2014b). The positive drift rates varied from 3.3 MHz/s for the burst at 05:55 UT to 0.3 MHz/s for the burst at 6:40 UT. The average positive drift rate for six bursts was 1.45 MHz/s and it was slightly larger than for the burst registered on June 3, 2011.

All caterpillar bursts had polarizations at or below 15% (Table 11.1, column 9). Such polarization is typical for the second harmonic of Type III bursts. Only five caterpillar bursts observed on August 18, 2012, had fine structures. The burst registered at 05:55 UT had stripes with frequency widths of about 500 kHz and with small negative drifts. Frequency widths of stripes at 08:05 UT were from 250 kHz to 500 kHz. Their frequency drifts were negative from high to low frequencies, however sometimes drift rates became positive. Therefore, the stripes of the bursts registered in this day are similar to the stripes in the burst of June 3, 2011.

Table 11.1: *Parameters of caterpillar bursts registered on August 18, 2012, by the radio telescope URAN-2. Column 1: time [UT]; column 2: full duration [s]; column 3: half flux duration [s]; column 4: forward frequency drift rate [MHz/s]; column 5: reverse frequency drift rate [MHz/s]; column 6: frequency cut-off [MHz]; column 7: turning frequency [MHz]; column 8: maximum flux [s.f.u].; column 9: polarization [%]; column 10: fine structure*

1	2	3	4	5	6	7	8	9	10
05:55	20-30	9	-0.8	3.3	24.5	18.3	$0.5 \cdot 10^2$	10	yes
06:40	30-35	15	-0.4	0.3	19.9	18.8	$0.5 \cdot 10^2$	10	yes
07:10	30-50	12	-0.5	0.9	18.4	12.7	$1.7 \cdot 10^2$	10	no
08:05	50-90	27	-0.6	2.5	26.3	17.4	$1.6 \cdot 10^3$	15	yes
08:16	40-50	18	-0.4	-	16.5	-	$4.0 \cdot 10^3$	10	no
11:06	30-50	16	-0.4	-	14.7	-	$0.8 \cdot 10^2$	10	no
11:36	40-50	18	-0.6	-	19.9	-	$4.0 \cdot 10^3$	10	no
11:38	50-70	28	-0.5	1.3	19	15.5	$6.0 \cdot 10^2$	15	yes
11:55	20-30	14	-0.4	0.8	21.1	18.5	$1.2 \cdot 10^2$	10	yes

The particular caterpillar burst registered on June 3, 2011, has been associated with an optically observed jet moving outwards the Sun. At some altitude it generated electron beams propagating to-

wards and away from the Sun. The former apparently was responsible for the part of the caterpillar burst with reverse (positive) drift rate and the latter responsible for the part of the caterpillar burst with forward (negative) drift rate. Trying to find similar jets on August 18, 2012, at the time of registration of caterpillar bursts this day, two jets were detected by SOHO and STEREO (Fig.11.15) at 6:40 UT and 7:10 UT when caterpillar bursts with forward and reverse drift rates were observed.

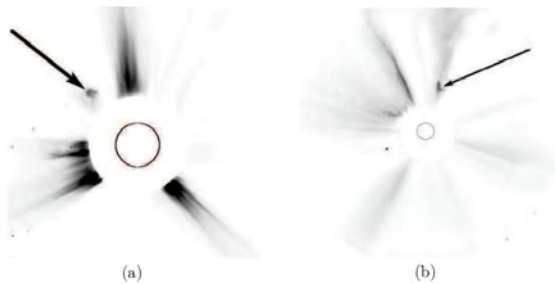


Figure 11.15: *Jets observed on August 18, 2012, by SOHO C2 (a) and STEREO-B/COR2 (b).*

Responsible for the unusual bursts are most likely active regions situated on the back side of the Sun (Fig. 11.16), namely, groups I and II and NOAA 1548. The connection between cut-off frequency and longitudinal angle is given by Eq. (11.4). If the latitude is not 0° then instead of $\cos\alpha$ we have to put $\cos\gamma = \sqrt{\sin^2\beta + \cos^2\beta\cos^2\alpha}$, where β is the latitude and γ is the longitude in the plane passing through the place of radio emission and line of sight. Supposing that the active regions II or NOAA 1548 with latitude $\beta \approx 30^\circ$ were responsible for the caterpillar bursts observed on August 18, 2012, we obtained longitudes in the range $50^\circ - 60^\circ$ for the cut-off frequencies 14.7 MHz - 26.3 MHz. Such longitudes correspond to the active region II. As a conclusion the caterpillar bursts of August 18, 2012, are associated with this active region.

Since the first identification of the caterpillar burst observed on June 3, 2011, the UTR-2 and URAN-2 radio telescopes registered some tens of such type of bursts in the decameter frequency range.

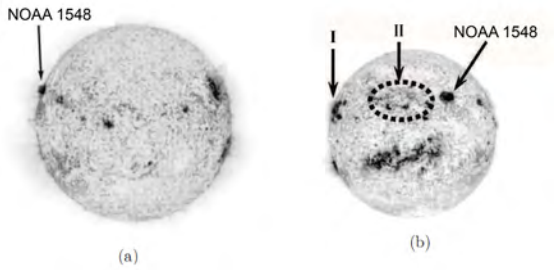


Figure 11.16: *Active regions at the solar disk on August 18, 2012, observed by SOHO/EIT 304 (a) and STEREO-B/SECCHI EUVI (b).*

These relatively rare events were detected simultaneously with small jets observed by SOHO/EIT 304 A and STEREO/SECCHI EUVI. It is worth mentioning that in most cases the caterpillar bursts were seen at times when no active regions were located on the visible hemisphere of the Sun, as seen from Earth, however observable by spacecraft. This indicates that caterpillar bursts are behind-limb events. It is possible to observe the radio emissions of caterpillar bursts by terrestrial radio telescopes if radiated at the second harmonic. All these bursts have low degrees of polarization which is characteristic for the second harmonic of the radio emission.

The main properties of caterpillar bursts can be summarized as follows:

- Durations of caterpillar bursts are twice as long as usual Type III bursts.
- Duration in average is about 17 s for caterpillar bursts and 9 s for Type III bursts; full durations of caterpillar bursts are equal to tens of seconds.
- Frequency drift rates of these bursts (0.4 MHz/s - 0.8 MHz/s) are smaller than those for decameter Type III bursts.
- Some caterpillar bursts change the sign of their drift rates from negative to positive ones.

- Positive drift rates of caterpillar bursts change in a wide range from 0.3 MHz/s up to 3.3 MHz/s which is close to the drift rates of decameter Type III bursts.
- The presence of fine spectral structures in the caterpillar bursts differs from usual decameter Type III bursts.
- The polarization degree of these bursts is low, in most cases not exceeding 15 %.
- At times when caterpillar bursts were registered, jets from behind-limb active regions have been observed.
- The proposed model for caterpillar bursts as second harmonic of behind-limb radio emission enables the definition of the location of the active regions.

12 Propagation and Radio Emission of Electron Beams in the Solar Corona

The only real mechanism that can be considered for the explanation of the solar sporadic radio emission in the meter and decameter range, is the plasma mechanism. The main reason for this is due to the large brightness temperature of observed radio emissions. The maximum of brightness temperature is about 10^{15} K and its average value is $10^{10} - 10^{12}$ K. At the same time the temperature of the plasma emitting this radiation is only $2 \cdot 10^6$ K. Thus, a non-thermal mechanism for the explanation of such radio emission is necessary. One of them is the plasma mechanism based on the transformation of Langmuir waves into electromagnetic waves. These waves must be generated by some source. It can be connected with solar flares because such a radio emission in the form of different types of bursts happened during or after solar flares. In solar flares, particles, in particular electrons, are accelerated to high energies and they can generate Langmuir waves. Their velocity must be about $10^{10} cm/s$, to propagate from the flare to the place, where radio emission is generated at a corresponding frequency. It should be noted that protons can also be considered a source of different bursts, including Type III bursts. But their number at such velocities may not be sufficient as an effective source of radio emission. Thus, the only particles that generate Langmuir waves, are high energy electrons with velocities of about $0.3c$. In a plasma with such electrons (electron beams) the so-called two-stream instability (i.e. beam instability) is developed and as a result Langmuir waves are generated in the plasma. The characteristic time of the instability (the so-called quasi-linear relaxation

time) is $\tau_q = \left(\omega_{pe}\frac{n'}{n}\right)^{-1}$, where n is the plasma density, n' is the density of high energy electrons, $\omega_{pe} = \sqrt{\frac{e^2 n}{m\epsilon_0}}$ is the plasma frequency. Assuming a density of the high energy electrons $\frac{n'}{n} = 10^{-5} - 10^{-7}$ close to the flare with a plasma density $10^8 - 10^9 \mathrm{cm}^{-3}$ (the plasma frequency is equal to $\omega_{pe} = 5 \cdot 10^8 - 1.5 \cdot 10^9$ Hz), this quasi-linear relaxation time is about $\tau_q = 10^{-2} - 10^{-4}$s. During this time τ_q Langmuir waves are generated and a plateau at the electron distribution function is established. Subsequently, the generation of waves stops. The corresponding length is $l_q = 10^6 - 10^8$ cm. Thus, only immediately near the flare is there a high level of Langmuir turbulence, and as a result plasma radio emission of electron beams should be excited near the flare or at frequencies $f = 10^8 - 3 \cdot 10^8$ Hz. The conclusion of Langmuir waves being generated near the flare is based on the assumption of an endless electron beam. But in reality the electron beam has a finite size so the result will be different. Even if the quasi-linear relaxation establishes a plateau at the electron distribution function at a small distance from the flare, the finite size of the electron beam again sets up the conditions for the two-stream instability. The fact of the matter is that fast electrons overrun slow electrons and then can again incite Langmuir waves due to the two-stream instability. Realizing this fact may support the understanding of the continuous radio emission of electron beams at large distances from flares.

In 1961, some groups simultaneously formulated kinetic equations for electron distribution functions and spectral energy density of Langmuir waves, which interacted with electrons (Zheleznyakov and Zaitsev, 1970). One of their main results was an understanding of the role of slow electrons overrun by fast electrons in the recovery of the two-stream instability. However, Zheleznyakov and Zaitsev did not find any analytical description of the problem. In 1970 Ryutov and Sagdeev (1970) analyzed kinetic equations, in which the interaction of electrons and Langmuir waves was accounted for, and proposed to shift the problem to a gas-dynamic description. This was justified in the cases when the time of electron-wave interaction was minor in comparison with other charactistic times in the problem. The situation in the problems of interacting particles is analogous to that at the

transition from a kinetic description to a gas-dynamic one. However, they did not obtain the complete system of gas-dynamic equations. They also found only self-similar solutions. This work, in particular the development of the gas-dynamic equations and these solutions, was later criticized. Nevertheless, Zaitsev et al. (1972) could find an explanation of Type III burst properties. They concluded that in spite of fast quasilinear relaxation, high-energy electrons really could generate Langmuir waves at great distances from the place of injection. In addition, the velocities of Type III bursts sources remained constant, in agreement with observations.

There are some attempts to numerically solve the kinetic equations describing the spread of fast electrons, which incite and absorb Langmuir waves, in application to Type III bursts. The results confirmed that fast electrons could propagate high in the solar corona and generate plasma waves of high level.

13 Radio Seismology of the Outer Solar Corona

Magnetohydrodynamic (MHD) waves and oscillations are ubiquitous in the solar corona (Nakariakov and Verwichte, 2005). The waves may heat the ambient plasma and accelerate solar wind particles (Aschwanden, 2004). Observations show the existence of almost all MHD modes (fast kink, fast sausage and slow magneto-acoustic waves) in the solar corona (Aschwanden et al., 1999; Nakariakov et al., 1999; Ofman et al., 1999; Nakariakov et al., 2003; Wang et al., 2003a,b; Wang and Solanki, 2004; Srivastava et al., 2008). Oscillations are mainly observed through imaging observations, but their spectroscopical indications are also possible. For example, purely incompressible torsional oscillation can be observed in coronal loops as periodic variations of spectral line broadening (Zaqarashvili, 2003). Observed MHD oscillations can be used to estimate plasma parameters in the solar corona using known theoretical properties of MHD waves (Roberts et al., 1984). This method, referred to as coronal seismology (Nakariakov and Ofman, 2001), has been used effectively to determine magnetic field strength, stratification and other plasma properties of coronal loops (Arregui et al., 2007; Van Doorsselaere et al., 2007; McEwan et al., 2008; Andries et al., 2009; Verth et al., 2010; Arregui and Asensio Ramos, 2011), spicules (Zaqarashvili et al., 2007; Zaqarashvili and Murawski, 2007; Zaqarashvili and Erdélyi, 2009; Verth et al., 2011) and prominences (Arregui et al., 2012, and references therein). The oscillations are mainly observed in the inner corona, where the intensity of EUV lines allows to detect active region coronal loops. In the outer corona, the oscillations are not yet detected because of EUV line intensity decrease with altitude. Besides the EUV part of spectrum, the solar corona can be observed in the radio frequency band, which is very important to study the rapid oscillations of the solar atmosphere owing to high temporal resolution. High-frequency oscil-

lations (< 1 min) are frequently detected in the radio observations (Aschwanden et al., 2004) (see Table (7.1)). According to Aschwanden et al. (2004) most of the reported oscillations fall in the frequency range of 100 MHz - 1000 MHz corresponding to the electron densities of $10^8 - 10^{10}\mathrm{cm}^{-3}$. Therefore, the radio emission originates from the inner corona and consequently the oscillations can be interpreted as fast sausage modes in short low-laying coronal loops (Nakariakov et al., 2003; Aschwanden et al., 2004). Long period modulation (with 5 min to 10 min) in the microwave range of $> 1\,\mathrm{GHz}$ can be explained by the kink oscillations of coronal loops (Khodachenko et al., 2011). Recent high-resolution data obtained with the Nobeyama Radioheliograph show the frequency drift of 3-min oscillations, which can be explained by the dispersive evolution of upward propagating wave pulses (Sych et al., 2012).

Hence, the radio observations are very important in studying the plasma properties of the inner corona. On the other hand, radio observations in the frequency range of 10 MHz - 100 MHz are very important in the outer corona. Flare related activity at decameter wavelengths is manifested in great variety of bursts: Type II-IV bursts, drifting pairs, S-bursts, spikes bursts in absorption etc. (Melnik et al., 2011b). Some of them are continuations of the same bursts from decimeter and meter bands such as Type III bursts, Type II bursts, Type IV bursts, spikes. There are some bursts, which are observed in the long meter and decameter range only, namely Type IIIb bursts, drifting pairs, S-bursts.

The plasma mechanism of radio emission is usually used for the explanation of these bursts (Ginzburg and Zhelezniakov, 1958). This mechanism has two stages. The first stage is the generation of Langmuir waves by fast electrons and the second stage is the emission of electromagnetic waves by the Langmuir waves. In this mechanism, the frequency of radio emission equals the local plasma frequency or double local plasma frequency. Then the radio emission at a given frequency is originated in the plasma at a corresponding height above the solar surface. Considering the decameter band (8 MHz - 32 MHz), therefore the radio emission at these frequencies is generated at heights $\geq 1R_S$ above the solar surface depending on the density structure of the solar corona.

Type IV bursts at decameter wavelength were first observed by the

UTR-2 radio telescope during the observational campaign in 2002 - 2004 (Melnik et al., 2008). The duration of the bursts was from 1.5 to several hours and fluxes were $10 - 10^3$ s.f.u. Decameter Type IV bursts were usually accompanied by coronal mass ejections (CMEs) but sometimes there was no CME visible during the Type IV burst. Specific features of decameter Type IV bursts were fine structure in the form of fiber-bursts and oscillations of radio emission intensity. The longest periods of these oscillations comprise tens of minutes. It was suggested that the radio emission of Type IV bursts originates either in a coronal loop disturbed by the CME or in the body of the CME itself. Hence, the observed oscillations can be connected either with CME oscillations or coronal loops. Oscillation in the intensity of Type IV bursts without accompanied CME is probably connected to the coronal loop oscillations triggered by a solar flare. Then, the analysis of these oscillations allows to estimate the plasma properties in the coronal loops. Among decameter bursts there are the so-called inverted U- and J- bursts generated by fast electron beams, which propagate in high coronal loops (Dorovsky et al., 2010). Active region coronal loops may expand up to helmet streamers. Additionally, very long transequatorial loops, which connect the active regions in opposite hemispheres, may reach up to the height of one solar radius above the solar surface. Chase et al. (1976) presented the first observational indication of transequatorial loops. Later, Pevtsov (2000) presented 87 transequatorial loops through the analysis of Yohkoh data set between October 1991 and December 1998. The radio emission at 10 MHz - 30 MHz is connected to those heights, where transequatorial and/or active region loops are located. Then, the long-period modulation of emission intensity at these frequencies can be caused by the oscillations of the loops. In the following the observation of Type IV radio burst from the large Ukrainian radio telescope URAN-2 are used for the seismological estimation of magnetic field strength and other plasma parameters of coronal loops at the heights of $\geq 0.2R_S$ above the solar surface.

13.1 Observations and their interpretation

As already pointed out in Section 7.5.1, a Type IV radio burst was detected in the frequency range of $\sim$ 12 MHz - 32 MHz during the time interval of 09:50 - 12:30 UT in April 14, 2011, with the frequency resolution of 4 kHz and time resolution of 100 ms. Fig. 7.39 shows the dynamic spectrum of solar radio emission observed by the radio telescope URAN-2 in April 14, 2011. The decameter Type IV burst started at 10:00 UT, continued about 4 hours and finished approximately at 14:00 UT. Polarization of Type IV burst was high at about 40 % - 50 %. The Type IV radio burst was probably connected to a small C2.3 flare in the active region AR11190 (Fig.7.40).

The dynamic spectrum (Fig. 7.39) visualizes variations of emission intensity, kind of quasi-periodic behavior. An estimation on the statistically significant periods may lead to an understanding of the reason of these variations.

The wavelet spectrum of emission intensity (Fig. 7.42) at four different frequencies (29 MHz, 25 MHz, 22 MHz, 14 MHz) yielded two main periods, 23 min and 34 min (Table (7.1)). Variations of electron beam density can cause amplitude variations of Langmuir oscillations directly responsible for the intensity variations of radio emission. However, also topographical variations (i.e. variation of angle between solar magnetic field direction and line of sight) may cause the observed oscillation. As outlined in Section 7.5.1 transequatorial loop systems (connecting active regions of the Northern and Southern solar hemisphere) can act as basic magnetic structures which are oscillating, triggered by solar flares, consequently triggering Langmuir oscillations. The observed oscillation periods enable an estimation of the plasma parameters of the outer solar corona by comparison of the theoretical oscillation spectrum of MHD waves in coronal loops (see Section 7.5.1.).

Bibliography

Abranin, E. and Bazelyan, L. (1986). Decameter radiation of the quiet Sun. *Preprint of Institute of Radio Physics and Electronics, UkrRSR Acad. Sci*, 1(304).

Abranin, E. P., Baselian, L. L., Goncharov, N. I., Zinichev, V. A., Rapoport, V. O., and Tsybko, I. G. (1979). Harmonic structure of type IIIb and III bursts. *Sol. Phys.*, 62:145–151.

Abranin, E. P., Bazelian, L. L., Goncharov, N. I., Zaitsev, V. V., Zinichev, V. A., Levin, B. N., Rapoport, V. O., and Tsybko, I. G. (1977). Some observational results on 'drift pair'-type solar radio bursts near frequencies of 12.5 and 25 MHz. *Astron. J.*, 54:146–157.

Abranin, E. P., Bazelian, L. L., Goncharov, N. I., Zaitsev, V. V., Zinichev, V. A., Rapoport, V. O., and Tsybko, I. G. (1976). Angular sizes of sources of solar radio bursts in the decameter range. *Soviet. Astron.*, 19:602–605.

Abranin, E. P., Bazelian, L. L., Goncharov, N. I., Zaitsev, V. V., Zinichev, V. A., Rapoport, V. O., and Tsybko, I. G. (1978). Angular sizes of stria-burst sources in the range 24-26 MHz. *Sol. Phys.*, 57:229–235.

Abranin, E. P., Bazelian, L. L., Goncharov, N. I., Zaitsev, V. V., Zinichev, V. A., Rapoport, V. O., and Tsybko, I. G. (1980a). Positions of solar storm burst sources by observations with a heliograph based on the UTR-2 antenna at 25 MHz. *Sol. Phys.*, 66:393–409.

Abranin, E. P., Bazelian, L. L., Rapoport, V. O., and Tsybko, I. G. (1980b). Variations of type III burst parameters during a decametric solar storm. *Sol. Phys.*, 66:333–346.

Abranin, E. P., Bazelyan, L. L., and Tsybko, Y. G. (1990). Stability of the Parameters of Decameter Type-Iii Bursts Over the 11-YEAR

Solar Activity Cycle - Rates of Frequency Drift of Radio Burst. *Soviet. Astron.*, 34:74.

Akhiezer, A. I., Akhiezer, I. A., Polovin, R. V., Sitenko, A. T., and Stepanov, K. (1974). Electrodynamics of plasma (in russian). page 92.

Allen, C. W. (1947). Interpretation of Electron Densities from Corona Brightness. *Mon. Not. R. Astron. Soc.*, 107:426.

Alvarez, H. and Haddock, F. T. (1973). Solar Wind Density Model from km-Wave Type III Bursts. *Sol. Phys.*, 29:197–209.

Andries, J., van Doorsselaere, T., Roberts, B., Verth, G., Verwichte, E., and Erdélyi, R. (2009). Coronal Seismology by Means of Kink Oscillation Overtones. *Space Sci. Rev.*, 149:3–29.

Arregui, I., Andries, J., Van Doorsselaere, T., Goossens, M., and Poedts, S. (2007). MHD seismology of coronal loops using the period and damping of quasi-mode kink oscillations. *Astron. Astrophys.*, 463:333–338.

Arregui, I. and Asensio Ramos, A. (2011). Bayesian Magnetohydrodynamic Seismology of Coronal Loops. *Astrophys. J.*, 740:44.

Arregui, I., Oliver, R., and Ballester, J. L. (2012). Prominence oscillations. *Living Reviews in Solar Physics*, 9(1):1–109.

Aschwanden, M. J. (2004). *Physics of the Solar Corona. An Introduction.* Praxis Publishing Ltd.

Aschwanden, M. J., Bastian, T. S., Benz, A. O., and Brosius, J. W. (1992). Decimetric solar type U bursts - VLA and PHOENIX observations. *Astrophys. J.*, 391:380–392.

Aschwanden, M. J., Fletcher, L., Schrijver, C. J., and Alexander, D. (1999). Coronal Loop Oscillations Observed with the Transition Region and Coronal Explorer. *Astrophys. J.*, 520:880–894.

Aschwanden, M. J., Nakariakov, V. M., and Melnikov, V. F. (2004). Magnetohydrodynamic Sausage-Mode Oscillations in Coronal Loops. *Astrophys. J.*, 600:458–463.

Aubier, M., Leblanc, Y., and Boischot, A. (1971). Observations of the Quiet Sun at Decameter Wavelengths - Effects of Scattering on the Brightness Distribution. *Astron. Astrophys.*, 12:435.

Aurass, H., Hofmann, A., Magun, A., Soru-Escaut, I., and Zlobec, P. (1993). Evaporation Causes Flare Related Radio Burst Continuum Depressions. *Sol. Phys.*, 145(1):151–168.

Aurass, H., Klein, K.-L., Zlotnik, E. Y., and Zaitsev, V. V. (2003). Solar type IV burst spectral fine structures . I. Observations. *Astron. Astrophys.*, 410:1001–1010.

Bain, H. M., Krucker, S., Saint-Hilaire, P., and Raftery, C. L. (2014). Radio Imaging of a Type IVM Radio Burst on the 14th of August 2010. *Astrophys. J.*, 782:43.

Bazelian, L. L., Goncharov, N. I., Zaitsev, V. V., Zinichev, V. A., Rapoport, V. O., and Tsybko, I. G. (1977). Collisionless deceleration of fast electron streams in the solar coronal plasma. *Sol. Phys.*, 52:141–152.

Bazelyan, L. L., Braude, S. Y., and Men', A. V. (1970). Scattering of the Decameter Radio Emission of the Crab Nebula by the Solar Corona. *Soviet. Astron.*, 14:153.

Benz, A. (2002). *Plasma Astrophysics, Kinetic processes in Solar and Stellar Coronae. Kluver Academic Publishers (Second edition)*, volume 279.

Benz, A. O. (1986). Millisecond radio spikes. *Sol. Phys.*, 104:99–110.

Benz, A. O., Jaeggi, M., and Zlobec, P. (1982). Fine structure near the starting frequency of solar type III radio bursts. *Astron. Astrophys.*, 109:305–313.

Benz, A. O. and Kuijpers, J. (1976). Type IV dm bursts: onset and sudden reductions. *Sol. Phys.*, 46(2):275–290.

Bhonsle, R. V., Sawant, H. S., and Degaonkar, S. S. (1979). Exploration of the solar corona by high resolution solar decametric observations. *Space Sci. Rev.*, 24:259–346.

Bobeiko, A. L., Bovkoon, V. P., Braude, S. I., Megn, A. V., and Sergienko, I. I. (1979). Measurements of radio emission from the compact source in the Crab nebula with the Uran-1 interferometer at 16.7, 20 and 25 MHz. *Astrophys. Space Sci.*, 66:211–221.

Boischot, A. (1957). Caractères d'un type d'émission hertzienne associé à certaines éruptions chromosphériques. *Academie des Sciences Paris Comptes Rendus*, 244:1326–1329.

Boischot, A. (1958). Étude du rayonnement radioélectrique solaire sur 169 MHz é l'aide d'un grand interféromètre à réseau. *Annales d'Astrophysique*, 21:273.

Boischot, A., Fokker, A. D., and Simon, P. (1959). The 1957 November 4 event. In Bracewell, R. N., editor, *URSI Symp. 1: Paris Symposium on Radio Astronomy*, volume 9 of *IAU Symposium*, page 263.

Borkowski, K. M. (1982). The quiet sun brightness temperature at 127 MHz. *Sol. Phys.*, 81:207–215.

Bougeret, J. L., Goetz, K., Kaiser, M. L., Bale, S. D., Kellogg, P. J., Maksimovic, M., Monge, N., Monson, S. J., Astier, P. L., Davy, S., Dekkali, M., Hinze, J. J., Manning, R. E., Aguilar-Rodriguez, E., Bonnin, X., Briand, C., Cairns, I. H., Cattell, C. A., Cecconi, B., Eastwood, J., Ergun, R. E., Fainberg, J., Hoang, S., Huttunen, K. E. J., Krucker, S., Lecacheux, A., MacDowall, R. J., Macher, W., Mangeney, A., Meetre, C. A., Moussas, X., Nguyen, Q. N., Oswald, T. H., Pulupa, M., Reiner, M. J., Robinson, P. A., Rucker, H., Salem, C., Santolik, O., Silvis, J. M., Ullrich, R., Zarka, P., and Zouganelis, I. (2008). S/WAVES: The Radio and Plasma Wave Investigation on the STEREO Mission. *Space Sci. Rev.*, 136:487–528.

Braude, S. I., Megn, A. V., Riabov, B. P., Sharykin, N. K., and Zhuk, I. N. (1978). Decametric survey of discrete sources in the Northern sky. I - The UTR-2 radio telescope: Experimental techniques and data processing. *Astrophys. Space Sci.*, 54:3–36.

Brazhenko, A., Melnik, V., Frantsuzenko, A., Dorovskyy, V., Rucker, H., and Panchenko, M. (2015). Evidence of primary and secondary

bursts in solar type iii emission. *Radio Physics and Radio Astronomy*, 20:99–108.

Brazhenko, A. I., Bulatsen, V. G., Vashchishin, R. V., Frantsuzenko, A. V., Konovalenko, A. A., Falkovich, I. S., Abranin, E. P., Ulyanov, O. M., Zakharenko, V. V., Lecacheux, A., and Rucker, H. (2005). New decameter radiopolarimeter URAN-2. *Kinematika i Fizika Nebesnykh Tel Supplement*, 5:43–46.

Brazhenko, A. I., Koval, A. A., Konovalenko, A. A., Stanislavsky, A. A., Abranin, E. P., Dorovsky, V. V., Melnik, V. N., Vashchishin, R. V., Frantsuzenko, A. V., and Borysyuk, O. V. (2012a). Peculiarity of Continuum Emission from the Upper Solar Corona at Decameter Wavelengths. *Radio Physics and Radio Astronomy*, 3:187–196.

Brazhenko, A. I., Melnik, V. M., Frantsuzenko, A. V., Rucker, H. O., and Panchenko, M. (2015a). Unusual Solar Decameter Radio Bursts with High Frequency Cut off. *Russian Radio Physics and Radio Astronomy*, 20:10.

Brazhenko, A. I., Melnik, V. M., Konovalenko, O. O., Dorovskyy, V. V., Frantsuzenko, A. V., Rucker, H. O., Panchenko, M., and Stanislavsky, A. A. (2012b). An Unusual Burst at Decameter Wavelengths. 1. Observations. *Russian Radio Physics and Radio Astronomy*, 17:99.

Brazhenko, A. I., Melnik, V. N., Frantsuzenko, A. V., Dorovskyy, V. V., Rucker, H. O., and Panchenko, M. (2015b). On the Harmonic Coupling of Components in Pairs of IIIb-III Bursts at Decameter Wavelengths. *Russian Radio Physics and Radio Astronomy*, 20:99.

Brazhenko, A. I., Mel'Nik, V. N., Konovalenko, A. A., Abranin, E. P., Dorovskyy, V. V., Vashchishin, R. V., Frantzusenko, A. V., and Rucker, H. O. (2010). Observations of the Solar Continuum Radio Emission at Decameter Wavelengths. In Chakrabarti, S. K., Zhuk, A. I., and Bisnovatyi-Kogan, G. S., editors, *American Institute of Physics Conference Series*, volume 1206 of *American Institute of Physics Conference Series*, pages 440–444.

Brazhenko, A. I., Pylaev, O. S., Melnik, V. M., Konovalenko, O. O., Frantsuzenko, A. V., Dorovskyy, V. V., Vashchishin, R. V., and Rucker, H. O. (2013). Observations of the Three Harmonic Components of Solar Type III Bursts at Decameter Wavelengths. *Russian Radio Physics and Radio Astronomy*, 18:283.

Cairns, I. H. (1987). Third and higher harmonic plasma emission due to Raman scattering. *Journal of Plasma Physics*, 38:199–208.

Cairns, I. H., Lobzin, V. V., Warmuth, A., Li, B., Robinson, P. A., and Mann, G. (2009). Direct Radio Probing and Interpretation of the Sun's Plasma Density Profile. *Astrophys. J. Lett.*, 706:L265–L269.

Cane, H. V. (1979). Spectra of the non-thermal radio radiation from the galactic polar regions. *Mon. Not. R. Astron. Soc.*, 189:465–478.

Caroubalos, C., Couturier, P., and Prokaxis, T. (1973). A U-Like Radio Burst Observed with High Space-Time Resolution. *Astron. Astrophys.*, 23:131.

Chase, R. C., Krieger, A. S., Svestka, Z., and Vaiana, G. S. (1976). SKYLAB observations of X-ray loops connecting separate active regions. In Rycroft, M. J., editor, *Space research XVI*, pages 917–922.

Chen, B., Bastian, T. S., Gary, D. E., and Jing, J. (2011). Spatially and Spectrally Resolved Observations of a Zebra Pattern in a Solar Decimetric Radio Burst. *Astrophys. J.*, 736:64.

Chen, H. S.-L. and Shawhan, S. D. (1978). Structure and evolution of solar radio bursts at 26.4 MHz. *Sol. Phys.*, 57:205–227.

Chernov, G. P. (2004). A Comparative Analysis of Zebra-Pattern Structures at Frequencies from 20 to 7000 MHz. *Astronomy Reports*, 48(10):853–870.

Chernov, G. P. (2006). Solar Radio Bursts with Drifting Stripes in Emission and Absorption. *Space Sci. Rev.*, 127:195–326.

Chernov, G. P., Kaiser, M. L., Bougeret, J.-L., Fomichev, V. V., and Gorgutsa, R. V. (2007a). Fine Structure of Solar Radio Bursts Observed at Decametric and Hectometric Waves. *Sol. Phys.*, 241:145–169.

Chernov, G. P., Stanislavsky, A. A., Konovalenko, A. A., Abranin, E. P., Dorovsky, V. V., and Rucker, G. O. (2007b). Fine structure of decametric type II radio bursts. *Astronomy Letters*, 33:192–202.

Claßen, H. T. and Aurass, H. (2002). On the association between type II radio bursts and CMEs. *Astron. Astrophys.*, 384:1098–1106.

Claßen, H.-T. and Mann, G. (1998). Electron acceleration and type II radio emission at quasi-parallel shock waves. *Radiophysics and Quantum Electronics*, 41:53–67.

Clette, F. (2021). The sunspot number: reconstructiong the past solar cycle for the future. *Space Research Today*, 210:10–23.

Cronyn, W. M. and Erickson, W. C. (1965). The Flux and Brightness Distribution of the Sun at 26.3 Mc/sec. *Astron. J.*, 70:672.

de Groot, T. (1960). Dynamic spectra and polarization of small bursts in solar radio emission. *Bull. of the Astron. Institutes of the Netherlands*, 15:229.

de La Noe, J. (1975). Spectral characteristics of stria, split pair and triple bursts. *Astron. Astrophys.*, 43:201–214.

De La Noe, J. and Boischot, A. (1972). The Type III B Burst. *Astron. Astrophys.*, 20:55.

de La Noe, J. and Moller Pedersen, B. (1971). Relationship between Drift Pair Bursts and Decametre Type III Solar Radio Emission. *Astron. Astrophys.*, 12:371.

Dorovsky, V. V., Melnik, V. N., Konovalenko, A. A., Rucker, H. O., Abranin, E. P., and Lecacheux, A. (2010). Decametric Solar u- and J-Type Bursts. *Radio Physics and Radio Astronomy*, 1:181–188.

Dorovskyy, V., Melnik, V., Konovalenko, A., Brazhenko, A., Poedts, S., Rucker, H., and Panchenko, M. (2016). Properties of groups

of solar S-bursts at the decameter band. *Planetary Radio Emissions VIII (G. Fischer, G. Mann, M. Panchenko, P. Zarka, Eds.) Austrian Academy of Sciences Press, Vienna*, pages 369–378.

Dorovskyy, V. V., Konovalenko, O. O., Falkovich, I. S., Bubnov, I. N., Gridin, A. A., Shevchuk, N. V., Koval, A. A., Rutkevych, B. P., Reznik, I. I., Rucker, H. O., Panchenko, M., Belov, A. S., Khristenko, A. D., Kvasov, G. V., Yerin, S. N., and Melnik, V. M. (2013). Observations of the Type U Burst in within 10-70 MHz with the GURT Radio Telescope. *Russian Radio Physics and Radio Astronomy*, 18:101.

Dorovskyy, V. V., Melnik, V. M., Konovalenko, O. O., Rucker, H. O., Abranin, E. P., and Lecacheux, A. (2010a). Solar U- and J-Bursts at the Decameter Waves. *Russian Radio Physics and Radio Astronomy*, 15:5.

Dorovskyy, V. V., Melnik, V. N., Konovalenko, A. A., Brazhenko, A. I., Panchenko, M., Poedts, S., and Mykhaylov, V. A. (2015a). Fine and Superfine Structure of the Decameter-Hectometer Type II Burst on 7 June 2011. *Sol. Phys.*, 290:2031–2042.

Dorovskyy, V. V., Melnik, V. N., Konovalenko, A. A., Bubnov, I. N., Gridin, A. A., Shevchuk, N. V., Rucker, H. O., Poedts, S., and Panchenko, M. (2015b). Decameter U-burst Harmonic Pair from a High Loop. *Sol. Phys.*, 290:181–192.

Dorovskyy, V. V., Mel'Nik, V. N., Konovalenko, A. A., Rucker, H. O., Abranin, E. P., and Lecacheux, A. (2006). Observations of Solar S-bursts at the decameter wavelengths. In Rucker, H. O., Kurth, W., and Mann, G., editors, *Planetary Radio Emissions VI*, pages 383–390. Austrian Academy of Sciences Press, Vienna.

Dorovskyy, V. V., Melnik, V. N., Konovalenko, A. A., Rucker, H. O., Abranin, E. P., and Lecacheux, A. (2010b). Solar U- and J- radio bursts at the decameter waves. In Chakrabarti, S. K., Zhuk, A. I., and Bisnovatyi-Kogan, G. S., editors, *American Institute of Physics Conference Series*, volume 1206 of *American Institute of Physics Conference Series*, pages 433–439.

Dorovskyy, V. V., Mel'Nik, V. N., Konovalenko, A. A., Rucker, H. O., Abranin, E. P., Stanislavsky, A. A., and Lecacheux, A. (2007). Decameter Type II radio burst with three harmonics. In *European Planetary Science Congress 2007*, page 688.

Droege, F. (1977). Millisecond fine-structures of solar burst radiation in the range 0.2 - 1.4 GHz. *Astron. Astrophys.*, 57(1-2):285–290.

Dulk, G. A., Erickson, W. C., Manning, R., and Bougeret, J.-L. (2001). Calibration of low-frequency radio telescopes using the galactic background radiation. *Astron. Astrophys.*, 365:294–300.

Dulk, G. A. and McLean, D. J. (1978). Coronal magnetic fields. *Sol. Phys.*, 57:279–295.

Dulk, G. A. and Suzuki, S. (1980). The position and polarization of Type III solar bursts. *Astron. Astrophys.*, 88:203–217.

Dulk, G. A., Suzuki, S., and Sheridan, K. V. (1984). Solar noise storms - The polarization of storm Type III and related bursts. *Astron. Astrophys.*, 130:39–45.

Edwin, P. M. and Roberts, B. (1983). Wave propagation in a magnetic cylinder. *Sol. Phys.*, 88:179–191.

Elgarøy, Ø. (1961). Studies in high-resolution spectrometry of solar radio emission. *Astrophysica Norvegica*, 7:123.

Elgaroy, O. and Lyngstad, E. (1972). High-Resolution Observations of Type III Solar Radio Bursts. *Astron. Astrophys.*, 16:1.

Ellis, G. R. A. (1969). Fine structure in the spectra of solar radio bursts. *Australian Journal of Physics*, 22:177.

Eremin, A. B. and Zaitsev, V. V. (1985). On the origin of type III fundamental. *Sol. Phys.*, 102:99–110.

Erickson, W. C. (1963). High-Resolution Studies of Type III Solar Emission at 11.4-Meter Wavelength. *J. Geophys. Res.*, 68:3169–3179.

Erickson, W. C., Gergely, T. E., Kundu, M. R., and Mahoney, M. J. (1977). Determination of the Decameter Wavelength Spectrum of the Quiet Sun. In *Bulletin of the American Astronomical Society*, volume 9 of *Bull. Am. Astron. Soc.*, page 371.

Fokker, A. D. (1966). The electron temperature of the solar corona as derived from radio observations. *Bull. of the Astron. Institutes of the Netherlands*, 18:359.

Fokker, A. D. (1970). Trajectories Followed by U-Like Solar Radio Bursts. *Sol. Phys.*, 11:92–103.

Gergely, T. E., Gross, B. D., and Kundu, M. R. (1985). The diameter of the sun at decameter wavelengths. *Sol. Phys.*, 99:323–331.

Gergely, T. E. and Kundu, M. R. (1974). Decameter Type IV Bursts Associated with Coronal Transients. *Sol. Phys.*, 34:433–446.

Gergely, T. E. and Kundu, M. R. (1975). Decameter storm radiation. II. *Sol. Phys.*, 41:163–188.

Ginzburg, V. L. and Zhelezniakov, V. V. (1958). On the Possible Mechanisms of Sporadic Solar Radio Emission (Radiation in an Isotropic Plasma). *Astronomicheskii Zhurnal*, 35:694.

Gopalswamy, N. (2011). Coronal Mass Ejections and Solar Radio Emissions. *in PlanetaryRadio Emissions VII (H.O. Rucker, W.S. Kurth, P. Louarn, G. Fischer, eds.) Austrian Academy of Sciences Press, Vienna*, pages 325–342.

Gopalswamy, N., Aguilar-Rodriguez, E., Yashiro, S., Nunes, S., Kaiser, M. L., and Howard, R. A. (2005). Type II radio bursts and energetic solar eruptions. *Journal of Geophysical Research (Space Physics)*, 110(A9):A12S07.

Gopalswamy, N., Akiyama, S., Mäkelä, P., Yashiro, S., and Cairns, I. H. (2016). On the Directivity of Low-Frequency Type IV Radio Bursts. *arXiv e-prints*.

Gopalswamy, N., Thejappa, G., and Sastry, C. V. (1983). Observations and interpretation of solar decametric absorption bursts. *Journal of Astrophysics and Astronomy*, 4:215–224.

Hey, J. S. (1946). Solar Radiations in the 4-6 Metre Radio Wave-Length Band. *Nature*, 157(3976):47–48.

Hillaris, A., Bouratzis, C., and Nindos, A. (2016). Interplanetary Type IV Bursts. *Sol. Phys.*, 291:2049–2069.

Jansky, K. G. (1982). *Directional Studies of Atmospherics at High Frequencies*, pages 10–22. Springer Netherlands, Dordrecht.

Joardar, S. and Bhattacharya, A. B. (2007). Design and Analysis of a Low-Frequency Radio Telescope for Jovian Radio Emission. *Precambrian Research*, 72:127–142.

Kai, K. (1973). Unusual Absorption of a Solar Type II Burst by 'Shadow' Type III Bursts. *Proceedings of the Astronomical Society of Australia*, 2:219.

Khodachenko, M. L., Kislyakova, K. G., Zaqarashvili, T. V., Kislyakov, A. G., Panchenko, M., Zaitsev, V. V., Arkhypov, O. V., and Rucker, H. O. (2011). Possible manifestation of large-scale transverse oscillations of coronal loops in solar microwave emission. *Astron. Astrophys.*, 525:A105.

Klassen, A. (1996). Radio Evidence for Electron Acceleration in a Cusp-Like Structure. *Sol. Phys.*, 167(1-2):449–452.

Klassen, A., Aurass, H., Klein, K.-L., Hofmann, A., and Mann, G. (1998). On Shock Wave Formation in the Solar Corona. In *CESRA Workshop on Coronal Explosive Events*, page 45.

Klecker, B., Kunow, H., Cane, H. V., Dalla, S., Heber, B., Kecskemety, K., Klein, K.-L., Kota, J., Kucharek, H., Lario, D., Lee, M. A., Popecki, M. A., Posner, A., Rodriguez-Pacheco, J., Sanderson, T., Simnett, G. M., and Roelof, E. C. (2006). Energetic Particle Observations. *Space Sci. Rev.*, 123:217–250.

Kleewein, P. (1997). *Spectral analysis of magnetospheric radio emissions,*. PhD thesis, University of Graz.

Kleewein, P., Rosolen, C., and Lecacheux, A. (1997). New Digital Spectrometers for Ground Based Decameter Radio Astronomy. In

Rucker, H. O., Bauer, S. J., and Lecacheux, A., editors, *in Planetary Radio Emission IV*, pages 349–357. Austrian Academy of Sciences Press, Vienna.

Kliem, B., Krueger, A., and Treumann, R. A. (1992). Third plasma harmonic radiation in type II bursts. *Sol. Phys.*, 140:149–160.

Konovalenko, A., Sodin, L., Zakharenko, V., Zarka, P., Ulyanov, O., Sidorchuk, M., Stepkin, S., Tokarsky, P., Melnik, V., Kalinichenko, N., Stanislavsky, A., Koliadin, V., Shepelev, V., Dorovskyy, V., Ryabov, V., Koval, A., Bubnov, I., Yerin, S., Gridin, A., Kulishenko, V., Reznichenko, A., Bortsov, V., Lisachenko, V., Reznik, A., Kvasov, G., Mukha, D., Litvinenko, G., Khristenko, A., Shevchenko, V. V., Shevchenko, V. A., Belov, A., Rudavin, E., Vasylieva, I., Miroshnichenko, A., Vasilenko, N., Olyak, M., Mylostna, K., Skoryk, A., Shevtsova, A., Plakhov, M., Kravtsov, I., Volvach, Y., Lytvinenko, O., Shevchuk, N., Zhouk, I., Bovkun, V., Antonov, A., Vavriv, D., Vinogradov, V., Kozhin, R., Kravtsov, A., Bulakh, E., Kuzin, A., Vasilyev, A., Brazhenko, A., Vashchishin, R., Pylaev, O., Koshovyy, V., Lozinsky, A., Ivantyshin, O., Rucker, H. O., Panchenko, M., Fischer, G., Lecacheux, A., Denis, L., Coffre, A., Grießmeier, J.-M., Tagger, M., Girard, J., Charrier, D., Briand, C., and Mann, G. (2016). The modern radio astronomy network in Ukraine: UTR-2, URAN and GURT. *Experimental Astronomy*, 42:11–48.

Konovalenko, A. A., Stanislavsky, A. A., Abranin, E. P., Dorovsky, V. V., Mel'Nik, V. N., Kaiser, M. L., Lecacheux, A., and Rucker, H. O. (2007). Absorption in Burst Emission. *Sol. Phys.*, 245:345–354.

Konovalenko, A. A., Stanislavsky, A. A., Rucker, H. O., Lecacheux, A., Mann, G., Bougeret, J.-L., Kaiser, M. L., Briand, C., Zarka, P., Abranin, E. P., Dorovsky, V. V., Koval, A. A., Mel'nik, V. N., Mukha, D. V., and Panchenko, M. (2013). Synchronized observations by using the STEREO and the largest ground-based decametre radio telescope. *Experimental Astronomy*, 36:137–154.

Kontar, E. P. (2001a). Dynamics of electron beams in the inhomogeneous solar corona plasma. *Sol. Phys.*, 202:131–149.

Kontar, E. P. (2001b). Dynamics of electron beams in the solar corona plasma with density fluctuations. *Astron. Astrophys.*, 375:629–637.

Kontar, E. P. and Pécseli, H. L. (2002). Nonlinear development of electron-beam-driven weak turbulence in an inhomogeneous plasma. *Phys. Rev. E*, 65(6):066408.

Kraus, J. D. (1966). *Radio astronomy*.

Krymkin, V. V. (1971). The Spectrum of Background Low-Frequency Radio Emission. *Radiophysics and Quantum Electronics*, 14:161–164.

Kundu, M. R., Erickson, W. C., and Gergely, T. E. (1977). Observations of the quiet sun at meter and decameter wavelengths. *Sol. Phys.*, 53:489–496.

Lantos, P. and Avignon, Y. (1975). The metric quiet sun during two cycles of activity and the nature of the coronal holes. *Astron. Astrophys.*, 41:137–142.

Leblanc, Y., Dulk, G. A., and Bougeret, J.-L. (1998). Tracing the Electron Density from the Corona to 1 AU. *Sol. Phys.*, 183:165–180.

Leblanc, Y., Dulk, G. A., Cairns, I. H., and Bougeret, J. L. (2000). Type II fixed on boards flare continuum in the corona and solar wind. *J. Geophys. Res.*, 105(A8):18215–18224.

Leblanc, Y. and Hoyos, M. (1985). Storms of U-bursts and the stability of coronal loops. *Astron. Astrophys.*, 143:365–373.

Leblanc, Y. and Le Squeren, A. M. (1969). Dimensions, Temperature and Electron Density of the Quiet Corona. *Astron. Astrophys.*, 1:239.

Lengyel-Frey, D. and Stone, R. G. (1989). Characteristics of interplanetary type II radio emission and the relationship to shock and plasma properties. *J. Geophys. Res.*, 94:159–167.

Lodge, O. J. (1906). *Signalling Through Space Without Wires*. D. Van Nostrand Company, Inc. New York, 4th edition edition.

Loi, S. T., Cairns, I. H., and Li, B. (2014). Production of Fine Structures in Type III Solar Radio Bursts Due to Turbulent Density Profiles. *Astrophys. J.*, 790:67.

MacDowall, R. J. (1989). Effects of interplanetary shocks on kilometric type III radio bursts. *Geophys. Res. Lett.*, 16(8):923–926.

Malitson, H. H. and Erickson, W. C. (1966). Observations of Type III and Type IV Solar Radio Bursts at 26.3 Mc/s. *Astrophys. J.*, 144:337.

Mann, G. (1995). Theory and Observations of Coronal Shock Waves. In Benz, A. O. and Krüger, A., editors, *Coronal Magnetic Energy Releases*, volume 444 of *Lecture Notes in Physics, Berlin Springer Verlag*, page 183.

Mann, G., Jansen, F., MacDowall, R. J., Kaiser, M. L., and Stone, R. G. (1999). A heliospheric density model and type III radio bursts. *Astron. Astrophys.*, 348:614–620.

Mann, G. and Klassen, A. (2005). Electron beams generated by shock waves in the solar corona. *Astron. Astrophys.*, 441:319–326.

Mann, G. and Luehr, H. (1994). Electron acceleration at quasi-parallel shocks in the solar corona and its signature in solar Type II radio bursts. *Astrophys. J. Suppl. Ser.*, 90.

Manning, R. and Dulk, G. A. (2001). The Galactic background radiation from 0.2 to 13.8 MHz. *Astron. Astrophys.*, 372:663–666.

Maxwell, A. and Swarup, G. (1958). A New Spectral Characteristic in Solar Radio Emission. *Nature*, 181:36–38.

McConnell, D. (1980). Fine spectral structure of solar radio storms. *Proceedings of the Astronomical Society of Australia*, 4:64–67.

McConnell, D. (1982). Spectral characteristics of solar S bursts. *Solar Physics*, 78:253–269.

McConnell, D. and Ellis, G. R. A. (1981). Fine structure in fast drift storm bursts. *Sol. Phys.*, 69:161–168.

McEwan, M. P., Díaz, A. J., and Roberts, B. (2008). Analytical determination of coronal parameters using the period ratio $P_1/2P_2$. *Astron. Astrophys.*, 481:819–825.

McKim Malville, J., Aller, H. D., and Jensen, C. J. (1967). Spike Bursts during the Type IV Event of February 5, 1965. *Astrophys. J.*, 147:711.

McLean, D. J., Nelson, G. J., and Dulk, G. A. (1985). *Solar flares*, pages 53–87.

Megn, A. V., Braude, S. Y., Rashkovskiy, S. L., Sharykin, N. K., Shepelev, V. A., Inutin, G. A., Khristenko, A. D., Bulatsen, V. G., Brazhenko, A. I., Koshovyy, V. V., Romanchev, Y. V., Thesevich, V. P., and Galanin, V. P. (1997). URAN System of the Decametric Interferometers (I). *Russian Radio Physics and Radio Astronomy*, 2:385.

Melnik, V. M., Brazhenko, A. I., Konovalenko, O. O., Briand, C., Rutkevych, B. P., Zarka, P., Zaqarashvili, T., Dorovskyy, V. V., Frantsuzenko, A. V., and Stanislavsky, A. A. (2013). Decametric type III bursts with variable sign of frequency drift rate. *Russian Radio Physics and Radio Astronomy*, 18:117.

Melnik, V. M., Brazhenko, A. I., Konovalenko, O. O., Dorovskyy, V. V., Frantsuzenko, A. V., Rucker, H. O., Panchenko, M., and Stanislavsky, A. A. (2012). An unusual burst at decameter wavelengths. 2. Interpretation. *Russian Radio Physics and Radio Astronomy*, 17:199.

Melnik, V. M., Konovalenko, O. O., Rucker, H. O., Boiko, A. I., Dorovskyy, V. V., Abranin, E. P., and Lecacheux, A. (2010a). Properties of Powerful Solar Type III Bursts at Decameter Wavelengths. *Russian Radio Physics and Radio Astronomy*, 15:129.

Mel'Nik, V. N. (1991). A nontraditional mechanism of emission of type III bursts at plasma double frequency. *Kinematika i Fizika Nebesnykh Tel*, 7:69–71.

Mel'Nik, V. N. (1995). "Gas-dynamic" expansion of a fast-electron flux in a plasma. *Plasma Physics Reports*, 21:89–91.

Melnik, V. N., Brazhenko, A. I., Konovalenko, A. A., Briand, C., Dorovskyy, V. V., Zarka, P., Frantsuzenko, A. V., Rucker, H. O., Rutkevych, B. P., Panchenko, M., Denis, L., Zaqarashvili, T., and Shergelashvili, B. (2015). Decameter Type III Bursts with Changing Frequency Drift-Rate Signs. *Sol. Phys.*, 290:193–203.

Melnik, V. N., Brazhenko, A. I., Konovalenko, A. A., Rucker, H. O., Frantsuzenko, A. V., Dorovskyy, V. V., Panchenko, M., and Stanislavskyy, A. A. (2014a). Unusual Solar Radio Burst Observed at Decameter Wavelengths. *Sol. Phys.*, 289:263–278.

Melnik, V. N., Brazhenko, A. I., Mann, G., Konovalenko, A. A., Frantzusenko, A. V., Rucker, H. O., and Panchenko, M. (2017a). Radio manifestation of CME observed on April 7, 2011 in the frequency band 8-32 MHz. *in Planetary Radio Emission VIII (G. Fischer, G. Mann, N. Panchenko, P. Zarka, eds.) Austrian Academy of Sciences Press, Vienna*, pages 381–390.

Mel'Nik, V. N., Konovalenko, A. A., Abranin, E. P., Dorovskyy, V. V., Stanislavsky, A. A., Rucker, H. O., and Lecacheux, A. (2005a). Solar sporadic radio emission in the decametre waveband. *Astronomical and Astrophysical Transactions*, 24:391–401.

Mel'Nik, V. N., Konovalenko, A. A., Abranin, E. P., Dorovskyy, V. V., Stanislavsky, A. A., Rucker, H. O., and Lecacheux, A. (2005b). Solar sporadic radio emission in the decametre waveband. *Astronomical and Astrophysical Transactions*, 24:391–401.

Melnik, V. N., Konovalenko, A. A., Brazhenko, A. I., Rucker, H. O., Dorovskyy, V. V., Abranin, E. P., Lecacheux, A., and Lonskaya, A. S. (2010b). Bursts in emission and absorption as a fine structure of Type IV bursts. In Chakrabarti, S. K., Zhuk, A. I., and Bisnovatyi-Kogan, G. S., editors, *American Institute of Physics Conference Series*, volume 1206 of *American Institute of Physics Conference Series*, pages 450–454.

Melnik, V. N., Konovalenko, A. A., Dorovskyy, V. V., Rucker, H. O., Abranin, E. P., Lisachenko, V. N., and Lecacheux, A. (2005). Solar Drift Pair Bursts in the Decameter Range. *Sol. Phys.*, 231:143–155.

Melnik, V. N., Konovalenko, A. A., Rucker, H. O., Boiko, A. I., Dorovskyy, V. V., Abranin, E. P., and Lecacheux, A. (2011a). Observations of Powerful Type III Bursts in the Frequency Range 10 - 30 MHz. *Sol. Phys.*, 269:335–350.

Melnik, V. N., Konovalenko, A. A., Rucker, H. O., Dorovskyy, V. V., Abranin, E. P., Lecacheux, A., and Lonskaya, A. S. (2010c). Solar S-bursts at Frequencies of 10 - 30 MHz. *Sol. Phys.*, 264:103–117.

Mel'Nik, V. N., Konovalenko, A. A., Rucker, H. O., Rutkevych, B. P., Dorovskyy, V. V., Abranin, E. P., Brazhenko, A. I., Stanislavskii, A. A., and Lecacheux, A. (2008). Decameter Type III-Like Bursts. *Sol. Phys.*, 250:133–145.

Mel'nik, V. N., Konovalenko, A. A., Rucker, H. O., Stanislavsky, A. A., Abranin, E. P., Lecacheux, A., Mann, G., Warmuth, A., Zaitsev, V. V., Boudjada, M. Y., Dorovskii, V. V., Zaharenko, V. V., Lisachenko, V. N., and Rosolen, C. (2004). Observations of Solar Type II bursts at frequencies 10-30 MHz. *Sol. Phys.*, 222:151–166.

Mel'Nik, V. N. and Kontar, E. P. (2003). Plasma Radio Emission of Beam-Plasma Structures in the Solar Corona. *Sol. Phys.*, 215:335–341.

Mel'Nik, V. N., Lapshin, V., and Kontar, E. (1999). Propagation of a Monoenergetic Electron Beam in the Solar Corona. *Sol. Phys.*, 184:353–362.

Melnik, V. N., Rucker, H. O., and Konovalenko, A. A. (2008). Solar Type IV Bursts at Frequencies 10-30 MHz. In Wang, P., editor, *Solar Physics Research Trends, Edited by Pingzhi Wang. ISBN 1-60021-987-x. Nova Publishers, 2008, p. 287-325*, pages 287–325.

Melnik, V. N., Rucker, H. O., Konovalenko, A. A., Dorovskyy, V. V., Abranin, E. P., and Lecacheux, A. (2011b). Decameter Radio Emission of the Sun: Recent Observations. *in Planetary Radio Emissions VII (H.O. Rucker, W.S. Kurth, P. Louarn, G. Fischer, eds.) Austrian Academy of Sciences Press, Vienna*, pages 343–350.

Melnik, V. N., Rucker, H. O., Konovalenko, A. A., Dorovskyy, V. V., and Tan, S. (2011c). Decameter IIIb-III pairs. In *EPSC-DPS Joint Meeting 2011*, page 796.

Melnik, V. N., Rucker, H. O., Konovalenko, A. A., Shevchuk, N. V., Abranin, E. P., Dorovskyy, V. V., and Lecacheux, A. (2010d). Type IIIb bursts and their fine structure in frequency band 18-30 MHz. In Chakrabarti, S. K., Zhuk, A. I., and Bisnovatyi-Kogan, G. S., editors, *American Institute of Physics Conference Series*, volume 1206 of *American Institute of Physics Conference Series*, pages 445–449.

Melnik, V. N., Shepelev, V., Brazhenko, A., Dorovskyy, V., Rucker, H., and Poedts, S. (2017b). Interferometer observations of solar type III bursts by the radio telescope UTR-2. *Sun and Geosphere*, 12, 2.

Melnik, V. N., Shevchuk, N. V., Konovalenko, A. A., Rucker, H. O., Dorovskyy, V. V., Poedts, S., and Lecacheux, A. (2014b). Solar Decameter Spikes. *Sol. Phys.*, 289:1701–1714.

Melrose, D. B. (1974a). The mechanism responsible for "shadow" type III solar radio bursts. I. Absorption due to Langmuir turbulence. *Australian Journal of Physics*, 27:259–269.

Melrose, D. B. (1974b). The mechanism responsible for "shadow" type III solar radio bursts. II. Absorption due to ion sound turbulence. *Australian Journal of Physics*, 27:271–277.

Melrose, D. B. (1982). Fine structures in Decametric noise storms : possible mechanisms. In *Solar Radio Storms, CESRA Workshop #4 (Benz, A. O. and Zlobec, P.)*, page 182.

Melrose, D. B. (1983). Frequency splitting in stria bursts - Possible roles of low-frequency waves. *Sol. Phys.*, 87:359–371.

Moller-Pedersen, B., Smith, R. A., and Mangeney, A. (1978). A theory of a solar radio burst - The drift pair. *Astron. Astrophys.*, 70:801–813.

Morosan, D. E., Gallagher, P. T., Zucca, P., O'Flannagain, A., Fallows, R., Reid, H., Magdalenić, J., Mann, G., Bisi, M. M., Kerdraon, A., Konovalenko, A. A., MacKinnon, A. L., Rucker, H. O., Thidé, B., Vocks, C., Alexov, A., Anderson, J., Asgekar, A., Avruch, I. M., Bentum, M. J., Bernardi, G., Bonafede, A., Breitling, F., Broderick, J. W., Brouw, W. N., Butcher, H. R., Ciardi, B., de Geus, E., Eislöffel, J., Falcke, H., Frieswijk, W., Garrett, M. A., Grießmeier, J., Gunst, A. W., Hessels, J. W. T., Hoeft, M., Karastergiou, A., Kondratiev, V. I., Kuper, G., van Leeuwen, J., McKay-Bukowski, D., McKean, J. P., Munk, H., Orru, E., Paas, H., Pizzo, R., Polatidis, A. G., Scaife, A. M. M., Sluman, J., Tasse, C., Toribio, M. C., Vermeulen, R., and Zarka, P. (2015). LOFAR tied-array imaging and spectroscopy of solar S bursts. *Astron. Astrophys.*, 580:A65.

Nakariakov, V. M., Melnikov, V. F., and Reznikova, V. E. (2003). Global sausage modes of coronal loops. *Astron. Astrophys.*, 412:L7–L10.

Nakariakov, V. M. and Ofman, L. (2001). Determination of the coronal magnetic field by coronal loop oscillations. *Astron. Astrophys.*, 372:L53–L56.

Nakariakov, V. M., Ofman, L., Deluca, E. E., Roberts, B., and Davila, J. M. (1999). TRACE observation of damped coronal loop oscillations: Implications for coronal heating. *Science*, 285:862–864.

Nakariakov, V. M. and Verwichte, E. (2005). Coronal waves and oscillations. *Living reviews in solar physics*, 2(1):1–65.

Nelson, G. J. and Melrose, D. B. (1985). Type II bursts. In *Solar Radiophysics: Studies of Emission from the Sun at Metre Wavelengths (McLean, D. J. and Labrum, N. R., eds.)*, pages 333–359. Cambridge University Press, Cambridge.

Newkirk, Jr., G. (1961). The Solar Corona in Active Regions and the Thermal Origin of the Slowly Varying Component of Solar Radio Radiation. *Astrophys. J.*, 133:983.

Nordmann, C. (1903). *Essai Sur le Role des Ondes Hertziennes en Astronomie Physique*. Gauthier-Villars, Paris, 4th edition edition.

Ofman, L., Nakariakov, V. M., and DeForest, C. E. (1999). Slow Magnetosonic Waves in Coronal Plumes. *Astrophys. J.*, 514:441–447.

Parker, E. N. (1958). Dynamics of the Interplanetary Gas and Magnetic Fields. *Astrophys. J.*, 128:664.

Pascoe, D. J., Nakariakov, V. M., Arber, T. D., and Murawski, K. (2009). Sausage oscillations in loops with a non-uniform cross-section. *Astron. Astrophys.*, 494:1119–1125.

Pesnell, W. D., Thompson, B. J., and Chamberlin, P. C. (2012). The Solar Dynamics Observatory (SDO). *Sol. Phys.*, 275:3–15.

Pevtsov, A. A. (2000). Transequatorial Loops in the Solar Corona. *Astrophys. J.*, 531:553–560.

Pick, M. and Vilmer, N. (2008). Sixty-five years of solar radioastronomy: flares, coronal mass ejections and Sun Earth connection. *Astron. Astrophys. Rev.*, 16:1–153.

Ramesh, R. (2000). Low Frequency Radio Emission from the 'Quiet Sun'. *Journal of Astrophysics and Astronomy*, 21:237.

Ramesh, R. and Ebenezer, E. (2001). Decameter Wavelength Observations of an Absorption Burst from the Sun and Its Association with an X2.0/3B Flare and the Onset of a "Halo" Coronal Mass Ejection. *Astrophys. J. Lett.*, 558(2):L141–L143.

Ramesh, R., Nataraj, H. S., Kathiravan, C., and Sastry, C. V. (2006). The Equatorial Background Solar Corona during Solar Minimum. *Astrophys. J.*, 648:707–711.

Raoult, A. and Pick, M. (1980). Space-time evolution of type III burst sources observed with the Nancay radioheliograph - Implications for the size of the emitting source. *Astron. Astrophys.*, 87:63–67.

Reber, G. (1984). Early radio astronomy at Wheaton, Illinois. In *The Early Years of Radio Astronomy - Reflections Fifty Years after Jansky's Discovery*, page 43.

Reid, H. A. S. and Ratcliffe, H. (2014). A review of solar type III radio bursts. *Research in Astronomy and Astrophysics*, 14:773–804.

Roberts, B., Edwin, P. M., and Benz, A. O. (1984). On coronal oscillations. *Astrophys. J.*, 279:857–865.

Roberts, J. A. (1958). Evidence of Echoes in the Solar Corona from a New Type of Burst. *Australian Journal of Physics*, 11:215.

Rust, D. M. (1979). *Solar flares*, volume 1, pages 51–98.

Rutkevych, B. P. and Melnik, V. N. (2012). Propagation of Type III Solar Bursts Radio Emission Through the Corona. Time Profile. *Radio Physics and Radio Astronomy*, 3:205–213.

Ryabov, V. B., Vavriv, D. M., Zarka, P., Ryabov, B. P., Kozhin, R., Vinogradov, V. V., and Denis, L. (2010). A low-noise, high-dynamic-range, digital receiver for radio astronomy applications: an efficient solution for observing radio-bursts from Jupiter, the Sun, pulsars, and other astrophysical plasmas below 30 MHz. *Astron. Astrophys.*, 510:A16.

Ryutov, D. D. and Sagdeev, R. Z. (1970). Quasi-gasdynamical Description of a Hot Electron Cloud in a Cold Plasma. *Soviet Journal of Experimental and Theoretical Physics*, 31:396.

Sastry, C. V. (1994). Observations of the continuum radio emission from the undisturbed Sun at a wavelength of 8.7 meters. *Sol. Phys.*, 150:285–294.

Sastry, C. V., Subramanian, K. R., and Krishan, V. (1983). Absorption Bursts in the Radio Emission from the Sun at Decameter Wavelengths. *Astrophysics Letters and Communications*, 23:95.

Scheiner, C. (1630). *Rosa Ursina*. Bracciani [Bracciano] : apud Andream Phaeum Typographum Ducalem, Impressio coepta anno 1626. finita vero 1630, ETH-Bibliothek Zürich, Rar 10152.

Schou, J., Scherrer, P., Bush, R., Wachter, R., Couvidat, S., Rabello-Soares, M., Bogart, R., Hoeksema, J., Liu, Y., Duvall Jr, T., et al. (2011). Design and ground calibration of the Helioseismic and

Magnetic Imager (HMI) instrument on the Solar Dynamics Observatory (SDO). In *The Solar Dynamics Observatory*, pages 229–259. Springer.

Shepelev, V. A. (2015). Determination of Angular Parameters of the Sources of Solar Radio Emission at Decameter Wavelengths. *Russian Radio Physics and Radio Astronomy*, 20:20.

Slottje, C. (1972). Peculiar absorption and emission microstructures in the type IV solar radio outburst of March 2, 1970. *Sol. Phys.*, 25(1):210–231.

Slottje, C. (1982). *Atlas of fine structures of dynamic spectra of solar type IV-dm and some type II radio bursts.* PhD thesis, Rijksuniversiteit Utrecht.

Smith, D. F. (1970). On the Relative Intensity of Second Branches of U-Like Solar Radio Bursts. *Sol. Phys.*, 13:444–447.

Solar Radio Group Utrecht (1974). Type III Bursts. *Space Sci. Rev.*, 16:45–89.

Srivastava, A. K., Zaqarashvili, T. V., Uddin, W., Dwivedi, B. N., and Kumar, P. (2008). Observation of multiple sausage oscillations in cool post-flare loop. *Mon. Not. R. Astron. Soc.*, 388:1899–1903.

Stanimirovic, S., Altschuler, D., Goldsmith, P., and Salter, C., editors (2002). *Single-Dish Radio Astronomy: Techniques and Applications*, volume 278 of *Astronomical Society of the Pacific Conference Series*.

Stanislavsky, A. A., Koval, A. A., and Konovalenko, A. A. (2013). Low-frequency heliographic observations of the quiet Sun corona. *Astronomische Nachrichten*, 334:1086.

Stepanov, A. V., Zaitsev, V. V., and Nakariakov, V. M. (2012). Coronal seismology. *Physics-Uspekhi*, 45(9):929–935.

Stewart, R. T. (1974). Harmonic ratios of inverted-U type III bursts. *Sol. Phys.*, 39:451–458.

Stewart, R. T. (1975). An example of a fundamental type IIIb radio burst. *Sol. Phys.*, 40:417–419.

Stewart, R. T. (1985). *Moving Type IV bursts, in Solar Radiophysics: Studies of Emission from the Sun at Metre Wavelengths (McLean, D. J. and Labrum, N. R., eds.)*, pages 361–383.

Stone, R. G. and Fainberg, J. (1971). A U-Type Solar Radio Burst Originating in the Outer Corona. *Sol. Phys.*, 20:106–111.

Stuart, R. T. (1985). *Solar Radio Physics*, chapter Moving Type IV Bursts, pages 361–384. Cambridge University Press, Cambridge.

Subramanian, K. R. (2004). Brightness temperature and size of the quiet Sun at 34.5 MHz. *Astron. Astrophys.*, 426:329–331.

Subramanian, K. R. and Sastry, C. V. (1988). The low-frequency radio spectrum of the continuum emission from the undisturbed sun. *Journal of Astrophysics and Astronomy*, 9:225–229.

Suzuki, S. and Dulk, G. A. (1985). Bursts of Type III and Type V. In McLean, D. J. and Labrum, N. R., editors, *Solar Radiophysics: Studies of Emission from the Sun at Metre Wavelengths*, pages 289–332.

Suzuki, S. and Gary, D. E. (1979). Position and polarization of solar drift pair bursts. *Proceedings of the Astronomical Society of Australia*, 3:379–383.

Sych, R., Zaqarashvili, T. V., Nakariakov, V. M., Anfinogentov, S. A., Shibasaki, K., and Yan, Y. (2012). Frequency drifts of 3-min oscillations in microwave and EUV emission above sunspots. *Astron. Astrophys.*, 539:A23.

Takakura, T. and Yousef, S. (1975). Type IIIb radio bursts - 80 MHz source position and theoretical model. *Sol. Phys.*, 40:421–438.

Tarnstrom, G. L. and Philip, K. W. (1972a). Solar Radio Spike Bursts. *Astron. Astrophys.*, 16:21.

Tarnstrom, G. L. and Philip, K. W. (1972b). Spike Burst – Type III Burst Associations. *Astron. Astrophys.*, 17:267.

Thejappa, G., Gopalswamy, N., Sastry, C. N., and Aubier, M. G. (1986). Some interesting features in the drift pair phenomena of solar decametric radiation. In Guyenne, T. D. and Zeleny, L. M., editors, *Plasma Astrophysics*, volume 251 of *ESA Special Publication*.

Thejappa, G. and Kundu, M. R. (1992). Unusually low coronal radio emission at the solar minimum. *Sol. Phys.*, 140:19–39.

Thompson, A. R., Moran, J. M., and Swenson, G. W. (1986). *Interferometry and synthesis in radio astronomy*.

Thompson, A. R., Moran, J. M., and Swenson, Jr., G. W. (2001). *Interferometry and Synthesis in Radio Astronomy, 2nd Edition*. John Wiley & Sons, Inc.

van de Hulst, H. C. (1947). Zodiacal Light in the Solar Corona. *Astrophys. J.*, 105:471.

Van Doorsselaere, T., Nakariakov, V. M., and Verwichte, E. (2007). Coronal loop seismology using multiple transverse loop oscillation harmonics. *Astron. Astrophys.*, 473:959–966.

Verth, G., Erdélyi, R., and Goossens, M. (2010). Magnetoseismology: Eigenmodes of Torsional Alfvén Waves in Stratified Solar Waveguides. *Astrophys. J.*, 714:1637–1648.

Verth, G., Goossens, M., and He, J.-S. (2011). Magnetoseismological Determination of Magnetic Field and Plasma Density Height Variation in a Solar Spicule. *Astrophys. J. Lett.*, 733:L15.

Viner, M. R. and Erickson, W. C. (1975). 26.3-MHz radio source survey. II - Radio source positions and fluxes. *Astron. J.*, 80:931–954.

Vršnak, B., Magdalenić, J., and Zlobec, P. (2004). Band-splitting of coronal and interplanetary type II bursts. III. Physical conditions in the upper corona and interplanetary space. *Astron. Astrophys.*, 413:753–763.

Wang, T. J. and Solanki, S. K. (2004). Vertical oscillations of a coronal loop observed by TRACE. *Astron. Astrophys.*, 421:L33–L36.

Wang, T. J., Solanki, S. K., Curdt, W., Innes, D. E., Dammasch, I. E., and Kliem, B. (2003a). Hot coronal loop oscillations observed with SUMER: Examples and statistics. *Astron. Astrophys.*, 406:1105–1121.

Wang, T. J., Solanki, S. K., Innes, D. E., Curdt, W., and Marsch, E. (2003b). Slow-mode standing waves observed by SUMER in hot coronal loops. *Astron. Astrophys.*, 402:L17–L20.

Weiss, A. A. and Sheridan, K. V. (1962). The Sizes of the Sources of Solar Radio Bursts at 40 and 60 Mc/s. *Journal of the Physical Society of Japan Supplement*, 17:223.

Wild, J. P. and McCready, L. L. (1950). Observations of the Spectrum of High-Intensity Solar Radiation at Metre Wavelengths. I. The Apparatus and Spectral Types of Solar Burst Observed. *Australian Journal of Scientific Research A Physical Sciences*, 3:387.

Wild, J. P. and Smerd, S. F. (1972). Radio Bursts from the Solar Corona. *Annual Review of Astron and Astrophys*, 10:159.

Wild, J. P., Smerd, S. F., and Weiss, A. A. (1963). Solar Bursts. *Annual Review of Astronomy and Astrophysics*, 1:291.

Young, C. W., Spencer, C. L., Moreton, G. E., and Roberts, J. A. (1961). A Preliminary Study of the Dynamic Spectra of Solar Radio Bursts in the Frequency Range 500-950 Mc/s. *Astrophys. J.*, 133:243.

Zaitsev, V., Zlotnik, E., Mann, G., Aurass, H., and Klassen, A. (1998). Herringbone bursts and efficiency of electron acceleration by shock waves in the solar corona. In *CESRA Workshop on Coronal Explosive Events*, page 70.

Zaitsev, V. V. (1974). Quasi-one-dimensional nature of the spectrum of plasma waves in type III radioburst sources. *Astronomicheskii Zhurnal*, 51:801–812.

Zaitsev, V. V. (1975). Quasi-one-dimensionality of plasma wave spectrum in type III radio burst sources. *Soviet. Astron.*, 18:475–481.

Zaitsev, V. V., Mityakov, N. A., and Rapoport, V. O. (1972). A Dynamic Theory of Type III Solar Radio Bursts. *Sol. Phys.*, 24:444–456.

Zaitsev, V. V. and Stepanov, A. V. (1975). On the origin of fast drift absorption bursts. *Astron. Astrophys.*, 45(1):135–140.

Zakharenko, V., Konovalenko, A., Zarka, P., Ulyanov, O., Sidorchuk, M., Stepkin, S., Koliadin, V., Kalinichenko, N., Stanislavsky, A., Dorovskyy, V., Shepelev, V., Bubnov, I., Yerin, S., Melnik, V., Koval, A., Shevchuk, N., Vasylieva, I., Mylostna, K., Shevtsova, A., Skoryk, A., Kravtsov, I., Volvach, Y., Plakhov, M., Vasilenko, N., Vasylkivskyi, Y., Vavriv, D., Vinogradov, V., Kozhin, R., Kravtsov, A., Bulakh, E., Kuzin, A., Vasilyev, A., Ryabov, V., Reznichenko, A., Bortsov, V., Lisachenko, V., Kvasov, G., Mukha, D., Litvinenko, G., Brazhenko, A., Vashchishin, R., Pylaev, O., Koshovyy, V., Lozinsky, A., Ivantyshyn, O., Rucker, H. O., Panchenko, M., Fischer, G., Lecacheux, A., Denis, L., Coffre, A., and Grießmeier, J.-M. (2016). Digital Receivers for Low-Frequency Radio Telescopes UTR-2, URAN, GURT. *Journal of Astronomical Instrumentation*, 5:1641010–738.

Zaqarashvili, T. V. (2003). Observation of coronal loop torsional oscillation. *Astron. Astrophys.*, 399:L15–L18.

Zaqarashvili, T. V. and Erdélyi, R. (2009). Oscillations and Waves in Solar Spicules. *Space Sci. Rev.*, 149:355–388.

Zaqarashvili, T. V., Khutsishvili, E., Kukhianidze, V., and Ramishvili, G. (2007). Doppler-shift oscillations in solar spicules. *Astron. Astrophys.*, 474:627–632.

Zaqarashvili, T. V., Melnik, V. N., Brazhenko, A. I., Panchenko, M., Konovalenko, A. A., Franzuzenko, A. V., Dorovskyy, V. V., and Rucker, H. O. (2013). Radio seismology of the outer solar corona. *Astron. Astrophys.*, 555:A55.

Zaqarashvili, T. V. and Murawski, K. (2007). Torsional oscillations of longitudinally inhomogeneous coronal loops. *Astron. Astrophys.*, 470:353–357.

Zhelezniakov, V. V. and Zaitsev, V. V. (1975). Some features of solar spike burst generation. *Astron. Astrophys.*, 39:107–111.

Zheleznyakov, V. V. and Zaitsev, V. V. (1970). The Theory of Type III Solar Radio Bursts. II. *Soviet. Astron.*, 14:250.

Zlobec, P., Messerotti, M., Karlicky, M., and Urbarz, H. (1993). Fine structures in time profiles of type II bursts at frequencies above 200 MHz. *Sol. Phys.*, 144:373–384.

Zlobec, P. and Thejappa, G. (1987). Type II Burst High Time Resolution and Polarization Characteristics at Frequencies Higher than 200 MHz. *Hvar Observatory Bulletin*, 11:111.

Zlotnik, E. I. (1981). The polarization of second harmonic radio emission in Type III bursts. *Astron. Astrophys.*, 101:250–258.

Zlotnik, E. Y. (2009). Origin of Zebra Pattern in Type IV Solar Radio Emission. *Central European Astrophysical Bulletin*, 33:281–298.

Zlotnik, E. Y., Klassen, A., Klein, K.-L., Aurass, H., and Mann, G. (1998). Third harmonic plasma emission in solar type II radio bursts. *Astron. Astrophys.*, 331:1087–1098.

Index

Alfvén speed, 144
Arecibo radio telescope, 52

Baumbach-Allen corona, 70, 241, 266, 283
Brightness temperature, 57, 119
Burst drift rate, 62
Bursts in absorption, 192, 208, 221
Butterfly diagram, 40

Carrington, 36
Caterpillar bursts, 15, 278, 286
Caterpillar polarization, 287
Chromosphere, 38
Clark Lake radio telescope, 52, 55
Corona, 38
Coronal arcs, 182
Coronal holes, 38
Coronal loop oscillations, 301
Coronal loops, 137
Coronal Mass Ejections, 15, 38, 40, 41, 148, 155, 171, 182
Coronal seismology, 212, 299
Coronal streamers, 154

Debye radius, 106
Digital spectral polarimeter, 261
Dog-leg Type III burst, 64, 91, 96
Double plasma resonance, 196
Drift pairs bursts, 15, 233
Drift pairs polarization, 243

Electron cyclotron frequency, 106, 242
Electron plasma frequency, 144

Faraday rotation, 254
Fast drift storm bursts, 249
Fiber burst, 80, 185, 193, 198, 207, 209
Fingerprint burst, 196, 200, 202
Fraunhofer, 37
Frequency drift rate, 70
Fundamental radio emission, 64

Galactic background radiation, 32
Galilei, 35
Gauribidanur radio telescope, 44, 53
Grotrian, 37

GURT radio telescope, 14, 17, 22, 23, 44, 133

Helmet streamers, 214
Herringbone structure, 142, 150
Hey, 13
Hodgson, 36

Interferometer mode, 116
Ion-sound waves, 145

J-burst, 14, 62, 125
J-bursts harmonic pair, 129
Jansky, 13

Kharkiv, 17

Langmuir turbulence, 15, 252
Langmuir wave frequency, 88, 242
Langmuir waves, 15, 61, 62, 88, 98, 103, 145, 182, 213, 266
Lodge, 13
LOFAR, 24, 44, 256
LWA, 44

Magnetic loops, 61
Magneto-acoustic oscillations, 204, 206
Maunder, 40

Nançay radio telescope, 14, 44, 85, 86, 268
NenuFAR, 44
Newkirk corona, 70, 119, 203, 276, 283
Nobeyama heliograph, 44
Nordmann, 13

O-waves, 106, 107
Owens Valley interferometer, 44

Penumbra, 39
Photosphere, 38
Plasma frequency, 70
Plasma mechanism, 213, 295, 300

Quiet Sun continuum radiation, 45

Radio seismology, 15, 221, 301
Radio source Taurus A, 46
RATAN-600 radio telescope, 44
Reber, 13

S-bursts, 15, 249, 251, 254
Scheiner, 35
Schwabe, 35, 39
Second harmonic emission, 63
Shock wave, 139, 146
Siberian Solar radio telescope, 44
SLAMS, 166
Solar continuum radio emission, 45
Solar active area, 78
Solar active regions, 14, 38
Solar decameter spikes, 15
Solar Dynamics Observatory, 153
Solar flare, 36–38, 62
Solar flux unit, 14

SOlar Heliospheric Observatory, 153
Solar magnetic loops, 124
Solar Orbiter spacecraft, 16, 24
Solar radio burst, 13, 14
Solar radio image, 44
Solar sunspot cycle, 40
Solar wind, 38
Southworth, 13
Spikes, 261
Spikes flux, 264
STEREO coronagraph, 153
STEREO spacecraft, 14, 24, 29, 44, 172, 278, 280
STEREO Waves instrument, 150
Striae, 98
Striae distribution, 78
Striae-burst, 62, 108
Sunspot relative number, 36
Sunspots, 35, 38

Tadpoles, 15, 165, 166
Transequatorial loop, 218, 301
Triple Type III burst, 109, 114
Turning Frequency Drift, 128
Two-stream instability, 295
Type II burst, 14, 52, 139, 145, 146, 149, 180
Type III burst, 14, 52, 61, 172
Type III burst fine structure, 73
Type IIIb burst, 62, 75
Type IIIb burst polarization, 103
Type IIIb-III pair, 65, 107
Type IV burst, 15, 52, 171, 172, 180, 188, 207

U-burst, 14, 62, 124
U-burst harmonic pair, 131, 138
Umbra, 39
Upper hybrid frequency, 253
URAN-2, 14, 21, 23, 24, 47, 85, 86, 149, 172, 243, 268, 292
URAN-2 polarization, 162
URAN-2 radio telescope, 45
UTR-2, 14, 17, 20, 21, 23, 24, 29, 45, 48, 51, 77, 85, 86, 146, 149, 180, 188, 243, 268, 292
UTR-2 radio telescope, 44
UTR-2 interferometry, 162

Visibility function, 54, 118, 160, 256
VLA, 45

WIND spacecraft, 24, 29, 44
WIND Waves instrument, 30
Wolf, 36
Wollaston, 37

X-waves, 106, 107

Z-waves, 106
Zebra pattern, 196, 198, 200, 202